Springer Theses
Recognizing Outstanding Ph.D. Research

Bruce L. Yoder

Steric Effects in the Chemisorption of Vibrationally Excited Methane on Nickel

Springer

Springer Theses

Recognizing Outstanding Ph.D. Research

For further volumes:
http://www.springer.com/series/8790

Aims and Scope

The series "Springer Theses" brings together a selection of the very best Ph.D. theses from around the world and across the physical sciences. Nominated and endorsed by two recognized specialists, each published volume has been selected for its scientific excellence and the high impact of its contents for the pertinent field of research. For greater accessibility to non-specialists, the published versions include an extended introduction, as well as a foreword by the student's supervisor explaining the special relevance of the work for the field. As a whole, the series will provide a valuable resource both for newcomers to the research fields described, and for other scientists seeking detailed background information on special questions. Finally, it provides an accredited documentation of the valuable contributions made by today's younger generation of scientists.

Theses are accepted into the series by invited nomination only and must fulfill all of the following criteria

- They must be written in good English.
- The topic should fall within the confines of Chemistry, Physics, Earth sciences and related interdisciplinary fields such as Materials, Nanoscience, Chemical Engineering, Complex Systems and Biophysics.
- The work reported in the thesis must represent a significant scientific advance.
- If the thesis includes previously published material, permission to reproduce this must be gained from the respective copyright holder.
- They must have been examined and passed during the 12 months prior to nomination.
- Each thesis should include a foreword by the supervisor outlining the significance of its content.
- The theses should have a clearly defined structure including an introduction accessible to scientists not expert in that particular field.

Bruce L. Yoder

Steric Effects in the Chemisorption of Vibrationally Excited Methane on Nickel

Doctoral Thesis accepted by
the École Polytechnique
Fédérale de Lausanne, Switzerland

Springer

Author
Dr. Bruce L. Yoder
University of British Columbia
Main Mall 2036
Vancouver
BC V6T 1Z1
Canada

Supervisor
Prof. Rainer D. Beck
Laboratory of Molecular
Physical Chemistry
Swiss Federale Institute of Technology
(EPFL), Station 6
1015 Lausanne, Switzerland

ISSN 2190-5053
ISBN 978-3-642-27678-1
DOI 10.1007/978-3-642-27679-8
Springer Heidelberg New York Dordrecht London

e-ISSN 2190-5061
e-ISBN 978-3-642-27679-8

Library of Congress Control Number: 2011946087

Printed on acid-free paper

Springer is part of Springer Science+Business Media (www.springer.com)

Parts of this thesis have been published in the following articles:

B.L. Yoder, R. Bisson, R.D. Beck, Steric effects in the chemisorption of vibrationally excited methane on Ni(100). Science **329**(5991), 553–556 (2010)

B.L. Yoder, R. Bisson, P.M. Hundt, R.D. Beck, Alignment dependent chemisorption of vibrationally excited $CH_4(v_3)$ on Ni(100), Ni(110), and Ni(111). J. Chem. Phys. **135**, p. 224703, (2011)

The article published in 2011 should be considered more up to date than the data contained in this thesis. The reader should defer to the JCP article for any minor discrepencies found between it and this thesis.

Supervisor's Foreword

Steric effects describe how the rate of a chemical reaction depends on the relative orientation of the reaction partners. The detection and exploration of steric effects are central to the field of chemical reaction dynamics, which seeks to describe chemical reactions at a microscopic level in terms of individual reactive collisions between reagent molecules. This thesis uncovers and explores a previously unknown steric effect in the dissociative chemisorption of methane on a nickel surface. The reaction is of critical importance for the chemical industry because the dissociation of methane on the surface of a nickel catalyst is the rate limiting step in the large scale transformation of natural gas into hydrogen used as clean fuel and as starting material for many other synthesis processes such as ammonia synthesis leading to synthetic fertilizers.

The experiments described in this thesis probe the reactivity of methane under highly defined conditions which specify most of the collision parameters such as speed of the incident molecules, their angle of incidence, as well as the composition and structure of the target surface, using a molecular beam of methane colliding with different faces of a Ni-single crystal in ultrahigh vacuum. Infrared laser excitation of the surface incident methane makes it possible to control the reagent's rotational and vibrational quantum state and probe how the methane reactivity depends on vibrational and rotational excitation.

In his thesis research described here, Bruce Yoder goes beyond what has been done in previous quantum state resolved gas/surface reaction dynamics experiments and also exerts control over the steric conditions. An intense molecular beam of vibrationally excited methane was produced by rapid adiabatic passage exploiting a new, continuous-wave, high-power, single-mode infrared optical parametric oscillator. During the infrared excitation of the antisymmetric (v_3) stretch vibration of CH_4 or the C–H (v_1) stretch of CD_3H by linearly polarized radiation, the angular momentum and vibrational transition dipole moment of methane are aligned in the laboratory frame. The excited, aligned molecular beam was used to probe the stereodynamics of the chemisorption reaction of vibrationally excited methane.

For methane dissociation on Ni(100), an increase in methane reactivity of nearly 60% is observed when the laser polarization is changed from normal to parallel to the surface. The dependence of the alignment effect on the rotational branch used for excitation (P-, Q-, or R-branch) indicates that alignment of the vibrational dipole moment rather than the angular momentum is responsible for the alignment dependent reactivity. Dephasing of the initially prepared alignment due to hyperfine coupling is observed to be on the timescale of 5–15 μs which does not preclude the study of alignment dependent reactivity in our experimental setup. Reactivity decreased monotonically from parallel to perpendicular alignment for both methane isotopologues studied. The alignment effect is shown to be independent of incident velocity for $CH_4(v_3)$ and appears to decrease with increasing velocity of $CD_3H(v_1)$.

For the Ni(110) surface, which consists of parallel rows of closely spaced Ni atoms separated by one-layer deep troughs, Yoder probed if the reactivity depends on the methane alignment relative to the direction of the surface rows. The $CH_4(v_3)$ reactivity increases by a factor of two when the laser polarization direction is changed from normal to parallel to the surface. Furthermore, alignment of the vibration perpendicular to the surface rows produced a higher reactivity than alignment parallel to the surface rows.

The detailed reactivity data described in this thesis provides stringent tests for theoretical models of methane/surface reactivity and thereby will aid the development of a better predictive theoretical description of methane/surface reactivity which in turn may lead to better catalysts and more energy efficient synthesis processes.

Switzerland, November 2011 Prof. Rainer D. Beck

Acknowledgments

My time in Lausanne has been a wonderful experience and I owe much of it to my friends and colleagues. I would like to address my sincere gratitude to all mentioned here for the valuable contributions they brought to this thesis work and to me.

To my thesis advisor, Prof. Rainer Beck: Thank you for taking me into your group, for always pushing me to do better, for your availability, your insight, your example, and your patience. I have learned a lot through working with you.

To Prof. Thomas Rizzo: Thank you for accepting me into the Laboratoire de Chimie Physique Moléculaire and for helpful advice during my doctoral work.

A Dr. Régis Bisson: Merci de m'avoir enseigné comment fonctionne notre laboratoire, pour ton enthousiasme, de m'avoir appris à parler français, et pour ton amitié.

A Marianne Dang: Merci beaucoup. Tu m'as tellement aidé.

To Dr. Thanh Tung Dang, Dr. Marco Sacchi, Li Chen and Morten Hundt: Thank you for making our group a friendly, positive place to work and for all the constructive input.

To Dr. Mathieu Schmid and Dr. Plinio Maroni: Thank you for constructing the surface science machine and developing the experimental setup to such a nice form.

To my thesis committee members Prof. Fleming Crim, Prof. Andreas Osterwalder, Prof. Bret Jackson and Prof. Vassily Hatzimanikatis: Thank you.

To the entire group at the Laboratoire de Chimie Physique Moléculaire: I am fortunate to have worked with such a dynamic, international group. I would like to particularly acknowledge Dr. Marcel Drabbels, Giorgos Papadopoulos, Dr. Monia Guidi, Dr. Annette Svendsen, Ulrich Lorenz, Dr. Evgeniy Loginov, Maxim Grechko, Dr. Jaime Stearns, Prof. Tino Gäumann and Dr. Oleg Boyarkine.

A l'atelier mécanique: Merci pour tous les projets bien réussis. Ca a toujours été un plaisir de travailler avec vous. J'aimerais remercier en particulier André Fattet, Yves Morier, Gil Corbaz, Christophe Clement, Roger Mottier et Cédric Mora.

A l'atelier électronique: Merci pour votre aide. Essentiellement Patrick Favre, Supardi Sujito, Frederic Gumy, Gabriel Roch et Pierre-André Perroud.

A mon amour, Maya Chelmis: Merci. Tu m'as donné plus que tu ne le sais. Sans toi, je n'y serait jamais arrivé. Je t'aime.

And finally, to my family- Beverly (mom), Dwight (dad), Derrick (Pete), Beth and Theodore: Thank you for your unconditional love and support. You are the stability of my life.

Switzerland, July 2010 Bruce L. Yoder

Contents

1 Introduction 1
1.1 Motivation 1
1.2 Gas-Surface Interactions 2
1.3 Gas-Surface Reaction Dynamics 5
1.4 Steric Effects in Gas-Surface Reactions 9
1.5 Inspiration From Gas-Phase Experiments 11
1.6 Outline 15
References 16

2 Experimental Setup 19
2.1 Overview of Experimental Setup 19
2.2 Molecular Beam Source 19
2.3 Surface Science UHV Chamber 21
2.3.1 Overview 21
2.3.2 Quadrupole Mass Spectrometer (QMS) 22
2.3.3 Sample Preparation 25
2.3.4 Auger Spectrometer 25
2.3.5 LEED Spectrometer 27
2.4 CW-IR State-Preparation Setup 28
2.4.1 Overview 28
2.4.2 Light Source 29
2.4.3 Wavemeter 31
2.4.4 Tunable $\lambda/2$ Wave Plate 32
2.5 Frequency Stabilization 33
2.5.1 Lamb Dip Detection and Characterization 36
2.5.2 Lamb Dip Locking 40
2.6 Pyroelectric Detection of Vibrationally Excited Molecules in a Molecular Beam 45
References 49

3 State Specific Preparation and Alignment of Gas-Phase Reagents . 51
3.1 Introduction 51
3.2 Rovibrational Excitation of Molecular Beam 51
3.2.1 Rapid Adiabatic Passage (RAP) 52
3.3 Alignment of Vibrationally Excited Molecules in the Laboratory Frame 78
3.3.1 Angular Momentum Alignment 79
3.3.2 Vibrational Transition Dipole Moment Alignment. 86
References 92

4 State-Resolved Steric Effects in Methane Chemisorption on Ni(100) 95
4.1 Introduction 95
4.2 $CH_4(v_3 = 1)$ Reactivity and Alignment Effects on Ni(100). 95
4.2.1 Independence of Excitation Efficiency Upon Polarization Rotation. 98
4.2.2 Polarization Dependence of Vibrationally Excited Methane Reactivity 99
4.2.3 Effect of Hyperfine Depolarization on $CH_4(v_3)$-R(0) Reactivity. 103
4.2.4 Comparison of Δ_p and Calculated Alignment Coefficients for $CH_4(v_3)$ 106
4.2.5 Detailed Polarization Angle Dependence of the $CH_4(v_3)$-R(0) Reactivity. 108
4.2.6 Absolute Sticking Coefficients of $CH_4(v_3)$-R(0) on Ni(100) 110
4.3 $CD_3H(v_1 = 1)$ Reactivity and Alignment Effects on Ni(100) . . . 115
4.3.1 Effect of Hyperfine Depolarization on $CD_3H(v_1)$-R(0) 117
4.3.2 Comparison of Δ_p and Calculated Alignment Coefficients for $CD_3H(v_1)$ 118
4.3.3 Effect of Polarization Rotation with Respect to the Surface for $CD_3H(v_1)$-R(0). 119
4.4 Discussion of Results. 121
References 129

5 State-Resolved Steric Effects in $CH_4(v_3)$ Dissociation on Ni(110) 133
5.1 Introduction 133
5.2 $CH_4(v_3)$ on Ni(110)-(*Parallel* vs. *Normal*) 135
5.3 $CH_4(v_3)$ on Ni(110)-(*Perpendicular* vs. *Normal*) 140
5.4 Discussion of Results. 142
References 146

6 Summary and Outlook 147
6.1 Summary 147
6.2 Experimental Improvements 151
6.2.1 Modulation of Excitation Laser Polarization 151
6.2.2 Free-Swinging UHV Pendulum for Molecular Beam Chopping 153
6.3 Future Directions 158
References 159

Appendix A: Procedure for 'Locking' OPO Idler Frequency to Lamb Dip 161

Appendix B: Beta Axis Calculation for R(0), R(1), P(1), Q(1) With and Without K-Resolution 167

Appendix C: $CD_3H(\nu_1)$ Rovibrational Transitions 173

Chapter 1
Introduction

1.1 Motivation

The search for insight into the microscopic details of chemical reactions is the central theme of all chemical dynamics investigations. With this goal in mind, experimental studies of gas/surface reaction dynamics have evolved with increasingly refined measurements and models. Understanding of gas/surface reactivity is imperative because of the critical role that these reactions play in many industrial processes such as hydrogen production, heterogeneous catalysis for chemical synthesis or chemical vapor deposition of thin films.

Methane, the simplest alkane, is an attractive candidate for the study of C–H bond activation. The methane–nickel system has become the prototype gas-surface reaction for the study of polyatomic reaction dynamics, as it is simple enough to allow detailed experimental control of the system and is tractable for high-level calculations. This system is practically significant as the activation of a carbon–hydrogen bond is the critical step in several relevant catalytic processes. The rate limiting step in steam reforming, the principal industrial process for the production of hydrogen, is the dissociation of methane on a nickel catalyst to form surface-bound methyl and hydrogen [1].

Today, highly detailed quantum state-resolved measurements can be used to reveal the underlying microscopic dynamics and reaction mechanism. Quantum state-resolved data also enable stringent tests of theoretical models of gas/surface reactivity, which are necessary for a predictive understanding of heterogeneous catalysis and other important technological processes involving surface reactions. Methane chemisorption on single crystal metal surfaces has been shown to be a highly dynamical process that is both vibrationally mode-specific [2] and bond-selective [3]. These observations are incompatible with statistical rate theory, which predicts reaction rates solely on energetics [4–6].

In this thesis work, I study steric effects in the chemisorption of vibrationally excited methane. Specifically, I investigate whether the reaction probability of

B. L. Yoder, *Steric Effects in the Chemisorption of Vibrationally Excited Methane on Nickel,* Springer Theses, DOI: 10.1007/978-3-642-27679-8_1,

quantum state-prepared methane on a metal surface depends on the alignment of the gas-phase molecule's angular momentum ($\vec{J}$) and/or its vibrational transition dipole moment (vibrational amplitude) relative to the surface. The results of this project provide detailed information for the understanding of the dissociative chemisorption of vibrationally excited gas-phase molecules on surfaces that will serve as a stringent test of multi-dimensional dynamics calculations.

1.2 Gas-Surface Interactions

As a gas phase molecule approaches a metal surface, the gas molecule experiences an attractive and then repulsive force between its nuclei and electrons and the surface. Figure 1.1 shows schematically a one dimensional potential energy curve of a methane molecule approaching a metal surface [7]. The binding of molecules on a surface due to gas-surface interactions is termed *adsorption*. At large molecule-surface distances (several angstroms) the gas-surface interaction is dictated by attractive Van der Waals' forces. Molecules trapped (bound by $\sim$5–500 meV/molecule) on the surface by these forces are said to be *physisorbed*. At smaller molecule-surface separation (a few angstroms) the electronic orbitals of the molecule and metal surface overlap. This overlap can rearrange the electron distribution enough to form a chemical bond between the molecule and surface, weakening and/or breaking intramolecular bonds. Molecules bound (binding energy $\sim$1–10 eV/molecule) to a surface in such a way are said to be *chemisorbed* [8]. The *physisorbed* and *chemisorbed* states are separated by a *transition state* (T.S.), which is a local maximum in the energy of the molecule-surface potential energy surface (PES) that corresponds to the barrier in the reaction $CH_4(g) \overset{Metal}{\longrightarrow} CH_3(ads.) + H(ads.)$, as shown in Fig. 1.1.

The molecule-surface interaction is described by its potential energy, the y-axis in Fig. 1.1, with bound states corresponding to local minima in energy. The role of different types of energy (i.e. translational, vibrational, etc.) is not explicit in this one dimensional model. Here, only the total energy and the molecule-to-surface distance are incorporated. This is, obviously, a quite crude description of an interaction between a gas molecule and a surface, though it does allow for the introduction of some central concepts.

One can gain insight into molecule-surface interactions by considering a bimolecular reaction in the gas phase. Figure 1.2 shows four two-dimensional PES for the model reaction of A + BC $\rightarrow$ AB + C, where r_1 and r_2 are the internuclear separations of B–C and A–B, respectively. These 'elbow' PES diagrams were first proposed by Polanyi [9, 10]. The contour lines in the diagrams indicate equipotential regions in the PES. The one-dimensional PES shown in Fig. 1.1 is contained in the two dimensional 'elbow' PES and corresponds to the minimum energy pathway connecting the reactants to products. The highest energy point along the minimum energy reaction pathway is the reaction's barrier or transition state (T.S. in Fig. 1.1) and is marked by an $\otimes$ in Fig. 1.2. In these 'elbow' PES,

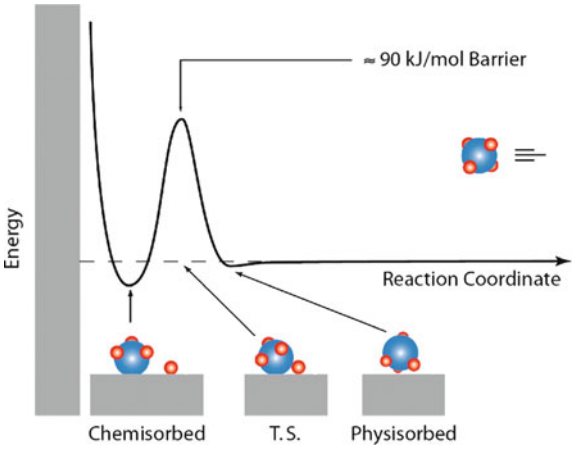

Fig. 1.1 One dimensional potential energy diagram for activation of methane on a metal surface [7]. Figure is reproduced with permission

the reactants approach the transition state from the lower-right corner and the products exit the reactive complex to the upper-left corner. In this framework, vibration of the BC reactant bond takes the form of an oscillation in the r_2 coordinate.

Polanyi et al. [9, 10] used classical trajectory simulations of the gas-phase reaction of A + BC to identify how the PES can affect energy consumption and disposal. It was demonstrated that the location of the reaction barrier (T.S.) in relation to the entrance and exit channel was an important feature of the PES. Figure 1.2 shows two distinct limiting cases, namely the 'Early barrier' and 'Late barrier' cases. For the 'Early barrier' case shown in Fig. 1.2a and b, the transition state is located in the reaction's entrance channel or near the equilibrium BC product bond length. Here, translational energy (E_{TRANS}) is found to be more effective in promoting the reaction than vibrational energy (E_{VIB}) because E_{TRANS} is directed along the minimum energy reaction pathway at the transition state. For the 'Late barrier' case depicted in Fig. 1.2c and d, the transition state is found at an extended BC bond length. Here, the E_{VIB} is more effective at promoting the reaction than E_{TRANS} because E_{VIB} causes an extension of the BC bond, and therefore is directed along the minimum energy reaction pathway at the transition state.

The trajectories drawn in Fig. 1.2a–d illustrate four limiting cases of the bimolecular reaction of A + BC → AB + C. By performing a large number of classical trajectory calculations averaged over a distribution of initial conditions (incident angle, vibrational excitation/phase, etc.…), Polyani and coworkers were able to model energy consumption and disposal in agreement with experimentally observed bimolecular reaction measurements. The reaction barrier in all four PES in Fig. 1.2 is 7 kcal/mol (29.4 kJ/mol). The reactive encounter on an 'Early barrier' PES, shown in Fig. 1.2a, is achieved by giving the reactants 9 kcal/mol (38 kJ/mol) solely in the form of E_{TRANS}. For the nonreactive encounter on the 'Early barrier' PES, in Fig. 1.2b, the reactants have 16 kcal/mol of energy (E_{TRANS} = 1.5 and E_{VIB} = 14.5 kcal/mol). E_{TRANS} was shown to be more effective at overcoming the

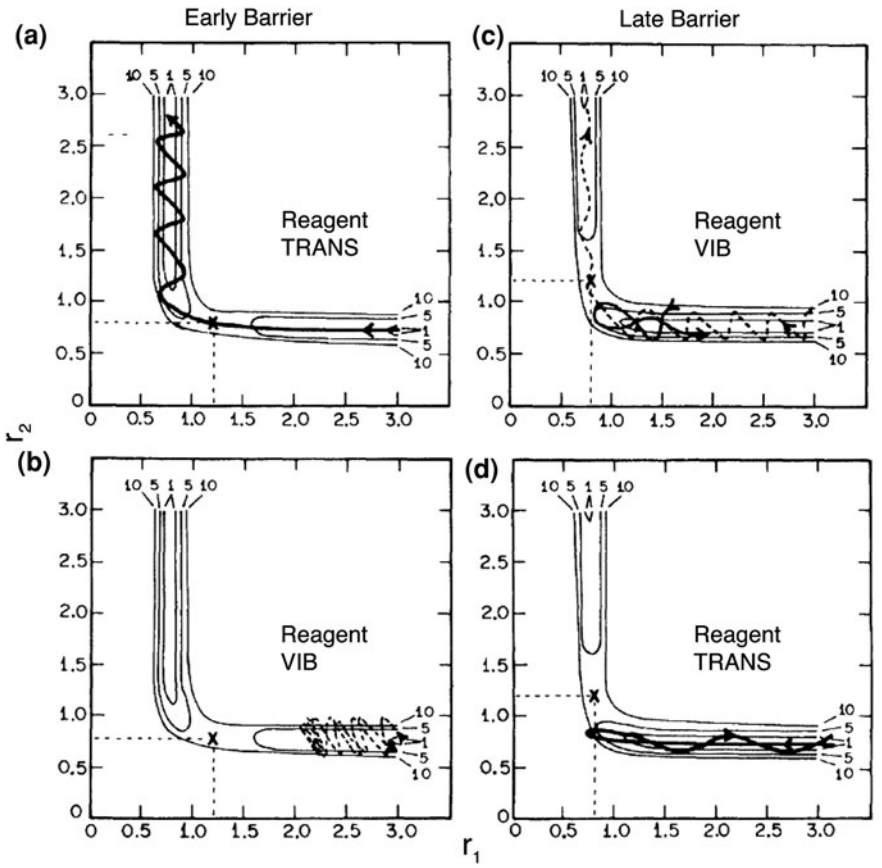

Fig. 1.2 Classical trajectories on different types of PES for reactions of the type A + BC → AB + C, where r_1 and r_2 represent the internuclear separation of BC and AB (in Angstroms), respectively [9, 10]. The reactant energy content in kcal/mol is **a** $E_{TRANS} = 9$, $E_{VIB} = 0$, **b** $E_{TRANS} = 1.5$, $E_{VIB} = 14.5$, **c** $E_{TRANS} = 1.5$, $E_{VIB} = 7.5$, **d** $E_{TRANS} = 16$, $E_{VIB} = 0$ and all barrier heights are 7 kcal/mol. Modified figure is reproduced with permission

'Early barrier' PES barrier with the products carrying away excess energy in the form of E_{VIB}. For the reactive encounter on the 'Late barrier' PES, in Fig. 1.2c, the reactants have 9 kcal/mol of energy ($E_{TRANS} = 1.5$ and $E_{VIB} = 7.5$ kcal/mol). While for the nonreactive encounter on the 'Late barrier' PES, the reactants have 16 kcal/mol of energy ($E_{TRANS} = 16$ and $E_{VIB} = 0$ kcal/mol). This illustrates the preference for reactant energy being in the form of E_{VIB} as the reactants approach the reaction's transition state in a 'Late barrier' PES, and the predicts the excess energy of the reactants disposed of as E_{TRANS} in the product channel.

The idea, described above, that either E_{VIB} or E_{TRANS} could be more efficient at promoting a reaction is inconsistent with statistical rate theory [4–6, 11]. Statistical rate theory assumes complete randomization of initial conditions in the reaction

complex. In this framework, reactivity is solely a function of the total available energy in the system. If this were true, then it should not matter how energy is partitioned in the reactants, but only how much energy is available to them.

These two dimensional, 'elbow', PES give insight into the dynamics of a chemical reaction, but do not resolve several possibly critical aspects of the reaction (i.e. different types of vibrations, rotations, molecular orientations, etc.…). As the number of degrees of freedom in a system increase, the complexity of a PES also increases. The potential energy of a system is written as a function of the system's nuclear coordinates taking advantage of the Born–Oppenheimer approximation (BOA) [12], which assumes that electronic motion is sufficiently faster that nuclei motion, so that the electronic a nuclear components of a molecular wavefunction can be separated. Though, this assumption has been called into question in recent years [13–15]. Assuming the BOA, the multidimensional potential energy surface of methane interacting with a frozen surface is a function of 15 coordinates: 3 translational, 3 rotational and 9 vibrational. This makes calculation of the full dimensional PES time consuming. Consequently, gas-surface interactions are usually discussed in terms of reduced dimensionality [16] in an attempt to capture only the most relevant degrees of freedom in the studied system.

Experimentalists can help to reduce the dimensionality of the PES needed in calculations by conducting well controlled experiments that produce highly detailed results. In order to produce such highly detailed experimental results, we have studied steric effects in the dissociative chemisorption of quantum state-prepared, aligned methane on single crystal nickel surfaces.

1.3 Gas-Surface Reaction Dynamics

For more than two decades, methane has been used as a prototype gas-phase reactant in experimental studies of gas-surface reactions. A recent review in Progress in Surface Science by Juurlink et al. [7] provides a thorough summary of research in the field of methane activation on metal surfaces with a focus on quantum state-resolved measurements. Drawing from Juurlink et al. [7], I discuss the recent evolution of control exerted over gas-surface reactions. The goal of highly detailed experiments is to dissect a complicated process (i.e. a gas/surface reaction) in order to understand how the various experimental parameters (i.e. E_{TRANS}, E_{VIB}, reactant geometries, etc.) affect the probability of reaction.

Supersonic molecular beams enabled the preparation of gas-phase reactants with well-defined E_{TRANS} and incident angle to study adsorption reactions, essentially eliminating the experimental averaging over these parameters that took place in bulb experiments [17–19]. Molecular beam studies clearly demonstrated that E_{TRANS} of the incident methane efficiently activates its dissociative chemisorption on a metal surface through the observation of a nearly exponential rise in reactivity with E_{TRANS} directed along the surface normal [20–23].

E_{TRANS} (eV)	$T_{surface}$ (K)	T_{nozzle} (K)	S_o
0.11 ± 0.01	800	770	2.5 ± 1.0 x10^{-5}
0.11 ± 0.01	800	340	5.0 ± 2.0 x10^{-6}
0.23 ± 0.02	800	720	4.0 ± 2.0 x10^{-5}
0.23 ± 0.02	800	305	7.0 ± 5.0 x10^{-6}

Fig. 1.3 Effect of nozzle temperature on the measured initial sticking probabilities, S_0, of CH_4 on W(110). Table reproduced from Ref. [22]

In the seminal work by Auerbach and coworkers [20], the initial sticking probability, S_0, of CH_4 on a clean W(110) was measured over a wide range of incident translational energies. S_0 was determined from the initial slope of coverage-versus-exposure (uptake) curves and found to rise almost exponentially from 3×10^{-6} to 2×10^{-1} as E_{TRANS} was increased from 5 to 100 kJ/mol. The fact that the methane reactivity scales with the normal component of the translational energy ($E_\perp$) provides evidence for a direct, activated reaction mechanism where the incident methane dissociates upon surface impact by using the E_{TRANS} to overcome the reaction barrier. The exponential rise in S_0 was attributed to a distribution of reaction barrier heights due to different orientations of the incident methane and a distribution of impact sites. A model of the dissociative chemisorption of methane in which a hydrogen atom tunnels through a barrier in the reaction coordinate was proposed. The semiempirical result for S_0 as a function of $E_\perp$ was determined to be

$$S_0 \cong \alpha \cdot \exp(\beta E_\perp). \tag{1.1}$$

where, the two parameters are (1) S_0 as $E_\perp$ goes to zero $(\alpha \cong 2\text{x}10^{-6})$ and (2) the efficacy $\left(\beta = \dfrac{\Delta \ln S_0}{\Delta E_\perp} \cong 12.5\ \text{eV}^{-1}\right)$. These values are consistent with tunneling through a parabolic reaction barrier having a height of 1.1 eV and half-width of 0.25 Å.

In a continuation of the work discussed in the previous paragraph, Auerbach and coworkers assessed the role of E_{VIB} in the dissociative chemisorption of methane on tungsten and rhodium surfaces [22]. They compared the reactivity of methane beams produced with different nozzle temperatures but at similar translation energy by seeding of methane in argon and helium. Rotational cooling had been shown to be nearly complete in supersonic expansions [24], so that the difference in reactivity for the iso- E_{TRANS} beams using different nozzle temperatures was attributed to the varying amount of E_{VIB} content. Figure 1.3 shows a table, taken from the article [22], with values of S_0 for two translational energies and nozzle temperatures.

For both translational energies of 0.11 and 0.23 eV, a nearly fivefold increase in S_0 was observed when raising the nozzle temperature from ~300 to ~750 K. Analogous to the expression for the E_{TRANS} dependence of S_0 shown in Eq. 1.1, Auerbach and coworkers determined the vibrational efficacy (β_{VIB}) by assuming

that all vibrations of methane produced an increase in reactivity in proportion to their energy content. Considering the 6 lowest vibrational levels in the analysis, they found a vibrational efficacy of $\beta_{VIB} = \frac{\Delta \ln S_0}{\Delta E_{\mathrm{VIB}}} \cong 12.4\ \mathrm{eV}^{-1}$ which is nearly identical to the value of the translational efficacy $\beta_{E\perp}$. This result led to the conclusion that E_{VIB} and E_{TRANS} are nearly equivalent in overcoming the chemisorption barrier for CH_4 dissociation on W(110) if all vibrations of the incident methane molecule participate equally in activating the reaction. However, the authors note that if only a subset of the vibrational modes are active in promoting methane's dissociation then their individual vibrational efficacies could exceed the translational efficacy.

Later, the addition of laser preparation of specific ro-vibrationally excited states in the incident molecular beam permitted the measurement of quantum state-resolved gas/surface reactivities [2, 3, 25–33]. This experimental improvement eliminated the averaging over vibrational and rotational populations in the molecular beam, and would lead to a more detailed understanding of the role of E_{VIB} in gas/surface reactions. Quantum state-resolved measurements enable experimentalists to address questions such as:

- Are there vibrations that are more efficient than others at promoting a reaction?
- Can vibrational energy be more efficient than translational at promoting a reaction?
- Could a bond be selectively broken by preparing a quantum state that stretches said bond?

Since 1999, three research groups have reported quantum state-resolved methane/surface reactivity measurements using nickel and platinum single crystal surfaces. The first three measurements quantified the reactivity of $CH_4(v_3 = 1)$ on Ni(100) [25], $CH_4(v_3 = 2)$ on Pt(111) [26] and $CH_4(v_3 = 2)$ on Ni(100) [34]. All three groups observed that the vibrationally excited molecules were much more reactive than ground state molecules. The $CH_4(v_3 = 1)$ on Ni(100) [25] and $CH_4(v_3 = 2)$ on Ni(100) [34] studies reported that E_{TRANS} and E_{VIB} were similarly effective at promoting dissociation, while the $CH_4(v_3 = 2)$ on Pt(111) [26] found E_{VIB} to be less effective than E_{TRANS}. These results demonstrated that methane dissociation is activated by E_{VIB}, but did not address the question whether different modes of methane differ in their efficacy of activation.

In 2003, Beck et al. [2] published the first example of 'mode-specific' reactivity in a gas/surface reaction. For CH_2D_2 dissociation on Ni(100), the authors demonstrated that the excitation of two quanta of C–H stretch in a single oscillator is more effective at promoting reaction than exciting one quantum of stretch in each of the two C–H oscillators. The symmetric (v_1) and the antisymmetric (v_6) C–H stretch normal modes can be described in a local mode basis as localized excitations of individual C–H bonds. Excitation of the molecular beam of CH_2D_2 with 5,880 cm^{-1} or 6,000 cm^{-1} light produced local mode states $|20\rangle$ or $|11\rangle$, respectively. In the local mode basis, $|20\rangle$ corresponds to a double-excitation of

one C–H and $|11\rangle$ corresponds to a single quantum excitation in each of the C–H bonds of CH_2D_2. At an $E_{TRANS} = 41$ kJ/mol, $S_0^{|20\rangle}$ was found to be >5 times higher than $S_0^{|11\rangle}$, even though the $|11\rangle$ state was the more energetic mode. This answered the question as to whether there are vibrations that are more efficient than others at promoting a gas/surface reaction. This reactivity difference was explained by the larger C–H bond extension of the molecules prepared in $|20\rangle$ than those prepared in $|11\rangle$. The study proved that energy redistribution in the incident reagent molecule is limited during its approach and collision with the reactive surface and that the molecule retains at least some memory of its initially prepared quantum state, which is inconsistent with a statistical mechanism of reactivity. In the experimental setup, it was not possible to determine if the vibrational excitation led to a selective cleavage of the C–H bond, rather than the C–D bond.

In 2005, Maroni et al. [30] used stimulated Raman pumping to excited the symmetric C–H stretch fundamental v_1 to prepare a molecular beam of $CH_4(v_1 = 1)$ for state-resolved reactivity measurements. The $CH_4(v_1 = 1)$ reactivity was measured to be about an order of magnitude higher than that of $CH_4(v_3 = 1)$ on Ni(100) even though v_1 and v_3 are nearly isoenergetic. In fact, $CH_4(v_1 = 1)$ was determined to be nearly as reactive as $CH_4(v_3 = 2)$ on Ni(100). E_{VIB} in the form of v_1 vibration was determined to be 1.4x as efficient as E_{TRANS} for promoting the dissociation of methane on N(100). This answered the question as to whether E_{VIB} can be more efficient than E_{TRANS} at promoting a gas/surface reaction.

The experimental results of Maroni et al. [30] agreed with the vibrationally adiabatic model proposed by Halonen et al. [35]. The authors used four-dimensional variational calculations to model the energy flow between CH_4 stretching vibrational states as a molecule approaches a metallic surface adiabatically. The model reduced the CH_4 molecule to a single H_3C–H oscillator with the 'active' C–H bond pointing toward and the 'spectator' CH_3 group pointing away from the surface. For the case of $CH_4(v_1 = 1)$ approaching a structureless metal surface, they found E_{VIB} localization into the unique, 'active' C–H bond pointing toward the surface. While for $CH_4(v_3 = 1)$, they found adiabatic energy flow into the 'spectator' CH_3 group, essentially quarantining the energy from participation in promoting the dissociation reaction.

In 2008, Killelea et al. [3] demonstrated bond-selective chemistry in a gas/surface dissociation reaction using CD_3H. The CD_3H molecule offers two dissociation reaction paths: breaking either its unique C–H bond or one of its three C–D bonds. The authors prepared a molecular beam of $CD_3H(v_1 = 1)$, where the v_1 normal mode corresponds to a local mode C–H stretch state [36] to a good approximation. This allowed the authors to measure the extent of energy flow from the initially prepared C–H stretch into the potentially reactive C–D bonds. To distinguish the reaction pathways, they titrated the CD_3 and CD_2H products bound to the surface upon dissociation of CD_3H with D-atoms that were absorbed into the sub-surface region prior to impinging the molecular beam of CD_3H on the nickel single crystal. CD_4 desorbed from the surface after deuteration of CD_3 (the product of C–H bond cleavage) and CD_3H from deuteration of CD_2H (the product

of C–D bond cleavage). Desorbing isotopologues of methane were detected by mass spectrometry, and revealed the dissociation pathway taken by the impinging $CD_3H(v_1 = 1)$.

The authors reported that the C–H bond was preferentially broken for the dissociation of $CD_3H(v_1 = 1)$ on Ni(100). They showed that a 'thermal ensemble' composed of $E_{TRANS} = 79.8$ kJ/mol and $E_{VIB} = 14.4$ kJ/mol dissociated statistically by breaking the C–H or C–D at a ratio of 1:3, but CD_3H prepared in $v_1 = 1$ with $E_{TRANS} = 57.4$ kJ/mol and $E_{VIB} = 36$ kJ/mol dissociated with a C–H:C–D ratio of >30:1. This result proves that energy redistribution does not (at least in favorable cases) prevent vibrationally assisted, bond-selective chemistry in a gas/surface reaction. Such bond-selective chemistry was demonstrated previously in bimolecular gas-phase reactions by Crim and coworkers [37–39] as well as by Zare and coworkers [40, 41].

The results of such detailed quantum state-resolved reactivity measurements of methane on single crystal metal surfaces clearly demonstrate that molecular vibrations play a critical role in reactivity. Progress in experimental techniques provides ever-increasing control over reactant preparation, and enables more and more detailed measurements. Here I have focused on vibrations in the gas-phase reactant, but the surface composition [29], impact site [32], structure [42] and temperature [33] have all been found to have an effect on reactivity.

In the present study, we take the detail of reactant preparation in gas/surface dynamics experiments to another level by using quantum state-prepared reagents that are aligned in the laboratory frame in order to address questions such as:

- Does the reactivity of state-prepared methane depend on its alignment with respect to the surface plane?
- Does the alignment of the incident molecule relative to the crystalline surface structure affect reactivity?

1.4 Steric Effects in Gas-Surface Reactions

Polanyi pointed out the opportunity to study stereochemistry in gas/surface reactions since the single crystal target surface represents a perfectly oriented reaction partner [10]. What is needed to completely define the collision geometry is a method to orient or align the incident molecules relative to the plane of the surface. Several techniques have been used successfully to study steric effects in gas/surface reactions, such as hexapole state-selection followed by reactant orientation in a static electric field before collision with a target surface [43–48], alignment of ionic reactants by resonant enhanced multi-photon ionization (REMPI) via linearly polarized light [49], and the exploitation of collisional rotational alignment in supersonic molecular expansions [50–54]. Another method to obtain information about gas/surface stereochemistry is REMPI by linearly polarized light of molecules desorbing from a surface and application of the

principle of detailed balance [55, 56]. Unfortunately, none of these techniques are applicable to CH_4.

Here, I highlight one gas/surface stereodynamics study to show the detailed information that can be gained in such studies. Wodtke, Auerbach and coworkers [55] used REMPI via a linearly polarized laser to selectively ionize D_2 in a specific ro-vibrational state whose bond axis is parallel to the excitation's electric field vector. They probed the quantum state-resolved velocity distributions and alignment of D_2 molecules leaving a Cu(111) surface after formation by recombinative desorption of D atoms. Applying the principle of detailed balance and microscopic reversibility, the authors used their state-resolved desorption data to draw conclusions about the reverse reaction which is the dissociative chemisorption of D_2 on Cu(111). The reactivity of both $D_2(v = 0, J = 11)$ and $D_2(v = 1, J = 6)$ on Cu(111) was found to be higher for broadside collisions (the bond axis parallel to the surface) than for end-on collisions (the bond axis along the surface normal) at the lowest translational energies studied. As the E_{TRANS} of incident D_2 increased much above the dissociative adsorption barrier, the steric preference of the reaction decreased rapidly. In these experiments, the degree of alignment for the dissociating $D_2(v, J)$ molecules was quantified using the state-resolved, polarization dependent data at several E_{TRANS} to calculate quadrupole alignment coefficients [57, 58].

Two competing explanations were offered to account for the E_{TRANS} dependence of the observed steric preference: (1) realignment or 'steering' effects and (2) changes in the ratio of the anisotropy energy (or 'aligned' component of the energy in the form of rotation and vibration) to E_{TRANS}. The first explanation stems from the idea that molecules approaching a surface in an unfavorable alignment can be realigned or 'steered' closer to the lowest energy pathway for reaction by an anisotropic interaction potential between the molecule and the surface. If steering were complete, the initial alignment is of little importance and no steric preference in the reaction would be observed. Steering should become increasingly important as E_{TRANS} of the approaching molecule is lowered, since the time spent by the molecule in the anisotropic part of the surface potential will increase with decreasing E_{TRANS}. Therefore, if steering were significant, one would predict the steric preference to decrease with decreasing E_{TRANS}. Wodtke, Auerbach and coworkers observed the opposite behavior and concluded that steering was not significant under their experimental conditions. The second explanation for the E_{TRANS} dependence of the steric preference considers the ratio of anisotropic to translational energy in excess of reaction's activation barrier. For E_{TRANS} below the activation barrier, only those molecules with an alignment closely matched to the minimum energy transition state configuration will be able to dissociate. As the available energy of the incident D_2 increases, a wider range of reactant alignments will be able to dissociate. Consequently, the steric preference for reaction should decrease with increasing energy. This explanation is in agreement with the experimental findings.

One can gain information about the reactive PES through careful experiments and analysis. The study produced interesting results that could be used to test

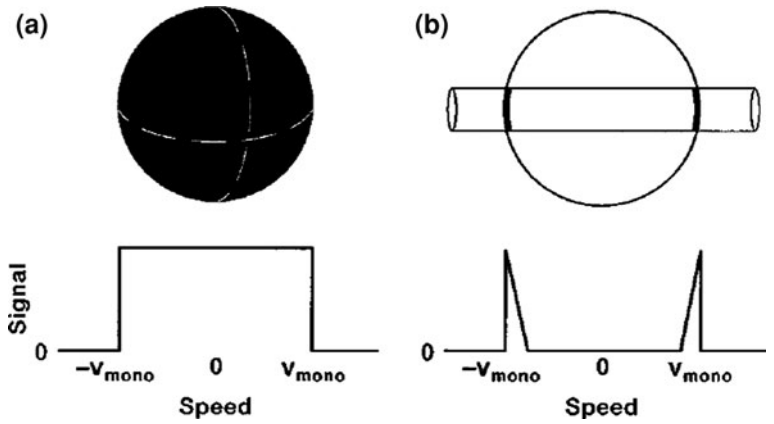

Fig. 1.4 Core extraction demonstrated for a spatially isotropic, monoenergetic speed distribution. **a** shows the detected speed distribution with core extraction. **b** shows the core extracted speed distribution [63]. Figure is reproduced with permission

models of gas-surface interactions, toward the goal of a predictive understanding of gas/surface reactions.

1.5 Inspiration From Gas-Phase Experiments

This thesis work was inspired in part by a series of well controlled experiments done on gas-phase reactions in the 1990s. Zare and coworkers investigated the mechanism for the reaction of atomic chlorine with vibrationally excited methane [59–62]. The studied reactions were:

$$Cl\left(^2P_{3/2}\right) + CH_4(v_3 = 1, J) \rightarrow HCl(v, J) + CH_3$$

$$Cl\left(^2P_{3/2}\right) + CD_3H(v_1 = 1, J) \rightarrow HCl(v, J) + CD_3$$

To realize the reactions, a supersonic expansion of methane, Cl_2 and helium was produced in a component ratio of 3:1:4. In the study, the authors prepared either the antisymmetric stretch (v_3) of CH_4 or the C–H stretch (v_1) of CD_3H. Excitation by linearly polarized light produced an alignment of the excited methane molecules' angular momentum ($\vec{J}$) and vibrational transition dipole moment (vibrational amplitude) in the laboratory frame. Then, monoenergetic Cl atoms were produced in the expansion by photolysis of the co-expanded Cl_2 using linearly polarized 355 nm light. The resulting ground state (>98% of total) Cl atoms have their E_{TRANS} (15.3 kJ/mol) highly aligned in the center-of-mass frame perpendicular to the polarization axis of the photolysis laser beam. Reaction products were allowed to build up for a few nanoseconds, and then HCl(v, J) was

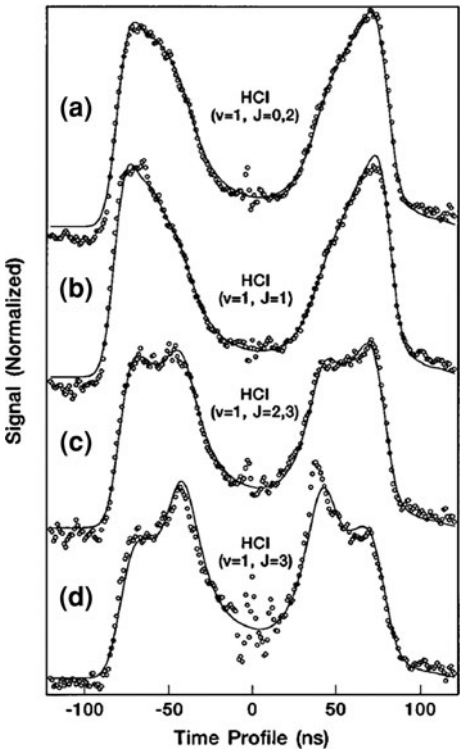

Fig. 1.5 Core-extracted time profiles for HCl(v, J) resulting from the reaction of Cl with $CH_4(v_3 = 1)$ [60]. Figure is reproduced with permission

detected with quantum state-resolution by (2 + 1) resonance-enhanced multi-photon ionization (REMPI) via a third laser.

A technique termed 'core extraction' [63] was employed to measure the velocity distributions of the HCl products. Core extraction is accomplished by measuring projections of a velocity distribution with a time-of-flight mass spectrometer that is masked to reject the off-axis HCl products. Figure 1.4 shows an example of how the product velocity distribution is simplified by the core extraction technique taking a cylindrical slice out of an isotropic velocity distribution of products.

They measured velocity scattering distributions with quantum state-resolution to produce core-extracted time profiles like those shown in Fig. 1.5. The core-extracted time profiles were converted into speed distributions of the HCl products and then into state-to-state differential cross-sections for the reactions assuming no E_{TRANS} was released into the CH_3 radical. Figure 1.6 shows typical data for the $Cl(^2P_{3/2}) + CH_4(v_3 = 1, J) \rightarrow HCl(v, J) + CH_3$ reaction study [60]. In the graph, θ is the angle that the HCl product velocity made with the attacking Cl atom's trajectory (i.e. $\theta = 0°$ for forward scattering and $\theta = 180°$ for back scattering).

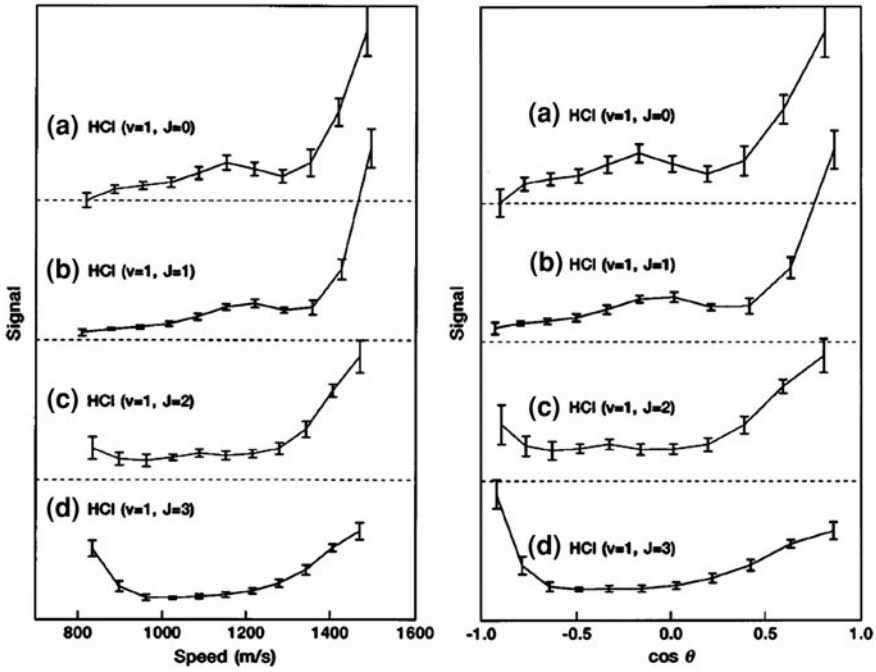

Fig. 1.6 (*left-hand side*) Speed distributions for HCl(v, J) from the reaction of Cl with $CH_4(v_3 = 1)$. (*right-hand side*) state-to-state differential cross sections for $Cl(^2P_{3/2}) + CH_4(v_3 = 1, J) \rightarrow HCl(v, J) + CH_3$ where θ is the angle that the HCl product velocity made with the attacking Cl atom's trajectory [60]. Figure is reproduced with permission

Through these measurements of quantum state specific scattering distributions, the authors were able to produce a highly detailed picture of this gas-phase reaction mechanism. HCl products detected in v = 0 and high J-states were predominately scattered sideways or perpendicular to the velocity of the attacking Cl atom. However, HCl products in v = 1 were mostly forward scattered for low J-states, but tended to be back scattered for higher J-states.

Figure 1.7 shows a cartoon [64] of the findings for the reaction of Cl atoms with $CH_4(v_3 = 1)$. Results for the reaction of Cl atoms with $CD_3H(v_1 = 1)$ were very similar to those of $CH_4(v_3 = 1)$ which suggested that the unobserved products (CH_3 or CD_3) were 'spectators' (or uninvolved parties) during the reaction. HCl(v = 0, J) products were attributed to nearly head-on collisions of the Cl atom with a C–H bond of methane, and are shown as the 'Glancing' trajectory in the figure. HCl(v = 1, high-J) products were attributed to a bull's-eye or center-to-center collision of the Cl atom with a vibrational excited methane molecule, and is shown as the 'Rebounding' trajectory in the figure. HCl(v = 1, low-J) products were attributed to a tangential collision of the Cl atom with an excited methane molecule, and is shown as the 'Stripping' trajectory in the figure.

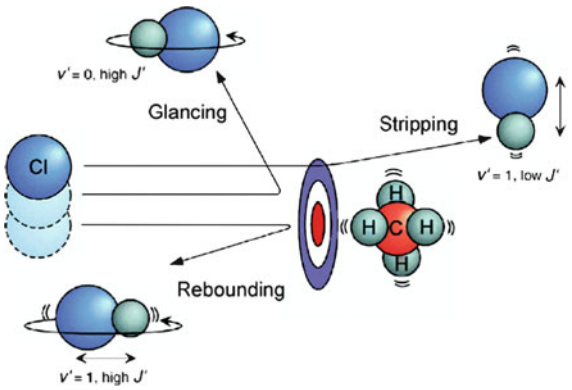

Fig. 1.7 Cartoon showing the variation in the HCl(v, J) product scattering for the reaction of $Cl(^2P_{3/2}) + CH_4(v_3 = 1, J) \rightarrow HCl(v, J) + CH_3$[63]. Figure is reproduced with permission

A significant steric effect was reported for the two reactions. The degree of alignment of the methane with respect to the IR-laser's linear polarization could be controlled by selection of the ro-vibrational transition and was quantified using calculated alignment coefficients (see Chap. 3). The polarization of the IR-laser was varied with respect to the Cl_2 photolysis laser in order to change the approach of the attacking Cl atoms to the excited, aligned methane. By measuring the polarization dependence of the HCl(v = 1, $J = 1$) product resulting from the reaction of Cl with methane excited perpendicular to the Cl direction or parallel to it, the authors were able to assign the alignment dependence of the reaction to an alignment of the vibrational amplitude rather than the angular momentum of the methane molecular. It was shown that aligning the C–H bond perpendicular the approaching Cl atom increased the scattering signal of HCl (v = 1, $J = 1$). This result was shown to be similar for the Cl reaction with both methane isotopologues, and was interpreted as the vibrational excitation opening the cone of acceptance for reaction by lessening the need for a collinear C–H–Cl geometry in the transition state region [61].

Zare and coworkers were able to gain detailed insight into the gas phase reaction of Cl atoms with vibrationally excited methane by alignment of the well-defined E_{TRANS} of the Cl atoms, alignment of the $\vec{J}$ and E_{VIB} of the state-prepared methane, and the state-specific detection of scattering profiles for the HCl(v, J) products. They constructed a detailed picture of the reactive encounter with the measurements.

We have taken the ideas of the gas-phase study discussed above and applied them to gas/surface reactions. The three model gas-surface reactions studied in this thesis work are:

$$CH_4(v_3 = 1, J)(g) \overset{Ni(100)}{\longrightarrow} CH_3(\text{ads.}) + H(\text{ads.})$$

$$CD_3H(v_1 = 1, J)(g) \overset{Ni(100)}{\longrightarrow} CD_3(\text{ads.}) + H(\text{ads.})$$

$$CH_4(v_3 = 1, J)(g) \xrightarrow{Ni(110)} CH_3(ads.) + H(ads.)$$

As in its gas-phase predecessor, the experimental method in this thesis work prepares a molecular beam of methane in a specific ro-vibrational eigenstate by resonant infrared pumping with alignment of the $\overrightarrow{J}$ and vibrational amplitude via a linearly polarized laser field [60] to study intricate details of a reaction. In the present work, the excited, aligned molecular beam is directed normal to a single-crystal nickel surface to provide information toward a molecular-level understanding of this industrially relevant gas-surface system.

The results of this thesis work demonstrate steric dependences on the reaction probability (sticking coefficients) of state-prepared methane dissociating on single crystal nickel surfaces for the first time. The observation of quantum state-resolved steric effects in the chemisorption of vibrationally excited methane will serve as stringent test in the development of predictive theoretical models of gas/surface interactions.

1.6 Outline

This thesis is organized in the following manner:

In Chap. 2, I describe the experimental setup. An overview of the experiment is given with attention focused on elements of the setup that were developed during my doctoral work for the collection of the data presented in this thesis.

In Chap. 3, I give an explanation of the state specific laser excitation process and the process of alignment of the angular momentum and vibrational transition dipole of the excited molecules in the laboratory frame. The state-prepared, aligned molecular beam was used for quantum state-resolved studies of stereodynamics in the chemisorption of vibrationally excited methane.

In Chap. 4, I report measurements of the alignment dependent reactivity for $CH_4(v_3)$ and $CD_3H(v_1)$ on Ni(100). The dephasing times of the alignments prepared by $CH_4(v_3)$ and $CD_3H(v_1)$ excited via their R(0) transition is studied. The alignment dependent reactivity of $CH_4(v_3)$ and $CD_3H(v_1)$ excited via several rovibrational transitions is compared to calculated alignment coefficients. The alignment dependent reactivity is reported as a function of the angle that the laser polarization makes with the surface. The effect of molecular beam speed on the alignment dependent reactivity is reported. State-resolved, absolute initial reaction probabilities (sticking coefficients) are reported for $CH_4(v_3)$ on Ni(100).

In Chap. 5, I report results of alignment dependent reactivity for $CH_4(v_3)$ on Ni(110), an anisotropic surface. The Ni(110) surface has surface rows that one can align in the laboratory frame. We performed the state-resolved chemisorption experiments with the excitation laser polarization parallel or perpendicular to the surface rows.

In Chap. 6, I summarize the most important results of this work, discuss improvements that could be made to the experimental setup and suggest future directions for the research.

References are placed at the end of each chapter. For clarity, supplementary material is provided in the form of appendices found at the end of this thesis. The appendices are referred to throughout Chaps. 2–6.

References

1. H.S. Bengaard et al., Steam reforming and graphite formation on Ni catalysts. J. Catal. **209**(2), 365–384 (2002)
2. R.D. Beck et al., Vibrational mode-specific reaction of methane on a nickel surface. Science **302**(5642), 98–100 (2003)
3. D.R. Killelea et al., Bond-selective control of a heterogeneously catalyzed reaction. Science **319**(5864), 790–793 (2008)
4. V.A. Ukraintsev, I. Harrison, A statistical-model for activated dissociative adsorption—application to methane dissociation on Pt(111). J. Chem. Phys. **101**(2), 1564–1581 (1994)
5. A. Bukoski, D. Blumling, I. Harrison, Microcanonical unimolecular rate theory at surfaces. I. Dissociative chemisorption of methane on Pt(111). J. Chem. Phys. **118**(2), 843–871 (2003)
6. H.L. Abbott, A. Bukoski, I. Harrison, Microcanonical unimolecular rate theory at surfaces. II. Vibrational state resolved dissociative chemisorption of methane on Ni(100). J. Chem. Phys. **121**(8), 3792–3810 (2004)
7. L.B.F. Juurlink, D.R. Killelea, A.L. Utz, State-resolved probes of methane dissociation dynamics. Prog. Surf. Sci. **84**(3–4), 69–134 (2009)
8. P. Maroni, (2005) Bond- and mode-specific reactivity of methane on Ni(100). Ecole Polytechnique Fédérale de Lausanne Thesis No. 3335
9. J.C. Polanyi, Some concepts in reaction dynamics. Acc. Chem. Res. **5**(5), 161 (1972)
10. J.C. Polanyi, Some concepts in reaction dynamics. Science **236**(4802), 680–690 (1987)
11. K.M. DeWitt et al., Using effusive molecular beams and microcanonical unimolecular rate theory to characterize CH4 dissociation on Pt(111). J. Phys. Chem. B **110**(13), 6705–6713 (2006)
12. M. Born, R. Oppenheimer, Quantum theory of molecules. Annalen Der Physik **84**(20), 0457–0484 (1927)
13. J.D. White et al., Conversion of large-amplitude vibration to electron excitation at a metal surface. Nature **433**(7025), 503–505 (2005)
14. A.M. Wodtke, D. Matsiev, D.J. Auerbach, Energy transfer and chemical dynamics at solid surfaces: The special role of charge transfer. Prog. Surf. Sci. **83**(3), 167–214 (2008)
15. N. Shenvi, S. Roy, J.C. Tully, Dynamical steering and electronic excitation in NO Scattering from a gold surface. Science **326**(5954), 829–832 (2009)
16. M.N. Carre, B. Jackson, Dissociative chemisorption of CH4 on Ni: The role of molecular orientation. J. Chem. Phys. **108**(9), 3722–3730 (1998)
17. L. Hanley, Z. Xu, J.T. Yates, Methane activation on Ni(111) at high-pressures. Surf. Sci. **248**(3), L265–L273 (1991)
18. B.O. Nielsen et al., Activated dissociative chemisorption of methane on Ni(100)—a direct mechanism under thermal conditions. Catal. Lett. **32**(1–2), 15–30 (1995)
19. J.H. Larsen, I. Chorkendorff, From fundamental studies of reactivity on single crystals to the design of catalysts. Surf. Sci. Rep. **35**(5–8), 165–222 (1999)
20. M. Balooch et al., Molecular-beam study of apparent activation barrier associated with adsorption and desorption of hydrogen on copper. Surf. Sci. **46**(2), 358–392 (1974)

21. C.T. Rettner, H.E. Pfnur, D.J. Auerbach, Dissociative chemisorption of CH4 on W(110—dramatic activation by initial kinetic-energy. Phys. Rev. Lett. **54**(25), 2716–2719 (1985)
22. C.T. Rettner, H.E. Pfnur, D.J. Auerbach, On the role of vibrational-energy in the activated dissociative chemisorption of methane on tungsten and rhodium. J. Chem. Phys. **84**(8), 4163–4167 (1986)
23. A.C. Luntz, CH4 dissociation on Ni(100)—comparison of a direct dynamical model to molecular-beam experiments. J. Chem. Phys. **102**(20), 8264–8269 (1995)
24. J.J. Repetski, R.E. Mates, Rotational temperature in an underexpanded jet. Phys. Fluids **14**(12), 2605 (1971)
25. L.B.F. Juurlink et al., Eigenstate-resolved studies of gas-surface reactivity: CH4 (nu(3)) dissociation on Ni(100). Phys. Rev. Lett. **83**(4), 868–871 (1999)
26. J. Higgins et al., State selective vibrational (2 nu(3)) activation of the chemisorption of methane on Pt (111). J. Chem. Phys. **114**(12), 5277–5283 (2001)
27. M.P. Schmid et al., Molecular-beam/surface-science apparatus for state-resolved chemisorption studies using pulsed-laser preparation. Rev. Sci. Instrum. **74**(9), 4110–4120 (2003)
28. L.B.F. Juurlink, R.R. Smith, A.L. Utz, *The role of rotational excitation in the activated dissociative chemisorption of vibrationally excited methane on Ni(100). in General discussion on excited states at surfaces* (Nottingham, England, Royal Soc Chemistry, 2000)
29. R. Bisson et al., State-resolved reactivity of CH4(2 nu(3)) on Pt(111) and Ni(111): Effects of barrier height and transition state location. J. Phys. Chem. A **111**(49), 12679–12683 (2007)
30. P. Maroni et al., State-resolved gas-surface reactivity of methane in the symmetric C–H stretch vibration on Ni(100). Phys. Rev. Lett. **94**(24), 4 (2005)
31. R.R. Smith et al., Preference for vibrational over translational energy in a gas-surface reaction. Science **304**(5673), 992–995 (2004)
32. R. Bisson, M. Sacchi, R.D. Beck, State-resolved reactivity of CH4 on Pt(110)-(1x2): The role of surface orientation and impact site. J. Chem. Phys. **132**(9), (2010)
33. D.R. Killelea et al., Surface temperature dependence of methane activation on Ni(111). J. Phys. Chem. C **113**(48), 20618–20622 (2009)
34. M.P. Schmid et al., Surface reactivity of highly vibrationally excited molecules prepared by pulsed laser excitation: CH4 (2 nu(3)) on Ni(100). J. Chem. Phys. **117**(19), 8603–8606 (2002)
35. L. Halonen, S.L. Bernasek, D.J. Nesbitt, Reactivity of vibrationally excited methane on nickel surfaces. J. Chem. Phys. **115**(12), 5611–5619 (2001)
36. L. Halonen, M.S. Child, Local mode theory for C3 V molecules—CH3D, CHD3, SiH3D, and SiHD3. J. Chem. Phys. **79**(9), 4355–4362 (1983)
37. F.F. Crim, State-selected and bond-selected unimolecular reactions. Science **249**(4975), 1387–1392 (1990)
38. A. Sinha, M.C. Hsiao, F.F. Crim, Bond-selected bimolecular chemistry—H+HOD(4nu-OH)-O+H2. J. Chem. Phys. **92**(10), 6333–6335 (1990)
39. F.F. Crim, Bond-selected chemistry: Vibrational state control of photodissociation and bimolecular reaction. J. Phys. Chem. **100**(31), 12725–12734 (1996)
40. M.J. Bronikowski et al., Bond-specific chemistry—OD:OH product ratios for the reactions H+HOD(100) and H+HOD(001). J. Chem. Phys. **95**(11), 8647–8648 (1991)
41. Z.H. Kim, H.A. Bechtel, R.N. Zare, Vibrational control in the reaction of methane with atomic chlorine. J. Am. Chem. Soc. **123**(50), 12714–12715 (2001)
42. L.B.F. Juurlink et al., Comparative Study of C–H Stretch and Bend Vibrations in Methane Activation on Ni(100) and Ni(111). Phys. Rev. Lett. **94**(20), 208303 (2005)
43. K.H. Kramer, R. Bernstein, Focusing and orientation of symmetric-top molecules with electric 6-pole field. J. Chem. Phys. **42**(2), 767 (1965)
44. A.W. Kleyn et al., Steric effects in scattering and adsorption on NO at Ag(111). J. Chem. Soc.-Faraday Trans. Ii **85**, 1337–1345 (1989)
45. E.W. Kuipers et al., Steric effects in molecular adsorption due to an anisotropic repulsion. Surf. Sci. **211**(1–3), 819–828 (1989)

46. S.I. Ionov et al., Surface-temperature dependence of the steric effect in the scattering of oriented tert-butyl chloride and fluoroform molecules by graphite(0001). J. Chem. Phys. **93**(10), 7406–7415 (1990)
47. A.J. Komrowski et al., Dissociative adsorption of NO upon Al(111): Orientation dependent charge transfer and chemisorption reaction dynamics. J. Chem. Phys. **117**(18), 8185–8189 (2002)
48. M. Brandt et al., The role of molecular state and orientation in harpooning reactions: N2O on Cs/Pt(111). Phys. Rev. Lett. **81**(11), 2376–2379 (1998)
49. J.N. Greeley et al., Scattering aligned NO + on Ag(111)—the effect of internuclear-axis direction on NO- and O- product formation. J. Chem. Phys. **102**(12), 4996–5011 (1995)
50. L. Vattuone et al., Stereodynamic effects in the adsorption of ethylene onto a metal surface. Angew. Chem. Int. Ed. **43**, 5200–5203 (2004)
51. A. Gerbi et al., Stereodynamic effects in the adsorption of propylene molecules on Ag(001). J. Phys. Chem. B **109**(48), 22884–22889 (2005)
52. A. Gerbi et al., New insights on the stereodynamics of ethylene adsorption on an oxygen-precovered silver surface. J. Chem. Phys. **123**(22), (2005)
53. A. Gerbi et al., Role of Rotational Alignment in Dissociative Chemisorption and Oxidation: O2 on Bare and CO-Precovered Pd(100)13. Angew. Chem. Int. Ed. **45**(40), 6655–6658 (2006)
54. L. Vattuone et al., Selective production of reactive and nonreactive oxygen atoms on Pd(001) by rotationally aligned oxygen molecules. Angew. Chem. Int. Ed. **48**(26), 4845–4848 (2009)
55. H. Hou et al., The stereodynamics of a gas-surface reaction. Science **277**(5322), 80–82 (1997)
56. W.A. Dino, H. Kasai, A. Okiji, Role of rotational motion in the dissociative adsorption and associative desorption dynamics of D-2/Cu(111). Phys. Rev. Lett. **78**(2), 286–289 (1997)
57. U. Fano, J.H. Macek, Impact excitation and polarization of emitted light. Rev. Mod. Phys. **45**(4), 553–573 (1973)
58. C.H. Greene, R.N. Zare, Photofragment alignment and orientation. Annu. Rev. Phys. Chem. **33**, 119–150 (1982)
59. W.R. Simpson, A.J. Orrewing, R.N. Zare, State-to-state differential cross-sections for the reaction Cl((2)P(3/2)) + CH4(nu-3 = 1, J = 1)-]HCL(nu′ = 1, J′) + CH3. Chem. Phys. Lett. **212**(1–2), 163–171 (1993)
60. W.R. Simpson et al., Reaction of Cl with vibrationally excited CH4 and CHD3—state-to-state differential cross-sections and steric effects for the HCl product. J. Chem. Phys. **103**(17), 7313–7335 (1995)
61. W.R. Simpson et al., Picturing the transition-state region and understanding vibrational enhancement for the Cl + CH4- → HCl + CH3 reaction. J. Phys. Chem. **100**(19), 7938–7947 (1996)
62. A.J. OrrEwing et al., Scattering-angle resolved product rotational alignment for the reaction of Cl with vibrationally excited methane. J. Chem. Phys. **106**(14), 5961–5971 (1997)
63. W.R. Simpson et al., Core extraction for measuring state-to-state differential-cross section of bimolecular reactions. J. Chem. Phys. **103**(17), 7299–7312 (1995)
64. A.J. Alexander, R.N. Zare, Anatomy of elementary chemical reactions. J. Chem. Edu. **75**(9), 1105–1118 (1998)

Chapter 2
Experimental Setup

2.1 Overview of Experimental Setup

Figure 2.1 shows the overview of our experimental setup. There are three main parts: a continuous molecular beam source, an ultra high vacuum chamber and a continuous infrared excitation setup.

I discuss the details of the experimental setup used during this thesis work in the next sections. Attention is focused on the components of the experimental setup that were developed during my thesis work.

2.2 Molecular Beam Source

The continuous (CW) molecular beam source (Thermionics, MSC-9800) consists of three differentially pumped stages, shown in Fig. 2.1. The 1st stage contains a temperature-controlled (25–200 °C) homebuilt pinhole nozzle ($\varnothing = 50$ μm orifice) and an electroformed nickel skimmer (Beam Dynamics, $\varnothing = 1$ mm). The nozzle is heated by an OMEGA CN8200 series temperature and process controller and a 12 V DC power supply sending current through thermal coax wrapped around the nozzle. For example, with 8 V and 0.55 A of heating power, the controller stabilizes the nozzle temperature at 150 °C. At a distance of ~ 2 cm from the nozzle, the skimmer extracts the cold core of the supersonic expansion. The first stage is evacuated by a 1,000 l/s turbo pump (Balzers, TMU1000) backed by a 20 m^3/h mechanical pump (Balzers, Duo 20), and has a base pressure of $<1 \times 10^{-7}$ mbar. When producing an expansion of 12% CH_4 in H_2 with a nozzle temperature of 50 °C and three bar backing pressure, the typical operating pressure is $\sim 2 \times 10^{-3}$ mbar.

The 2nd pumping stage houses a chopper wheel ($\varnothing = 127$ mm) rotating at 200 Hz driven by a water-cooled AC-synchronous motor (Globe 18A1003-2).

B. L. Yoder, *Steric Effects in the Chemisorption of Vibrationally Excited Methane on Nickel*, Springer Theses, DOI: 10.1007/978-3-642-27679-8_2,

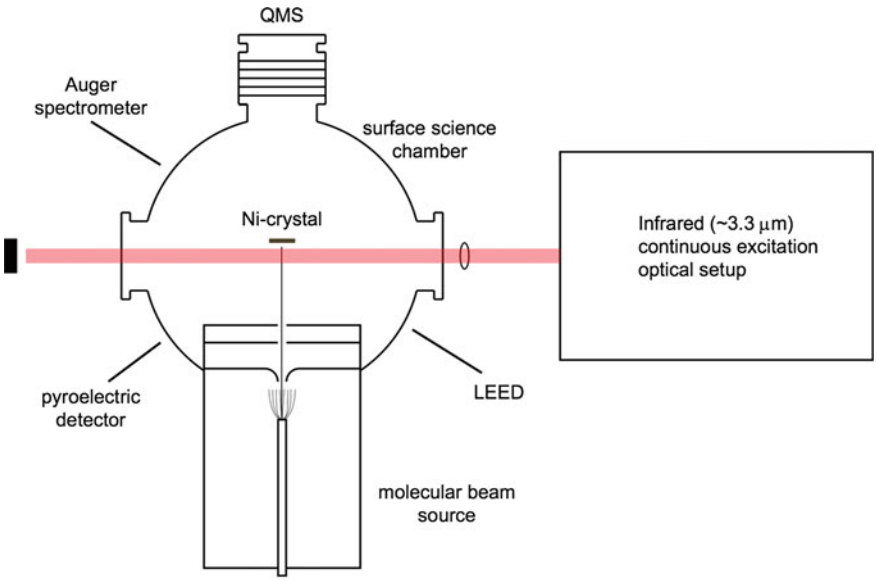

Fig. 2.1 Overall view of experimental setup

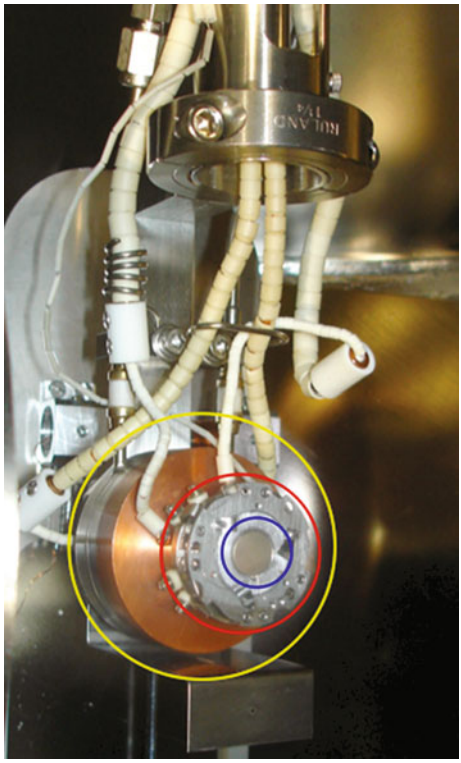

Fig. 2.2 Photo of Ni(100) surface (*encircled in blue*) mounted on sample platen (*encircled in red*) attached to XYZ sample manipulator (copper cooling block *encircled in yellow*) in the UHV chamber

We use the chopper to produce short molecular beam pulses for velocity measurements of the molecular beam by time-of-flight (TOF). A 500 l/s turbo pump (Balzers TMU520) backed by a dry membrane pump (Pfeiffer MDT4) gives a working pressure of $\sim 2 \times 10^{-5}$ mbar in the second stage. A manually operated gate-valve separates the 2nd and 3rd stages, so that the molecular beam source can be vented for servicing without breaking vacuum in the UHV chamber.

The 3rd stage serves to minimize the gas load from the source chamber into the UHV chamber. The molecular beam diameter entering the UHV chamber is defined by a removable aperture (currently $\varnothing = 1$ mm) at the exit of the 3rd stage. The 3rd stage is pumped by a 500 l/s turbo pump (Pfeiffer TMU521 P) backed by a dry membrane pump (Pfeiffer MDT4) to a working pressure of $\sim 2 \times 10^{-6}$ mbar.

2.3 Surface Science UHV Chamber

2.3.1 Overview

Our state-resolved reactivity measurements are done in a custom built Ultra-High Vacuum (UHV) surface science chamber that is pumped by a 1,000 l/s turbo pump (Pfeiffer, TMU 1000P) backed by an oil free membrane pump (KNF N920, speed 1 m^3/h). Typically, the UHV chamber's base pressure is $<5 \times 10^{-11}$ mbar, and rises to $>1 \times 10^{-8}$ mbar when the continuous molecular beam is in use. The UHV chamber has a three-level design. The lower level contains vacuum gauges, two calibrated leaks, an electrical feed through for a pyroelectric detector, the swivel arm for a mica flag used to scatter the molecular beam during King and Wells experiments [1], and a load lock enabling us to change the single crystal sample without breaking the UHV chamber's vacuum. The middle level has the entrance aperture of the molecular beam, an entrance and exit window for the excitation laser to traverse the molecular beam, and a quadrupole mass spectrometer (Hiden, HAL 301/3FPIC) for molecular beam time-of-flight and flux measurements. The upper level is for surface cleaning and analysis. It houses a low energy electron diffraction spectrometer (LEED) (Omicron, SPECTALEED) for surface structure analysis, an Auger electron spectrometer (AES) (Omicron, CMA150) for surface composition analysis, and an ion sputter gun (Omicron, ISE10) for surface preparation.

Figure 2.2 shows a picture of a Ni-crystal mounted onto the sample manipulator in the UHV chamber. The sample surface is mounted on a four axis manipulator (Thermionics) with a 40 cm stroke (resolution = 12.7 μm) along the vertical Z-axis, ±20 mm displacement (resolution = 2.5 μm) of X or Y in the horizontal plane, and 360° rotation about the Z-axis. A doubly differentially pumped rotation stage with three spring-loaded Teflon seals permits the rotation under UHV. All electrical and cooling connections to the manipulator are made through the rotating top flange to prevent in vacuum flexing of electrical wires and tubing. The

X-axis and Z-axis micrometer drives are equipped with stepper motors for automated motion of the sample via home-written Labview code. This automated motion is used to produce AES profile scans across the sample surface quantifying the amount of carbon present on the surface after a molecular beam deposition experiment.

A 10 mm diameter Ni(100) or Ni(110) single crystal is mounted on a removable sample holder (platen) that attaches to a copper dewar-heater assembly on the sample manipulator. The sample, with a K-type thermocouple is either slid into a spark eroded hole in the crystal's edge or spot-welded onto the side of a top-hat shaped crystal, can be transferred to/from the copper dewar assembly without breaking vacuum via a magnetically coupled rotary-linear feed through (Thermionics, FLRE) through a load lock chamber.

The sample is heated by electron impact and cooled by flowing liquid nitrogen through the dewar. The heating is commercially available (Thermionics, STLC-TTC platen) with power supply (SPS series) and PID controller (Omicron, E5AK). A 0.3 mm tungsten filament situated behind the crystal sample provides heat via electron bombardment. Electrons are accelerated toward the grounded sample by the negative potential (filament HV) applied to the filament (max = 2 kV). The PID controller regulates the sample temperature by 'current regulation', changing the alternating current used to heat the filament. To stabilize the crystal temperature at 200 °C, the filament HV and current are limited to –500 V and 9 A, respectively. These settings produce a temperature stability to within 1 °C. Liquid nitrogen is continuously flowed through the copper dewar assembly.

2.3.2 Quadrupole Mass Spectrometer (QMS)

For absolute reactivity measurements, it is necessary to determine the molecular beam's velocity/translational energy and its flux impinging on the crystal surface. We use a quadrupole mass spectrometer (Hiden, HAL 301/3FPIC) for molecular beam time-of-flight and flux measurements.

2.3.2.1 Time-of-Flight Velocity Measurements

The molecular beam velocity or translational energy is characterized by time-of-flight (TOF) measurements. For this, we use the chopper (located in the 2nd stage of the molecular beam source), an aperture in the UHV stage, and an on-axis QMS. The chopped molecular beam is skimmed by the aperture and continues into the ionization source of the QMS. Arrival time distributions of CH_4^+ (or CD_3H^+) ions are recorded by a multichannel scaler (Turbo-MCS, Ortec). The measured TOF data is fit by a model function based on a flux-weighted Maxwell–Boltzmann distribution of velocities convoluted with an experimentally determined chopper

Table 2.1 Expansion conditions with velocity and translational energy data for the gas mixtures used in this work

Mixture (%)	T_{nozzle} (°C)	$P_{backing}$ (bar)	Velocity (m/sec)	$E_{trans.}$ (kJ/mol)
100 CH_4	50	3	1,061	9.0
100 CH_4	200	3	1,371	15.1
25 CH_4 in H_2	200	3	2,056	33.9
12 CH_4 in H_2	50	3	2,056	33.9
12 CH_4 in H_2	200	3	2,471	49.0
3 CH_4 in He	50	3	1,782	25.5
1 CH_4 in H_2	100	3	2,854	65.3
3.6 CD_3H in He	40	3	1,722	28.3
3.6 CD_3H in He	100	3	1,894	34.2
1.5 CD_3H in H_2	50	3	2,611	65.0
1.5 CD_3H in H_2	100	3	2,727	70.9
100 H_2	50	3	2,789	7.8
100 H_2	200	3	3,499	12.3
100 He	50	3	1,849	6.8
100 He	200	3	2,285	10.5

transmission function. Detailed description of the TOF measurement and analysis is given in the theses of Schmid [2] and Maroni [3].

Table 2.1 shows the gas mixtures used in the deposition experiments presented in this thesis. It gives CW expansion conditions with resulting molecular beam velocities and translational energies for each mixture. I have included pure beams of H_2 and He for comparison.

2.3.2.2 Molecular Beam Flux Monitor

Flux measurements of the molecular beam are taken so that we can calculate the dose of molecules impinging on the surface during a molecular beam deposition experiment. This allows for correction of dose differences in deposition experiments and for the calculation of absolute sticking coefficients or reaction probabilities.

Figure 2.3 shows a flux measurement for a deposition of CH_4 on Ni(100). In this experiment, we deposited four molecular beam footprints or "spots" on the Ni surface with a 33.9 kJ/mol molecular beam for subsequent analysis by AES. For flux monitoring of CH_4, the QMS is set to measure $m/z = 16$, averaging over a dwell time of 5–15 s for each data point (15 s dwell time for data in Fig. 2.3). In contrast to the time of flight measurements, the methane beam does not enter the ionization source directly for the flux monitoring, but is scattered by the surface sample, in order to measure the partial pressure rise of the species of interest in the UHV chamber. During molecular beam deposition experiments on a reactive surface, not all of the molecular beam flux is scattered by the surface. Some impinging molecules stick (either physisorption or chemisorption) to the surface

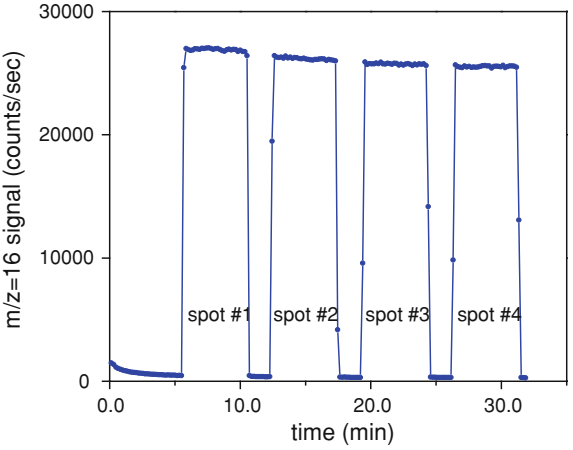

Fig. 2.3 Typical flux measurement during a CH_4 molecular beam deposition experiment using a 33.9 kJ/mol (12% mixture) translational energy

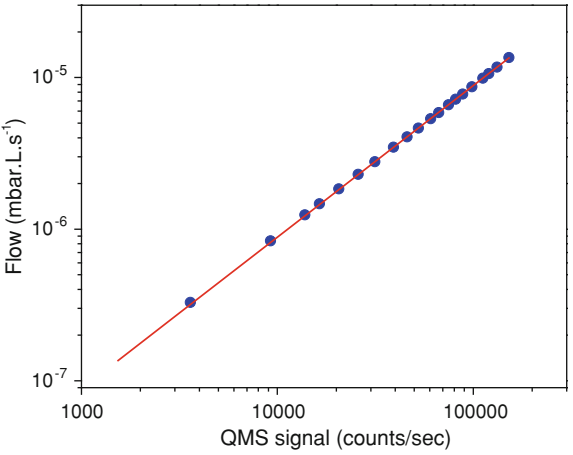

Fig. 2.4 QMS signal calibration by calibrated leak standard for CH_4. The slope of the fitted line gives the QMS sensitivity

and cause the scattered flux to be lower than the incident. The absolute reaction (sticking) probabilities of methane reactions presented in this work are <0.005 (or less than one molecule in 200), so I take the QMS measured methane signal as the incident flux.

The QMS signal is calibrated by recording a series of steady state signals (counts/sec) for known fluxes (mbar.L/sec) introduced into the UHV by a calibrated leak standard. Figure 2.4 shows data taken to calibrate the QMS signal. From data in Fig. 2.4, we determine QMS sensitivity of 1 count/sec per 8.846×10^{-11} mbar.L/sec (2.148×10^{9} molecules/sec). For a molecular beam deposition lasting 300 s (seen in Fig. 2.3) with an average QMS signal of 26,500 counts/sec, I calculate a dose of 5.69×10^{13} molecules impinging on the surface. Dividing the dose by the molecular beam's surface area (3.14×10^{-2} cm^2), I estimate the areal density of methane molecules that impinged on the surface during the deposition to be 1.81×10^{15} molecules/cm^2.

Table 2.2 Observed pressure rises in the state-resolved gas/surface dynamics machine stages with measured flux for selected gas mixtures

Mixture (%)	T_{nozzle} (°C)	ΔP_{1st} (mbar)	ΔP_{2nd} (mbar)	ΔP_{3rd} (mbar)	ΔP_{UHV} (mbar)	Flux (count/sec)
100 CH_4	200	$1.6 \cdot 10^{-3}$	$2.2 \cdot 10^{-5}$	$1.9 \cdot 10^{-6}$	$3.9 \cdot 10^{-8}$	195,000
12 CH_4 in H_2	50	$2.3 \cdot 10^{-3}$	$2.3 \cdot 10^{-5}$	$2.6 \cdot 10^{-6}$	$5.5 \cdot 10^{-8}$	165,000
3.6 CD_3H in He	40	$1.6 \cdot 10^{-4}$	$8.0 \cdot 10^{-6}$	$1.0 \cdot 10^{-6}$	$2.1 \cdot 10^{-8}$	24,500
3.6 CD_3H in He	100	$1.4 \cdot 10^{-4}$	$8.0 \cdot 10^{-6}$	$1.1 \cdot 10^{-6}$	$1.9 \cdot 10^{-8}$	33,000
1.5 CD_3H in H_2	50	$1.6 \cdot 10^{-3}$	$2.4 \cdot 10^{-5}$	$2.6 \cdot 10^{-6a}$	$5.2 \cdot 10^{-8a}$	2,600[a]
1.5 CD_3H in H_2	100	$1.4 \cdot 10^{-3}$	$2.5 \cdot 10^{-5}$	$4.5 \cdot 10^{-7a}$	$8.2 \cdot 10^{-9a}$	2,200[a]

[a] indicates spinning of the chopper wheel located in the 2nd stage, causing 7.15x less flux to enter the 3rd and UHV stages

Table 2.2 gives typical values for the observed pressure rises in the four chambers of the machine as well as the measured flux of methane.

2.3.3 Sample Preparation

Before every molecular beam deposition experiment, the Ni surface must be free from contaminants (i.e. carbon, oxygen, sulfur) and have a well defined crystal structure. We clean the nickel crystal by sputtering with energetic argon ions (1 kV) from a commercial ion gun (Omicron, ISE 10). A total current leaving the gun of 20 μA corresponds to $\sim$2 μA impinging on the 19 mm diameter crystal sample holder [2]. During the sputtering, the partial pressure of argon (PanGas, 99.999% purity) in the UHV chamber is $\sim 5 \times 10^{-7}$ mbar. Under these conditions, the ion dose on the surface after 5 min of sputtering is 1,015 ions/cm^2. After sputtering, the crystal structure is restored by annealing the sample for 5 min at 800 °C. The cleanliness of the sample surface is verified before every deposition experiment by AES, which is discussed in the following section.

2.3.4 Auger Spectrometer

We use an Auger spectrometer (Omicron CMA 150) with a single pass cylindrical mirror analyzer (CMA) and an integrated electron-gun (EKI 25) to assess the cleanliness of the sample surface and to quantify the amount of adsorbate (i.e. carbon) on the surface after a molecular beam deposition. Auger electron spectroscopy (AES) is a common surface science technique consisting of the detection of inelastically scattered electrons. The Auger process begins with the removal of an electron from an atom's inner shell to form a vacancy. This vacancy is filled by a second atomic electron that resided in a higher shell. As the second electron relaxes to the inner shell, energy is released. A third electron, the Auger electron, is

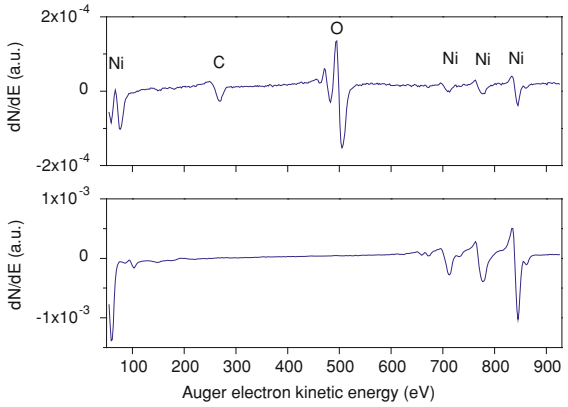

Fig. 2.5 Auger spectra of a Ni(110) single crystal upon introduction to UHV chamber (*upper panel*) and after a few sputtering/annealing cycles (*lower panel*)

ejected from the atom's electronic shell and carries away as kinetic energy any energy in excess to its binding energy. Since the kinetic energy of the Auger electron depends solely on the energy level spacings of the parent atom, AES is an ideal probe of the atomic composition on a surface. It is possible to detect any atomic species with AES except hydrogen and helium, as they do not have three electrons.

A detailed description of our AES setup, calibration, and procedure is outlined in the theses of Schmid [2] and, more recently, Maroni [3]. A brief description is given here. Primary electrons are produced by the electron-gun, with adjustable energy and emission current via the electron-gun controller. The Auger electrons emitted from the nickel surface are filtered in energy in the CMA. The energy of the transmitted electrons depends on the voltage applied on the cylindrical mirrors, controlled remotely via a 0–10 V digital-to-analog (DAC) of a DAQ card. The CMA controller supplies the HV (1.8 kV) for the channeltron detector. The derivative of the Auger electron current relative to the Auger electron kinetic energy is recorded by modulating the CMA HV with a sine wave (5.5 V peak-to-peak at 9.7 kHz) generated by the oscillator of a digital dual-phase lock-in amplifier (SR830). The Auger signal from the channeltron is pre-amplified (300x) and detected by the SR830 that is remotely controlled via a GPIB interface. Phase sensitive detection is employed to suppress the background signal due to elastically scattered electrons from the surface.

As mentioned in the previous section, Auger spectroscopy is used to check the cleanliness of a sample surface before a deposition experiment. The upper panel in Fig. 2.5 shows an Auger spectrum of a contaminated (dirty) Ni(110) sample upon transfer into the UHV chamber. The lower panel shows an Auger spectrum of the same sample after cleaning. Typical operating conditions for Auger spectra collection are 1 μA of electron current, a dwell time of 20 ms, step width of 2 eV and the channeltron set to 1,800 V. Data is collected with 5.5 V modulation at 9.7 kHz, by a lock-in amplifier with sensitivity of 10 mV(nA) and time constant of 10 ms.

AES is also used to quantify the reactivity of methane in a molecular beam. The dissociative chemisorption reaction of methane on a 200 °C nickel crystal yields carbon atoms chemisorbed to the surface. Methane is completely dehydrogenated

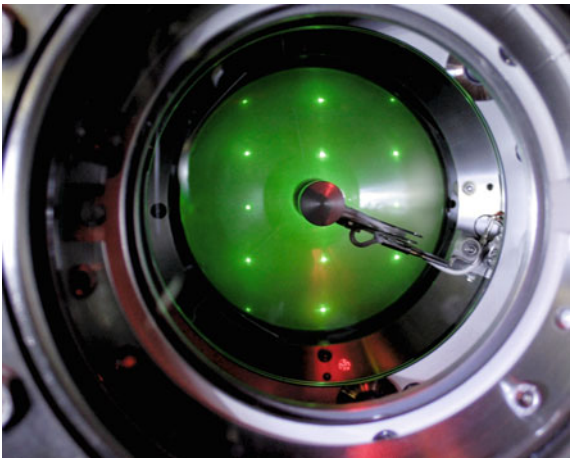

Fig. 2.6 LEED pattern of a Ni(110) single crystal

and the hydrogen leaves the surface by recombinative desorption at 200 °C surface temperature.

After an exposure to a known dose of methane in a molecular beam, the amount of carbon on the surface is quantified as the ratio between carbon and nickel peak intensities (C/Ni ratio) to compensate for variations in collection efficiencies and e-beam current. When analyzing the surface for carbon products of methane's dissociative chemisorption, AES signals are recorded in two regions. The first region of 260–290 eV is for the detection of the KLL transition of carbon, and the second region from 825 to 870 eV contains the intense LMM transition of nickel. The carbon (C) and nickel (Ni) peaks used to generate the C/Ni ratio are visible in Fig. 2.5. After calibration (discussed in Sect. 4.2.2), the C/Ni ratio produces a quantitative measure of the amount of carbon. The AES C/Ni signal is measured at several points along the surface to produce a 'profile' of the carbon 'spot' formed during the molecular beam exposure to the single crystal nickel surface. Auger 'profile' scans are used throughout this thesis.

2.3.5 LEED Spectrometer

Low energy electron diffraction (LEED) is used to obtain qualitative information about the sample's surface structure and to characterize the azimuthal orientation of the single crystal samples. The spectrometer (Omicron, SPECTALEED) has a low profile integrated electron gun. In LEED, a crystalline surface is bombarded with a collimated beam of low-energy electrons. The diffracted electrons are imaged as spots on a fluorescent screen. A LEED pattern of the Ni(110) crystal after cleaning (sputtering and annealing) is shown in Fig. 2.6. This confirms that the annealing process reconstructs the surface to its single crystal configuration.

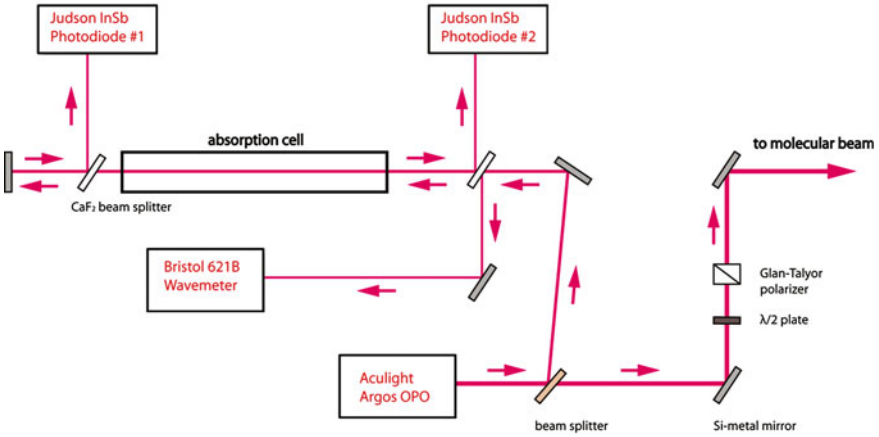

Fig. 2.7 Optical layout for the experiments conducted in this thesis work

LEED is used in Chap. 5 to characterize the alignment of the surface rows of Ni(110) in the laboratory frame.

2.4 CW-IR State-Preparation Setup

During this thesis work, the experimental setup (i.e. molecular beam and optical excitation scheme) changed from 'pulsed' to 'continuous'. Nevertheless, the goal of the experiment remains: quantum state-preparation of a molecular beam of methane for state-resolved gas/surface reactivity measurements, with the addition of alignment of the gas-phase reactant and the surface structure for the study of steric effects in vibrationally excited methane chemisorption. In this section, I discuss the CW-excitation scheme that has been developed during this thesis project.

2.4.1 Overview

Figure 2.7 presents the optical layout of our experimental setup and will be referred to throughout this section. I describe the light source (Aculight Argos OPO), the wavemeter (Bristol 621B), the tunable $\lambda/2$ wave plate (Alphalas GmbH) individually in the following sections of this chapter.

Tunable, single mode infrared radiation is generated by an optical parametric oscillator (OPO) which is pumped by a fiber laser. After separation of the signal and pump radiation, we split off between 5 and 15% of the horizontally polarized idler output towards a frequency stabilization and diagnostic setup consisting of an

absorption cell, IR-photodiodes and an IR-wavemeter. The angle of this beam splitter is chosen to give a sufficient amount of power to the frequency stabilization setup to generate a Lamb dip in a 1.6 m long absorption cell, typically filled with 20–100 μbar of gas at room temperature. The two CaF_2 beam splitters are used to send light to the wavemeter and the two photodiodes used as direct absorption detectors of the light traversing the absorption cell. Photodiode #1 is used for absorption measurements after the light makes a single pass through the cell. Photodiode #2 is used for absorption measurements after the light makes a round-trip through the absorption cell. Both measurement types are discussed in this chapter.

The five mirrors used in the optical setup, represented as gray rectangles with black edges, are silver (Ag) coated silicon discs ($\varnothing = 50.8$ mm) and have a polarization-independent reflectivity of >96% at 3.3 μm. They are used to steer the laser beam into the wavemeter, through the absorption cell (back and forth), and to cross the molecular beam.

The Glan-Taylor linear polarizer in this optical setup is used in conjunction with tunable $\lambda/2$ wave plate to serve as a continuously variable power attenuator of the linearly polarized CW excitation laser. We varied the excitation laser power from ~ 0 mW (polarizer axis aligned perpendicular to the horizontal polarized OPO idler output) to $\sim 90\%$ transmission of the polarizer using the $\lambda/2$ waveplate to rotate the polarization of light incident on polarizer). For the experiments presented in this thesis, we employed a YVO_4 Glan-Taylor polarizer from AlphaLas GmbH. The YVO_4 Glan-Taylor polarizer is composed of two right-angled YVO_4 (birefringent) prisms separated by an air gap between their long faces at nearly Brewster's angle. It has a wavelength range of 500–4,000 nm (20,000–2,500 cm^{-1}).

2.4.2 Light Source

The light source used here is an Argos model 2400 continuous wave, single mode optical parametric oscillator (OPO) produced by the Lockheed Martin Acculight corporation [4]. Optical parametric oscillation is a parametric process in which a coherent 'pump' laser beam is split into two lower frequency beams, termed 'signal' and 'idler' in a crystal that has sufficiently large nonlinear susceptibility. The 'signal' refers to the frequency that is resonant in the OPO cavity for a singly-resonant cavity. Due to the law of the conservation of energy, the equation dictating how the 'pump' frequency ω_{pump} can be split into 'signal' ω_{signal} and 'idler' ω_{idler} is

$$\omega_{pump} = \omega_{signal} + \omega_{idler}. \tag{2.1}$$

The Argos 2400 mid-infrared light source offers a continuously tunable idler wavelength range from 2.3 to 3.9 μm (4,350–2,600 cm^{-1}) using three different OPO modules (A from 2.3 to 2.5 μm, B from 2.5 to 3.2 μm and C from 3.2 to 3.9 μm). In this work we are using module 'C' (3,100–2,600 cm^{-1}). The attractive features of the Argos model 2400 are its high power (>1 W over entire tuning

range), narrow linewidth (<1 MHz for both signal and idler), CW output, good beam quality ($M^2 < 1.1$) and linear polarization.

The OPO pump source is a continuous, 15 W, single mode, diode pumped, fiber amplifier operating at 1,064 nm and continuously tunable over 50 GHz without mode hops. It consists of a distributed feedback (DFB) Yb-doped fiber laser with a bandwidth of <100 kHz that seeds a 15 W fiber amplifier. The pump light is transmitted through an armored fiber cable to the OPO module. The pump source output is a collimator lens barrel that can be 'keyed' to the input of the OPO module, allowing for 'alignment free' pump changing between the various modules that cover the system's frequency range. Only the signal wavelength is resonant in the OPO cavity. The idler exits the OPO after a single pass.

The nonlinear material in the OPO is a lithium niobate, $LiNbO_3$ (LN), crystal. The crystal is periodically-poled (PP), meaning that the birefringent material is formed with domains of alternating orientation such that the alternation period is a multiple of the desired wavelength of operation. Periodic poling is often accomplished by 'ferroelectric domain engineering' which uses micro-structured electrodes to apply a strong electric field to the crystal so that the crystal orientation and the sign of the nonlinear coefficient are permanently reversed under the electrodes [5]. This structured medium is used to achieve quasi-phase matching (QPM) in the material. Furthermore, the periodic poling is engineered in a 'fan out' pattern such that the poling period varies continuously across the LN crystal. This 'fan out' pattern allows for a wide tuning range of the OPO for a single PPLN crystal by translating the crystal to sample different poling periods with the pump laser.

Tuning of the OPO output wavelengths (signal and/or idler) is accomplished in three steps: coarse, intermediate and fine tuning. Course tuning ($\sim 13\ cm^{-1}$ steps as defined by the free spectral range of the etalon in the laser cavity) of the OPO signal frequency is accomplished by translation of the PP-LN crystal, changing the poling period of the $LiNbO_3$ exposed to the pump beam to achieve phase matching for the desired signal and idler combination. Intermediate frequency tuning of the signal is accomplished by changing the angle of an intracavity Fabry–Perot etalon with a free spectral range of 400 GHz (or $\sim 13\ cm^{-1}$) in the oscillator cavity via a galvanometer ($\sim 1\ cm^{-1}$ steps in signal frequency defined by the cavity mode spacing). Tilting the etalon by 2° (±1°) covers a complete free spectral range of the etalon. Fine tuning of the OPO idler frequency can be achieved by applying strain to the DFB seed laser via a piezo element with a voltage (0–90 V allows continuous tuning over $1.7\ cm^{-1}$) (50 GHz). Straining the DFB seed laser causes a frequency change in the pump laser and therefore in the idler output since the resonant signal frequency is fixed by the OPO cavity. This is due to Eq. 2.1.

Figures 2.8a and b show the idler intensity profile in the horizontal and vertical direction as a function of distance from the OPO's output. This data was collected by a model TS50 infrared camera from ThermoSENSORIK GmbH.

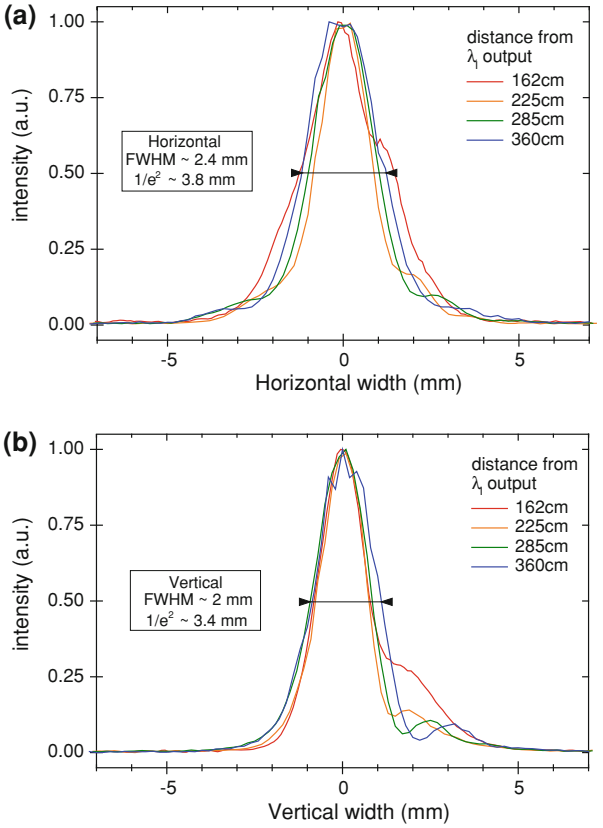

Fig. 2.8 **a** OPO idler beam profile (*horizontal*) as a function of distance. **b** OPO idler beam profile (*vertical*) as a function of distance

2.4.3 Wavemeter

A Bristol Instruments model 621B Laser Wavemeter is used to measure the frequency the excitation laser. The wavemeter has a specified wavelength range of 1.0–5.0 μm, an absolute accuracy of ±0.0023 cm^{-1} (±70 MHz) and a repeatability of ±10 MHz (standard deviation for a 5 min measurement) at 3,000 cm^{-1}. Typically, less than 1 mW of idler power is needed for frequency characterization. As shown in Fig. 2.7, the light used for the wavemeter reading is split from the excitation laser beam directly before it enters into the absorption cell. As discussed in Sect. 2.5, we stabilize the laser frequency to better than the repeatability limit of the wavemeter. Therefore, the wavemeter is a useful tool to bring the excitation frequency close to the ro-vibrational transition of interest, but can not give an exact measurement of the laser's frequency stability when

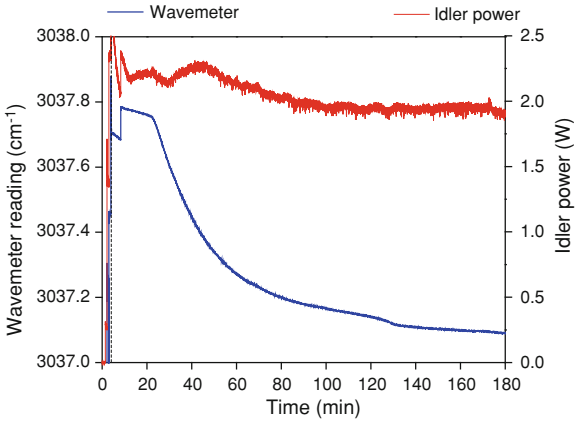

Fig. 2.9 Data showing the idler frequency and power stability of the OPO as function of time

we are locked to a narrow spectral feature such as a Lamb dip with a typical full width at half maximum (FWHM) of <2 MHz.

Figure 2.9 shows frequency data collected by the wavemeter as a function of time with zero-time corresponding to the OPO pump laser being turned ON. The frequency instabilities during the first 3 min in both idler power and wavemeter reading are due to the pump power being increased from 0 to 15 W in increments of 3 W. The idler frequency drifts from 3,037.8 cm^{-1} to 3,037.25 cm^{-1} during the first 60 min of operation at 15 W pumping. This corresponds to a frequency drift of ~16.5 GHz (~275 MHz/min) which makes locking of the laser frequency to ~1 MHz a challenge during the warmup period. However, from the 60th to the 180th minute the frequency drifts smoothly from 3,037.25 cm^{-1} to 3,037.1 cm^{-1} or ~4.5 GHz (~38 MHz/min). A frequency drift of this magnitude can be counteracted by changing the seed laser frequency in order to maintain the frequency 'locked' to <1 MHz for several hours. The frequency stabilization technique is described in the following section. Before attempting to actively stabilize the OPO idler frequency, we typically allow the laser system (the OPO pump) to warm up for ~1 h.

As shown in Fig. 2.9, the idler power drops from 2.37 W to 2.13 W or ~11% during the first 60 min of operation at 15 W pump power. From the 120th to the 180th minute, the OPO idler power decreases from 1.96 to 1.89 W or ~3.5%. This laser (idler) power data was collected using a calibrated photodiode, and is offered as a demonstration of the stability of the OPO over an extended period of time.

2.4.4 Tunable λ/2 Wave Plate

The tunable $\lambda/2$ wave plate (Alphalas GmbH) in the optical setup serves two purposes: (1) In combination with a polarizer, it acts as a continuously variable power attenuator for the collection of excitation fluence dependence curves of the

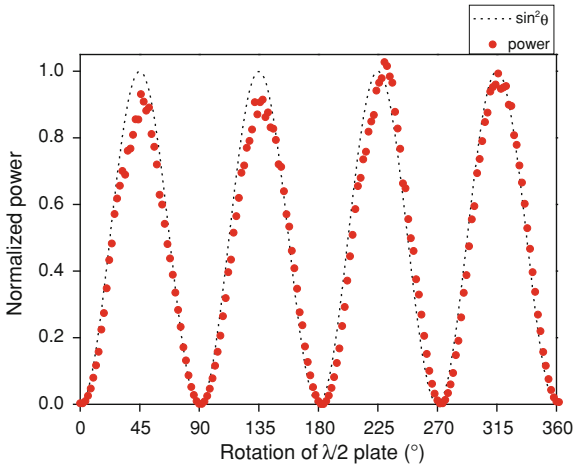

Fig. 2.10 Normalized idler power transmitted through a vertical, linear polarizer as a function of $\lambda/2$ waveplate angle

molecular beam absorption and (2) it is used to rotate the polarization direction of the excitation beam which controls the alignment of the ro-vibrationally excited molecules in the molecular beam.

Figure 2.10 shows the idler power transmitted through a linear polarizer (aligned vertically in the laboratory frame) as a function of $\lambda/2$ plate angle. The maximum power is for vertically polarized radiation, while the minimum corresponds to horizontally polarized radiation. The extinction ratio is measured to be $<0.6\%$, confirming that the laser polarization is well defined.

2.5 Frequency Stabilization

The goal of the optical setup is to prepare a molecular beam of methane in a specific quantum state. For example, we want to excite CH_4 with one quantum of the antisymmetric stretch (ν_3) of CH_4 with a band origin at 3018.825 cm^{-1} and the CH-stretch (ν_1) of CD_3H with a band origin at 2992.745 cm^{-1}. For reliable excitation of rovibrational transitions in the molecular beam, the frequency of the excitation laser needs to be stable to within the homogeneous linewidth of the transition in the molecular beam. For our experimental conditions, transit time broadening dictates the absorption linewidth to be ~ 1 MHz [6]. This frequency stability is needed on the time scale of minutes to hours for our quantum state-prepared molecular beam deposition experiments.

The OPO pump laser is sensitive to temperature fluctuations and air currents in the laboratory. Its frequency can drift several MHz on the minute time scale and hundreds of MHz in an hour. Figure 2.11 shows the inherent frequency stability of the OPO output is not sufficient to maintain resonance with a given transition in the molecular beam of ~ 1 MHz (FWHM). The data in Fig. 2.11 was collected at

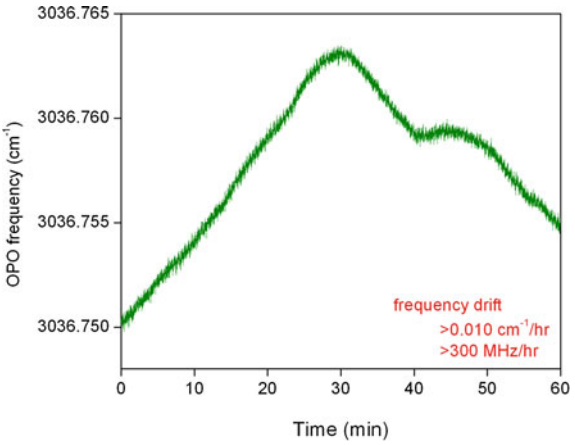

Fig. 2.11 Data taken for 1 h (after 3 h at 12 W pump power) to demonstrate the inherent frequency stability of OPO idler output

a frequency of 1 Hz with the Bristol Instruments wavemeter in our optical setup, see Fig. 2.7.

Since the OPO frequency is not inherently stable to 1 MHz, even on the second time scale, a way to stabilize or 'lock' the frequency of the OPO resonant to a rovibrational transition in the molecular beam is needed. This can be accomplished by a feedback control loop. The reference signal of the control loop must be well defined at the rovibrational transition frequency and be 'signed'. By 'signed', I mean that if the laser frequency drifts off-resonance, the reference signal should contain information as to the drift direction. We have chosen to actively stabilize the excitation laser frequency to the first derivative of a Lamb dip generated in a Doppler broadened transition [7]. The signal generation and utility is explained in this section.

To bring the laser frequency into resonance with and actively stabilize it to a rovibrational transition, we can use an absorption cell filled with the gas of interest, see Fig. 2.7. The laser frequency is modulated about a rovibrational transition of the gas in the cell. After the excitation laser makes a single pass through the absorption cell, the absorption of light due to the Doppler broadened transition in the room temperature cell can be detected with a photodiode #1, as depicted in Fig. 2.12(left).

Phase sensitive detection of the absorption signal by a lock-in amplifier produces the first derivative (derivative) of the Doppler broadened transition, as depicted in Fig. 2.12(right). The 'derivative' is generated by multiplying the absorption signal (signal) by the modulation (reference) and averaging the result by a low pass filter. The zero crossing of the 'derivative' represents a maximum (or minimum) in the signal. Furthermore, the 'derivative' contains information for the direction of the corrective response as its sign is dependent on frequency drift direction. The derivative signal can be processed by a regulator circuit to generate a control signal to be feedback to the frequency determining element of the excitation laser. Via this control loop, the laser frequency can be stabilized to

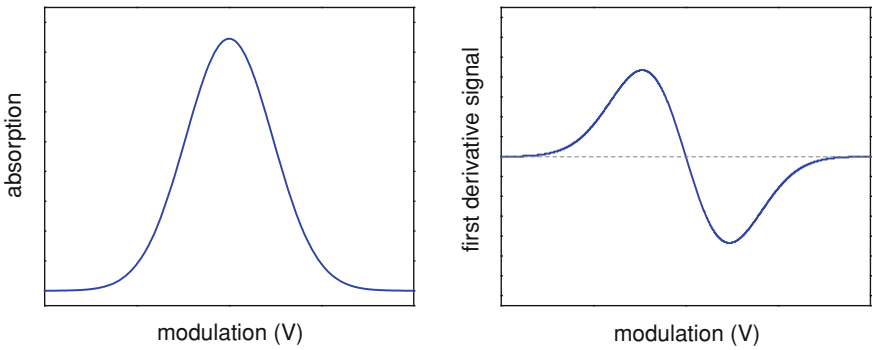

Fig. 2.12 Simulated Doppler broadened absorption signal (*left*) and its first derivative signal (*right*) as a function of a modulation voltage that dictates the frequency of the excitation laser

the maximum of the Doppler broadened transition by actively stabilizing the absorption's derivative signal to its zero crossing.

The only problem with frequency stabilization to the maximum of the Doppler broadened transition is the achievable frequency definition. A typical Doppler broadened linewidth for methane excited with 3 μm light in a room temperature gas is $\sim$300 MHz (FWHM). As stated above, we need to stabilize the laser frequency to $\sim$1 MHz in order to maintain resonance with a transition in the molecular beam. Frequency stabilization to a $\sim$300 MHz absorption line will not fulfill this requirement.

Retroreflection of the excitation laser produces a saturation dip in the center of the Doppler broadened absorption signal. This well known spectral feature [8–11] is called a Lamb dip, after the American physicist Willis Eugene Lamb. When the excitation laser frequency is slightly detuned from the Doppler broadened (transition), the counterpropagating laser beams interact with different subgroups of the velocity distribution characterized by Doppler shifts ($\Delta\omega_B$) from

$$\Delta\omega_B = {}^{\omega_B v_z}/_{c}. \tag{2.2}$$

Here, v_z is the velocity component along the laser propagation axis, ω_B is the transition's center or Bohr frequency, and c is the speed of light. As the excitation laser frequency approaches ω_B, the counterpropagating laser beams compete to excite the same Doppler sub-set of molecules, namely those molecules with no velocity along the propagation axis of the excitation laser. This competition leads to a decrease in the absorption signal if the laser power is sufficiently high to saturate the transition.

Figure 2.13(left) shows a simulated Lamb dip in a Doppler broadened absorption. With phase sensitive detection, a steep zero crossing corresponding to the Lamb dip minimum is observed. The first derivative of a Lamb dip signal is depicted in Fig. 2.13(right). Typical Lamb dip linewidths are in the vicinity of

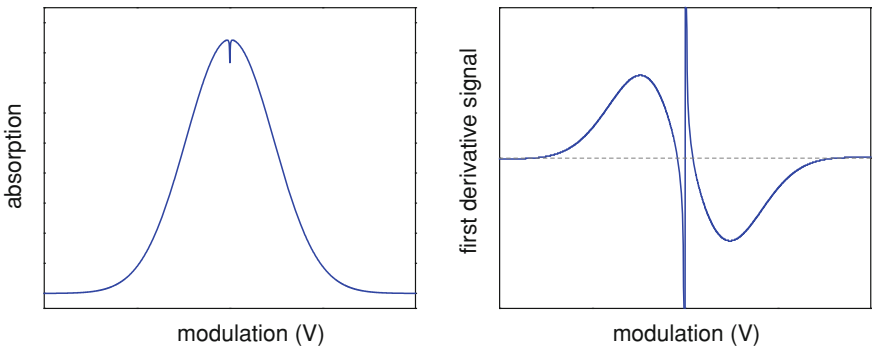

Fig. 2.13 Simulated Lamb dip in Doppler broadened absorption signal (*left*) and its first derivative signal (*right*) as a function of a modulation voltage that dictates the frequency of the excitation laser

1 MHz and allow for a much higher definition of the laser frequency than the Doppler broadened transition would.

The Lamb dip signal corresponds precisely to the zero-Doppler shifted molecular absorption frequency, which is the needed frequency for excitation of the molecular beam. The center-line trajectory of a molecular beam has a zero-Doppler shifted absorption when the excitation crosses at a right angle to it (as we do).

2.5.1 Lamb Dip Detection and Characterization

Below, I discuss the details of the excitation laser frequency stabilization. Typically, Lamb dip spectra are generated with the absorption cell filled to a pressure of 20–30 μbar for $CH_4(\nu_3)$ or 80–100 μbar for $CD_3H(\nu_1)$.

The Doppler broadened absorption profile of $CH_4(\nu_3)$-R(0) shown in Fig. 2.14 was recorded by sending a single pass of 8 mW of the OPO idler through the absorption cell, filled with 30 μbar of CH_4. The OPO idler frequency was modulated by 'scanning' the voltage applied to the OPO pump's seed laser with an 8 V amplitude, 10 Hz triangle waveform. The transmitted idler intensity was detected by photodiode #1, (see Fig. 2.7) connected to the analog/digital converter input of a 12-bit National Instruments model 6023-E data acquisition card (DAQ) at a sampling rate of 100,000 samples/sec. The spectrum consists of 5,000 points.

A Gaussian fit of the measured absorption line is shown in Fig. 2.17. At the absorption peak, the absorption cell transmission was 46% which corresponds to an absorbance of 0.78. I calibrated the frequency scale of the OPO idler using the calculated 278.3 MHz linewidth of the Doppler broadened $CH_4(\nu_3)$-R(0) line (3028.75218 cm^{-1}) [12] at room temperature and the FWHM of the Gaussian fit of 1,383 samples (data points). This gave a calibration of 4.97 samples/MHz (or 1,383/278.3 samples/MHz) for these specific experimental conditions.

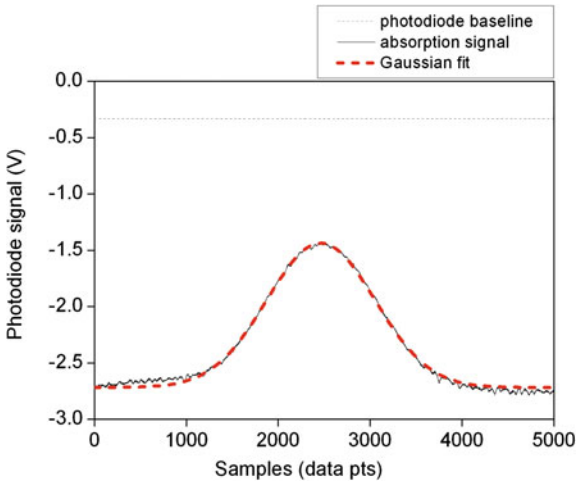

Fig. 2.14 Characteristic Doppler broadened $CH_4(\nu_3)$-R(0) transition at room temperature. $P_{cell} = 30$ μbar, $P_{idler} = 8$ mW, OPO frequency modulation by an 8 V amplitude triangle wave at 10 Hz. The photodiode baseline is shown to display the raw data used to determine cell transmission

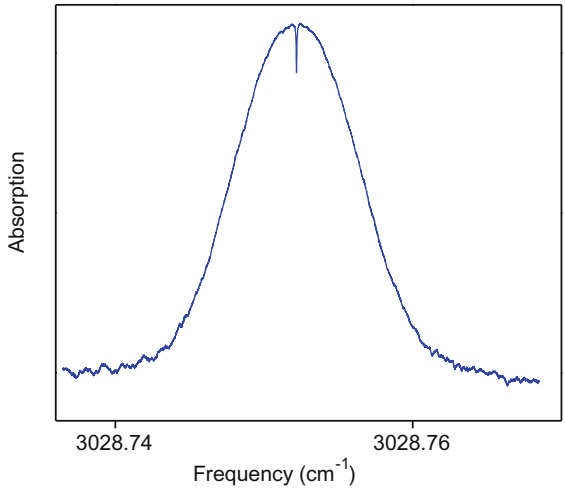

Fig. 2.15 Doppler-free saturation Lamb dip within a Doppler broadened $CH_4(\nu_3)$-R(0) transition at room temperature. $P_{cell} = 30$ μbar, $P_{idler} = 85$ mW, modulation by an 8 V amplitude triangle wave at 10 Hz

Under the same experimental modulation conditions as the calibration described above, I produced a saturation (Lamb) dip in the $CH_4(\nu_3)$-R(0) Doppler broadened absorption profile. Figure 2.15 shows an absorption profile that was recorded with photodiode #2 (see Fig. 2.7) after the excitation beam was retroreflected through the cell. In Fig. 2.15, the x-axis is displayed in cm^{-1} using the known absorption line center for $CH_4(\nu_3)$-R(0) and the 4.97 samples/MHz calibration from above.

The Lamb dip shown in Fig. 2.15 has a 'contrast ratio' (intensity ratio of the Lamb dip to its Doppler broadened absorption) of 13%. This sharp, Doppler-free spectral feature is important, since we stabilize the excitation beam's frequency to it. The infrared absorption of methane in the molecular beam is homogeneously

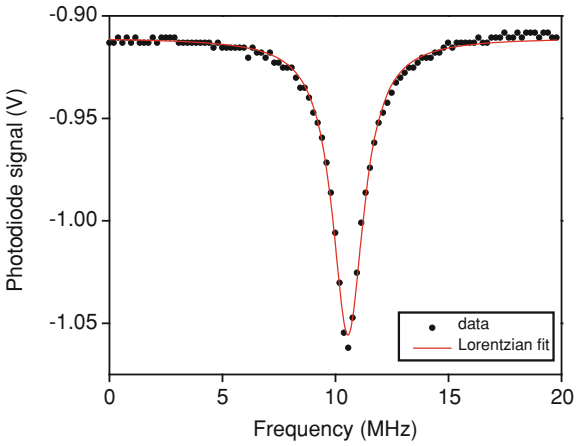

Fig. 2.16 Zoomed view of Lamb dip in previous figure. FWHM determined to be 1.76 MHz from this Lorentzian fit. From repeated measurements, the FWHM of a Lamb dip in $CH_4(\nu_3)$ using 30 mbar of in the cell and a power of 85 mW at its input is found to be 1.52 ± 0.27 MHz

broadened to approximately 1 MHz. To maintain the excitation laser resonant with a molecular beam transition, it is necessary to define the laser frequency to better than the linewidth of the transition in the molecular beam.

I measured the Lamb dip linewidth on three separate days and determined its FWHM to be 1.52 ± 0.27 MHz for the $CH_4(\nu_3)$ excited via the R(0) transition with 30 μbar of CH_4 in the room-temperature cell and 85 mW idler power at the cell input. Figure 2.16 shows a zoomed-in view of the Lamb dip of Fig. 2.15, using a relative MHz scale as the X-axis for clarity. Fitting the Lamb dip feature with a Lorentzian profile, I determined the linewidth (FWHM) of the Lamb dip to be 1.76 MHz for this spectrum.

Lamb dips in $CH_4(\nu_3)$ transitions have been reported in literature [10, 11, 13, 14]. I follow the linewidth calculations in Ref. [10] to determine the expected linewidth of the Lamb dip under our experimental conditions. The linewidth of a Doppler-free Lamb dip is determined by:
pressure broadening

$$\Delta_{pressure} = \frac{\partial \Delta_{pressure}}{\partial p} p, \tag{2.3}$$

transit-time broadening,

$$\Delta_{transit} = \frac{1}{4\omega_B}\sqrt{\frac{2k_B T}{m}} \tag{2.4}$$

and power broadening

$$\Delta_{power} = \Omega. \tag{2.5}$$

In the above equations, p is the gas pressure in the absorption cell, ω_0 is the excitation beam radius, k_B is the Boltzmann constant, T is temperature, m is the mass of the absorbing molecule, Ω is the Rabi frequency [15, 16].

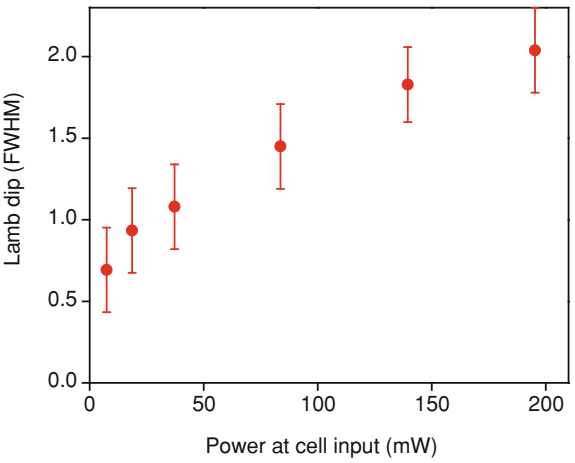

Fig. 2.17 Study of $CH_4(\nu_3)$-R(0) Lamb dip linewidth as a function of excitation laser power for cell. *Error bars* represent the standard deviation of repeated measurements at laser power of 85 mW at the cell input. $P_{cell} = 30$ μbar

Using a pressure-broadening coefficient of $\Delta_{pressure} = 5.1$ kHz/μbar [17], a broadening of 153 kHz (FWHM) due to a pressure of 30 μbar in the absorption cell is expected.

Using an average beam radius of 1.5 mm ($\frac{1}{e^2}$) and a temperature of 295 K, transit time broadening is expected to be 185 kHz (FWHM) for CH_4 (mass of 16 amu).

To calculate expected power broadening, we must calculate Ω. Where,

$$\Omega = \frac{\mu_{21} \cdot E}{\hbar} \tag{2.6}$$

and

$$E = \sqrt{\frac{2I}{\varepsilon_0 c}} \tag{2.7}$$

and

$$I = \frac{P}{A}. \tag{2.8}$$

Here, μ_{21} is the vibrational transition dipole moment (1.80×10^{-31} C.m for $CH_4(\nu_3)$) [12], E is the electric field strength, I is the electric field intensity and is calculated simply dividing the laser power P by its area A (using the $\frac{1}{e^2}$ width of 3 mm as a diameter). I find that $I = 19.8\,\mathrm{kW/m^2}$ and $E = 3.86\,\mathrm{kV/m}$. This results in $\Omega = 0.82$ MHz which means 0.82 MHz of power broadening is expected when using an excitation power 85 mW.

I find that the dominant broadening mechanism in the experimental setup is power broadening. Figure 2.17 shows experimentally observed $CH_4(\nu_3)$-R(0) Lamb dip linewidths (FWHM) as a function of excitation laser power at the absorption cell

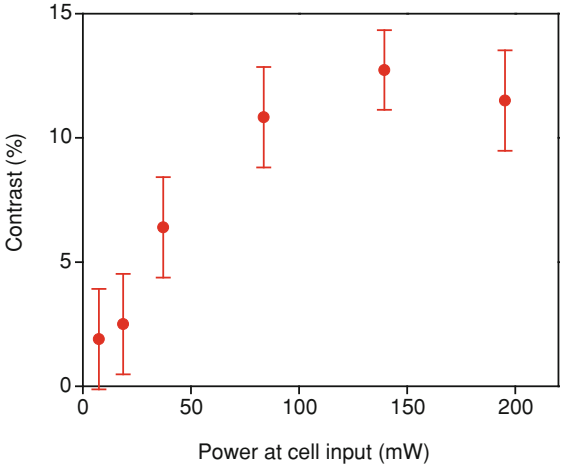

Fig. 2.18 Study of $CH_4(\nu_3)$-R(0) Lamb dip contrast ratio as a function of excitation laser power. *Error bars* represent the standard deviation of repeated measurements at laser power of 85 mW at the cell input. $P_{cell} = 30$ μbar

input. The data were taken with 30 μbar of CH_4 in the absorption cell, frequency modulating the OPO idler at 10 Hz with an 8 V amplitude triangle wave and collection data at 100,000 samples/sec (spectra consisting of 5,000 points).

Figure 2.18 shows the experimentally observed Lamb dip 'contrast ratio', or the Lamb dip's amplitude as a percentage of the peak absorption of the Doppler broadened transition.

I typically use between 40 and 200 mW of OPO idler power to produce a Lamb dip used for active stabilization of the OPO idler frequency (<100 mW for CH_4, >100 mW for CD_3H). For $CH_4(\nu_3)$-R(0), this gives a Lamb dip FWHM of 1–2 MHz and a contrast ratio of 6.5–12.5%. In the following section, I discuss the same case presented in this section of 85 mW of OPO idler power for Lamb dip stabilization.

2.5.2 Lamb Dip Locking

To maintain the OPO output frequency locked to a rovibrational transition of methane for an extended amount of time, the OPO frequency (0–2 MHz) is dithered by sending a small amplitude (0–13 mV peak-to-peak) sine wave to the OPO pump's seed laser. Then, the Lamb dip absorption signal is collected via a Judson (J10D-M204-R01 M-30) liquid nitrogen cooled photodiode with PA-7-60 pre-amplifier, and used as the AC-coupled amplifier output with a gain of 2.5×10^4 as the input of the LaseLock 3.0 Universal Laser Stabilization Electronics.

Frequency stabilization is done with the LaseLock 3.0 Universal Laser Stabilization Electronics produced by TEM Messtechnik GmbH. Figure 2.19 shows a schematic of the device. The LaseLock 3.0 is composed of:

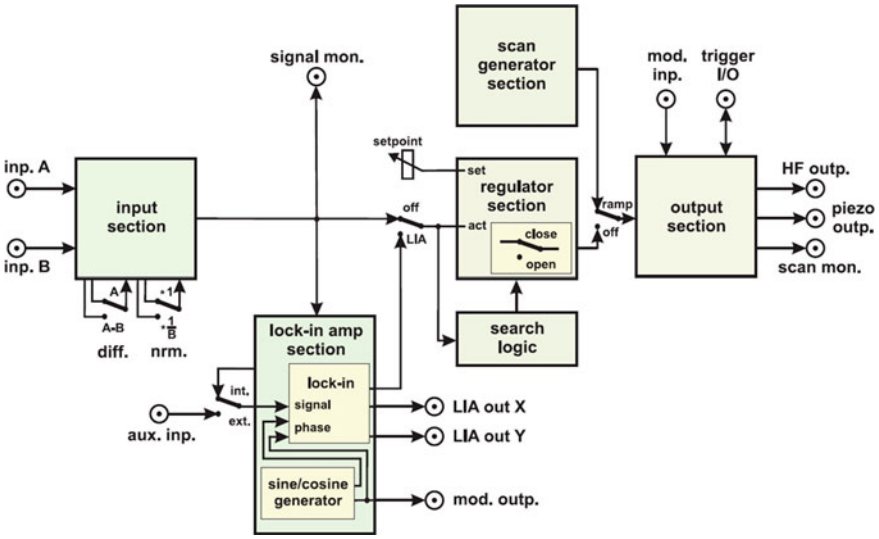

Fig. 2.19 Schematic of the LaseLock 3.0 (TEM Messtechnik GmbH). Figure is reproduced with permission

1. input amplifier
2. lock-in amplifier
3. 2 independent PID regulators
4. scan generator (0 to ±10 V triangle wave)
5. voltage output (0–90 V DC).

The voltage output of the LaseLock 3.0 is connected to the piezo element of the OPO pump seed laser, so that a voltage sent from the LaseLock 3.0 corresponds to a frequency shift in the OPO's pump and, in turn, idler frequency as the signal frequency is fixed due to its oscillation in the OPO cavity. There are three ways of changing the voltage output of the LaseLock 3.0 (i.e. the OPO idler output frequency). The first is a DC offset (0–90 V) (via 'piezo outp.') that is controlled manually with a knob on the device's front panel. This allows one to tune close to the frequencies of rovibrational transitions in the absorption cell. From the Argos 2400 manual, we expect a frequency shift of 50 GHz for a 0–90 V DC variation. Another way of varying the output voltage (OPO idler frequency) is by a 'scan generator' that produces a triangle waveform (0 to ±10 V) (via 'piezo outp.') which is useful for viewing a Doppler broadened transition and diagnosing the optical setup (i.e. alignment of counter-propagating laser beams). The third way to vary the output voltage (OPO idler frequency) is by producing a sine wave (via 'mod. outp.') with the lock-in amplifier section of the LaseLock 3.0. The sine wave modulation (0–13 mV) is used to periodically dither the idler frequency about the Lamb dip minimum so that the lock-in amplifier has a referenced signal for differentiation.

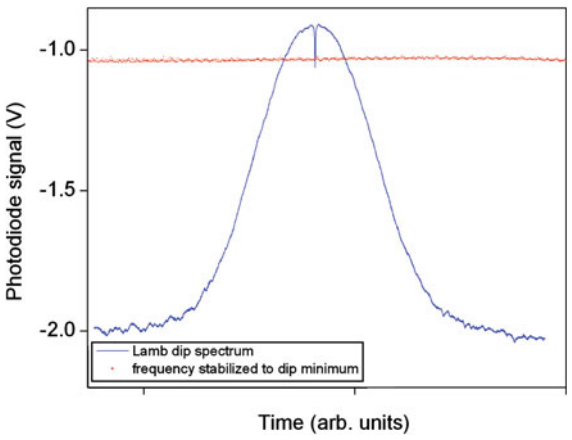

Fig. 2.20 Example photodiode signal for frequency stabilized OPO. Stabilized signal modulated at ~500 Hz with <1 mV amplitude sine wave. The Lamb dip was produced in Doppler broadened $CH_4(\nu_3)$-R(0) transition at room temperature. $P_{cell} = 30$ μbar, $P_{idler} = 85$ mW, modulation by an 8 V amplitude triangle wave at 10 Hz

We stabilize the OPO idler frequency to the Lamb dip minimum by modulating the OPO pump laser's frequency on the Lamb dip feature with a 0–13 mV amplitude sine wave which corresponds practically to 0–2 MHz frequency modulation. The photodiode signal ('inp. A' in Fig. 2.19) of the Lamb dip is multiplied with the modulation signal, and then averaged by a low pass filter. The resulting waveform (lock-in signal) is the first derivative of the Lamb dip with respect to the OPO idler frequency, analogous to the derivative signal in Fig. 2.13 (right).

The zero-crossing of the derivative signal represents the minimum of the Lamb dip which is the excitation line center. To stabilize the OPO idler frequency, the derivative signal is processed by a Proportional-Integral–Differential (PID) regulator ('regulator section' block in Fig. 2.19) which generates a control signal that is fed back to the piezo element allowing fine tuning of the OPO pump seed and in turn the idler frequency. This closes the control loop and actively locks the idler's output frequency. A more detailed description of the frequency locking procedure and optimized settings for the LaseLock 3.0's lock-in amplifier and PID regulator are given in Appendix A.

Figure 2.20 shows two traces. The first trace is a Lamb dip spectrum of the $CH_4(\nu_3)$-R(0) line collected with photodiode #2. The second trace is the signal collected with the same photodiode when the OPO frequency is actively stabilized to the Lamb dip minimum. The fact that the diode signal stays constant at a voltage level which corresponds to the minimum of the Lamb dip demonstrates that the idler frequency of the OPO remains stable on the Lamb dip minimum. Any instability of the idler frequency would be detected as significant amplitude noise in the photodiode signal.

Figure 2.21 shows the effect that decreasing the sine wave modulation (from 13 mV to <<1 mV) has on the Lamb dip signal seen by photodiode #2. The full Lamb dip height was from –0.911 to –1.056 V ($\Delta_{Full} =$ 145 mV). I locked the excitation laser frequency loosely (with a sine wave modulation of 13 mV) to

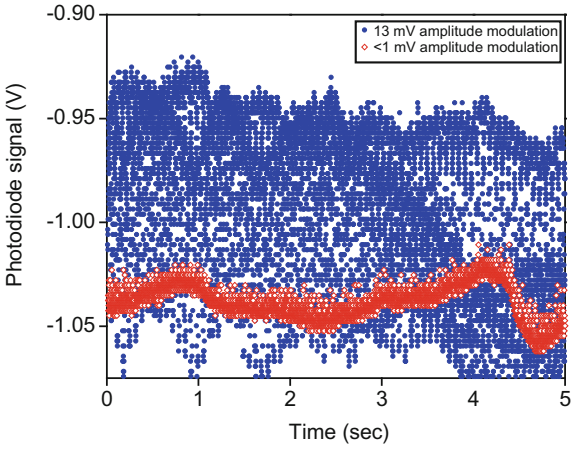

Fig. 2.21 Demonstration of frequency locking to Lamb dip. The Lamb dip was produced in Doppler broadened $CH_4(\nu_3)$-R(0) transition at room temperature. $P_{cell} = 30$ μbar, $P_{idler} = 85$ mW

produce an absorption signal varying between –0.920 V and –1.086 V ($\Delta_{Loose} = 166.0$ mV) with an average value $\Delta_{Loose}^{Average}$ of –0.994 ± 0.040 for a 5 s measurement collected at 1 sample/msec. Under tight locking conditions (modulation <<1 mV), the signal varied between –1.011 and –1.062 V ($\Delta_{Tight}^{Total} = 51$ mV) with an average value $\Delta_{Tight}^{Average}$ of –1.038 ± 0.008 V for a 5 s measurement.

The photodiode output voltage is sensitive to the absorption signal and therefore gives a measure of the Lamb dip linewidth, but the photodiode is also sensitive to vibrations on the optical table and any variation in the excitation laser power. Therefore, any linewidth determination from the photodiode signal voltage is an upper limit (conservative estimate) to the true linewidth achieved in our experimental setup.

For the idler's linewidth determination in the 'tightly' locked configuration, I used Δ_{Full} and the average of a 5 s signal as described above. The tightly locked configuration's variation $\Delta_{Tight}^{Average}$ lies at 12.4% of the Lamb dip's full depth. Figure 2.22 shows the Lorentzian fit (FWHM = 1.76 MHz) of the data from Fig. 2.16. The full-width at 87.6% maximum (100–12.4%) gives a linewidth of 650 ± 180 kHz for the 5 s measurement. Using Δ_{Tight}^{Total}, the total photodiode signal variation for the 5 s measurement, the total frequency variation for the 5 s measurement is 1.28 MHz. The 1.28 MHz is taken from the full-width at 65% of the dip minimum, since $\Delta_{Tight}^{Total}/\Delta_{Full} = 0.35$. Again, this determination is a conservative estimate of the linewidth of the actively stabilized laser frequency.

I display the long term stability achieved by the frequency locking technique with wavemeter data. Fig. 2.23 shows the wavemeter reading as a function of time after the laser system was running at a pump power of 10.5 W for an hour. For the first 38 min of the measurement, the stabilization is not used (Not Locked). During that time, the frequency drifts 0.04 cm^{-1} or 1,200 MHz. Then, the laser frequency is

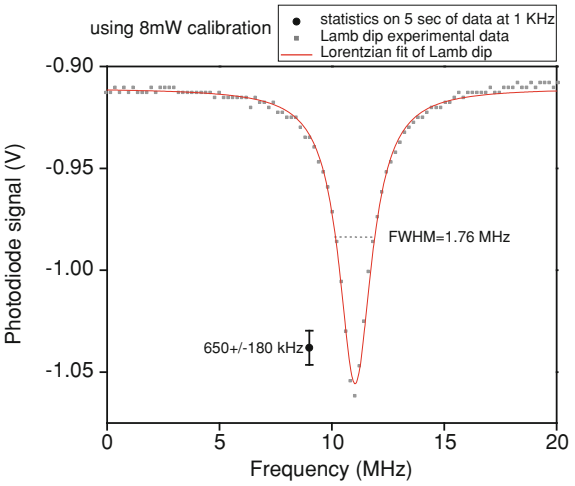

Fig. 2.22 Simulated $CH_4(\nu_3)$-R(0) Lamb dip with Lorentzian profile to illustrate frequency locking ability

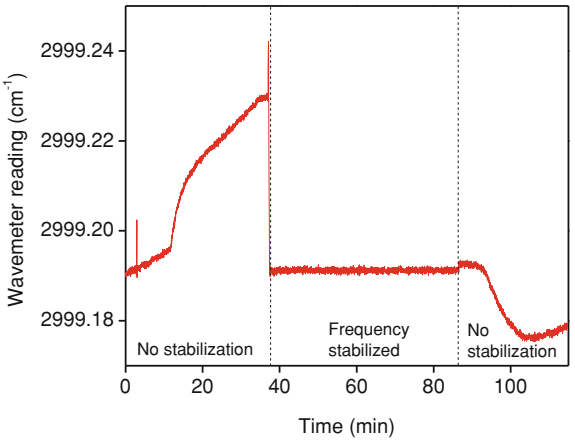

Fig. 2.23 OPO idler frequency with and without active stabilization to $CD_3H(\nu_1)$-R(0) Lamb dip as measured by the Bristol 621B wavemeter

actively stabilized to a Lamb dip produced in the absorption cell. For this data, I stabilized the laser frequency to the R(0) transition of $CD_3H(\nu_1)$ using 190 mW of idler output from the OPO and a pressure of 80 μbar in the cell. I calculated the absorption line to be at 2999.1928 cm^{-1} (see Appendix C) and measured it to be at 2999.1912 ± 0.0004 cm^{-1} (±11 MHz) over the 48 min that the laser was stabilized to the Lamb dip. Both the absolute accuracy and the repeatability of the wavemeter reading are within the specifications of the wavemeter, as stated in Sect. 2.4.3.

The data in this section show that the excitation laser is actively stabilized to a rovibrational transition in methane via Lamb dip locking to <1.2 MHz on a 5 s timescale and maintains the locking on the hour timescale. In the following section, I characterize the excitation of the molecular beam.

2.6 Pyroelectric Detection of Vibrationally Excited Molecules in a Molecular Beam

To monitor the IR-absorption of methane and the extent of rovibrational excitation in the molecular beam, we use a pyroelectric detector. Pyroelectric detectors use the pyroelectric property of certain crystals to respond to a temperature change with an electric potential difference. Pyroelectric crystals can be thought of as possessing a permanent electric polarization. When the crystal is at a constant temperature, this polarization is compensated by free charge carriers that reach its surface by conduction through the crystal and from the surroundings. If the crystal experiences a change in temperature, the atoms in the crystal lattice modify their position which changes the permanent electric polarization of the crystal and manifests itself as pyroelectricity. The polarization potential is temporary, only present while the temperature is changing.

A pyroelectric detector responds to temperature changes and therefore is well suited for the detection of modulated signals. This lends itself to phase-sensitive detection by a lock-in amplifier. We impinge a continuous molecular beam onto a pyroelectric detector, exciting the molecular beam with a periodically chopped laser excitation. The signal on the pyroelectric detector is due to a change in the vibrational energy content in the molecular beam (excitation ON/OFF) and can be lock-in detected using the optical chopper frequency as a reference. The details of this setup are given below.

An ELTEC 406 M pyroelectric detector with a 2 mm dia. active area on a rotating arm was installed in the UHV system mounted such that the pyroelectric detector is able to be positioned into the molecular beam path.

Figure 2.24 is a photo of the interior of the UHV chamber, and shows the experimental configuration for impinging the molecular beam onto the pyroelectric detector. The molecular beam enters the UHV chamber through a 1 mm aperture, blue (upper-left) circle. The pyroelectric detector, red (upper-right) circle, is positioned in the molecular beam path by a rotation-translation feed through (yellow or lower circle) which permits positioning in two dimensions perpendicular to the molecular beam.

As the pyroelectric detector is sensitive only to changes in temperature, a continuous molecular beam will not generate a signal, after the pyroelectric detector's initial warming up from the translational energy deposited on the detector by the molecular beam. Figure 2.25 shows the signal registered by a 34 kJ/mol translational energy molecular beam of CH_4 in H_2 on the pyroelectric detector after an amplification of 10x by a home-built amplifier (design from ELTECdata 136, ELTEC Instruments, Inc.) that has variable gain of 10x and 95x. The initial voltage rise is the introduction of the molecular beam into the UHV and onto the pyroelectric detector that is positioned in the molecular beam's path. Approximately 300 ms after the CW molecular beam begins to impinge on the pyroelectric detector, the detector reaches its peak voltage. Approximately 8 s

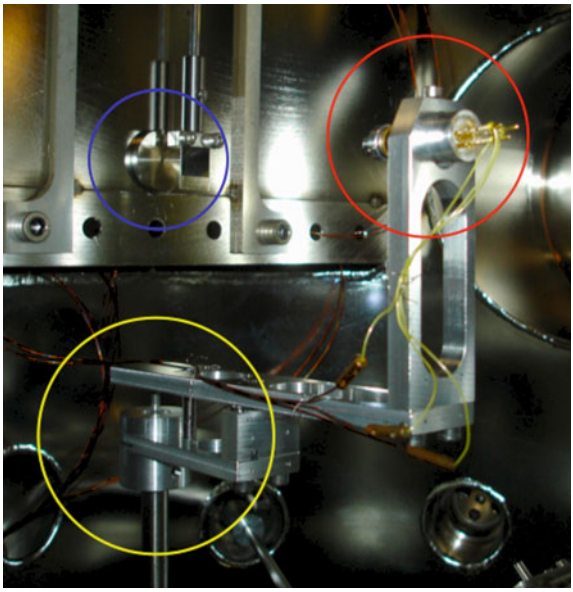

Fig. 2.24 Photo of pyroelectric detector (*red circle*) positioned in molecular beam path (whose input aperture to the UHV, *blue circle*) by rotation of swivel arm (*yellow circle*) in the UHV chamber

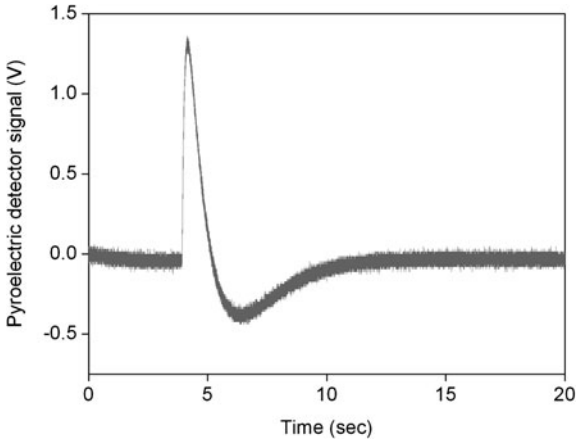

Fig. 2.25 Response of the pyroelectric detector (10x amplification) translational energy deposited by a 34 kJ/mol CW molecular beam

after introduction of the CW molecular beam, the pyroelectric detector has re-stabilized to its baseline signal of 0 V.

Figure 2.26 shows the optical setup for pyroelectric detection of IR absorption in a CW molecular beam. IR absorption of methane in a continuous molecular beam is detected by modulating the resonant excitation laser light (ON/OFF) via a shutter (Uniblitz) at a frequency within the bandwidth of the pyroelectric detector circuit (5 Hz). This modulation produces a signal proportional to the number of excited molecules prepared with by laser excitation. We lock-in detect the modulated signal from the pyroelectric detector amplified 95x via the aforementioned

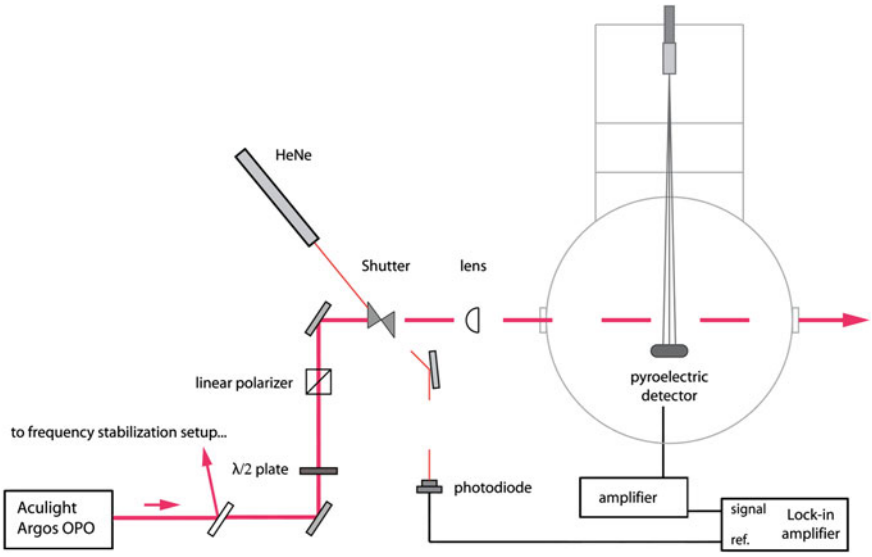

Fig. 2.26 Optical layout for pyroelectric detection of rovibrational excitation in the molecular beam

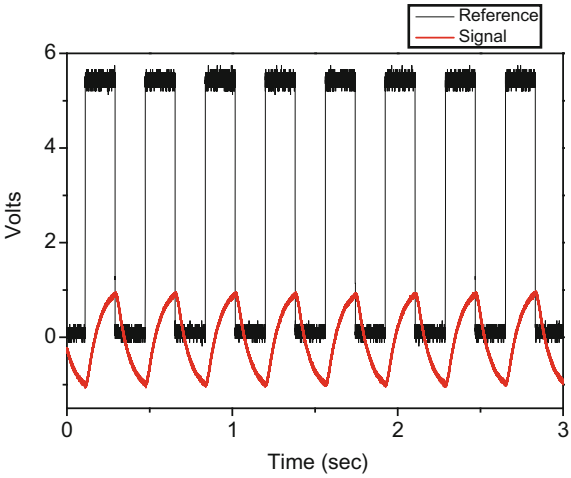

Fig. 2.27 Response of the pyroelectric detector (95x amplification) to a CW molecular beam excited by a modulated laser beam. An example of raw signals used as the lock-in amplifier's 'Reference' and 'Signal'

home-built amplifier. The lock-in reference is generated by a He–Ne laser passing through the open shutter.

Figure 2.27 shows the 2.75 Hz modulated signal on the pyroelectric detector (Signal trace), after 95x amplification. The reference signal (Reference trace) is used to define the frequency and phase of modulation for the lock-in amplifier.

In Fig. 2.27, the Uniblitz shutter is OPEN (laser ON) when the (Reference) photodiode is 'high' ($\sim$5.5 V) and the shutter is CLOSED (laser OFF) when the

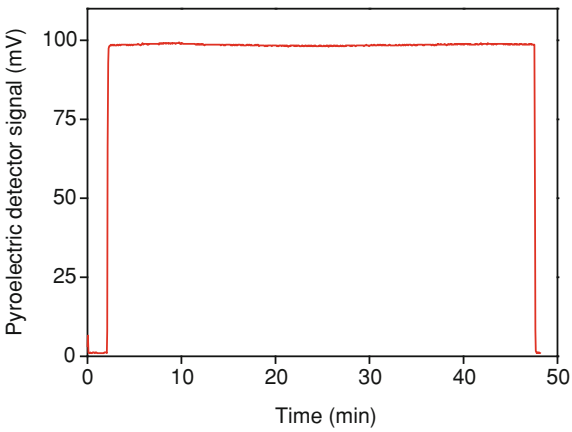

Fig. 2.28 Long term stability of our frequency locking technique as observed by the lock-in detected pryoelectric signal

photodiode is 'low' (0 V). When the shutter is OPEN, the pyroelectic detector signal increases. This voltage increase corresponds to heating of the detector due to vibrational energy being deposited on the detector. When the shutter is CLOSED, the pyroelectric detector signal decreases, due to cooling of the detector. Here, the excitation is modulated at a sufficiently high rate so that the temperature of pyroelectric detector never stabilizes. This produces the saw-tooth signal shown in Fig. 2.27.

Figure 2.28 shows a trace of data collected from a lock-in detected pyroelectric detector signal using a CW molecular beam of 100% CH_4 with 3 bar backing pressure and 50 °C nozzle temperature. The excitation laser was actively stabilized to a $CH_4(\nu_3)$-R(0) Lamb dip, as discussed in the previous section. The lock-in detected signal was 98.58 ± 0.25 mV for the 45 min measurement taken by modulating the excitation laser with a Uniblitz shutter operating at 2.75 Hz with a 50% duty cycle. Data points were collected every 3 s by reading the 'R' analog output (R,θ mode of lock-in amplifier) via 12-bit analog-to-digital conversion by a National Instruments 6023-E data acquisition card and saved in Labview. The lock-in amplifier was set to a sensitivity of 300 mV and time constant of 1 s. The signal-to-noise ratio of this measurement is ∼400.

Comparison of the noise of the measurement with and without the laser excitation can provide some information on the stability of the excitation setup. The standard deviation of the lock-in signal between minute 0.5 and 1.5 (no excitation) is ± 0.12 mV on a 1.06 mV signal. The standard deviation of the lock-in signal between minute 3.5 and 4.5 (modulated excitation) is ± 0.09 mV on a 98.60 mV signal. The fact that the noise is not larger with the excitation than without excitation argues that the excitation efficiency is constant on the timescale of the measurement. Furthermore, the noise in this measurement cannot be related to the frequency stability of the excitation laser since it is not due to variations in the number of excited molecules but the intrinsic noise of the measurement system. The only assertions regarding the excitation laser frequency that can be made from

this data are (1) the laser is resonant with a rovibrational transition in the molecular beam, (2) the extent of molecular beam excitation is constant on the sec timescale for nearly an hour.

In the following chapters, the method described here for pyroelectric detection of vibrationally excited molecules is used extensively to characterize the extent of excitation of the molecular beam.

References

1. D.A. King, M.G. Wells, Molecular-beam investigation of adsorption kinetics on bulk metal targets—nitrogen on tungsten. Surf. Sci. **29**(2), 454 (1972)
2. M.P. Schmid, (2003) Interaction of highly excited molecules with solid surfaces. Ecole Polytechnique Fédérale de Lausanne Thesis No. 2662
3. P. Maroni, in *Bond- and mode-specifice reactivity of methane on Ni(100). La Faculte Sciences de Base* (Ecole Polytechnique Federale de Lausanne, Lausanne, 2005), p. 182
4. Argos model 2400 Aculight Corporation, Lockheed Martin Corporation
5. R. Paschotta, *Encyclopedia of Laser Physics and Technology* (Berlin, Wiley-VCH, 2008)
6. K. Shimoda, in *High-Resolution Laser Spectroscopy*, ed. by K. Shimoda. Topics in Applied Physics, vol 13, (Springer, Berlin, 1976)
7. S. Borri et al., Lamb-dip-locked quantum cascade laser for comb-referenced IR absolute frequency measurements. Opt. Exp. **16**(15), 11637–11646 (2008)
8. E.V. Kovalchuk, T. Schuldt, A. Peters, Combination of a continuous-wave optical parametric oscillator and a femtosecond frequency comb for optical frequency metrology. Opt. Lett. **30**(23), 3141–3143 (2005)
9. P. Maddaloni et al., A 3.5-mW continuous-wave difference-frequency source around 3 mu m for sub-Doppler molecular spectroscopy. Appl. Phys. B Lasers Opt. **80**, 141–145 (2005)
10. K. Anzai, et al., Narrow lamb dip of 3.4 mu m band transition of methane with difference frequency generation and enhancement cavity. Jpn. J. Appl. Phys. Part 1 Regul. Pap. Brief Commun. Rev Pap. **45**(4A), 2771–2775 (2006)
11. K. Takahata et al., Absolute frequency measurement of sub-Doppler molecular lines using a 3.4-mu m difference-frequency-generation spectrometer and a fiber-based frequency comb. Phys. Rev. A **80**(3), 032518(6) (2009)
12. L.S. Rothman et al., The HITRAN 2008 molecular spectroscopic database. J. Quant. Spectrosc. Radiat. Transf. **110**(9–10), 533–572 (2009)
13. K. Uehara, Stark effect of F1(2) line of methane at 3.39 mu-M observed by method of inverted Lamb dip. J. Phys. Soc. Jpn. **34**(3), 777–780 (1973)
14. S. Mandal, P.N. Ghosh, Line-shape and frequency-shift of Lamb dip and crossover-resonance dip in closely spaced transitions. Phys. Rev. A **45**(7), 4990–4997 (1992)
15. I.I. Rabi, Space quantization in a gyrating magnetic field. Phys. Rev. **51**(8), 0652–0654 (1937)
16. I.I. Rabi, N.F. Ramsey, J. Schwinger, Use of rotating coordinates in magnetic resonance problems. Rev. Mod. Phys. **26**(2), 167–171 (1954)
17. P. Varanasi, Collision-broadened half-widths and shapes of methane lines. J. Quant. Spectrosc. Radiat. Transf. **11**(11), 1711 (1971)

Chapter 3
State Specific Preparation and Alignment of Gas-Phase Reagents

3.1 Introduction

Quantum state-specific preparation and alignment of a molecular beam of methane are two central concepts in this thesis work. In this chapter, I explain the processes by which the molecules in the molecular beam are rovibrationally excited and aligned. Experimental evidence of the extent of state-specific preparation is shown.

3.2 Rovibrational Excitation of Molecular Beam

In the experiments described in this thesis, a molecular beam of methane is prepared in specific rovibrational eigenstates of the IR active C–H stretch fundamental vibration ($CH_4(\nu_3)$ or $CD_3H(\nu_1)$) by optical pumping with a continuous-wave, linearly polarized, single-mode infrared laser radiation produced by an optical parametric oscillator (OPO) [1]. The high power (>1 W), single mode bandwidth (<60 kHz on 500 μs timescale), and near Gaussian beam profile of the OPO output enables complete (100%) population transfer from a specific ground state to a rovibrationally excited state by a coherent excitation method termed rapid adiabatic passage (RAP) [2–4]. RAP is rather insensitive to excitation power variations, in contrast to the well-known case of Rabi oscillations [5–9] of the excited population, which makes it particularly suitable for the experiments conducted for this thesis work. Below, I discuss the details of the RAP excitation scheme employed in our experiments.

B. L. Yoder, *Steric Effects in the Chemisorption of Vibrationally Excited Methane on Nickel*, Springer Theses, DOI: 10.1007/978-3-642-27679-8_3,

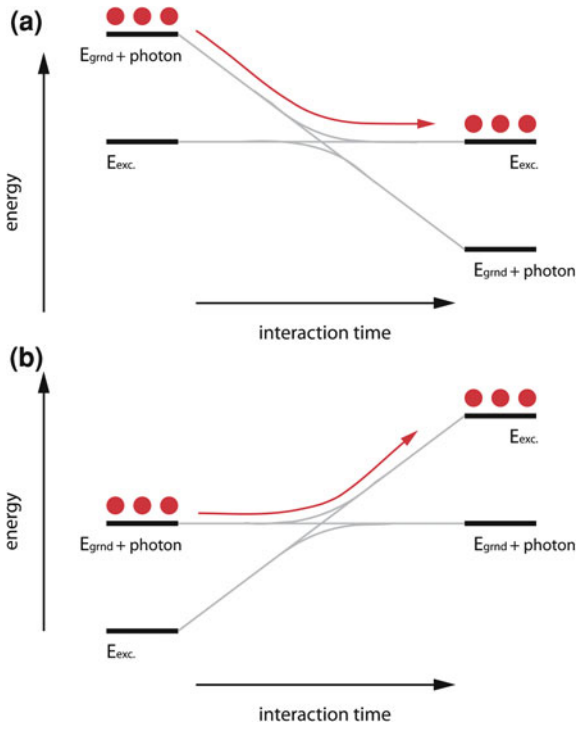

Fig. 3.1 **a** Illustration of an adiabatic following from a ground state to an excited state by rapid adiabatic passage. The *red dots* signify population. The energy scale is referenced to the excited state energy ($E_{exc.}$). **b** Illustration of the adiabatic following from the ground state to an excited state. The *red dots* signify population by rapid adiabatic passage. The energy scale is referenced to the coupled energy of the ground state ($E_{grnd.}$) and the photon

3.2.1 Rapid Adiabatic Passage (RAP)

The physical picture of RAP is one of an adiabatic following from a ground state to an excited state of an atomic or molecular species which is achieved by a suitable sweep of the excitation laser frequency across an optically allowed rovibrational transition.

Figure 3.1a illustrates population transfer in a two-level system. The energy scale is referenced to the excited state energy ($E_{exc.}$). Before interacting with the excitation field, all molecules (red balls) reside in the ground state ($E_{grnd.}$). As the molecules enter the excitation field, the ground state is 'dressed' by a photon [10], making its energy the coupled energy of the ground state plus that of a photon. If the photon energy is swept from the 'blue' to the 'red' of the transition frequency, the coupled state ($E_{grnd.}$ + photon) is swept from above to below the excited state ($E_{exc.}$). If the frequency sweep has sufficient magnitude and a slow enough rate to couple the ground state and photon and there is sufficient excitation power, we can realize an adiabatic following from ground to excited state (or vice versa) as depicted in Fig. 3.1a [3].

Figure 3.1b represents the same process shown in Fig. 3.1a, but the energy scale has been referenced to the coupled energy of $E_{grnd.}$ + photon. Figure 3.1b is

less intuitive than the physical picture in Fig. 3.1a because it is the photon frequency that is swept. I include Fig. 3.1b because the mathematical description of RAP presented in this section uses the $E_{grnd.}$ + photon energy as a reference.

A frequency sweep of the excitation radiation can be realized via the Doppler effect as the molecules in a molecular beam move through a resonant excitation field with curved wavefronts. The molecules will perceive a time dependent frequency due the excitation's wavefront curvature. The rate and magnitude of the frequency sweep are determined by the molecular beam's speed and the radius of curvature of the Gaussian laser beam's wavefronts at its intersection with the molecular beam. The frequency sweep as the molecules traverse the excitation radiation is expressed by the time dependent Doppler shift $\Delta\omega_B(t)$ given by [22]

$$\Delta\omega_B(t) = \frac{\omega_B V_X(t)}{c}. \tag{3.1}$$

Here, ω_B is the rovibrational transition's center frequency (or the 'true' frequency of the resonant excitation field), c is the speed of light, and $V_X(t)$ is the molecular beam velocity component normal to the excitation's curved wavefront as a function of time ($t = 0$ at the center of the excitation field and corresponds to a Doppler shift of zero or $\Delta\omega_B(t) = 0$).

To produce curved wavefronts in the excitation beam, we use a cylindrical lens to focus the excitation laser beam to a line perpendicular to the molecular beam axis. Crossing the molecular beam past the focus causes the molecules to traverse curved wavefronts in the spatially and temporally coherent diverging Gaussian laser beam. When the excitation laser is resonant with a transition in the molecular beam, the wavefront curvature produces a frequency sweep from above to below the rovibrational transition frequency as the molecules traverse the laser beam. Figure 3.2 shows a 'from above perspective' depiction of a methane molecule traversing a continuous, resonant excitation field. The wavefront curvature of the Gaussian beam can be varied by judicious selection of the cylindrical lens's focal length (f) and the lens-to-molecular beam distance (d).

Figure 3.3 illustrates the linear frequency sweep across a rovibrational transition experienced by the molecules traversing the curved wavefronts of the excitation field assuming that the laser is monochromatic and resonant.

The crossing times A, B and C in Fig. 3.2 correspond to detuning values A, B and C in Fig. 3.3 and are intended to illustrate the tuning. At time A, the molecules experience a laser frequency that is blue-shifted from the molecular transition due to a Doppler shift from the curved wavefronts. As the molecules reach position B, the resonant laser is experienced with zero-shift from the molecular transition (zero Doppler shift). At position C, the resonant laser is perceived red-shifted.

Rapid Adiabatic Passage (RAP) is called 'rapid' because it occurs on a timescale that is much shorter than the lifetime of the prepared excited state [4]. For our purposes, RAP used to excite all of the molecules in a given ground state $\psi_1(t) = \left|J''K''M''\right\rangle$ to a corresponding excited state $\psi_2(t) = |JKM\rangle$ that are linked

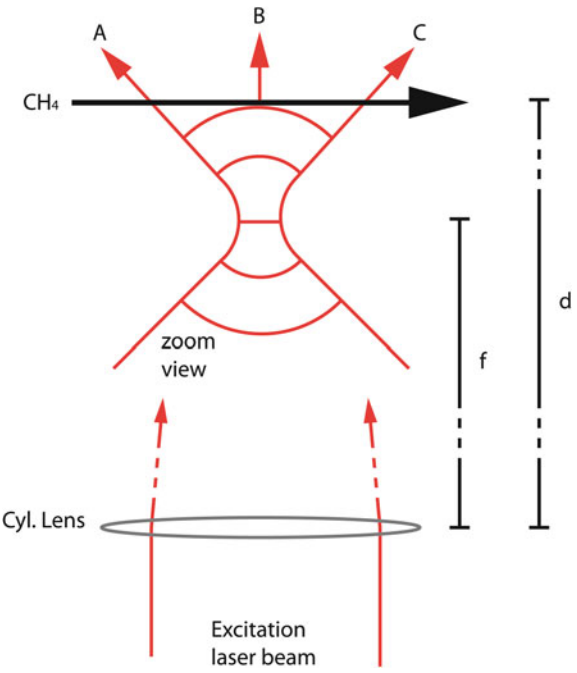

Fig. 3.2 Schematic of Doppler tuning through rovibrational transition in molecular beam as molecules traverse curved wavefronts of a focused laser beam. Focal length = *f*. lens-to-molecular beam distance = *d*

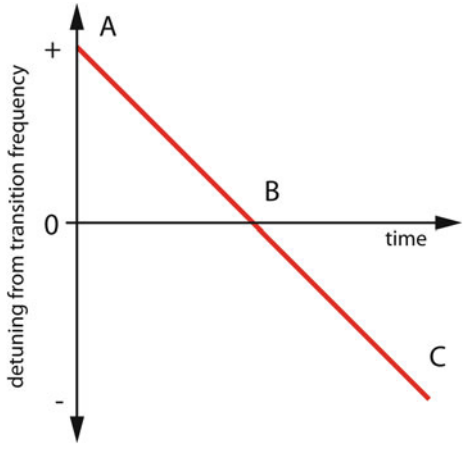

Fig. 3.3 Illustration of apparent frequency sweep seen by the molecular beam as it traverses the curved wavefronts of the excitation field

by an infrared (IR) allowed transition. In the following sections, I discuss the mechanics of RAP, our experimental setup to produce RAP and offer experimental evidence of the RAP of $CH_4(\nu_3)$ using the setup.

3.2.1.1 Theory of Rapid Adiabatic Passage

I consider an ideal two-level system to discuss the solution of the time-dependent Schrödinger equation, following the description of rapid adiabatic passage in references [3, 9, 11–16]. All relevant properties of the system can be defined by two states. State 1, the ground state in Fig. 3.1, is represented by ψ_1. State 2, the excited state in Fig. 3.1, is represented by ψ_2. One can, therefore, write

$$\Psi(t) = C_1(t)\psi_1 + C_2(t)\psi_2. \tag{3.2}$$

where $C_n(t)$, the complex-valued expansion coefficient, is the projection of the state vector $\Psi(t)$ onto the ortho-normal basis vectors, ψ_n. And, the probability of finding the system in state n at time t is given by

$$P_n(t) = |C_n(t)|^2 \equiv |\langle \psi_n \mid \Psi(t) \rangle|^2. \tag{3.3}$$

Since the system is required to reside in either ψ_1 or ψ_2, a normalization condition can be imposed on the probability amplitudes.

$$1 = |C_1(t)|^2 + |C_2(t)|^2 \tag{3.4}$$

I, now, introduce a time-dependent interaction energy $\widehat{V}(t)$ into the Hamiltonian of the system that represents the electric field acting on the system. This perturbation can cause transitions between states of the system. Inclusion of $\widehat{V}(t)$ forms the Hamiltonian

$$\widehat{H}(t) = \widehat{H}^0 + \widehat{V}(t). \tag{3.5}$$

I have neglected to include any 'relaxation' terms (describing processes that return the system to its initial equilibrium) in the Hamiltonian. The exclusion of 'relaxation' terms is done, since the most important relaxation processes are spontaneous emission and collisions. In our experiments, relaxation by spontaneous emission should be negligible since the lifetime of $CH_4(v_3)$ is $\sim$39 ms while the interaction time of the molecules with the excitation field is <1 μs. Collisional relaxation should be negligible since we are working with a molecular beam of molecules. The operator $\widehat{V}(t)$ acts on basis vectors to make new linear combinations of basis vectors by a rotation of the state vector in 2D-space. Basically, the electric field is able to transfer population from ψ_1 to ψ_2 and vice versa. The action can be expressed as a superposition of two possible states

$$\widehat{V}(t)\psi_n = \psi_1 V_{1n}(t) + \psi_2 V_{2n}(t) \tag{3.6}$$

or,

$$V_{nm} = \langle \psi_n | \widehat{V} | \psi_m \rangle \equiv \langle n | \widehat{V} | m \rangle.$$

To ensure that the eigenvalues of $\widehat{H}(t)$, or the observed excitation energies, are real, we require the matrices of $\widehat{H}^0$, $\widehat{V}$ and $\widehat{H}$ to be Hermitian. Therefore,

$$V_{nm}(t) = V_{mn}(t)^*. \tag{3.7}$$

The probability amplitudes $C_n(t)$ are the basic variables in the Schrodinger picture of quantum mechanics. They must be chosen such that $\Psi(t)$ satisfies the time-dependent Schrodinger equation.

$$\hbar \frac{\partial}{\partial t}\Psi(t) = -i\widehat{H}(t)\Psi(t) \tag{3.8}$$

After substitution of $\Psi(t) = C_1(t)\psi_1 + C_2(t)\psi_2$ and $\widehat{H}(t) = \widehat{H}^0 + \widehat{V}(t)$ and $\widehat{V}(t)\psi_n = \psi_1 V_{1n}(t) + \psi_2 V_{2n}(t)$, evaluation of the Schrodinger equation yields

$$\begin{aligned} 0 = \psi_1\left[\hbar\tfrac{\partial}{\partial t}C_1(t) + iC_1(t)E_1^0 + iC_1(t)V_{11}(t) + iC_2(t)V_{12}(t)\right] + \\ \psi_2\left[\hbar\tfrac{\partial}{\partial t}C_2(t) + iC_2(t)E_2^0 + iC_1(t)V_{21}(t) + iC_2(t)V_{22}(t)\right] \end{aligned} \tag{3.9}$$

As the basis vectors ψ_n are ortho-normal, we produce two coupled equations. We write the time-dependent Schrodinger equation in matrix form

$$\hbar\tfrac{\partial}{\partial t}\begin{bmatrix} C_1(t) \\ C_2(t) \end{bmatrix} = -i\begin{bmatrix} E_1^0 + V_{11}(t) & V_{12}(t) \\ V_{21}(t) & E_2^0 + V_{22}(t) \end{bmatrix}\begin{bmatrix} C_1(t) \\ C_2(t) \end{bmatrix} = -i\widehat{H}(t)\begin{bmatrix} C_1(t) \\ C_2(t) \end{bmatrix}. \tag{3.10}$$

Let the off-diagonal elements of the $\widehat{H}(t)$ matrix be the interaction of the laser field on the two level system. We use $\Omega(t)$, the Rabi [5, 6] frequency, to parameterize $V_{nm}(t)$.

$$V_{12}(t) = V_{21}(t) = \tfrac{1}{2}\hbar\Omega(t) \tag{3.11}$$

We are free to choose the zero point of the energy scale of the system. Choosing $E_1^0 + V_{11}(t)$ to be zero, the energy of ψ_1 dressed by the laser field is the reference energy. This is depicted in Fig. 3.1b. Therefore, the energy of ψ_2 can be expressed as:

$$E_2^0 + V_{22}(t) = \omega_B(t) - \phi(t) = \Delta(t). \tag{3.12}$$

Here ω_B(t) is the Bohr transition frequency or the transition's center frequency, $\phi(t)$ is the time dependent carrier frequency of the laser radiation or the excitation frequency as seen by the molecule as it traverses the excitation field, and the quantity $\Delta(t)$ is referred to as 'detuning' or the difference of energy between the dressed ground state and the excited state at a given moment of the frequency sweep.

In practice, the time dependence of $\Delta(t)$ can be realized by a frequency sweep of the laser field (i.e. Doppler tuning via $\phi(t)$) or a change of the Bohr transition frequency (i.e. Zeeman or Stark shifting via ω_B(t)). As noted previously, we use Doppler tuning via curved wavefronts in the continuous excitation field ($\phi(t)$) to control the time dependence of $\Delta(t)$ as the molecules in the molecular beam traverse the excitation. In our experiments, there is no time dependence of ω_B. I can recast the matrix $\widehat{H}(t)$ into a new form $W(t)$ using two real-valued functions of time $\Delta(t)$ and $\Omega(t)$, such that

$$\widehat{H}(t) = \hbar W(t) = \hbar \begin{bmatrix} 0 & \frac{1}{2}\Omega(t) \\ \frac{1}{2}\Omega(t) & \Delta(t) \end{bmatrix}. \tag{3.13}$$

Now, let's consider the case of a molecule interacting with a linearly polarized laser field having an electric field E such that

$$E(t) = \hat{e}\varepsilon(t)\cos(\phi(t)t). \tag{3.14}$$

In the above equation, $\widehat{e}$ is a unit vector defining the laser polarization direction and $\varepsilon(t)$ is the magnitude of the electric field vector. In this case, the important interaction energy is that of the transition dipole moment μ_{21} in the electric field.

$$V(t) = -\mu_{21} \cdot E(t) \tag{3.15}$$

And the strength of the interaction is parameterized by the Rabi frequency [5, 6]

$$\Omega(t) = \sqrt{\left(\frac{\mu_{21}E(t)}{\hbar}\right)^2 + (\omega_B - \phi(t))^2}. \tag{3.16}$$

In Eq. 3.16, μ_{21} is the projection of the transition dipole moment on the laser polarization $\widehat{e}$, and. Under these circumstances, we evaluate the time-dependent Schrodinger equation.

$$\frac{\partial}{\partial t}\begin{bmatrix} C_1(t) \\ C_2(t) \end{bmatrix} = -i\begin{bmatrix} 0 & \frac{1}{2}\Omega(t) \\ \frac{1}{2}\Omega(t) & \Delta(t) \end{bmatrix}\begin{bmatrix} C_1(t) \\ C_2(t) \end{bmatrix} \tag{3.17}$$

For complete definition of the system, we need to specify the initial state, more precisely the probability amplitudes, $C_n(t)$. We can say that the system is initially in ψ_1 or the ground state.

$$\begin{bmatrix} C_1(t_i) \\ C_2(t_i) \end{bmatrix} = \begin{bmatrix} 1 \\ 0 \end{bmatrix} \tag{3.18}$$

And we are interested in situations of complete population transfer to ψ_2 or the excited state.

$$\begin{bmatrix} C_1(t_f) \\ C_2(t_f) \end{bmatrix} = \begin{bmatrix} 0 \\ 1 \end{bmatrix} \tag{3.19}$$

If the excitation laser frequency is nearly resonant with the transition frequency, time independent (i.e. $\left|\frac{d\phi}{dt}\right| = 0$) and relaxation is negligible, the population of a two level system will oscillate between ψ_1 and ψ_2 at its Rabi frequency (see Eq. 3.16). In practice, excitation of the two level system in this way (Rabi cycling) will produce an excitation probability of 50% or equal probabilities of excitation and deexcitation at high (saturating) laser powers. This is undesirable in our experimental setup.

Bloch, Feynmann, Vernon and Hellwarth developed a geometric (vectorial) picture for a two level system interacting with an electric field [17, 18]. The model defines two vectors: the pseudo field vector (or excitation field vector) and the Bloch-Feynman vector (or state vector) in an abstract three-dimensional space. For the non-resonant excitation case, analytical solution of the equations of motion in the Bloch-Feynman formalism is rather complicated [17, 18], and beyond the scope of this thesis. For the state vector to adiabatically follow the field vector (or for RAP) from the ground state to the excited state (or vice versa), there are a few experimental conditions [14, 18] that need to be fulfilled. I have adapted the conditions to an easily readable form and use them to characterize the excitation scheme outlined in the following section.

Condition #1

$$\frac{\left|\frac{d\phi}{dt}\right|}{\Omega_0^2} \ll 1 \tag{3.20}$$

where $\left|\frac{d\phi}{dt}\right|$ is the carrier frequency's rate of change (frequency sweep rate) and Ω_0 is the Rabi frequency at the excitation's center or peak intensity for a Gaussian laser pulse. This condition stipulates that the frequency sweep must be slow compared to the Rabi frequency, and is the requirement for an adiabatic following from ψ_1 to ψ_2.

Condition #2

$$\frac{\left|\frac{(\omega_B - \phi)d\Omega(t)}{dt}\right|}{\left[\Omega_0^2 + (\omega_B - \phi)^2\right]^{3/2}} \ll 1 \tag{3.21}$$

This condition requires a smooth laser pulse in power as the frequency is being swept. Sudden switching of an electric field (i.e. a square pulse in power) is not favorable for RAP. A Gaussian power profile is preferable.

Condition #3

$$\frac{\left|\frac{d\phi}{dt}\right| T_{transit}}{\Omega_0} > 1 \tag{3.22}$$

This condition requires that the total frequency sweep exceeds the maximum Rabi frequency. If the above conditions are met, we can estimate the adiabatic following

transition probability as one minus the probability of a diabatic transition using the Landau–Zener formula [4, 19, 20].

$$P = 1 - p \tag{3.23}$$

where,

$$p = \exp\left[-\frac{\pi\Omega_0^2}{2\left|\frac{d\phi}{dt}\right|}\right]. \tag{3.24}$$

I use the expressions shown in this section to characterize our experimental setup in the following section.

3.2.1.2 Experimental Setup and Quantitative Description for Rapid Adiabatic Passage

Figure 3.4 shows the optical setup for excitation of the molecular beam. The wavefront curvature which produces the Doppler tuning required for RAP can be manipulated by choice of the lens's focal length, f, and its distance from the molecular beam, d. I use a +25.4 cm focal length cylindrical lens placed a distance of 36 cm from the molecular beam. These parameters fulfill the conditions for RAP as outlined in the present and previous section.

The aim of the quantum state-preparation setup is to produce a homogeneous and quantifiable population in a specific rovibrationally excited state in the molecular beam. Ideally, we would like to create 100% population inversion over the entirety of the molecular beam that is insensitive to the intensity variation within the Gaussian laser beam profile. In addition, we want to use the polarization of the laser radiation to align the excited molecules. Excitation via RAP is able to produce 100% population inversion that is relatively insensitive to power variations [4]. To produce complete RAP throughout the molecular beam, certain conditions on the magnitude of the frequency sweep and laser power have to be satisfied as described in the previous section.

Below, I show the details of the experimental conditions used to produce RAP in a 2000 m/s velocity molecular beam. Most of the alignment measurements for methane were performed with this velocity. Since the nozzle-to-surface distance is 210 mm and the molecular beam diameter is measured to be 2 mm on the surface, the molecular beam has a divergence of ±0.273°. The residual Doppler width for a 2000 m/s molecular beam with a divergence of ±0.273° is 5.8 MHz (±2.9 MHz) for the $CH_4(\nu_3)$-R(0) transition at 3028.752 cm^{-1} [21], see eq. 2.02. Therefore, the frequency sweep needs to be large enough to produce RAP over a 5.8 MHz variation in ω_B. I address this condition at the end of this section.

In order to quantitatively describe the RAP process, a few terms and equations must be introduced [22]. Figure 3.5 shows the parameters defining a simple Gaussian TEM00 laser beam and its wavefront curvature.

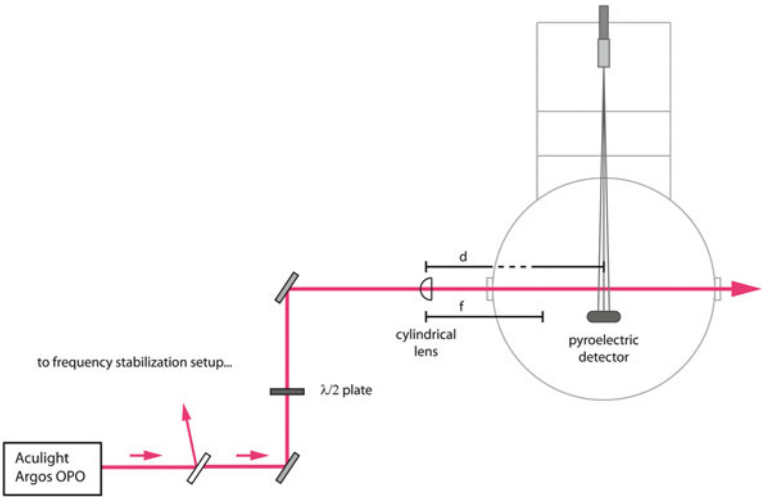

Fig. 3.4 Optical setup used to excite the molecular beam by rapid adiabatic passage

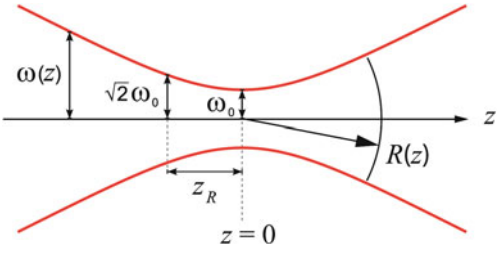

Fig. 3.5 Focusing of a Gaussian beam (TEM00 mode) with relevant quantities describing the wavefront curvature used to control RAP in the experimental setup

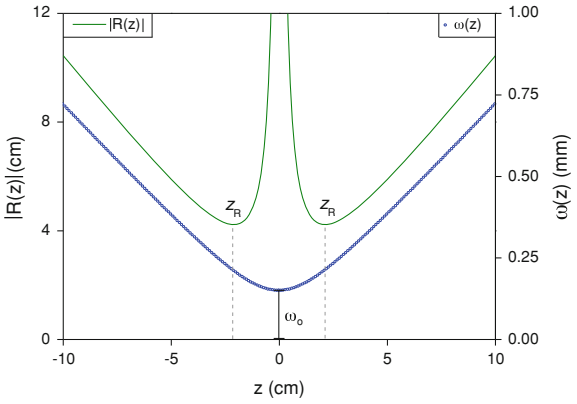

Fig. 3.6 Plot of a TEM00 Gaussian beam's wavefront curvature, $R(z)$, and beam radius, $\omega(z)$, as a function of z. where, $\lambda = 3.3\,\mu m$, f = 25.4 cm, $\omega_0 = 150$ μm and $z_R = 21$ mm

The beam waist (power or intensity $\rightarrow 1/e^2$) ω_0 of the focused laser beam is given by

$$\omega_0 = \frac{\lambda f}{\pi r}. \tag{3.25}$$

For a $\lambda = 3.3$ μm wavelength Gaussian beam with a measured radius r = 1.8 mm at the lens before focusing by a lens f = 25.4 cm, ω_0 is 150 μm. The excitation laser beam has an $r(1/e^2) = 1.5$ mm at the output of the OPO, but diverges to $r(1/e^2) = 1.8$ mm at a distance of 1.7 m from the OPO output (where the cylindrical lens is placed). Excitation laser beam profiles are shown in Sect. 2.4.2. The beam radius after the lens is denoted $\omega(z)$ and is defined as the radius where the electric field amplitude has decreased to 1/e or the intensity to $1/e^2$ of the maximum value in the center of the beam at $\omega(z) = 0$, respectively. For a TEM00 Gaussian beam $\omega(z)$ is given by

$$\omega(z) = \omega_0 \sqrt{1 + \frac{z^2}{z_R^2}}. \tag{3.26}$$

where z_R, the Rayleigh range, is defined as the length over which the beam radius increases by a factor of $\sqrt{2}$ from radius ω_0 at the tightest waist. The wavefront radius of curvature, $R(z)$ depends on z_R and z (with z measured from $z = 0$ at ω_0) such that

$$R(z) = z + \frac{z_R^2}{z}. \tag{3.27}$$

The wavefront radius of curvature reaches a minimum at the Rayleigh range z_R which is given by,

$$z_R = \frac{\pi \omega_0^2}{\lambda}. \tag{3.28}$$

Figure 3.6 shows a plot of $\omega(z)$ and $|R(z)|$ as a function of z for the experimental parameters: $\lambda = 3.3$ μm, f = 25.4 cm, and $\omega_0 = 150$ μm. $R(z)$ has a minimum at $z = z_R = \pm 21$ mm. This is marked by the vertical dashed line in the figure. For $z < 2.1$ cm, $R(z)$ increases quickly. As $z \rightarrow 0$, $R(z) \rightarrow \infty$. This means that the wavefronts of the focused excitation beam are flat at the waist. Therefore, crossing the molecular beam at the focus of the laser beam would produce no Doppler tuning as the molecules traverse the excitation field.

We use a cylindrical lens rather than a spherical lens for creating the wavefront curvature because we want all molecules crossing the laser beam to experience the same RAP conditions, independent of their position in the molecular beam. In our experimental setup, the molecular beam has a diameter of 2 mm and the unfocused laser beam has a diameter of $\sim$3.6 mm ($1/e^2$) at their crossing point, as shown in the laser beam profiles in Sect. 2.4.2. The relatively large laser beam diameter

ensures that all molecules in the molecular beam interact with nearly the same excitation field.

Figure 3.7 shows $R(z)$ as a function of distance from the cylindrical lens. At a lens-to-molecular beam distance of 36 cm (or $z = +10.6$ cm), the radius of curvature is 9.6 cm. The choice of 36 cm may appear arbitrary at this point. In the following pages, I show that it does, indeed, produce the desired frequency sweep at a desirable rate for RAP of all Doppler shifts in the molecular beam.

To quantify the molecule-light interaction time, I define the molecules' transit time ($T_{transit}$) through the excitation field as a function of $\omega(z)$ and the molecular beam velocity (v). This produces limits of the frequency sweep. The transit time is given by

$$T_{transit} = \frac{2\omega(z)}{\mathrm{v}}. \tag{3.29}$$

Figure 3.8 shows the transit time (right-hand vertical axis) and the frequency sweep rate (left-hand vertical axis) as a function of distance for the set of parameters given above. At a distance of 36 cm from the lens, $\omega(z) = 660$ μm and the transit time $T_{transit} = 0.66$ μs for v = 2000 m/s. For a specific frequency sweep rate, the finite interaction time limits the magnitude that the excitation frequency can be swept.

From geometric considerations, the frequency sweep rate $d\phi/dt$ is given by:

$$\frac{d\phi}{dt} = \frac{\mathrm{v}^2}{\lambda R(z)}. \tag{3.30}$$

and the total sweep amplitude:

$$\Delta_\phi = \frac{d\phi}{dt} \cdot T_{transit}. \tag{3.31}$$

Figure 3.9 shows the total frequency sweep Δ_ϕ produced by 2000 m/s molecules traversing a monochromatic excitation field of wavelength as a function of distance from the lens. At a lens to molecular beam distance of 36 cm, this experimental setup generates a frequency sweep rate of 12.6 MHz/μs and a total frequency sweep of $\Delta_\phi = 8.32$ MHz. The 8.32 MHz frequency sweep magnitude is larger than the largest Doppler shift in the divergent molecular beam, as discussed at the beginning of this section.

To achieve RAP in the molecular beam one must consider not only the frequency sweep amplitude (chirp), but also the interaction of the excitation field with the molecules in the molecular beam, i.e. the optical pumping rate. This rate is characterized by the Rabi frequency, Eq. 3.16. The equation shows that the Rabi frequency varies linearly with electric field strength and therefore varies across the Gaussian laser beam profile. To simplify, I use the Rabi frequency for the molecular beam trajectory that traverses the center of the Gaussian excitation profile to characterize the RAP setup. I calculated the transition dipole moment μ_{21}

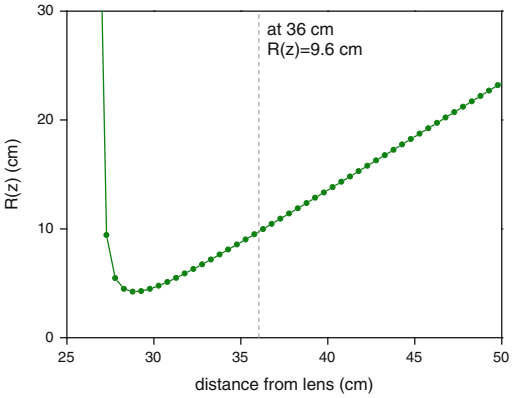

Fig. 3.7 Plot of a Gaussian beam's radius of wavefront curvature $R(z)$ as a function of distance from the +25.4 cm cylindrical lens

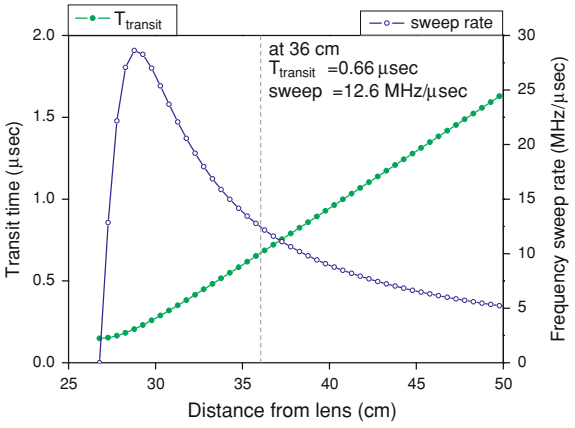

Fig. 3.8 Plot of the transit time $T_{transit}$ (*left-hand vertical axis*) and frequency sweep rate $\frac{d\phi}{dt}$ (*right-hand vertical axis*) for a 2000 m/s molecular beam traversing an excitation field as a function of distance from the cylindrical lens

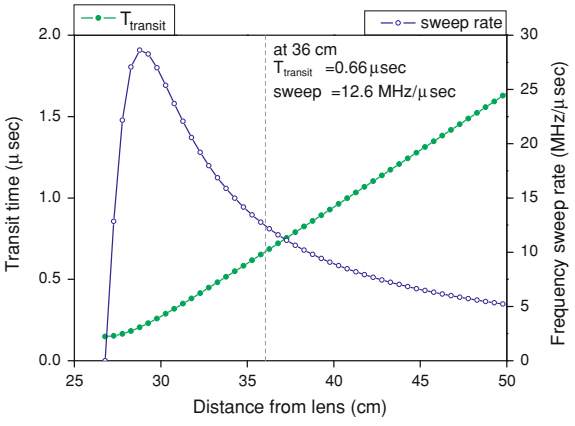

Fig. 3.9 Plot of the frequency sweep Δ_ϕ for a 2000 m/s molecular beam traversing an excitation field as a function of distance from the cylindrical lens

of $CH_4(\nu_3)$ to be 1.8×10^{-31} C m $= 5.4 \times 10^{-2}$ Debye from its Einstein A_{21} coefficient of 25.6 Hz [21]. The conversion [23] from A_{21} to μ_{21} is given by

$$\mu_{21}^2 = \frac{3\varepsilon_0 hc^3}{2\omega_B^3} A_{21}. \tag{3.32}$$

Here, ε_0 is the permittivity of free space, h is Planck's constant, c is the speed of light, and ω_B is the transition frequency as used above.

Figure 3.10 shows the Rabi frequency as a function of distance from the cylindrical lens for 500 mW of excitation laser power. This measure of the Rabi frequency is an upper limit since any vertical shift from the molecular trajectory that traverses the maximum of the Gaussian laser beam profile will interact with an electric field that is smaller.

With the excitation characteristics determined, I show that the focusing conditions given in this section are reasonable for RAP of the molecular beam using the set of conditions from the previous section. Condition #1 requires that the frequency sweep be slow compared to the square of the Rabi frequency. The excitation scheme outlined produces a maximum Ω_{Rabi}, or $\Omega_0 = 6.4$ MHz and a $\frac{d\phi}{dt} = 12.6\,\text{MHz}/\mu\text{s}$. In our setup $\frac{\left|\frac{d\phi}{dt}\right|}{\Omega_0^2} = 0.3$, which fulfills condition #1 for RAP. Condition #2 required a smooth temporal profile of the power as the frequency is swept. For this experimental parameter set, Condition #2 equals 9×10^{-15}, easily fulfilling the RAP requirement. Condition #3 requires the chirp to exceed the Rabi frequency. With $\frac{d\phi}{dt} = 12.6\,\text{MHz}/\mu\text{s}$, $T_{transit} = 0.66\,\mu\text{s}$ and $\Omega_0 = 6.4$ MHz I obtain $\frac{\left|\frac{d\phi}{dt}\right| T_{transit}}{\Omega_0} = 1.3$ which satisfies Condition #3.

As condition #2 is easily met in this setup due to the smooth Gaussian profile of the laser beam (see beam profile measurements in Chap. 2), it is the simultaneous requirements of Condition #1 and #3 that must be considered when selecting a focal length and lens position. The square of the Rabi frequency must be larger than the frequency sweep rate, but the Rabi frequency must be less than the total frequency sweep. These two equations define a range of experimental conditions where RAP can be achieved. Figure 3.11 shows the values of left-hand side of conditions #1, 2 and 3 as a function of distance from the lens using the experimental parameters discussed in this section.

The vertical line in Fig. 3.11 marks the lens-to-molecular beam distance of 36 cm used in our experiments. I have chosen to place the lens at this distance because it satisfies Condition #1 and #3, simultaneously. But, when the left-hand side of condition #1 approaches unity, we cease to produce RAP. Therefore, I have worked to minimize the left-hand side of condition #1 in our setup while maintaining condition #3.

RAP is robust in the sense that I could move the lens a bit closer to or further from the molecular beam axis and maintain RAP conditions. I have colored yellow the range of lens-to-molecular beam distances that should produce RAP in the molecular beam. The lens must to be at least 33.5 cm from the molecular beam or

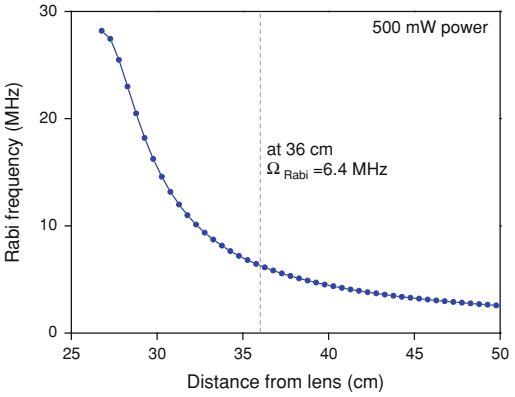

Fig. 3.10 Plot of the Rabi frequency, Ω_0 as a function of distance from the cylindrical lens

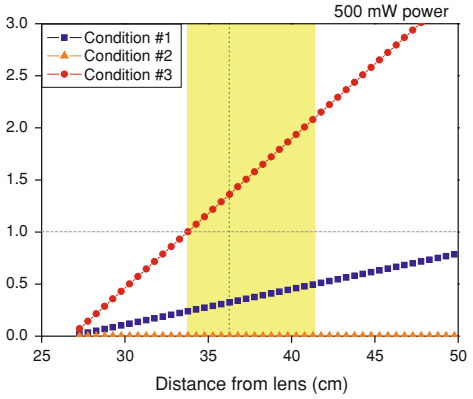

Fig. 3.11 Plot of the required conditions for RAP as a function of distance from the +25.4 cm cylindrical lens for a typical excitation laser power of 500 mW

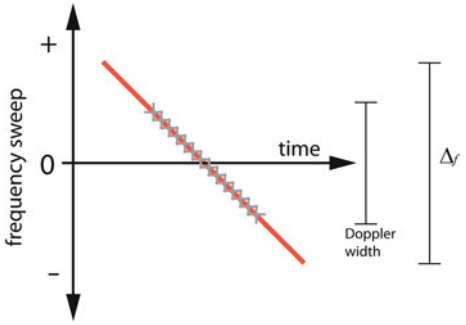

Fig. 3.12 Depiction of frequency sweep needed to produce RAP across all Doppler shifts present in the molecular beam. Doppler width of molecular beam is marked by xxxxxx

the total frequency sweep is too small compared to the Rabi frequency. Taking 0.5 as the limiting value for condition #1, the lens should be closer 41.5 cm from the molecular beam or the frequency sweep rate is too large compared to the Rabi frequency.

As mentioned above, the goal is to produce a homogeneous excitation over all Doppler shifts in the molecular beam. Figure 3.12 shows the total frequency sweep Δ_ϕ being swept through the Doppler width of molecular beam absorption line (gray xxxx in figure). It is not sufficient to produce Δ_ϕ equal to the molecular beam's Doppler width, as a frequency sweep across the transition is also needed for RAP of molecules located at the edge of the slightly divergent molecular beam.

Therefore, the total frequency sweep Δ_ϕ must be large enough to produce RAP over the Doppler width of the molecular beam. To determine if the largest Doppler shifts (± 2.9 MHz) are in RAP conditions, I need to consider Condition #3 or if the frequency sweep across the Doppler shifted trajectories is larger than Ω_0. The extreme Doppler shifts in the molecular beam will have a reduced Ω_0 due to the excitation's Gaussian power profile. For this setup, Ω_0 is reduced to ~ 4 MHz at a Doppler shift of ± 2.9 MHz. This means that Δ_ϕ needs to be ± 4.9 MHz (from $\pm 2.9 \pm 0.5\,\Omega_0$ MHz) to bring the entire Doppler width of the molecular beam into RAP conditions. The total sweep Δ_f was determined to be 8.32 MHz or ± 4.16 MHz.

By these calculations, we should produce RAP conditions for 85% of the molecular beam's Doppler width. The remaining 15% of the molecular beam should be excited, but not necessarily to complete population inversion by RAP. The transition probability can be estimated by the Laundau-Zener formula, shown in the previous section. Under these experimental conditions, the adiabatic transition probability is calculated to be 99.9% for the center trajectory of the molecular beam.

In the following section, I show experimental verification of RAP in the molecular beam using pyroelectric detection to measure the extent of rovibrational excitation in the molecular beam. Furthermore, with a spatially resolved measurement across the Doppler width of the molecular beam excitation, we should expect a flat-top in the center that corresponds to 100% fractional excitation (complete population inversion). The excitation may be less than 100% efficient at the molecular beam edges. I show an example of this in Sect. 3.2.1.4, using Auger electron spectroscopy.

3.2.1.3 Characterization of Excitation Setup with Pyroelectric Detector

Experimental evidence of RAP of the molecular beam is shown in this section. Figure 3.13 shows the laser fluence dependence of the pyroelectric detector signal which monitors the fraction of vibrationally excited methane molecules $CH_4(v_3 = 1)$ in a molecular beam of 2056 m/s average speed with and without focusing of the laser beam.

In the 'no focusing' case, one observes partial Rabi cycling in the form of a local maximum in the excited fraction at 35 mW and a local minimum at ~ 100 mW. Here, Rabi cycling refers to the oscillation of population in a two level

system. The coherent excitation with 'flat' wavefronts is resonant with the molecular beam transition for the entire molecule/excitation field interaction time. The excitation will excite all the molecules (initially in ground state) to an excited state and then stimulates the population back to the ground state. After many Rabi cycles, the transition is said to be 'saturated' which means that there is an equal population in the ground and excited state. The averaging over a varying electric field, molecular beam velocity spread, and several Doppler shifts, makes Rabi oscillations challenging to detect in the laboratory. Nonetheless, the 'no focusing' case of Fig. 3.13 shows a partial Rabi oscillation.

For the conditions chosen to produce RAP, there is a smooth rise of the excited fraction that approaches an asymptote of $\sim$1000 mV at a laser power of 500 mW. At a power of 450 mW, the RAP conditions (+25.4 cm cylindrical lens at a distance of 36 cm from the molecular beam) excites 2.75x as many molecules in the molecular beam as does the 'No focusing' conditions.

As seen in Fig. 3.13, the RAP excitation is a more efficient optical pumping scheme than using the laser beam without wavefront curvature. The increase in the excited fraction is not simply due to the focusing of the laser beam since this would have no effect for a single photon transition. For RAP, the theoretical limit of a 2-level system (R-branch rovibrational excitation) is 100% inversion of all molecules excited from in a given ground state. In the high excitation power limit for the case of planar excitation wavefronts, the molecules will be Rabi cycled between the ground and excited state. After a sufficiently large number of cycles, This will result in equal population of ground and excited state (saturation). One might expect the 'no focusing' conditions to approach an asymptotic pyroelectric signal equal to exactly half the asymptote of RAP excitation if the Rabi cycling is completely randomized at high power.

To produce an asymptote in the fluence dependence of the 'no focusing' excitation would require more laser power than is available in our experimental setup because it relies on power broadening to bring all Doppler shifts in the molecular beam into resonance with the excitation laser ($\sim$1 MHz). If we reduced the Doppler angles/shifts present in the molecular beam, we should observe that our RAP setup produces a pyroelectric detector signal at its high power asymptote that is twice that of the 'No focusing' setup. The Doppler shifts in the molecular beam could be minimized by using a smaller molecular beam aperture at the UHV entrance. We currently use a 1 mm diameter aperture which diverges (angle of 0.273°) to about a 2 mm diameter where the molecules collide with the 2 mm diameter circular pyroelectric detector element.

The fraction of excited molecules prepared by RAP was further quantified by crossing the molecular beam with two laser beams termed PUMP and PROBE at two positions separated by 2.54 cm. The molecular beam first traverses the PUMP laser beam which transfers a certain fraction of the ground state molecules into the excited state by RAP. Subsequently, the interaction with the PROBE beam pumps any residual ground state molecules into the excited state but also de-excites excited molecules back to the ground state by stimulated emission. Figure 3.14 shows a schematic of the 'pump up, pump down' [14, 24] experiment. The excited

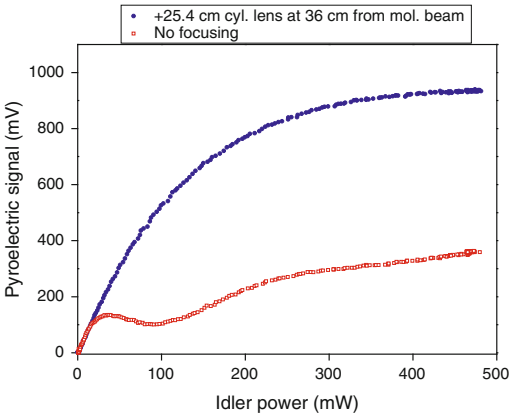

Fig. 3.13 Pyroelectric detector fluence dependences for a 2056 m/s molecular beam of $CH_4(\nu_3)$ excited via R(1) for RAP and 'No focusing' conditions

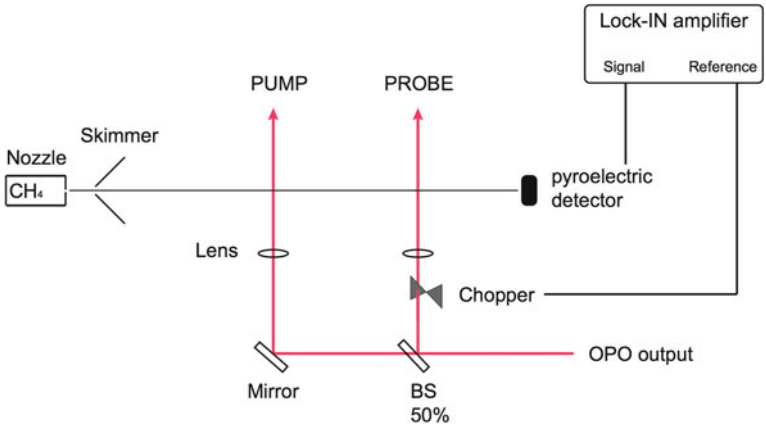

Fig. 3.14 Schematic for 'Pump Up, Pump Down' experiment. The excitation laser beam is split into two parallel beams (PUMP and PROBE) by a beam splitter (BS). The two 1″ diameter lenses (f = 25.4 cm) have a center-to-center distance of 1″ and are placed 36 cm from the molecular beam

state fraction produced in the molecular beam by the PUMP, the PROBE, or the interaction of the two laser beams is monitored by lock-in detection of the pyroelectric detector signal as described in Chap. 2.

To explain the principle of this 'pump-up, pump-down' experiment, I consider the following two cases: (1) the PROBE laser saturates the excitation through Rabi cycling, i.e. it excites 50% of the ground state molecules at the 'saturation' limit. In the ideal limit of complete saturation of the overlapping excitation volumes, addition of a PUMP laser will cause no change in the excited fraction since the rate of excitation and de-excitation produced by the PROBE laser will be identical [7, 11, 13]. (2) In the event that the PUMP produces complete RAP over all Doppler shifts in the molecular beam, 100% of the molecules will be in the excited

state after interaction with the PUMP. If the PROBE produces complete RAP, all of the molecules in the excited state will be de-excited back to the ground state leaving the excited fraction of the beam at zero. Thus, the molecules complete a round-trip from their 'ground' to an 'excited' and back to their 'ground' state due to sequential population inversions.

Since the pyroelectric detector used here is sensitive only to changes in temperature, the effect produced by PUMP and PROBE can be distinguished by modulation (chopping) of either laser beam. I chose to modulate the PROBE ('downstream') beam, as defined in Fig. 3.14. Lock-in detection of the pyroelectric signal with the PROBE chopper function as the reference input is then used to detect selectively the effect of the PROBE laser on the excited fraction in the molecular beam. For the case (1) of the 'pump-up, pump-down' experiment, the lock-in signal is expected to drop from its saturation value down zero when adding the continuous (cw) PUMP laser to the chopped PROBE laser. The signal drops to zero because the PROBE laser beam no longer has an effect on the excited fraction if the PUMP laser already saturated the excitation. For case (2), the lock-in signal is expected to flip in sign when adding the PUMP laser because the second laser beam will now stimulate the population down which reduces the vibrational energy content of the molecular beam and results in a 180° phase change of the lock-in signal. The sign change indicates an inversion and the relative magnitude of the PUMP and PROBE lock-in signal compared to PROBE only signal gives a lower limit of the extent of inversion.

We used a $\sim$1000 m/s molecular beam of $CH_4(\nu_3)$ excited via the R(1) transition at 3038.5 cm^{-1} for the 'pump up, pump down' experiment because it produced a slower tuning rate $\frac{d\phi}{dt}$ of the excitation. Less excitation power is required to achieve RAP if the tuning rate is slower and we needed to achieve RAP with less than half of the OPO output since the total output power is divided in two beams. To quantify the extent of excitation in the cw molecular beam, we used the lock-in detected pyroelectric detector signal. The PROBE laser was modulated by a shutter at 2.77 Hz, and the lock-in amplifier was set in XY-mode with a fixed phase angle to have the entire pyroelectric signal on the X-channel (set such that $Y = 0$).

To realize case (1) of the 'pump up, pump down' experiment, the PUMP and PROBE beams were not focused. The cylindrical lenses were removed from the optical setup in Fig. 3.14. Section A of Fig. 3.15 gives the lock-in signal for the cw molecular beam excited by the modulated, resonant, 150 mW PROBE beam. Section B is the lock-signal after introduction of the cw-PUMP beam to the configuration in section A. Section C shows the lock-in signal from configuration B, but with nonresonant laser beams (frequency stabilization feedback loop disabled). The signal in section C is due to scattered light impinging on the pyroelectric detector and is taken to be the baseline for comparing sections A and B. Section D shows the lock-in signal from the nonresonant PUMP and PROBE beams without a cw molecular beam impinging on the pyroelectric detector. The signal of section D confirms that the signal in section C is not due to the molecular

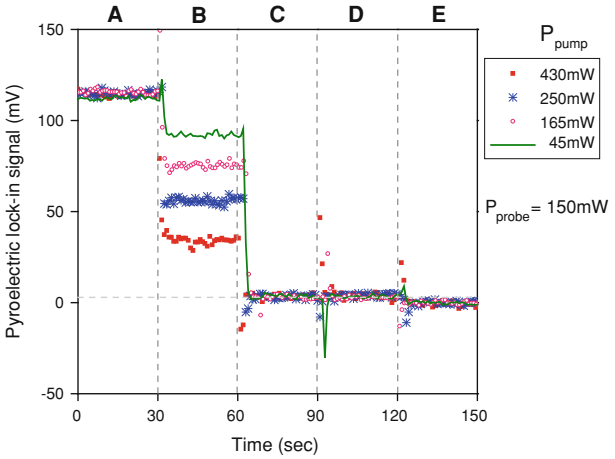

Fig. 3.15 Lock-in detected pyroelectric detector signals for the 'pump up, pump down' experiment, no focusing case

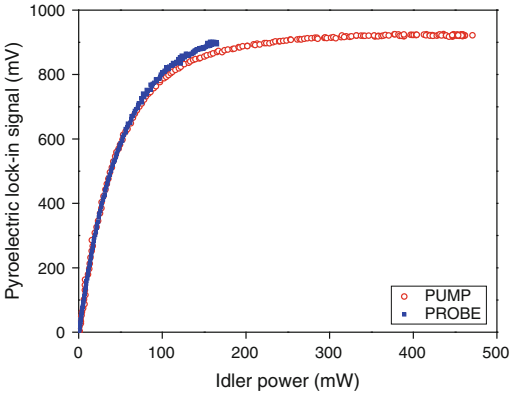

Fig. 3.16 Individual pyroelectric detector fluence dependences for 1000 m/s molecular beam of $CH_4(\nu_3)$ excited via R(1) for the 'Pump Up, Pump Down' experiment

beam but to scattered light. Section E shows the lock-in signal without the cw molecular beam and both laser beams blocked at the entrance to the UHV chamber. Section E is shown to demonstrate that the lock-in signal does have a baseline value of 0 mV.

The data in Fig. 3.15 allow for a couple of observations. First, the lock-in signal for the PUMP + PROBE (section B) does, indeed, go toward zero as the PUMP power is increased. At the laser powers studied, we did not reach a lock-in signal of zero because of incomplete saturation of the transition over the 2.9 MHz Doppler width present in the molecular beam ($\pm 0.273°$ divergence, v = 1000 m/s). I calculate the saturation broadening to be approximately 1 MHz for 150 mW of excitation power, so the excitation is resonant with about one third of the

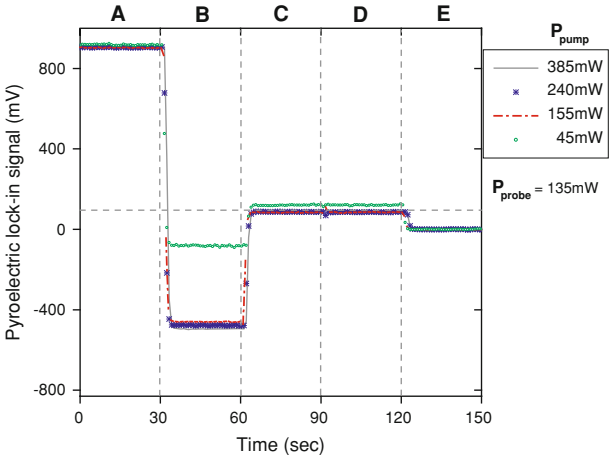

Fig. 3.17 Lock-in detected pyroelectric signals for the 'pump up, pump down' experiment

Doppler width in the molecular beam, i.e. the excitation only excites the central third of the solid angle captured by the pyroelectric detector. Second, the pyroelectric detection system appears reliable for monitoring the 'pump up, pump down' experiment, in that the signals generated in sections A-E were predictable.

To realize case (2) of the 'pump up, pump down' experiment, I placed two +25.4 cm cylindrical lenses separated by 2.54 cm at a distance of 36 cm from the molecular beam. Figure 3.16 shows the single laser beam fluence dependences for the PUMP and the PROBE. The two fluence dependences are within 3% of each other at a power of 160 mW, and the pyroelectric signal increases by only 6.5% between 150 and 450 mW excitation power. The power of the PUMP and PROBE beams is different due to the beamsplitter reflecting 25% and transmitting 75% of the s-polarized, 3.3 μm laser beam.

Figure 3.17 shows the lock-in detected pyroelectric signals for case (2) of the 'pump up, pump down' experiment, for the experimental conditions to produce RAP in the molecular beam. Section A of Fig. 3.17 gives the lock-in signal (920 mV) for the cw molecular beam excited by the modulated, resonant, 135 mW PROBE beam. Section B is the lock-signal upon introduction of the cw PUMP beam to the section A configuration. Section C shows the lock-in signal from configuration B, but with nonresonant laser beams. The signal in section C is due to scattered light impinging on the pyroelectric detector and is used as the zero-point reference for comparison of the pump-up and pump-down signals. Section D shows the lock-in signal due to the nonresonant PUMP and PROBE beams without a cw molecular beam impinging on the pyroelectric detector, confirming that the signal in section C is due to scattered light and not the molecular beam. Section E shows the lock-in signal without the cw molecular beam and both laser beams blocked at the entrance to the UHV chamber. Section E is shown to demonstrate that the lock-in signal does have a baseline of 0 mV.

It is clear from Fig. 3.17 that the signal due to the PROBE laser beam in section A is inverted by the addition of the PUMP laser beam in section B. The inversion should be evaluated relative to the baseline produced by scattered light shown in section C. This is experimental proof of an inversion produced by RAP. Figure 3.18 shows the percent inversion signal, defined as $|B-C|/(A-C)$ from Fig. 3.16, on the right-hand vertical axis as a function of PUMP power. Also shown is the PUMP beam's fluence dependence of the pyroelectric signal on the left-hand vertical axis. The two vertical axes have been scaled to coincide at $x = 0$ and maximum pump power of 385 mW. The single beam saturation curve and the percent inversion of the 'pump up, pump down' experiment match well in relative terms, but the percent inversion of the PROBE excitation by the combined PUMP + PROBE excitation is never more than 71%.

The observed $\sim$70% inversion of the lock-in detected pyroelectric detector signal represents a lower limit on the extent of population inversion for all Doppler shifts in the molecular beam. The actual inversion might be larger because of: (1) incomplete overlap of the molecular beam volume sampled by the two laser beams and (2) insufficient power in the excitation beams for complete population inversion over all Doppler shifts present in the molecular beam. Care was taken to produce two identical RAP excitation beams, and I assert that RAP was produced to at least 70% efficiency with 135 mW of excitation power.

Calculations, the asymptotic fluence dependence of the excited fraction as monitored by the pyroelectric detector, and the homogeneous excitation over all Doppler shifts in the molecular beam (shown in 3.2.1.4 and in Chaps. 4 and 5) suggest that RAP is complete in our experimental setup for excitation laser powers significantly higher than 135 mW.

3.2.1.4 Auger Electron Spectroscopy as a Probe of $CH_4(v_3)$ Excitation

We typically excite $CH_4(v_3)$ and $CD_3H(v_1)$ via RAP using 500 mW to 1 W of excitation power. No significant difference in the amount of carbon deposited on the single crystal surface is observed when changing the excitation laser power by a factor of two (0.5–1 W). We have used Auger electron spectroscopy (AES) to measure the amount of carbon deposited on Ni(100) after exposure to a molecular beam of $CH_4(v_3 = 1)$, as described in Sect. 2.3.4 and Sect. 4.2.2. For the molecular beam translational energies shown in this section, the vibrationally excited molecules are much more reactive (2–3 orders of magnitude) than ground state molecules [25]. Therefore, AES produces spatially resolved profiles of the excited molecular beam. I characterize the molecular beam after excitation (1) with an un-focused laser and (2) with RAP conditions.

Figure 3.19 shows a cross-section view of the 2 mm diameter molecular beam directed out of the page. The excitation is directed perpendicular to the molecular beam axis. The Doppler width is contained in the horizontal (X) slice of molecular beam, as shown by the green circles along the excitation arrow. A vertical (Z) slice through the zero-Doppler shifted trajectory samples the varying powers of the

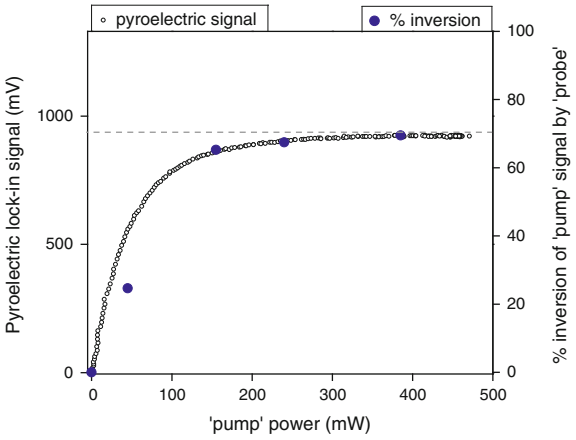

Fig. 3.18 Comparison of single laser beam saturation curve (*left-hand vertical axis*) with the inversion of the lock-in signal (*right-hand vertical axis*) detected in the 'pump up, pump down' experiment

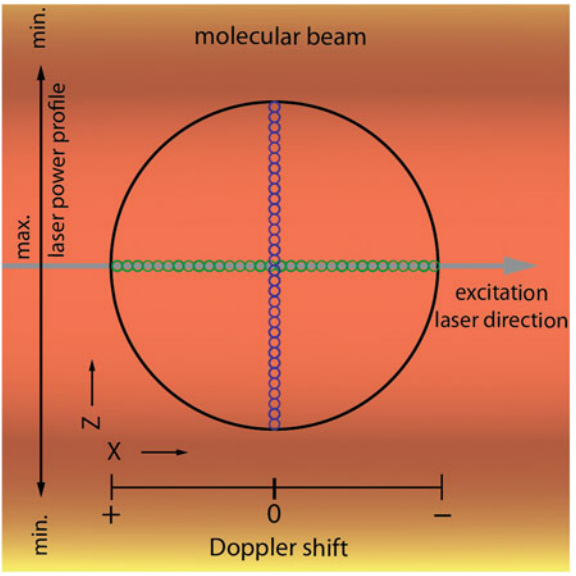

Fig. 3.19 Cross-section of molecular beam directed out of the page. Defines X and Z axis for Auger spectroscopy profiles

excitation arising from its Gaussian profile. AES profile scans of the molecular beam's carbon 'footprint' resulting from the methane dissociation on the Ni-surface allows for the relative extent of excitation to be measured. I have used X- and Z- profile scans to characterize the excitation.

First, I show AES (deposited carbon from molecular beam exposure) profiles resulting from state-preparation of the molecular beam with an unfocused excitation laser. Figure 3.20 shows the amount of carbon deposited on the surface after excitation with various laser powers. The profiles are across the molecular beam's Doppler width (X-direction in Fig. 3.19). These carbon footprints resulted from a

45 s deposition of $CH_4(v_3)$-R(1) with a translational energy (E_{TRANS}) of 49 kJ/mol directed onto a Ni(100) crystal held at 200°C.

As seen in the pyroelectric detector fluence dependences of the unfocused excitation, the excited fraction is sensitive to the power used to excite the molecular beam. We observed an oscillation of the excited fraction with a maximum ~50 mW excitation and a minimum ~125 mW. This corresponds qualitatively to the 'no focusing' pyroelectric detector fluence dependence shown in Fig. 3.13 for a 2056 m/s molecular beam. The local maximum and minimum pyroelectric detector signals are shifted a bit to higher excitation power due to the higher velocity molecular beam that was used in the current study (2471 m/s). The complicated power dependence of the excitation makes this excitation scheme undesirable.

Another striking feature of the AES profiles is their widths. The molecular beam diameter is 2 mm. I have placed a 2 mm wide rectangle around each of the deposited carbon profiles in Fig. 3.20 to show that the excitation is far from exciting the entire molecular beam in the X-direction. The full width at half maximum (FWHM) of the excited fraction goes from ~300 μm to ~600 μm as the excitation is increased from 13 mW to 440 mW, highlighting the effect of power broadening. This excitation scheme is far from the desired power insensitive, homogeneous excitation of the entire molecular beam.

Figure 3.21 shows AES profiles in the Z-direction as defined in Fig. 3.19. These AES profiles show the effect that the excitation's power profile has on the excitation efficiency. AES profiles in the Z-direction probe a single Doppler-shifted trajectory in the molecular beam. The 2 mm diameter of the molecular beam is observed in these profiles. Nevertheless, the excitation is difficult to characterize because the extent of excitation is sensitive to which part of the molecular beam is probed (i.e. to the variation of excitation power due to the Gaussian profile TEM00 laser beam). State-resolved reactivity measurements would be very difficult to quantify using this excitation setup because of significant uncertainties in the excited fraction.

In contrast to the unfocused excitation, RAP produces a reasonably homogenous excitation over the entire molecular beam. Figure 3.22 shows X-profiles of deposited carbon resulting from depositions of a $E_{TRANS} = 34$ kJ/mol (2056 m/s) molecular beam of $CH_4(v_3)$-R(0) (excited via RAP) directed onto a Ni(100) crystal held at 200°C. As predicted from calculations shown in the previous sections, RAP produces a homogeneous extent of excitation over the 5.9 MHz Doppler width in the 2 mm diameter molecular beam. The three deposition experiment results shown in Fig. 3.22 were obtained over the course of six months and were using different gas-mixtures to produce the ~2000 m/s molecular beam. The difference in peak heights is within the reproducibility of our experiment.

Figure 3.23 shows the Z-profiles of deposited carbon for the same three molecular beam depositions used above. Again, the extent of excitation is homogeneous over the diameter of the molecular beam. Furthermore, the 34 kJ/mol (2056 m/s) molecular beam can be excited with powers between 500 mW and

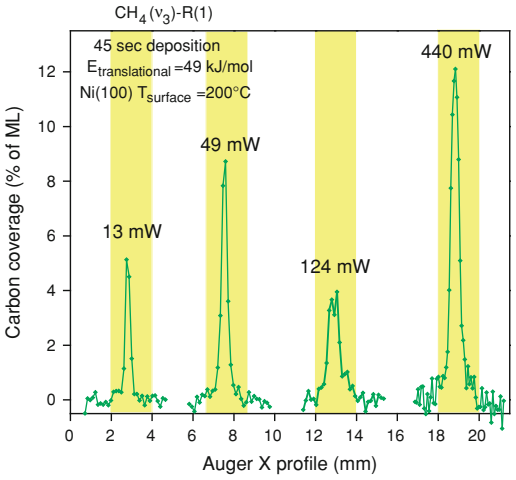

Fig. 3.20 Deposited carbon X-profiles resulting from the deposition of a 49 kJ/mol molecular beam of $CH_4(v_3)$-R(1) excited by unfocused excitation on Ni(100)

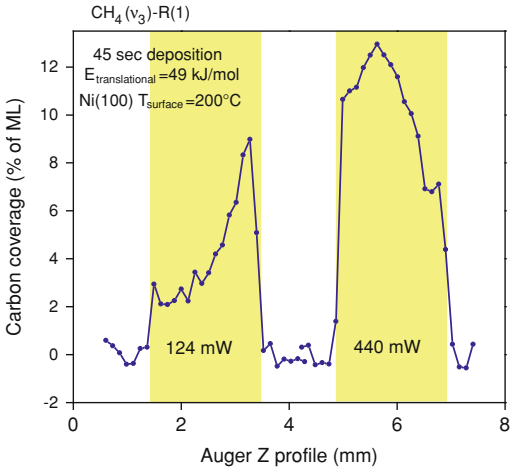

Fig. 3.21 Deposited carbon Z-profiles resulting from the deposition of a 49 kJ/mol molecular beam of $CH_4(v_3)$-R(1) excited by unfocused excitation on Ni(100)

1 W without an appreciable difference in the excited fraction as detected by Auger spectroscopy of carbon footprints.

3.2.1.5 Fluence Dependent Excited Fraction for $CH_4(v_3 = 1)$

The state preparation by laser excitation, detailed in the previous sections, produces predictable and reproducible excitation of the molecular beam. Figure 3.24 shows an example of a fluence dependence of the pyroelectric detector signal for excitation of $CH_4(v_3)$ excited via R(1), R(0), Q(1) and P(1) transitions in a 34 kJ/mol (2056 m/s) molecular beam produced by a 12% CH_4 in H_2 mixture expanded

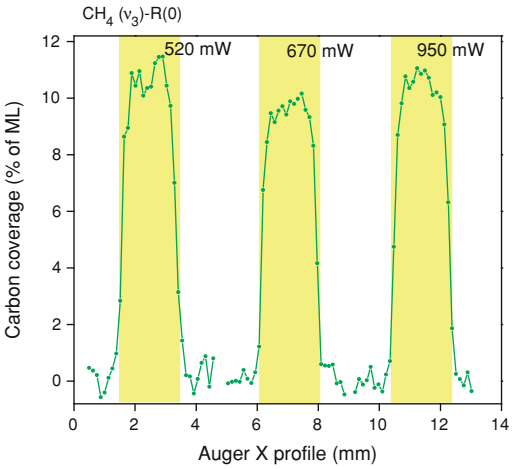

Fig. 3.22 Deposited carbon X-profiles of a Ni(100) surface resulting from a deposition of a 34 kJ/mol molecular beam of $CH_4(v_3)$-R(0) excited by RAP

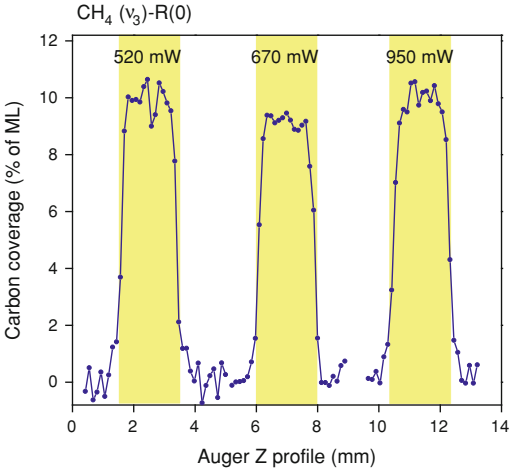

Fig. 3.23 Deposited carbon Z-profiles of a Ni(100) surface resulting from the deposition of a 34 kJ/mol molecular beam of $CH_4(v_3)$-R(0) excited by RAP

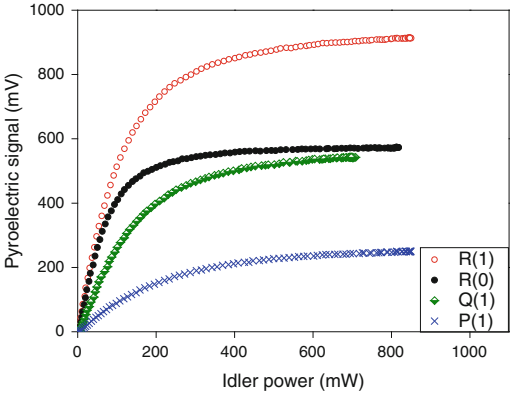

Fig. 3.24 Fluence dependent pyroelectric detector signal for different transitions of $CH_4(v_3)$ in the molecular beam

through a 50 μm pinhole with a nozzle temperature of 50°C and a backing pressure of 3 bar. This molecular beam excited by these transitions was used for most of the CH_4 alignment dependent reactivity experiments presented in this thesis.

The signal asymptotes in Fig. 3.24 reflect the relative excited population prepared by the four transitions. Since the R(1), Q(1) and P(1) transitions share a common lower level ($v = 0$ and $J = 1$), one might wonder why the excited fraction differs for the three transitions. The answer can be found in the $\Delta M = 0$ selection rule for excitation by linearly polarized radiation. The allowed $\Delta M = 0$ transitions for R(1), Q(1) and P(1) connect different M levels in the excited state for each transition which produces a different excited fraction and also produces different degrees of angular momentum alignment for the three transitions. Figure 3.28, in the following section, shows that population is removed from all three possible M-levels ($M = \pm 1, 0$) of the $J = 1$ lower state in the case of R(1) transition, whereas only the $M = \pm 1$ levels are connected to the excited state by the Q(1) transition and finally only the $M = 0$ level is depopulated by P(1). Assuming an isotropic M-level distribution in the ground state and an excited fraction that is independent of the transition strength, one expects relative excited fraction given by the asymptotes of R(1):Q(1):P(1) to be 3:2:1. Experimentally, we observe relative pyroelectric detector signals of 3:1.82:0.82 from asymptotic signals of 900, 545 and 245 mV. The measured ratios are close to the expect ratios. The difference is most likely due to a weak dependence of the excited fraction on the relative transition strength for the three transitions which scale as ~1:0.8:0.5. The transition strengths are discussed below. For excitation with unpolarized radiation ($\Delta M = \pm 1, 0$ selection rule), the ratio of the fluence dependence asymptotes should be 1:1:1 for R(1):Q(1):P(1) due to the 100% excitation of all allowed transitions by RAP. The $\Delta M = 0$ selection rule for linearly polarized excitation is clearly visible in laser fluence dependences shown in Fig. 3.24.

When increasing the excitation power from 500 to 700 mW, we observe an increase in the pyroelectric detector signal, shown in Fig. 3.24, of 2.7, 3.9 and 6.3% for the R(1), Q(1) and P(1) transitions, respectively. Furthermore, we routinely excite the rovibrational transitions with 500–900 mW of power without observing significant variations in the amount of deposited carbon on the single crystal surface after similar molecular beam deposition experiments. These two observations tell us that the asymptote in the pyroelectric detected saturation curves does correspond to a maximum in the number of molecules excited in the molecular beam.

The initial slopes of the individual laser fluence dependences should reflect the relative transition strengths of R(0), R(1), Q(1) and P(1) transitions. Figure 3.25, shows the pyroelectric signal, normalized to the asymptotic value for each transition separately. The initial slopes of R(0), R(1), Q(1) and P(1) are 0.91, 0.67, 0.49 and 0.36 (in units of fractional excitation/100 mW), using a linear fit of the data from 0 to 50 mW excitation power to determine the initial slope.

Rovibrational transition probabilities are proportional to the square of the Clebsch-Gordan coefficients, $\left\langle J''M'', J_{\text{photon}}M_{\text{photon}} \,\middle|\, J'M' \right\rangle^2$, where the double

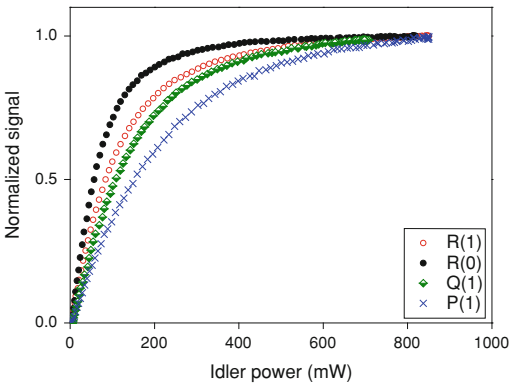

Fig. 3.25 Normalized laser fluence dependence curves for the transitions of $CH_4(\nu_3)$ in the molecular beam (data from Fig. 3.24)

prime denotes the initial state and the single prime denotes the final state [26]. Omitting the double primes for clarity, the analytical expressions are:

$$\mathrm{R}-\mathrm{branch}: \left\langle JM, J_{\mathrm{photon}}M_{\mathrm{photon}} \mid (J+1)M \right\rangle^2 = \frac{(J-M+1)(J+M+1)}{(2J+1)(J+1)} \tag{3.33}$$

$$\mathrm{Q}-\mathrm{branch}: \left\langle JM, J_{\mathrm{photon}}M_{\mathrm{photon}} \mid JM \right\rangle^2 = \frac{M^2}{J(J+1)} \tag{3.34}$$

$$\mathrm{P}-\mathrm{branch}: \left\langle JM, J_{\mathrm{photon}}M_{\mathrm{photon}} \mid (J-1)M \right\rangle^2 = \frac{(J-M)(J+M)}{J(2J+1)} \tag{3.35}$$

Evaluation of these analytical expressions for R(0), R(1), Q(1) and P(1) yields the relative transition probabilities, which are 1.0, 0.67, 0.50, 0.33. The R(1) transition is comprised of three 'allowed' M-level transitions (from $M'' = 0$ and $M'' = \pm 1$) with squared Cebsch-Gordan coefficients of 0.67 and 0.50, respectively. The larger of the two coefficients determines the initial slope of the excitation fluence dependence for R(1). All other rovibrational transitions in this study involve a single |M|-level transition. The measured relative initial slopes in Fig. 3.25 agree well with the calculated $\left\langle J''M'', J_{\mathrm{photon}}M_{\mathrm{photon}} \mid J'M' \right\rangle^2$ values.

3.3 Alignment of Vibrationally Excited Molecules in the Laboratory Frame

To realize steric control over the gas-phase reagent (i.e. methane), we use the linear polarization of the excitation laser's electric field vector to produce an aligned molecular ensemble in the prepared rovibrational state. The two entities that can be aligned by excitation with linearly polarized light are the angular

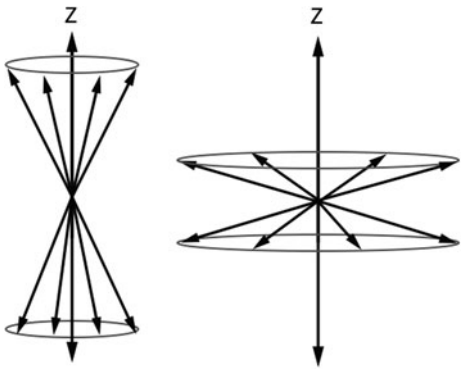

Fig. 3.26 Double-headed arrows lying preferentially parallel (*left*) to a reference axis (Z) and preferentially perpendicular (*right*) to some reference axis, Z [30]

momentum $\left(\vec{J}\right)$ and the vibrational transition dipole moment $(\vec{\mu}_{21})$ of the rovibrationally excited molecule.

Generally speaking, 'alignment' can be thought of as a double-headed arrow. A double-headed arrow can be 'aligned' parallel or perpendicular relative to some reference, but with no directional information (i.e. parallel or anti-parallel). Figure 3.26 shows a set of double-headed arrows lying preferentially along (either parallel or anti-parallel) or preferentially perpendicular to some reference axis, Z. This simple picture is offered to introduce the concept of alignment and attention is drawn to the cylindrical symmetry of the 'aligned' ensembles.

The alignments produced in our experiment exhibit cylindrical symmetry about the laser polarization direction, defined by the direction of the electric field vector. $\overrightarrow{J}$ is aligned relative to the excitation's polarization axis by exploiting the selection rules for infrared-active transitions excited by linearly polarized radiation. This section describes the origin and quantification of spatial alignment that occurs upon rovibrational excitation via a linearly polarized laser field.

3.3.1 Angular Momentum Alignment

The angular momentum of a quantum mechanical system such as an atom or molecule is denoted $\overrightarrow{J}$. If no external torque is applied, $\overrightarrow{J}$ is a strictly conserved quantity. The angular momentum $\overrightarrow{J}$ is a vector quantity that can take $2J + 1$ orientations relative to a quantization axis which are characterized by the $2J + 1$ values of the magnetic quantum number $M = +J, \ldots 0, \ldots -J$. In other words, M describes the projection of $\overrightarrow{J}$ onto a quantization axis in the laboratory frame (i.e. a magnetic or electric field). In the vector model of angular momentum, the state $|JM\rangle$ is represented by $\overrightarrow{J}$ precessing about some quantization axis Z while making a constant projection M onto it [26]. Figure 3.27 shows the state $|JM\rangle$.

$\overrightarrow{J}$ is said to precess about Z leaving information regarding the projection of $\overrightarrow{J}$ onto X and Y unknown. This results from the fact the quantum mechanical angular momentum operators L_X, L_Y and L_Z do not commute. Therefore, the system is cylindrically symmetric, characterized by the length of $\overrightarrow{J}$ and its projection M on Z. Furthermore, $\overrightarrow{J}$ cannot lie exactly along Z as that would allow the projection of $\overrightarrow{J}$ on X and Y to be known precisely. The length of $\overrightarrow{J}$ is defined as $\sqrt{J(J+1)}$, though M takes integer values between $+J$ and $-J$. The fact that the length of $\overrightarrow{J}$ is more than its maximum possible projection on Z allows for the necessary uncertainty of $\overrightarrow{J}$'s projection on X and Y.

We prepared $CH_4(v_3,J)$ and $CD_3H(v_1,J)$, both being infrared (IR) active vibrational transitions, with a linearly polarized excitation field $\left(J_{\text{photon}} = 1, M_{\text{photon}} = 0\right)$. The usual selection rules for IR-active transitions of a symmetric or spherical top molecule excited by linearly polarized radiation are:

$$\begin{aligned}
&\text{R} - \text{branch}: \ \Delta J = +1 \text{ and } \Delta M = 0\\
&\text{P} - \text{branch}: \ \Delta J = -1 \text{ and } \Delta M = 0\\
&\text{Q} - \text{branch}: \ \Delta J = 0 \text{ and } \Delta M = 0, \ M \neq 0
\end{aligned}$$

Figure 3.28 shows the four rovibrational transitions used to prepare $CH_4(v_3)$ and $CD_3H(v_1)$ in our study of quantum state-specific, alignment dependent surface reactivity. Excitation of $CH_4(v_3 = 1)$ via these transitions prepares a varying degree of $\overrightarrow{J}$ alignment in the laboratory frame. The alignment is a direct consequence of the selection rules of each transition.

Figure 3.29 shows a vectorial depiction of the $\overrightarrow{J}$ alignment produced in the vibrationally excited state by excitation of the transitions shown in Fig. 3.28. For the R(0) transition, we prepare $CH_4(v_3 = 1)$ with $J = 1$ and $M = 0$ aligning $\overrightarrow{J}$ perpendicular to Z or the polarization axis of the excitation laser. R(0) excitation produces the highest achievable $\overrightarrow{J}$ alignment in our experiments. With P(1) excitation, we prepare a $CH_4(v_3 = 1)$ with $J = 0$ and populate the only possible value of M, $(M = 0)$, resulting in no alignment of the excited molecule. The R(1) and Q(1) transitions exhibit intermediate degrees of $\overrightarrow{J}$ alignment due to the selection rules for linearly polarized excitation.

If we consider the $\overrightarrow{J}$ as an arrow, an **oriented** $\overrightarrow{J}$ distribution is one with a preferred direction (either parallel or antiparallel to Z) characterized by a M-level distribution whose average value is either positive or negative. An **aligned** $\overrightarrow{J}$ distribution is one where the M-level distribution is non-isotropic in the absolute values of M, see Fig. 3.28. Excitation via linearly polarized light obeys the $\Delta M = 0$ selection rule, but will excite positive and negative M values indistinguishably. Therefore, in our experimental setup, we produce **aligned** ensembles of molecules: with $\overrightarrow{J}$ either preferentially parallel or perpendicular to Z.

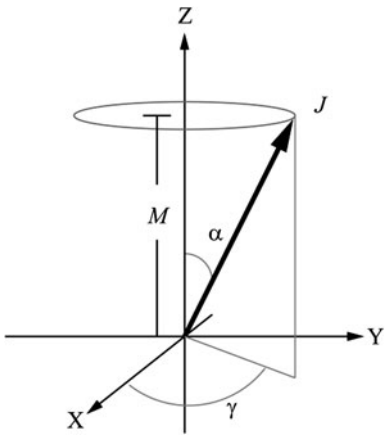

Fig. 3.27 Vector model for the state $|JM\rangle$

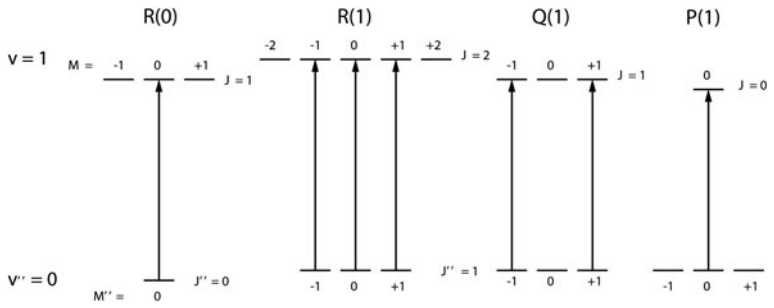

Fig. 3.28 Level diagrams for $CH_4(\nu_3)$ transitions used in the study of alignment dependent reactivity

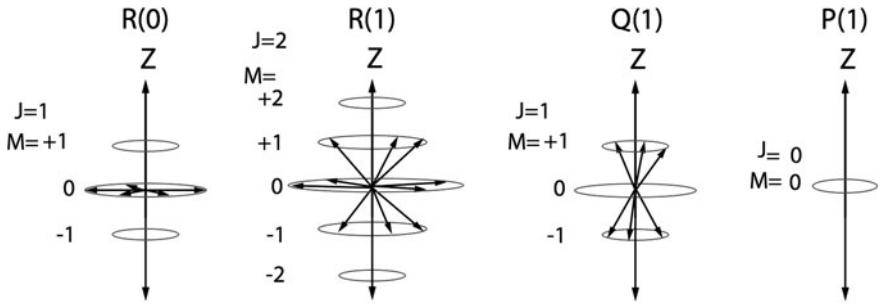

Fig. 3.29 Anisotropic M-level distributions produced by $CH_4(\nu_3)$ transitions used in the study of quantum state-resolved, alignment dependent reactivity

A convenient method for describing the distribution of $\overrightarrow{J}$, relative to some quantization axis Z, uses calculated orientation and alignment coefficients [27–30]. Quantification of angular momentum alignment was originally developed to describe the degree of polarization of light emitted by an atom or molecule after collisional excitation or electron impact [27, 31–34], and has been used successfully to study stereodynamics in gas-phase reactions [35–38].

The Z axis is selected to be the polarization axis of the excitation laser. This choice of Z takes advantage of the system's cylindrical symmetry. As shown in Fig. 3.27, the location of $\overrightarrow{J}$ relative to Z, is parameterized by α, the angle $\overrightarrow{J}$ makes with Z, and γ, the angle $\overrightarrow{J}$ makes with X. For our case of cylindrical symmetry, the distribution of $\overrightarrow{J}$ about Z is independent of γ. Therefore, the alignment coefficients can simply be related to M level populations and the orientation and alignment coefficients of $\overrightarrow{J}$ are defined in terms of the Legendre polynomial with normalization chosen to give convenient limits of the coefficients. The odd moments are termed orientation coefficients because their value changes sign between parallel and antiparallel arrangement of $\overrightarrow{J}$ about Z, which is not the case for the even moments therefore called alignment coefficients. Below, I focus the discussion on alignment coefficients since orientation is not possible in our current experiment.

In a classical mechanics treatment, the location of $\overrightarrow{J}$ about some symmetry axis Z is defined by a continuous distribution of polar coordinates α and γ. For our case of cylindrical symmetry of $\overrightarrow{J}$ about Z, there is no γ dependence. Following the explanation of $\overrightarrow{J}$ alignment given in Ref. [30, 39], the distribution of $\overrightarrow{J}$, defined as $N(\widehat{J},\widehat{Z})$, can be written as an expansion of Legendre polynomials:

$$N(\widehat{J},\widehat{Z}) = \frac{1}{4\pi}\sum_{n} A_0^{(n)} P_n(\cos\alpha) \tag{3.36}$$

In Eq. 3.36, α is the angle between $\overrightarrow{J}$ and Z (see Fig. 3.27), $P_n(x)$ denotes Legendre polynomials, the carats indicate unit vectors and their index is given by n. In practice, n is limited to $2J$. This means that the maximum achievable multipolar moment is limited to twice the angular momentum quanta of the excited state, $|JM\rangle$. The expansion coefficients, $A_0^{(n)}$, give the distribution multipolar moments:

$$A_0^{(n)} = (2n+1)\langle P_n(\cos\alpha)\rangle = (2n+1)\int_0^{2\pi} d\gamma \int_0^{\pi} \sin\alpha d\alpha N(\widehat{J},\widehat{Z}) P_n(\cos\alpha) \tag{3.37}$$

In the case of cylindrical symmetry, alignment coefficients are defined as $A_0^{(n)}$ by convention, where n is the coefficient's order. Here, the subscript zero denotes the case of cylindrical symmetry. The first couple of alignment coefficients become:

$$A_0^{(0)} = \langle P_0(\cos\alpha)\rangle = 1 \tag{3.38}$$

$$A_0^{(2)} = 2\langle P_2(\cos\alpha)\rangle = 3\cos^2\alpha - 1 \tag{3.39}$$

Here, $A_0^{(0)}$ describes the monopole of $\overrightarrow{J}$ and is the only non-zero term for an isotropic distribution. The alignment coefficient $A_0^{(2)}$ represents the quadrupolar contribution to the anisotropy of $\overrightarrow{J}$ about Z, and is the useful quantity for the description of $\overrightarrow{J}$ alignment in our experiments. Limits of $A_0^{(2)}$ were chosen to be -1 for perpendicular alignment ($\alpha = 90°$, $\cos\alpha = 0$) and +2 for parallel alignment ($\alpha = 0°$, $\cos\alpha = 1$) [29]. The angular distribution of $\overrightarrow{J}$ expanded in the alignment coefficients yields the classical expression

$$N(J,\alpha) = \frac{1}{4\pi}\left\{A_0^{(0)} + \frac{5}{2}A_0^{(2)}P_2(\cos\alpha)\right\}$$

$$N(J,\alpha) = \frac{1}{4\pi}\left\{1 + \frac{5}{2}A_0^{(2)}P_2(\cos\alpha)\right\}. \tag{3.40}$$

Quantum mechanically, the probability of finding the system in $|JM\rangle$ after absorption of linearly polarized light $\left(J_{\text{photon}} = 1,\, M_{\text{photon}} = 0\right)$ is proportional to the square of the Clebsch-Gordan coefficient $\left\langle J''M'', J_{\text{photon}}M_{\text{photon}} \,\middle|\, JM\right\rangle$ where $|J''M''\rangle$ denotes the system's initial state. The Clebsch-Gordan coefficient can be interpreted as the probability amplitude that the uncoupled state $\left|J''M'', J_{\text{photon}}M_{\text{photon}}\right\rangle$ will couple to form a resultant state $|JM\rangle$. The square of the Clebsch-Gordan coefficient represents the probability of said coupling and can take values between 0 and 1. In Sect. 3.2.1.5, I showed the analytical expressions for the excitation branch dependent $\left\langle J''M'', J_{\text{photon}}M_{\text{photon}} \,\middle|\, JM\right\rangle^2$. Therefore, the probability of $\overrightarrow{J}$ to be at some angle α with respect to the linear polarization axis of the excitation field (i.e. at some M-level) is given by

$$\rho_J(\alpha) = \sum_{M''} \langle J''M'', 10 \mid JM\rangle^2 |Y_{JM}(\alpha,\gamma)|^2. \tag{3.41}$$

Here, $|JM\rangle = |Y_{JM}(\alpha,\gamma)|$.

Similar to the classical treatment, evaluation of the Clebsch-Gordan coefficients for linearly polarized light exciting a cylindrically symmetric system yields

$$\rho_J(\alpha) = \frac{A_0^{(0)} + A_0^{(2)}P_2(\cos\alpha)}{4\pi} = \frac{1 + A_0^{(2)}P_2(\cos\alpha)}{4\pi}. \tag{3.42}$$

where,

$$A_0^{(2)} = \sum_M P(M)\frac{3M^2 - J(J+1)}{J(J+1)}. \tag{3.43}$$

Here, $P(M)$ is the probability for the coupled (excited) state $|JM\rangle$ to make a projection M. For example, the probability of preparing state $|JM_1\rangle$ upon excitation of $|J''M_1\rangle$ by a linearly polarized photon is

$$P(M_1) = \frac{\langle J''M_1, 10 \mid JM_1\rangle^2}{\sum_m \langle J''M_m, 10 \mid JM_m\rangle^2}. \tag{3.44}$$

where the index m takes integer values from $+J''$,…0,…$-J''$ and represent all M-levels of J''. This is where the weak optical pumping condition is relevant. Zare and coworkers [26, 28, 39] developed this machinery for quantifying alignment upon excitation by exploiting the differences in coupling probabilities (Clebsch-Gordan coefficients) for different M-level transitions comprising a P-, Q- or R-branch rovibrational transition. Therefore, weak optical pumping was required to not disturb the initial M-level populations. If the different M-level transitions were driven into saturation, then the values of their Clebsch-Gordan coefficients would not reflect the $\overrightarrow{J}$ distribution in space. The weak pumping conditions allows for alignment of high J-states since it is due to differences in angular momentum coupling probabilities.

Figure 3.30 displays the calculated $A_0^{(2)}$ values for the rovibrational transitions employed in the experiments presented in Chaps. 4 and 5. These $A_0^{(2)}$ coefficients quantify the $\overrightarrow{J}$ alignment produced by excitation via the rovibrational transitions shown in Fig. 3.28 assuming unresolved K-structure in the preparation of $CD_3H(\nu_1)$.

The calculation results in Fig. 3.30 are for the case of 'strong optical pumping'. By 'strong optical pumping', I have assumed that all allowed rovibrational transitions have been excited equally to 100% by rapid adiabatic passage. Therefore, $P(M)$ in the strong pumping limit become either "1'' for allowed transitions or "0'' for forbidden transitions. The R(0), Q(1) and P(1) transitions connect a single $|M|$-level which means that their alignment coefficients are valid at any level of pumping. In our study, the only transition affected by the strong pumping condition is R(1).

R(1) is comprised of two 'allowed' transitions that possess different Clebsch-Gordan coefficients. The most intense transition is from $|J''M''\rangle = |10\rangle$ to $|JM\rangle = |20\rangle$ with $|\langle 10, 10 \mid 20\rangle|^2 = 0.67$. The other transition composing R(1) is $|J''M''\rangle = |1 \pm 1\rangle$ to $|JM\rangle = |2 \pm 1\rangle$ with $|\langle 1 \pm 1, 10 \mid 2 \pm 1\rangle|^2 = 0.5$. This produces $P(M = 0) = \frac{0.67}{0.5+0.67+0.5} = 0.4$ and $P(M = \pm 1) = \frac{0.5}{0.5+0.67+0.5} = 0.3$ in the limit of weak optical pumping.

I have assumed that all of the R(1) M-level transitions are equally probable due the strong pumping conditions of our experiments. For R(1) excitation, the $A_0^{(2)}$ coefficient is lowered from -0.7 to -0.67 because of the strong pumping conditions. As J increases, $A_0^{(2)}$ will rapidly decrease to zero for Q- and R-branch

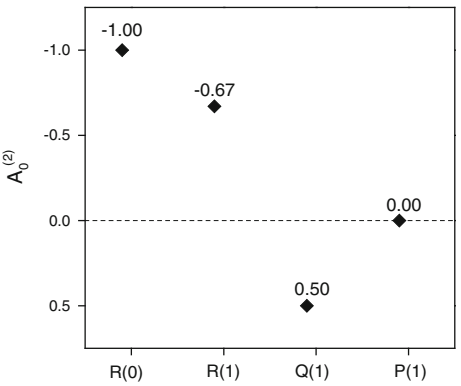

Fig. 3.30 Calculated alignment coefficients, $A_0^{(2)}$, valid for the various rovibrational transitions of $CH_4(\nu_3)$ and $CD_3H(\nu_1)$ used in the study of alignment dependent reactivity

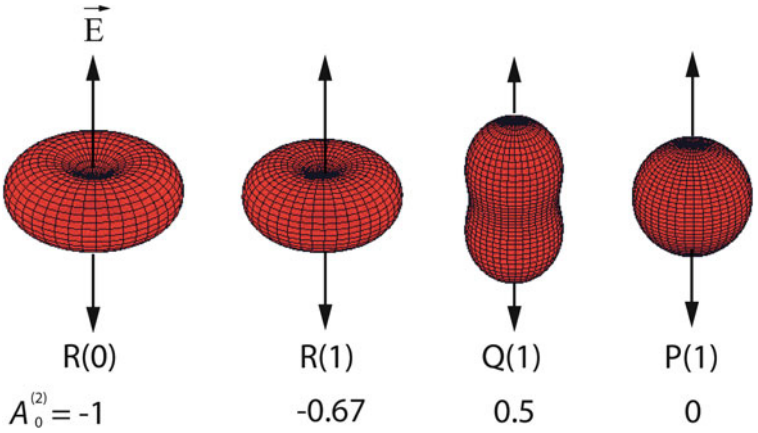

Fig. 3.31 $\vec{J}$ probability distributions upon excitation by linearly polarized light. These distributions are valid for the various rovibrational transitions of both $CH_4(\nu_3)$ and $CD_3H(\nu_1)$ used in the study of alignment dependent reactivity

transitions. Furthermore, alignment via P-branch excitation is not possible in the strong pumping limit.

Since $A_0^{(2)} = 3\cos^2\alpha - 1$, it has the limits of +2 and −1. If $\alpha = 0°$, then $A_0^{(2)} = 2$. If $\alpha = 90°$, then $A_0^{(2)} = -1$. Note that for R(0) excitation, the $\vec{J}$ of the excited state is aligned perpendicular to Z, or $A_0^{(2)} = -1$. This is readily seen from Figs. 3.28 and 3.29, since the excited state prepared has $M = 1$ with a projection of zero onto the laser's polarization axis (i.e. $M = 0$). Furthermore, the P(1) transition produces an $A_0^{(2)} = 0$ which corresponds an isotropic $\vec{J}$ distribution. This, too, is readily understood from Figs. 3.28 and 3.29. Since all M-levels are populated in the excited state prepared via P(1) excitation, there is no $\vec{J}$ alignment

in the laboratory frame. Finally, the Q(1) transition produces an $A_0^{(2)} = 0.5$ corresponding to an alignment of the $\overrightarrow{J}$ preferentially parallel to Z.

In practice [36], the probability of finding the $\overrightarrow{J}$ of a vibrationally excited ensemble at α with respect to Z is given by Eq. 3.42. Inserting the tabulated values of $A_0^{(2)}$ into Eq. 3.42, I determined the probability of finding the $\overrightarrow{J}$ at an angle α with respect to the linear polarization axis of the excitation laser Z. Figure 3.31 shows the resulting cylindrically symmetric, three dimensional probability distributions of the $\overrightarrow{J}$ for the various transitions used in our experiments.

These probability distributions produce a quantitative description of the localization of the $\overrightarrow{J}$ after excitation by the various rovibrational transitions. $\overrightarrow{J}$ can be considered 'space-fixed' and defining the rotation axis of the molecule. It is the $\overrightarrow{J}$ alignment that allows for the vibrational transition dipole moment (initially defined along the excitation's linear polarization) alignment to persist. I discuss the alignment of the net vibrational amplitude of $CH_4(\nu_3)$ or the vibrationally excited C–H bond axis of $CD_3H(\nu_1)$ in the following section.

3.3.2 Vibrational Transition Dipole Moment Alignment

Here, I discuss the alignment of a symmetric top's vibrational dipole moment in the laboratory frame by excitation with a linearly polarized photon. In a simplistic view, the vibrational transition dipole moment ($\overrightarrow{\mu}_{21}$) for the C–H stretch of $CD_3H(\nu_1)$ is along the C–H or the figure axis of the molecule. I define $\overrightarrow{\mu}_{21}$ as equal to $\langle\psi_2|\widehat{\mu}|\psi_1\rangle$. So, alignment of $\overrightarrow{\mu}_{21}$ in the laboratory frame is synonymous with alignment of the unique C–H bond axis for $CD_3H(\nu_1)$. The $\overrightarrow{\mu}_{21}$ for the antisymmetric stretch of $CH_4(\nu_3)$ can be thought of as the axis containing the net vibrational amplitude (or the vibrational direction). Therefore, alignment of $\overrightarrow{\mu}_{21}$ $CH_4(\nu_3)$ can be thought of as analogous to that of $CD_3H(\nu_1)$ without the bond axis alignment. A pictorial description of $\overrightarrow{\mu}_{21}$ for $CD_3H(\nu_1)$ (left) and $CH_4(\nu_3)$ (right) is given in Fig. 3.32. This picture is a gross oversimplification of $CH_4(\nu_3)$, but is offered as an introduction to the discussion of vibrational alignment for this molecule.

The mathematical treatment for vibrational transition dipole moment alignment, presented here, is for a symmetric top molecule, but the resulting alignment should be similar for $CH_4(\nu_3)$ [36] with one important qualification. I consider the alignment of $\overrightarrow{\mu}_{21}$ for $CD_3H(\nu_1)$ and $CH_4(\nu_3)$ to be equivalent with the only difference being that we have information on the alignment of the C–H bond axis for $CD_3H(\nu_1)$. For the case of $CH_4(\nu_3)$, we do not align the C–H bonds, but polarize the vibration in space. Classically thinking, we align the net vibrational amplitude of $CH_4(\nu_3)$ in the laboratory frame.

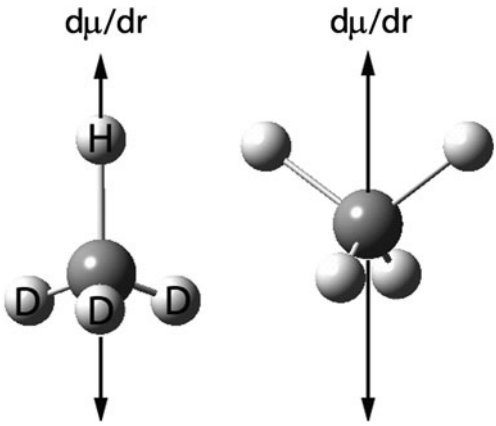

Fig. 3.32 Depiction of the vibrational transition dipole moment ($\vec{\mu}_{21}$) of $CD_3H(\nu_1)$ (left) and $CH_4(\nu_3)$ (right)

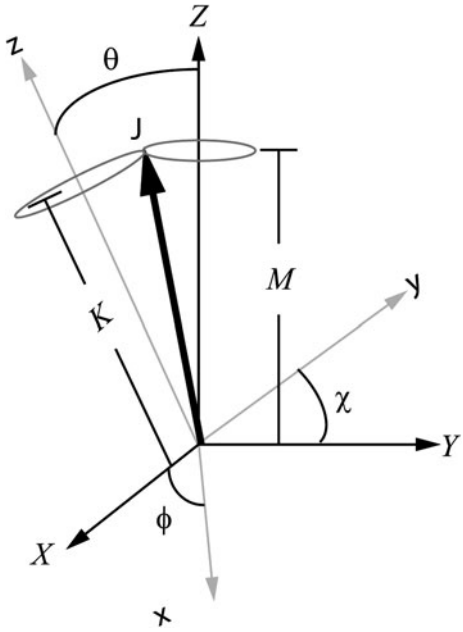

Fig. 3.33 Vectorial representation of variables describing $|JKM\rangle$ of symmetric top

We consider a symmetric top, such as CD_3H, with angular momentum $\vec{J}$ making a projection M onto a space-fixed axis Z and a projection K on a body-fixed axis z. The body-fixed frame axes are denoted (x,y,z). Here, z defines the symmetric top's figure axis (the C_3-axis of CD_3H). Figure 3.33 is a vectorial representation of these quantities. $|JKM\rangle$ denotes the wavefunction of the symmetric top molecule.

$$|JKM\rangle = \psi_{JKM}(\phi, \theta, \chi) \tag{3.45}$$

The probability of finding a symmetric top's figure axis at an angle θ from some quantization axis in the laboratory frame is given by [40],

$$\rho_{JKM}(\theta) = (-1)^{M-K}\frac{2J+1}{2}\sum_{n=0}^{2J}(2n+1)\begin{pmatrix} J & J & n \\ M & -M & 0 \end{pmatrix}\begin{pmatrix} J & J & n \\ K & -K & 0 \end{pmatrix}P_n(\cos\theta). \tag{3.46}$$

Here, Wigner 3-j symbols are used to describe the probability that the coupled state $|JKM\rangle$ will be found from $\overrightarrow{J}$ making a simultaneous projection of M onto Z and K onto z [26]. Wigner 3-j symbols are related to the Clebsch-Gordan coefficients by [26]

$$\begin{pmatrix} J_1 & J_2 & J_3 \\ M_1 & M_2 & M_3 \end{pmatrix} = (-1)^{J_1-J_2-M_3}\frac{\langle J_1M_1, J_2M_2 \mid J_3 - M_3\rangle}{\sqrt{2J_3+1}}. \tag{3.47}$$

In Eq. 3.46, $P_n(cos\theta)$is a Legendre polynomial of rank/order$n$. As for $\overrightarrow{J}$ alignment, the achievable alignment moments are $2J$ (i.e. For $J = 1$, the alignment moments $n = 0, 2$ are possible) [26, 30, 41]. Analogous to the above discussion for the $\overrightarrow{J}$, the first two alignment moments are defined as,

$$\begin{aligned} P_0(\cos\theta) &= 1 \\ P_2(\cos\theta) &= 2P_2(\cos\theta) = \frac{1}{2}\left(3\cos^2\theta - 1\right). \end{aligned} \tag{3.48}$$

As was the case for $\overrightarrow{J}$ alignment, we need only to concern ourselves with $n = 0$ and $n = 2$ (the possible even ranks of the expansion) for J-states of 0 and 1 that are excited in the molecular beam. For the R(1) excitation, $J = 2$ in the excited state. This state allows for $n = 4$ multipolar moment alignment, but this has been neglected in our study as it was not needed in the interpretation of our data. We choose to compare our experimental data to the quadrupolar moment alignment coefficient ($n = 2$) for all transitions excited, and found good agreement. The probability of finding the figure axis of the symmetric top at some angle θ from the quantization axis becomes

$$\rho_{JKM}(\theta) = (-1)^{M-K}\frac{2J+1}{2}\left\{\begin{array}{l} \begin{pmatrix} J & J & 0 \\ M & -M & 0 \end{pmatrix}\begin{pmatrix} J & J & 0 \\ K & -K & 0 \end{pmatrix}P_0(\cos\theta) + \\ (5)\begin{pmatrix} J & J & 2 \\ M & -M & 0 \end{pmatrix}\begin{pmatrix} J & J & 2 \\ M & -M & 0 \end{pmatrix}P_2(\cos\theta) \end{array}\right\}. \tag{3.49}$$

After evaluation of the Wigner 3-j coefficients, the probability of the angular distribution of a symmetric top's figure axis with respect to an angle θ from the

quantization axis Z after excitation by linearly polarized light is given by the compact formula [42],

$$\rho_{JKM}(\theta) = \frac{1 + \beta_{axis} P_2(\cos\theta)}{4\pi}. \tag{3.50}$$

where β_{axis} is defined as the vibrational transition dipole moment alignment coefficient [26, 36, 42], and has the form

$$\beta_{axis} = \sum_M P(M) \sum_K P(K) \frac{5[3M^2 - J(J+1)][3K^2 - J(J+1)]}{J(2J+3)(J+1)(2J-1)}. \tag{3.51}$$

Here, $P(M)$ is defined in the same way as the previous section, and $P(K)$ is the probability for the coupled (excited) state $|JKM\rangle$ to make projection K onto the figure axis of the symmetric top molecule. Equation 3.50 provides a quantification of the vibrational alignment in space. The classical limits of β_{axis} are the same as that of $A_0^{(2)}$. Specifically, $\beta_{axis} = +2$ for alignment of the vibrational transition dipole moment parallel to Z, and $\beta_{axis} = -1$ for alignment perpendicular to Z. The value of β_{axis} is dependent on the rovibrational transition used to excite the molecule.

The individual calculations of β_{axis} are presented in Appendix B for the R(0), R(1), Q(1) and P(1) transitions in the case of strong optical pumping and unresolved K-structure, using Eq. 3.51. Again, all allowed rovibrational transitions were taken to be equally probable.

For the R(1) transition, I also calculated β_{axis} for the case of resolved K-structure, as we were able to resolve the K-structure in of $CD_3H(\nu_1)$. I have treated $CH_4(\nu_3)$ as a symmetric top with unresolved K-structure, as the K-levels of a given J-state are degenerate in a spherical top. I defined the 'figure axis' of vibrationally excited $CH_4(\nu_3)$ as the axis containing the net vibrational amplitude.

Figure 3.34 shows the calculated β_{axis} values for the transitions used to probe the steric effects in the dissociative chemisorption of vibrationally excited $CH_4(\nu_3)$, which are assumed to be equivalent to those of a symmetric top with unresolved K-structure in the limit of strong optical pumping. These calculated alignment coefficients are compared to experimental data in Chaps. 4 and 5.

Figure 3.35 shows the cylindrically symmetric, three-dimensional probability of finding the vibrational dipole moment at an angle θ from Z. To generate the probabilities, I used Eq. 3.50 and the tabulated β_{axis} coefficients from Eq. 3.51.

Figure 3.36 shows the calculated β_{axis} values for the transitions used to probe the steric effects in vibrationally excited $CD_3H(\nu_1)$ chemisorption on Ni(100). These β_{axis} coefficients describe the vibrational transition dipole moment alignment of a symmetric top with resolved K-structure in the limit of strong optical pumping.

The alignment produced in the rovibrationally excited molecules is due to the selection rules for rovibrational excitation via linearly polarized radiation. Quantification of the angular momentum and vibrational alignment upon excitation is

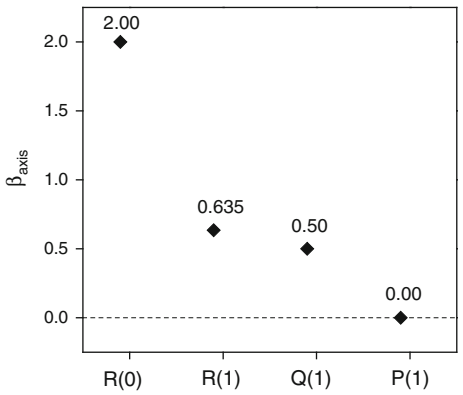

Fig. 3.34 Calculated alignment coefficients β_{axis} valid for the indicated rovibrational transitions of $CH_4(v_3)$ and $CD_3H(v_1)$ in the case of unresolved K-structure

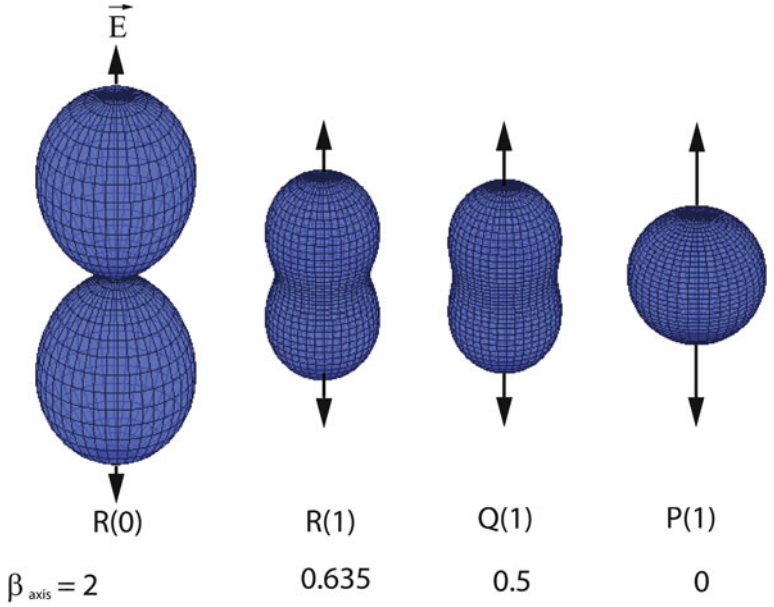

Fig. 3.35 Vibrational transition dipole moment probability distributions upon excitation by linearly polarized light. These distributions are valid under the conditions of strong optical pumping for the indicated rovibrational transitions of $CH_4(v_3)$ and $CD_3H(v_1)$ in the case of unresolved K-structure

conveniently expressed by the alignment coefficients $A_0^{(2)}$ and β_{axis}, respectively. The calculated alignment coefficients can be used to tabulate a probability of finding $\vec{J}$ and the vibrational transition dipole moment at some angle with respect to the excitation's linear polarization axis.

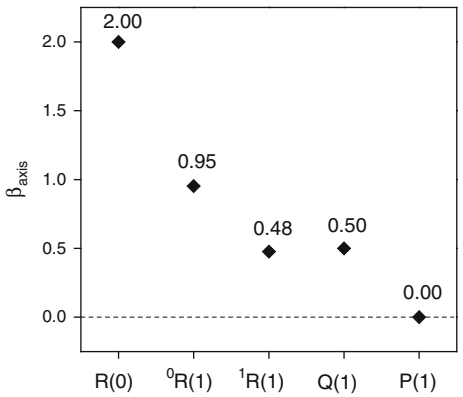

Fig. 3.36 Calculated alignment coefficients, β_{axis}, valid for the indicated rovibrational transitions of $CD_3H(\nu_1)$ in the case of resolved K-structure

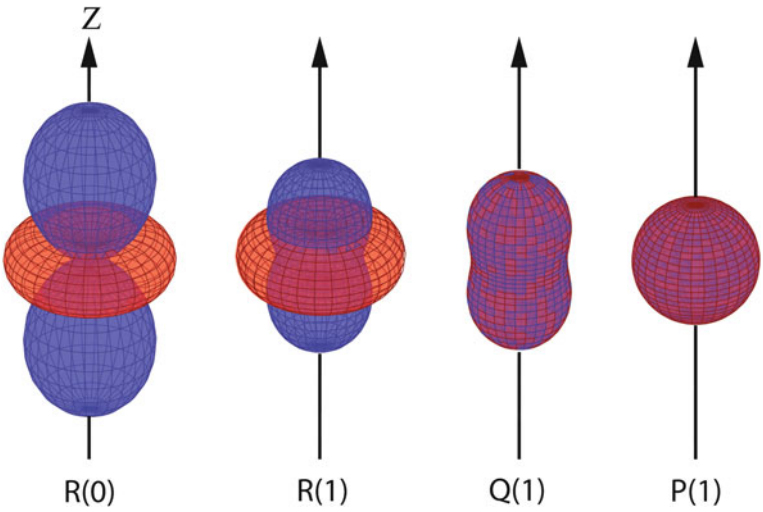

Fig. 3.37 Calculated probability distribution of the $\vec{J}$ (in red) and $\vec{\mu}_{21}$ (in blue) about the linear polarization axis of the excitation field

Figure 3.37 shows the gas-phase reactant alignment produced upon P-, Q- and R-branch excitation in the limit of strong optical pumping. These results are strictly valid for a parallel transition of a symmetric top molecule (i.e. $CD_3H(\nu_1)$), but should be applicable to a spherical top (i.e. $CH_4(\nu_3)$) if we consider the spherical top as a symmetric top with degenerate K-levels. The probability distribution of the $\vec{J}$ with respect to the excitation's polarization Zaxis is given in red. The probability distribution of $\vec{\mu}_{21}$ is shown in blue. Q(1) and P(1) have the $\vec{J}$ and $\vec{\mu}_{21}$ distributions overlapping. Figure 3.37 is intended to give the reader a reference for the alignment produced in the vibrationally excited methane upon

excitation by these rovibrational transitions. R(0) excitation produces the highest degree of alignment. R(1) alignment depicted in Fig. 3.37 is for the case of un-resolved K-structure.

References

1. Argos model 2400 Aculight Corporation
2. U. Hefter et al., Preparation and detection of alignment with high ||m|| selectivity by saturated laser optical pumping in molecular beams. J. Chem. Phys. **85**(1), 286–302 (1986)
3. B.W. Shore et al., Simple mechanical analogs of rapid adiabatic passage in atomic physics. Am. J. Phys. **77**(12), 1183–1194 (2009)
4. N.V. Vitanov et al., Laser-induced population transfer by adiabatic passage techniques. Annu. Rev. Phys. Chem. **52**, 763–809 (2001)
5. I.I. Rabi, N.F. Ramsey, J. Schwinger, Use of rotating coordinates in magnetic resonance problems. Rev. Mod. Phys. **26**(2), 167–171 (1954)
6. I.I. Rabi, Space quantization in a gyrating magnetic field. Phys. Rev. **51**(8), 0652–0654 (1937)
7. P.L. Knight, P.W. Milonni, The Rabi frequency in optical-spectra. Phys. Rep.-Rev. Sect. Phys. Lett. **66**(2), 21–107 (1980)
8. S. Avrillier et al., Supersonic beam spectroscopy of low J-transitions of the nu-3 band of SF6 - Rabi oscillations and adiabatic passage with a CW laser. Opt. Commun. **39**(5), 311–315 (1981)
9. A.G. Adam et al., Rabi oscillations and rapid-passage effects in the molecular-beam CO2-laser stark spectroscopy of CH3F. Phys. Rev. A **32**(3), 1451–1457 (1985)
10. C.C. Tannoudji, *Frontiers in Laser Spectroscopy* (North-Holland, Amsterdam, 1977)
11. B.W. Shore, *The Theory of Coherent Atomic Excitation*, vol. 1 (Wiley-Interscience, New York, 1990)
12. M.M.T. Loy, Observation of population inversion by optical adiabatic passage. Phys. Rev. Lett. **32**(15), 814–817 (1974)
13. J.P.C. Kroon et al., Rabi oscillations in the optical-pumping of a metastable neon beam with a CW dye-laser. Phys. Rev. A **31**(6), 3724–3732 (1985)
14. C. Liedenbaum, S. Stolte, J. Reuss, Inversion produced and reversed by adiabatic passage. Phys. Report. **178**(1), 1–24 (1989)
15. V.S. Malinovsky, J.L. Krause, General theory of population transfer by adiabatic rapid passage with intense chirped laser pulses. Eur. Phys. J. D **14**(2), 147–155 (2001)
16. V.S. Malinovsky, J.L. Krause, Efficiency and robustness of coherent population transfer with intense, chirped laser pulses. Phys. Rev. A **63**(4), 1 (2001)
17. L. Allen, J.H. Eberly, *Optical Resonance and Two Level Atoms* (Wiley, New York, 1975)
18. M.D. Levenson, S.S. Kano, *Introduction to Nonlinear Laser Spectroscopy. Quantum Electronics: Principles and Applications* (Harcourt Brace Jovanovich, Boston, 1988)
19. C. Zener, Non-adiabatic crossing of energy levels. Proc. Royal Soc. London Ser. a-Contain. Pap. Math. Phys. Character **137**(833), 696–702 (1932)
20. K.A. Suominen, B.M. Garraway, Population transfer in a level-crossing model with 2 time scales. Phys. Rev. A **45**(1), 374–386 (1992)
21. L.S. Rothman et al., The HITRAN 2008 molecular spectroscopic database. J. Quant. Spectrosc. Radiat. Transf. **110**(9–10), 533–572 (2009)
22. W. Demtröder, *Laser Spectroscopy: Basic Concepts and Instrumentation* (Springer, Berlin, 1998)
23. R.C. Hilborn, Einstein coefficients, cross-sections, F values, dipole-moments, and all that. Am. J. Phys. **50**(11), 982–986 (1982)

24. C. Liedenbaum, S. Stolte, J. Reuss, Multi-photon excitation of a beam of SF6 molecules pumped and probed by CW CO2 lasers. Chem. Phys. **122**(3), 443–454 (1988)
25. L.B.F. Juurlink et al., Eigenstate-resolved studies of gas-surface reactivity: CH4 (nu(3)) dissociation on Ni(100). Phys. Rev. Lett. **83**(4), 868–871 (1999)
26. R.N. Zare, *Angular Momentum: Understanding Spatial Aspects in Chemistry and Physics* (Wiley, New York, 1988)
27. U. Fano, J.H. Macek, Impact excitation and polarization of emitted light. Rev. Mod. Phys. **45**(4), 553–573 (1973)
28. C.H. Greene, R.N. Zare, Photonization-produced alignment of CD. Phys. Rev. A **25**(4), 2031–2037 (1982)
29. C.H. Greene, R.N. Zare, Photofragment alignment and orientation. Annu. Rev. Phys. Chem. **33**, 119–150 (1982)
30. A.J. Orr-Ewing, R.N. Zare, Orientation and Alignment of Reaction Products. Annu. Rev. Phys. Chem. **45**(1), 315–366 (1994)
31. D. Dill, Angular- distributions of photoelectrons from H2-effects of rotational autoionization. Phys. Rev. A **6**(1), 160 (1972)
32. D. Dill, U. Fano, Parity unfavoredness and distribution of photofragments. Phys. Rev. Lett. **29**(18), 1203 (1972)
33. U. Fano, D. Dill, Angular-momentum transfer in theory angular-distributions. Phys. Rev. A **6**(1), 185–192 (1972)
34. E.D. Poliakoff et al., Polarization of fluorescence following molecular photo-ionization. Phys. Rev. Lett. **46**(14), 907–910 (1981)
35. W.R. Simpson, A.J. Orrewing, R.N. Zare, State-to-state differential cross-sections for the reaction Cl((2)P(3/2)) + CH4(nu − 3 = 1, J = 1)–]HCL(nu' = 1, J') + CH3. Chem. Phys. Lett. **212**(1–2), 163–171 (1993)
36. W.R. Simpson et al., Reaction of Cl with vibrationally excited CH4 and CHD3 - state-to-state differential cross-sections and steric effects for the HCl product. J. Chem. Phys. **103**(17), 7313–7335 (1995)
37. W.R. Simpson et al., Picturing the transition-state region and understanding vibrational enhancement for the Cl + CH4 - > HCl + CH3 reaction. J. Phys. Chem. **100**(19), 7938–7947 (1996)
38. J.P. Camden et al., Comparing reactions of H and Cl with C-H stretch-excited CHD3. J. Chem. Phys. **124**(3), (2006)
39. E.H. Van Kleef, I. Powis, Anisotropy in the preparation of symmetric top excited states I. One-photon electric dipole excitation. Mol. Phys. **96**(5), 757–774 (1999)
40. S.E. Choi, R.B. Bernstein, Theory of oriented symmetrical-top molecule beams – precession degree of orientation, and photofragmentation of rotationally state-selected molecules. J. Chem. Phys. **85**(1), 150–161 (1986)
41. S. Stolte et al., Analysis of the steric dependence of the CH3I + Rb reaction using a Legendre expansion technique. Chem. Phys. **71**(3), 353–361 (1982)
42. R.N. Zare, Optical preparation of aligned reagents. Berichte Der Bunsen-Gesellschaft-Phys. Chem. Chem. Phys. **86**(5), 422–425 (1982)

Chapter 4
State-Resolved Steric Effects in Methane Chemisorption on Ni(100)

4.1 Introduction

Our experiment is designed to probe steric effects in a gas-surface reaction. In this chapter, I present results for the study of $CH_4(v_3 = 1)$ and $CD_3H(v_1 = 1)$ reactivity on Ni(100). We exploit the linear polarization of the excitation laser to align the excited molecule's angular momentum $(\vec{J})$ and vibrational dipole moment $(\vec{\mu}_{21})$ to probe the dynamical stereochemistry of vibrationally excited methane chemisorption on a Ni(100) surface. An explanation of how the alignments are produced and quantified is given in Chap. 3 of this thesis.

Ni(100) was chosen for this study because it is the surface that has been studied in most detail using quantum state-resolved techniques [1–4]. The crystal structure of nickel is face-centered cubic (fcc) symmetry with a lattice parameter of a = 3.52 Å. The Ni(100) surface has nearest-neighbor atom spacing of 2.49 Å (center-to-center). Figure 4.1 shows a model of an fcc lattice and Ni(100) surface which corresponds to one of the lattice faces.

Figure 4.2 is a low energy electron diffraction (LEED) pattern of the Ni(100) crystal used in the experiments presented here. Our nickel single crystal sample is cut to within 0.1° of the (100) plane. The LEED pattern in Fig. 4.2 was taken after a typical cleaning cycle and confirms the 100 surface structure of the Ni sample.

4.2 $CH_4(v_3 = 1)$ Reactivity and Alignment Effects on Ni(100)

The antisymmetric stretch (v_3) of CH_4 is the triply degenerate infrared active C–H stretch normal mode (F_2 symmetry) with a band origin at 3018.825 cm^{-1}. We prepared $CH_4(v_3 = 1)$ by IR-excitation with linearly polarized light via the R(0), R(1), Q(1) and P(1) transitions to produce varying degrees of molecular

B. L. Yoder, *Steric Effects in the Chemisorption of Vibrationally Excited Methane on Nickel*, Springer Theses, DOI: 10.1007/978-3-642-27679-8_4,

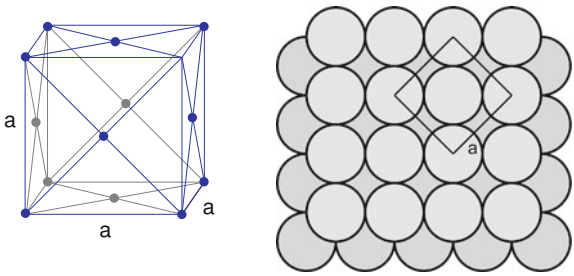

Fig. 4.1 Model of an fcc-lattice with lattice parameter (a) and a Ni(100) surface with unit cell shown by *square*, length $a = 3.52$ Å

Fig. 4.2 LEED pattern of a clean Ni(100) acquired using a 103 eV electron beam energy [5, 6]

Table 4.1 $CH_4(v_3)$ transitions used in this thesis to probe steric effects in vibrationally excited methane chemisorption

$CH_4(v_3)$ transition	cm^{-1}
R(0)	3028.752
R(1)	3038.498
Q(1)	3018.824
P(1)	3009.011

alignment in the laboratory frame. Table 4.1 gives the transition frequencies [7] for rovibrational transitions of $CH_4(v_3 = 1)$ used in the experiments.

To determine if steric effects occur in the dissociative chemisorption of $CH_4(v_3 = 1)$, we probe if the methane reactivity depends on the polarization direction of the excitation laser relative to the surface plane. To quantify this polarization dependence, we compared pairs of $CH_4(v_3 = 1, J)$ molecular beam

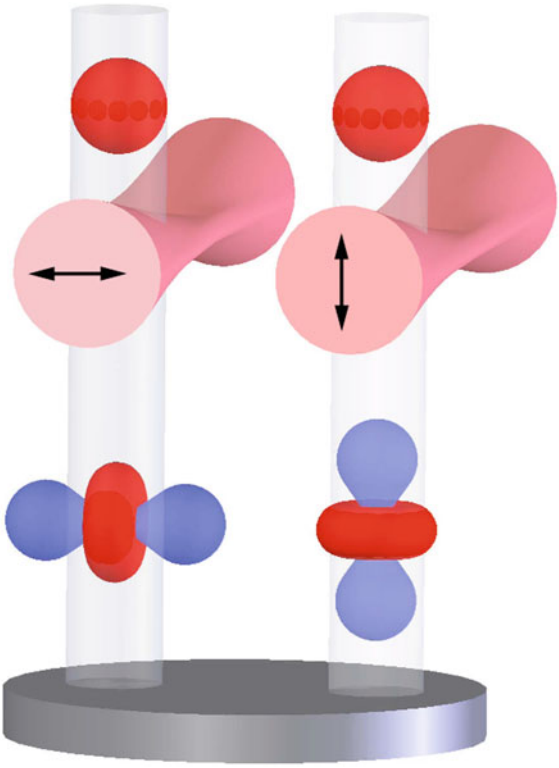

Fig. 4.3 Cartoon depiction of the alignment probability distributions produced in vibrationally excited methane by R(0) excitation. A ground state methane molecule without alignment (*red sphere*) in the molecular beam is incident on a Ni(100) surface. Prior to collision with the surface, the methane molecule traverses a laser beam focused in the direction of the molecular beam which rovibrationally excites and aligns the molecule 1 mm from the surface. The polarization direction is shown by *double-headed arrows*. Following excitation via the R(0) transition, the molecule's vibrational amplitude (*blue dumbbell*) is aligned preferentially along the laser's polarization and its $\overrightarrow{J}$ (*red torus*) is aligned perpendicular to the laser's polarization [8]

depositions on Ni(100) where the direction of the laser polarization with respect to the Ni-surface plane is changed from parallel to normal (or vice versa).

A typical deposition experiment for the study of state-resolved steric effects in chemisorption is depicted in Fig. 4.3. It shows a molecular beam of ground state methane molecules without alignment (red sphere) incident on a single crystal metal surface. In the molecular beam, most methane molecules are in their ground electronic and vibrational states and occupy the lowest rotational state of each of the three nuclear spin isomers (I = 2 (meta) $J = 0$, I = 1 (ortho) $J = 1$, and I = 0 (para) $J = 2$) with isotropic M-level populations. Prior to collision with the surface, the methane molecules traverse a continuous laser field (shown in red coming out of the page) locked resonant to a rovibrational transition which prepares it in a specific quantum state ($v_3 = 1$, $J = 0$, 1, 2). The excitation simultaneously aligns the rovibrationally excited molecule due to the $\Delta M = 0$ selection rule for infrared excitation by linearly polarized light. Figure 4.3 shows the case of R(0) excitation as an example because it leads to the highest degree of alignment in the laboratory frame. Upon excitation, the vibrational transition dipole is aligned preferentially along the polarization direction indicated by the double-headed arrow and its $\overrightarrow{J}$ distribution is aligned preferentially perpendicular to this axis. The laser beam width is 1.4 mm in the molecular beam direction at the crossing point. Typically,

the center of the excitation to surface distance is 1 mm resulting in a time delay of 500 nsec between excitation and surface impact for a molecular beam speed of 2000 m/s. Most of the experiments discussed in this chapter used a molecular beam velocity of approximately 2000 m/s (translational energy $\sim$34 kJ/mol) directed normal to the surface.

4.2.1 Independence of Excitation Efficiency Upon Polarization Rotation

To compare the reactivity of excited molecules as a function of laser polarization angle, we must be sure that the rotation of the excitation's polarization does not cause a change in the number of excited molecules in the molecular beam. This can be demonstrated by monitoring the fraction of excited molecules produced by the excitation with a pyroelectric detector, assuming that there is no collisional alignment of methane in the molecular beam. If the pyroelectric detector signal remains constant as the laser polarization is rotated, the excitation efficiency is independent of the polarization angle. Also, excitation via the P(1) transition which can cause no alignment can serve as a check if rotating the polarization causes a change in reactivity by an effect other than alignment. Both the pyroelectric detector and P(1) excitation tests are presented in this chapter as proof that the observed alignment dependence of the methane reactivity is free from experimental artifacts.

Between molecular beam depositions, the laser polarization is rotated 90° by a $\lambda/2$ waveplate. A small displacement of the laser beam could arise during polarization rotation if the excitation laser's propagation axis is not parallel to the rotation axis of the waveplate. Any displacement could alter the overlap of the excitation with the molecular beam and change the excited state population. To ensure that there is no polarization dependence in the excited state population, we use the lock-in detected pyroelectric detector measurement, as described in Sect. 2.6.

Figure 4.4 shows that the excited fraction prepare by laser excitation is independent of the laser polarization direction. The data in Fig. 4.4 was generated by excitation of $CH_4(v_3)$-R(0) with the excitation laser modulated at 2.75 Hz with a 50% duty cycle via an electromechanical shutter (Uniblitz). The modulated signal from vibrationally excited molecules in the molecular beam is collected with a pyroelectric detector and amplified 95$\times$ via a home-built amplifier. This amplified signal was fed into the lock-in amplifier, using a 500 mV sensitivity setting and 300 ms time constant. The 'R' analog output (R, θ mode of lock-in) of the lock-in amplifier was collected by a 12-bit analog-to-digital converter using Labview software.

The pyroelectric signal is collected first while rotating the laser polarization from horizontal to vertical in 90 s with a motorized rotation optical mount (rotation rate of $1°s^{-1}$), shown in Fig. 4.4(a). Then, with the excitation polarization fixed vertically, we continue to collect the pyroelectric signal for 90 s (4.4(b)) to monitor the signal stability.

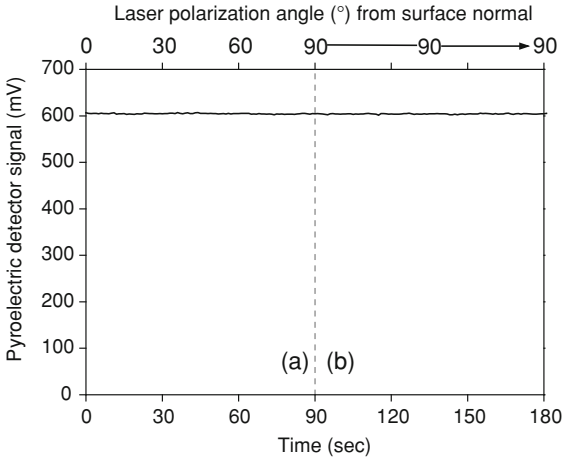

Fig. 4.4 Pyroelectric signal of a 34 kJ/mol molecular beam of $CH_4(v_3)$ excited via R(0)

Comparison of the pyroelectric detector signals from the 'rotating' and 'stationary' waveplate (Fig. 4.4(a) and (b), respectively) shows that there is no effect of rotating the laser polarization via the waveplate. During the waveplate rotation, Fig. 4.4(a), the pyroelectric signal varied between 602.5 and 607.0 mV with a mean value of 605.0 mV and standard deviation of 0.9 mV. When the waveplate was stationary, Fig. 4.4(b), the pyroelectric signal varied between 601.6 and 606.0 mV with a mean value of 604.1 mV and standard deviation of 0.8 mV. Before every series of molecular beam depositions, the pyroelectric measurement of the extent of excitation as a function of polarization angle is used to verify that the excitation laser is well aligned on the molecular beam.

It is worth noting that the lock-in detected pyroelectric detector signal has a signal to noise ratio of 140 for this measurement. The high signal to noise ratio of the pyroelectric measurements allows for detection of relatively small excited state populations in the molecular beam, as is the case when using dilute gas mixtures of methane or exciting from sparsely populated ground states.

4.2.2 Polarization Dependence of Vibrationally Excited Methane Reactivity

To ensure that the observed reactivity changes between deposition experiments are due only to the laser polarization direction, we always compare depositions done in the same run on the same clean Ni-surface. The deposition coordinates on the surface are alternated in a way to cancel out any potential local variations in surface reactivity of the nickel single crystal. We are able to deposit up to four molecular beam spots with a carbon footprint of 2 mm diameter each on a single clean Ni-surface of 10 mm diameter.

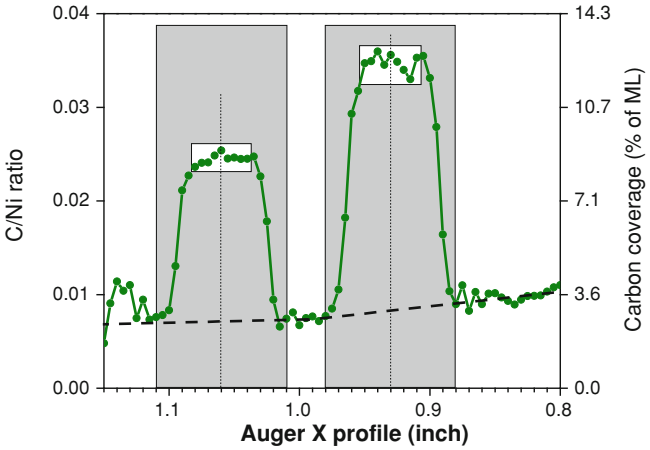

Fig. 4.5 Raw horizontal AES profile of a two spot deposition of a 34 kJ/mol molecular beam of $CH_4(v_3 = 1)$ excited via its R(0) transition

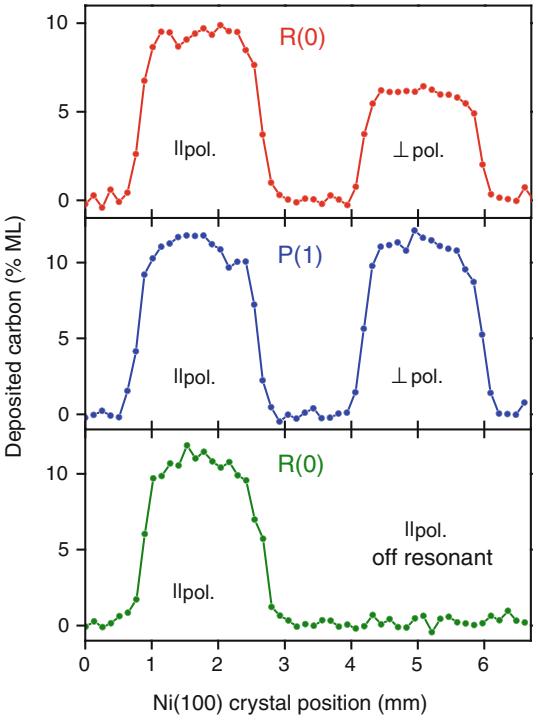

Fig. 4.6 AES profiles depicting deposited carbon after exposure of a clean Ni(100) surface to a 34 kJ/mol molecular beam of $CH_4(v_3)$ excited 1 mm from surface with the excitation polarization parallel (*left*) and perpendicular (*right*) to the surface plane. (*upper panel*) excited via R(0) transition. (*middle panel*) excited via P(1). (*lower panel*) left-excited via R(0), right- laser slightly detuned from R(0) transition frequency [8]

Quantum state-resolved reaction probabilities of methane on Ni(100) were measured using Auger electron spectroscopy (AES) detection of the surface bound carbon reaction product as described previously [8, 9]. AES 'profiles' were recorded by taking AES spectra in the region of the KLL transition of carbon, C, at 273 eV and the LMM transition of nickel, Ni, at 848 eV at different points along the surface. The amount of surface bound carbon product from the dissociation of methane on nickel is quantified by the C/Ni ratio which is used to guard against day-to-day experimental variations such as channeltron detector sensitivity degradation, the surface-to-electron gun distance and electron current drift. The C/Ni ratio signal for the specific settings used in our Auger spectrometer takes a value of 0.14 at saturation coverage of carbon on NI(100) which corresponds to a coverage of 0.5 monolayer (ML) [6, 10]. This information is used to calibrate the C/Ni ratio in units of 'percent of a ML' or %ML carbon coverage on Ni(100).

AES 'profiles' can be recorded in the horizontal (X) and vertical (Z) directions by moving the surface sample relative to the fixed Auger spectrometer by X and Z stepper motors under Labview control. Figure 4.5 shows a horizontal (X) AES profile (step size = 0.005 inch) of two carbon spots deposited on a Ni(100) surface by two 50 s exposures to a molecular beam produced from 12% CH_4 in H_2 at a backing pressure of 3 bar and a nozzle temperature of 50° C (CH_4 translational energy of 34 kJ/mol). The carbon footprint on the left of Fig. 4.5 was produced by a deposition of $CH_4(v_3)$-R(0) excited 1 mm from the surface using 860 mW of resonant excitation power with the laser polarized perpendicular the surface. The carbon footprint on the right of the figure was produced by identical experimental conditions as the footprint on the left except that the excitation's polarization axis was rotated to be parallel to the surface.

Below, I describe how the AES data is analyzed, using Fig. 4.5 as an example. The first step in the data analysis is a baseline subtraction of the C/Ni signal using a linear subtraction defined by three points: to the left, between and to the right of the two peaks. We usually observed a raising C/Ni baseline during an AES profile scan (from left to right of graph) which results from carbon deposition during the $\sim$40 min AES analysis by cracking and emission of carbon containing species from the Auger electron gun. Since this carbon is added after the carbon from the methane molecular beam exposure, it does not affect the reactivity of the Ni(100) during the molecular beam exposure and can simply be subtracted.

Next, the center of mass (COM) of each spot (in X) is determined inside an interval of 0.10 inch (gray rectangles in Fig. 4.5). Then, the COM (dotted line to X-axis in Fig. 4.5) is rounded to the nearest data point and an average value of the nine data points about the COM is tabulated (nine data points are highlighted by the white rectangle in Fig. 4.5). This nine point average is taken as the C/Ni signal for a given deposition. We limit the data analysis to nine points about the COM in order to avoid any edge effects which could result from an unknown molecular beam intensity profile or a decrease in laser intensity at the edge of the laser beam. Nevertheless, I have analyzed the data in Fig. 4.5 by integration of the C/Ni ratio of the entire footprint and obtained the same result to that found from the method outlined here.

The C/Ni signal is corrected for coverage dependent sticking probability (S/S_0) in order to take into account the decrease in methane sticking coefficient with increasing carbon coverage. As carbon builds up on the nickel surface, the reaction probability or sticking coefficient, S, decreases from $S = S_0$ for a clean surface to $S = 0$ at a saturation coverage. The coverage dependent sticking probability is assumed to be a linear function decreasing from $S/S_0 = 1$ at S_0 (zero carbon coverage) to $S/S_0 = 0$ at 50% ML carbon coverage. The C/Ni AES signal was calibrated for Ni(100) by recording an uptake curve of ethylene which leads to a saturation coverage of 50% of a monolayer [5]. The AES C/Ni signal is taken to vary linearly from zero to 0.14 at a carbon coverage of 50% of a monolayer. The S/S_0 correction for a deposition of 10% ML carbon coverage is therefore 0.90 from the average of initial and final S/S_0 corrections of $S/S_0 = 1$ and $S/S_0 = 0.80$, respectively. Typically, we deposit $\leq$10% ML, so the S/S_0 correction is usually between 0.90–0.95. The 'nine point average' C/Ni signal is divided by a deposition's averaged S/S_0 correction to account for the decreasing sticking probability with increasing carbon coverage.

The average C/Ni signal for each deposition is normalized to the measured molecular beam dose for the two deposition experiments. The flux of CH_4 ($m/z = 16$) in the molecular beam is monitored by a quadrupole mass spectrometer located in the UHV chamber but out of the molecular beam's line-of-sight. We determine the average CH_4 flux over an entire deposition and multiply it by the deposition time to determine the methane dose of each deposition. Then, all molecular beam doses in a series of depositions (up to four depositions for a cleaned Ni-crystal) are normalized to the first deposition in the series. This produces a 'relative dose' for the compared depositions. The S/S_0 corrected C/Ni signal is divided by the relative dose to correct for any dose differences between compared depositions. This difference in molecular beam dose between a pair of depositions is typically 0–3% due to a small variation in flux between the two depositions of the same time. This data analysis yields a measure of the gas-phase reagent's reactivity on the metal crystal that is proportional to $S_0^{\parallel}$ and $S_0^{\perp}$ the state-resolved, initial sticking coefficients for the excited state of methane prepared with laser polarization parallel and perpendicular to the surface, respectively.

Figure 4.6 (upper panel) shows the AES detected carbon coverage on Ni(100) after exposing the surface to two identical doses, in two different locations, of vibrationally excited CH_4 prepared via the v_3-R(0) transition. Comparison of the amount of carbon detected after identical depositions with laser polarization parallel ($\parallel$ pol.—left) and perpendicular ($\perp$ pol.—right) to the surface indicates that the CH_4 reactivity is nearly 60% higher for parallel than perpendicular alignment. The observed alignment effect is quantified by calculating the *alignment contrast* Δ_p, which is defined as:

$$\Delta_p = \frac{S_0^{\parallel} - S_0^{\perp}}{S_0^{\parallel} + S_0^{\perp}} \tag{4.1}$$

Δ_p can take values from +1 (if $S_0^{\parallel} \gg S_0^{\perp}$) to −1 (if $S_0^{\perp} \gg S_0^{\parallel}$). $\Delta_p = 0$ signals the absence of an alignment effect. Based on nine repeated measurements, we find $\Delta_p = 0.216 \pm 0.025$ (or $S_0^{\parallel} = 1.55 \times S_0^{\perp}$) for excitation of the v_3-R(0) transition of CH_4.

In order to ascertain that the observed reactivity difference is due solely to alignment of vibrationally excited methane, we repeated the corresponding pair of deposition experiments exciting the v_3-P(1) transition for which no alignment of the laser excited molecules is expected [11] since this transition populates the only possible M = 0 levels of the excited $J = 0$ state. No significant difference in the state-resolved $CH_4(v_3)$-P(1) reactivity was observed between parallel and perpendicular laser polarizations ($\Delta_p = 0.016 \pm 0.029$), confirming the interpretation of the reactivity difference as being due to an alignment effect of the incident laser excited methane. As mentioned in Sect. 4.2.1, this result is a clear confirmation that there are no experimental artifacts such as a change in laser power or a beam displacement caused by the waveplate rotation which could affect the amount of deposited carbon via a change in the number of excited methane molecules in the beam.

The large difference in reactivity between $CH_4(v = 0)$ ($S_0 = 1 \times 10^{-6}$) [1, 2] and $CH_4(v_3 = 1)$ ($S_0 = 2.5 \times 10^{-4}$ [12]) combined with the large excited fraction prepared by RAP ensures that essentially all the carbon detected is due to the state-prepared $CH_4(v_3 = 1)$. We experimentally verified that the detected carbon is formed exclusively by the chemisorption of vibrationally excited methane and that passing the up to 1 W laser beam close to the target surface does not have a detectable effect on the carbon deposition. This was done by repeating the deposition experiment with the excitation laser slightly detuned from resonance with the R(0) transition. With the laser detuned, no increase in the carbon signal compared to the laser-off baseline was detected where the molecular beam was incident on the Ni(100) surface. Figure 4.6 (lower panel) confirms that the contribution from $CH_4(v = 0)$ and thermally vibrationally excited states of methane to the detected surface carbon for the laser-on experiments is negligible for 34 kJ/mol translation energy.

4.2.3 *Effect of Hyperfine Depolarization on $CH_4(v_3)$-R(0) Reactivity*

By changing the excitation-to-surface distance, we can experimentally observe to what extent dephasing of the initially prepared alignment might reduce the observed steric effects. In the presence of nuclear spin angular momentum ($\vec{I}$), the angular momentum ($\vec{J}$) alignment prepared by optical pumping dephases with time due to coupling the nuclear spin (I), which is left randomly oriented during the dipole allowed transition. The aligned $\vec{J}$ couples to randomly oriented $\vec{I}$ to form the total

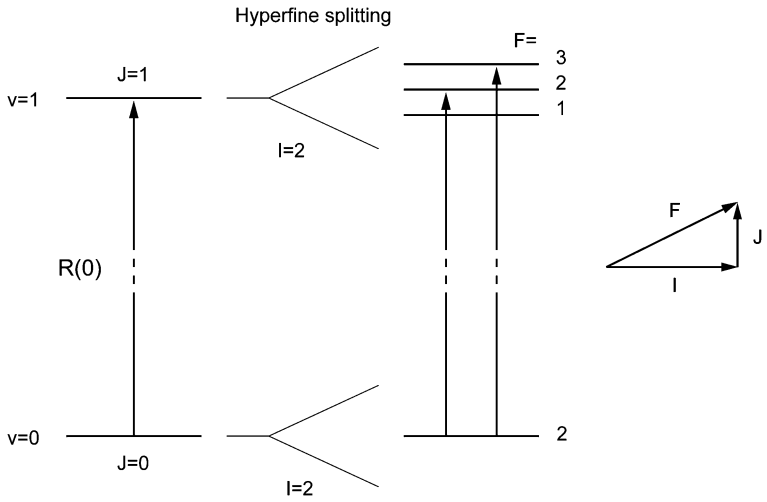

Fig. 4.7 Schematic of the hyperfine splitting in the v = 0, $J = 0$ and v = 0, $J = 1$ levels of $CH_4(v_3)$

angular momentum vector $\overrightarrow{F}$ (where F = $I + J$, $I + J - 1$, …, $I - J$) which is a conserved quantity for an isolated molecule [13]. I show a simple schematic of the vector addition of $\overrightarrow{J}$ and I to form F in Fig. 4.7. In the vector model, the coupled $\overrightarrow{J}$ and $\overrightarrow{I}$ vectors are said to precess about $\overrightarrow{F}$, and it is the precession of $\overrightarrow{J}$ about $\overrightarrow{F}$ that dephases the alignment produced during the excitation. This dephasing of the alignment is termed hyperfine depolarization since it is due to a molecule's hyperfine structure, resulting from the interaction of the electron distribution with the magnetic moment of the nuclei. In the absence of stray magnetic fields, the alignment should periodically rephase. There has been significant work regarding hyperfine depolarization of molecular alignment produced by optical pumping methods [14–18].

A CH_4 molecule has four identical hydrogen nuclei, each with I = ½. Vector addition of the four nuclear spins yields three possible spin isomers for a CH_4 molecule: meta-methane (I = 2), ortho-methane (I = 1) and para-methane (I = 0). A detailed explanation of the spin isomers and their allowed rotational energy levels is given in a thesis from our group by Maroni [6]. Meta-, ortho- and para-methane populate separate rotational ground states of $J = 0$, 1 and 2, respectively, at the cold ($\sim$10 K) rotational temperatures of the molecular beam. Therefore, no hyperfine depolarization is expected if I = 0 para-methane were excited/aligned. Unfortunately, the ground state of para-methane is v = 0, $J = 2$. Molecular alignment coefficients for the R-branch transition from $J = 2$ ($\beta_{axis} = 0.333$) are significantly lower than those from $J = 0$,1 ($\beta_{axis} = 2.0$ and 0.635, respectively).

To detect the effect of hyperfine depolarization, I prepared $CH_4(v_3 = 1)$ via R(0), the transition which creates the highest degree of alignment. This transition

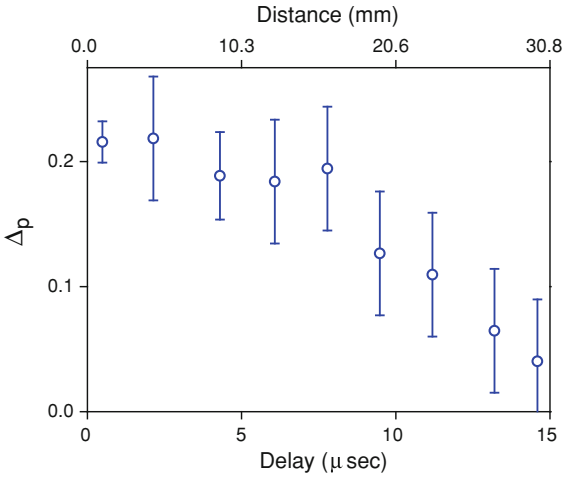

Fig. 4.8 Experimental measurement of the dephasing time for the initially prepared alignment for $CH_4(v_3)$-R(0) [8]. Error bars represent $\pm 2\sigma$ of up to 9 measurements

excites meta-methane (I = 2) from v = 0, $J = 0$ to a state with $v_3 = 1$ and $J = 1$. The homogeneous linewidths of the rovibrational transitions in our experiment are determined by transit time broadening to 0.5–1.5 MHz (molecular beam velocities of 1000–2900 m/s). RAP coherently excites transitions to multiple hyperfine levels of the upper-state J which are split by 50–90 kHz [19] at t = 0 when the methane molecules pass through the excitation laser beam. Following excitation, hyperfine depolarization will dephase the initially prepared alignment since the hyperfine transitions are not resolved by the rovibrational excitation but excited simultaneously and coherently in our setup.

Figure 4.7 shows a schematic of the hyperfine level splitting of the R(0) transition in $CH_4(v_3)$ [20]. The J-level of the ground and excited state is split by the coupling of $\overrightarrow{J}$ and $\overrightarrow{I}$ to form $\overrightarrow{F}$, as described above. Since $J \leq$ I, the J-level is split by nuclear spin into $(2J + 1)$ components [13]. I have displayed the strongest individual hyperfine transitions ($\Delta F = \Delta J$ [21] and $\Delta F = 0$ [19]) occurring for the excitation of $CH_4(v_3)$-R(0).

Figure 4.8 shows the effect of varying the excitation-to-surface distance which effectively changes the time delay between coherent excitation and reaction for a 34 kJ/mol (2056 m/s) molecular beam of $CH_4(v_3)$-R(0) on Ni(100). Following the excitation at t = 0, the interaction between methane's randomly oriented nuclear spin and the aligned angular momentum $(\overrightarrow{J})$ leads to hyperfine depolarization on a time-scale of the inverse of methane's hyperfine level splittings [16, 17].

As shown in Fig. 4.8, the alignment dephasing of $CH_4(v_3)$-R(0) is on a time-scale of $\sim$15 μs by measuring Δ_p for excitation of the R(0) transition in a 2056 m/s molecular beam at distances between 1 mm and 30 mm from the target surface. This alignment dephasing timescale is consistent with the hyperfine splitting observed by Hall and Bordé [19]. Using Doppler-free saturation spectroscopy of the $CH_4(v_3)$-P(7) transition (I = 1), they resolved hyperfine splittings of +59.2 and −89.5 kHz in the

vibrationally excited state, and splittings of +70.3 and −100.9 kHz in the ground state. Extrapolation of the measured hyperfine decay of Δ_p shown in Fig. 4.8 towards t = 0 predicts an insignificant alignment reduction for excitation 1 mm from the surface (delay of ∼500 ns for a v = 2000 m/s molecular beam) compared to a hypothetical preparation occurring directly on the surface.

A strong influence of stray magnetic fields on measured Δ_p values was excluded by the observation of no significant change in Δ_p when a strong permanent magnet was placed in the vicinity of the laser/molecular beam interaction region.

One would expect to be able to see a rephasing of the produced alignment, but our experimental setup is limited to a maximum excitation-to-surface distance of ∼30 mm. It might be possible to observe alignment rephasing in $CH_4(v_3)$-R(0) using a slow (<1000 m/s) methane beam.

As mentioned above, the preparation of $CH_4(v_3 = 1, J = 3)$ via the R(2) transition would not suffer from hyperfine depolarization effects. I show in Sect. 4.2.6 that we can selectively excite para-methane (I = 0) via an R(2) transition at 3048.1690 cm^{-1}. There is sufficient para-methane populating the $v = 0, J = 2$ state in the molecular beam to do state-resolved reactivity measurements. Even though the calculated alignment coefficients are small for this transition ($\beta_{axis} = 0.333$), it would be interesting to perform alignment dependent, state-resolved reactivity measurements using this transition because they could serve as an experimental test of the assumption that hyperfine depolarization is, indeed, negligible during the hundreds of nanoseconds delay between excitation and surface collision.

4.2.4 Comparison of Δ_p and Calculated Alignment Coefficients for $CH_4(v_3)$

In Chap. 3, I tabulated and discussed the alignment coefficients $A_0^{(2)}$ and β_{axis} which quantify the degree of alignment of the angular momentum ($\vec{J}$) and vibrational transition dipole moment (net vibrational amplitude), respectively. The alignment coefficients depend on the transition used for excitation. To explore the origin of the alignment dependent surface reactivity of methane, we experimentally determined Δ_p for excitation of $CH_4(v_3)$ via the -R(0), -R(1), -Q(1) and -P(1) transitions. By comparing Δ_p to the calculated $A_0^{(2)}$ and β_{axis} coefficients for these four transitions, we are able to determine whether the alignment dependent reactivity is due to an alignment of $\vec{J}$ or $\vec{\mu}_{21}$ relative to the surface.

Figure 4.9a shows the calculated $\vec{J}$ alignment coefficients $A_0^{(2)}$ of four $CH_4(v_3)$ transitions compared to experimentally determined Δ_p values for $CH_4(v_3)$ dissociation on Ni(100) [8]. The two vertical axes of the graph are scaled such that their origins and the values for Δ_p and $A_0^{(2)}$ coincide for R(0) excitation. Inspection of the $A_0^{(2)}$ alignment coefficients shows that the sign of $A_0^{(2)}$ changes from negative to positive in switching from R-branch to Q-branch transitions. The physical meaning

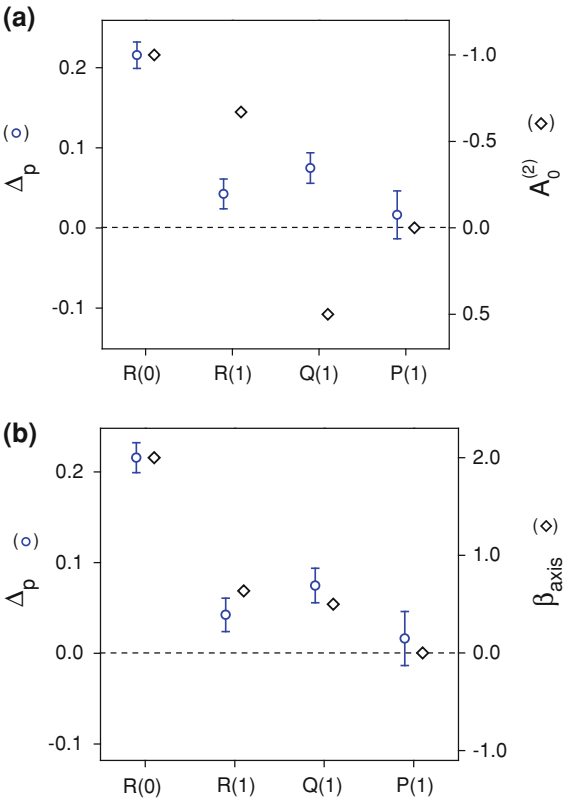

Fig. 4.9 **a** Comparison of Δ_p for $CH_4(v_3)$ excited via the indicated transitions to the corresponding calculated $\vec{J}$ alignment coefficients $\left(A_o^{(2)}\right)$ [8]. Error bars represent $\pm 2\sigma$ from repeated measurements, **b** Comparison of Δ_p for $CH_4(v_3)$ excited via the indicated transitions to the corresponding calculated vibrational transition dipole moment alignment coefficients (β_{axis}) [8]. Error bars represent $\pm 2\sigma$ from repeated measurements

of this sign change in $A_0^{(2)}$ is a change in the $\vec{J}$ alignment from perpendicular to the linear polarization axis (the quantization axis) of the laser for R-branch excitation to parallel to the quantization axis for Q-branch excitation. This change in sign of the $A_0^{(2)}$ coefficient is a consequence of the selection rules for excitation of the R- and Q-branch transitions. Specifically, the R(0) transition prepares a state where $J = 1$, $M = 0$, while the Q(1) transition prepares a state where $J = 1$, $M = \pm 1$. Since M is defined as the projection of $\vec{J}$ onto the quantization axis (here, the polarization axis of the laser radiation), it is clear that R(0) excitation prepares a state with $\vec{J}$ aligned perpendicular to the laser's polarization axis (as $\vec{J}$ has a projection of zero onto the quantization axis), while Q(1) excitation prepares a state with $\vec{J}$ aligned preferentially parallel to the laser's polarization axis (having a large projection of $\vec{J}$ onto the quantization axis). If the alignment dependent reactivity were due to alignment of $\vec{J}$ in the laboratory frame, one would expect Δ_p to change sign when changing from R- to Q-branch excitation. This sign change is not observed in the data.

Figure 4.9b shows the calculated vibrational transition dipole moment (or net vibrational amplitude) alignment coefficients β_{axis} of four rovibrational transitions to prepare $CH_4(v_3)$ for the case of strong pumping versus experimentally determined Δ_p for each transition [8]. The vertical axes of the graph are scaled such that the origins and the values for Δ_p and β_{axis} coincide for R(0) excitation.

Inspection of calculated β_{axis} alignment coefficients in Fig. 4.9(b) shows that the sign of β_{axis} remains positive for both R- and Q-branch transitions. The positive β_{axis} alignment coefficients signify a preferential alignment of the vibrational transition dipole moment (or net vibrational amplitude) parallel to the polarization axis of the excitation laser for both R- and Q-branches. The fact that Δ_p does not change sign (larger reactivity always for parallel polarization for R(0), R(1) and Q(1)), leads to the conclusion that the observed alignment effect is dominated by an alignment of the vibrational transition dipole moment or net vibrational amplitude rather than $\vec{J}$ alignment. For all transitions excited (except P(1), where $\Delta_p = 0$), a higher reactivity is observed for molecules having their $\vec{\mu}_{21}$ or net vibrational amplitude aligned parallel to the surface rather than perpendicular to it. These results are similar to the findings of Zare et al. for the reaction of $CH_4(v_3)$ and $CD_3H(v_1)$ with Cl atoms [22], as discussed in Chap. 1.

4.2.5 Detailed Polarization Angle Dependence of the $CH_4(v_3)$-R(0) Reactivity

Since a clear difference in $CH_4(v_3)$ reactivity between aligning the vibration parallel and perpendicular to the Ni(100) surface was observed, there must exist an alignment angle of the vibration with respect to the surface that is the most efficient at promoting methane dissociation. To obtain the detailed polarization angle dependence of the alignment effect, we measured the reactivity for $CH_4(v_3)$-R(0) excitation at several intermediate polarization angles in addition to 0° (∥-pol) and 90° (⊥-pol) measurements. Figure 4.10 shows the results of these measurements [8]. The angle dependent reactivity exhibits a monotonic decrease from parallel to perpendicular polarization.

The reactivity data at intermediate angles (15–75°) can be predicted from the measured reactivities for parallel and perpendicular alignment $S_0^{\parallel}$ and $S_0^{\perp}$ by a simple geometric model. At any angle θ with respect to the surface plane, the angle dependent reactivity $S_0(\theta)$ is assumed to be composed of a parallel and perpendicular reactivity contributions given by $S_0^{\parallel}\cos\theta$ and $S_0^{\perp}\sin\theta$, respectively. The vector addition of the two components gives $S_0(\theta)$ as a function of $S_0^{\parallel}$, $S_0^{\perp}$ and θ:

$$S_0(\theta) = \sqrt{\left(S_0^{\parallel}\right)^2 - \sin^2\theta \cdot \left[\left(S_0^{\parallel}\right)^2 - \left(S_0^{\perp}\right)^2\right]} \tag{4.2}$$

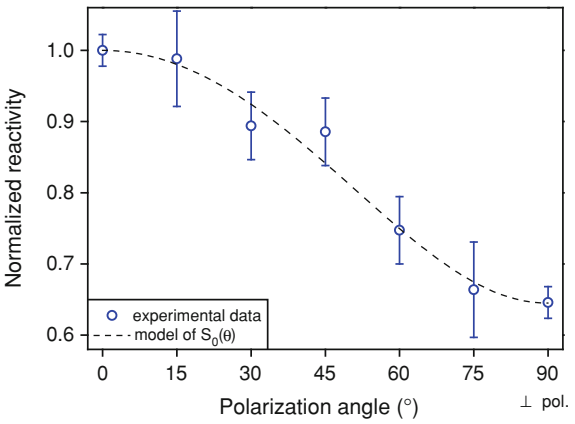

Fig. 4.10 Effect of rotating the excitation polarization on the reactivity for a 34 kJ/mol kinetic energy beam of $CH_4(v_3)$-R(0). The measured reactivities are normalized to the II-polarization reactivity [8]. Error bars represent $\pm 2\sigma$ from repeated measurements

Using the normalized reactivity of $S_0^{\parallel} = 1$ and $S_0^{\perp} = 0.645$ found for $CH_4(v_3)$-R(0) from repeated measurements, I calculate $S_0(\theta)$ using Eq. 4.2 as function of θ. Dashed line in Fig. 4.10). The measured normalized reactivities at the intermediate polarization angles agree with this functional form of $S_0(\theta)$.

To understand this angular dependence of reactivity, we must consider the alignment produced in the excited molecule. $CH_4(v_3)$ has four identical C–H bonds which share the antisymmetric stretch-excitation. The R(0) excitation prepares $CH_4(v_3)$ in a state with $N = 0$, $L = 1$, and $J = 1$ [22]. Here, N and L designate the rotational and vibrational angular momentum, respectively. J is the sum of N and L. Due to the $\Delta N = 0$ selection rule, the state of $CH_4(v_3)$ prepared by R(0) excitation is rotationless ($N = 0$). This means it is characterized by a spatially isotropic rotational wave function for which any orientation of the hydrogen atoms is equally probable. Only the C–H stretch net vibrational amplitude, given by the vibrational transition dipole moment direction, is aligned in space by the laser excitation. Therefore, the angular dependence of $CH_4(v_3)$ reactivity on a surface does not reflect an angular dependence of aligned C–H bond axes relative to some lowest energy transition state geometry.

A classical mechanics analog for this vibrational state would be a vibrating ellipsoid. The four H-atoms of CH_4 can be thought of as located at some unknown position on the surface of the ellipsoid. Figure 4.11 shows a cartoon depiction of $CH_4(v_3)$-R(0) excited with linearly polarized light parallel (left) and perpendicular (right) to the surface. The methane molecules are shown in the figure for clarity, but display only one of the possible H-atom configurations on the surface of the vibrating ellipsoid.

The ellipsoid oscillates back and forth along its principle axis which is parallel to the excitation's polarization direction [22]. Therefore, the alignment of net vibrational amplitude is controlled in the laboratory frame, but no information regarding the orientation or alignment of the four C–H bonds is available.

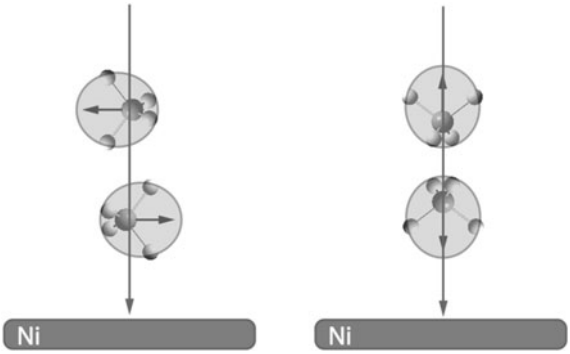

Fig. 4.11 Cartoon depiction of $CH_4(v_3)$ impinging on a nickel surface with its net vibrational amplitude directed parallel (*left*) and perpendicular (*right*) to the surface

4.2.6 Absolute Sticking Coefficients of $CH_4(v_3)$-R(0) on Ni(100)

I have calculated the initial reaction probabilities or initial sticking coefficients, $S_0(v_3)$, for the dissociative chemisorption of $CH_4(v_3 = 1)$ on Ni(100). If all of the carbon on the surface after a molecular beam deposition is due to the dissociation of $CH_4(v_3)$ prepared by the laser excitation, the general formula for the calculation of the vibrationally excited state sticking coefficient in the limit of zero coverage is:

$$S_0(v_3) = \frac{N_{\text{adsorbed}}}{N_{\text{excited}}}. \tag{4.3}$$

In the above expression, N_{adsorbed} is the number of carbon atoms absorbed on the surface after a deposition experiment and N_{excited} is the number of rovibrationally excited methane molecules in the molecular beam impinging on the surface. For the CH_4 dissociation on Ni(100) system, the ground state sticking coefficient, $S_0^{v=0}$, is negligible in comparison to $S_0(v_3)$ for the molecular beam translational energies presented in this section. This assertion comes from published sticking coefficients of $CH_4(v_3 = 1)$ dissociation on Ni(100) [1] and was experimentally verified using our setup. For a molecular beam with translational energy of 49 kJ/mol, $S_0(v_3)$ is approximately $200_0^{v=0}$. As the translational energy of the molecular beam decreases, the disparity between $S_0(v_3)$ and $S_0^{v=0}$ increases. Extensive explanations of the $S_0(v_3)$ calculation are given in previous works from our group [2, 5, 6].

For the calculation of $S_0(v_3)$, one must determine N_{excited}, where $N_{\text{excited}} = F_{\text{Total}} \cdot P_J^{v=0} \cdot f_{\text{exc}}$. Here, F_{Total} is the total dose of methane during a molecular beam deposition. $P_J^{v=0}$ is the initial (ground state) rovibrational population. f_{exc} is the fractional excitation of a transition in the molecular beam, meaning the fraction of molecules from a given ground state that are excited to a corresponding rovibrational level by resonant infrared pumping. In practice, F_{Total} is determined by monitoring the methane mass spectrum signal (m/z = 16) during the deposition, and comparing it to a calibration standard as explained in Chap. 2. I assume the fractional excitation, f_{exc}, equal to 1 for all allowed M-level transitions excited for

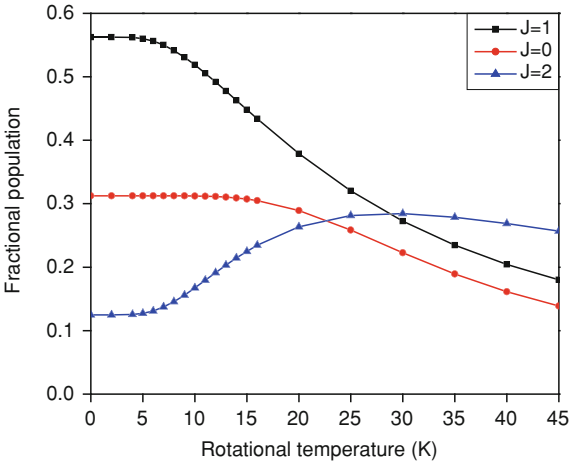

Fig. 4.12 Fractional J-level population in ground vibrational state of CH_4 as a function of temperature

a given P-, Q-, R-branch transition due to complete population inversion of a given ground state by rapid adiabatic passage (see Chap. 3). Assuming an isotropic M-level distribution for a given initial J-state, f_{exc} becomes the number of allowed M-level transitions (dictated by the selection rules for P-, Q-, and R-branch transitions) divided by the number of M-levels in the ground rovibrational state (M″). For example, any R-branch transition connects all M″ to the excited state, so $f_{exc} = 1$. However, P-branch transitions produce an f_{exc} of (M″−2)/M″, or $f_{exc} = 0.33$ for P(1) excitation. Q-branch transitions produce an f_{exc} of (M″−1)/M″, or $f_{exc} = 0.66$ for Q(1) excitation. See Chap. 3 for a discussion of allowed transitions in the P-, Q- and R-branch excitations via linearly polarized radiation.

The population of the rotational states J in the ground vibrational state, $P_J^{v=0}$, is a function of the rotational cooling in the supersonic expansion. Given a rotational temperature of the beam, the populations can be calculated using the nuclear spin statistics of CH_4, the rotational degeneracies and the energy level spacings. The fractional population of a rotational level J at a given temperature can be calculated by the summation of the fractional populations of each spin isomer contributing to that J-level.

Figure 4.12 shows the fractional population for v = 0, $J = 0$, 1 and 2 of CH_4 as a function of rotational temperature. This plot was generated using a model calculation [6] that considered the five lowest rotational levels. As mentioned in Sect. 4.2.4, CH_4 has four identical hydrogen nuclei, each with nuclear spin of ½. Three spin isomers are present: nuclear spin (I) of 2, 1 and 0 which are termed meta-, ortho- and para-methane, respectively. Due to the lack of interconversion between the three spin species [23], they can be treated as three separate types of molecules that cool during a jet expansion to three different sets of rotational levels due to their symmetries. The $J = 0$ rotational level can only be occupied by meta-methane (I = 2). The $J = 1$ level can only be populated by ortho-methane (I = 1), and $J = 2$ by ortho- and para- (I = 0) methane.

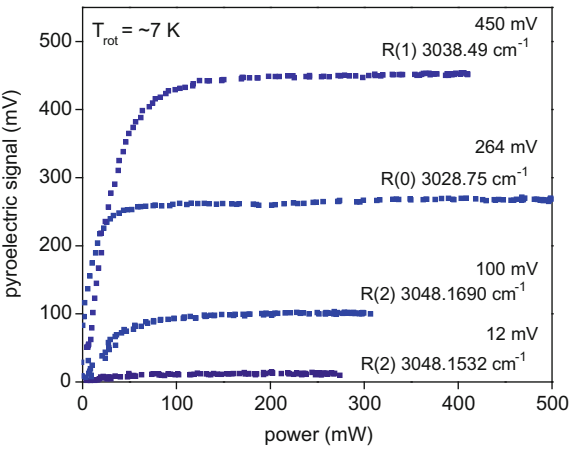

Fig. 4.13 Fluence dependence curves of the first four R-branch transitions for a 30% CH_4 in Ar mixture using a backing pressure of 3 bar and a nozzle temperature of 50 °C

To determine the relative population of the rotational states, I measured the rotational temperature using the pyroelectric detector signals from the preparation of $CH_4(v_3)$ via the R(0), R(1) and R(2) transitions. Excitation fluence dependences were collected by lock-in detected pyroelectric measurements. I chose to use R-branch transitions for these measurements because they allow for all M-levels of the ground state to be excited. So, the excited state J-population is a direct measure of the ground state J-population. Therefore, the asymptotes in the excitation fluence dependences of the R(0), R(1) and R(2) transitions reflect the populations of the v = 0 in $J = 0$, $J = 1$ and $J = 2$ rovibrational levels, respectively. Using the calculated fractional populations of $J = 0$, 1 and 2 shown in Fig. 4.12, the rotational temperature of the molecular beam can be determined by comparison of the pyroelectric detector signals in the asymptotic, high power limit of the excitation fluence dependences.

Figure 4.13 shows an example data set used to determine the relative population of CH_4 in $J = 0$, 1 and 2 in the ground vibrational state in our experimental setup. The molecular beam used in this study was a continuous expansion of 30% CH_4 in Ar with a backing pressure of 3 bar and nozzle temperature of 50 °C (v ~600 m/s). The ratio of R(0)/R(1) and R(2)/R(1) corresponds directly to the ratio of $(J = 0)/(J = 1)$ and $(J = 2)/(J = 1)$ in the ground vibrational state. The R(2) transition is split with ortho- and para-methane populating individual transitions. The R(2) transition at 3048.1690 cm^{-1} is that of para-methane, at 3048.1532 cm^{-1} is that of ortho-methane [7]. The sum of the two R(2) pyroelectric signals represents the population residing in v = 0, $J = 2$ in the molecular beam prior to excitation.

Using the measured pyroelectric detector asymptote values of 264, 450 and 112 mV for R(0), R(1) and R(2) the population ratio of $(J = 0)/(J = 1)$ and $(J = 2)/(J = 1)$ in the ground vibrational state are 0.59 and 0.25, respectively. From the calculation of the rotational level population as a function temperature, one can predict the population ratio $(J = 0)/(J = 1)$ and $(J = 2)/(J = 1)$ as a

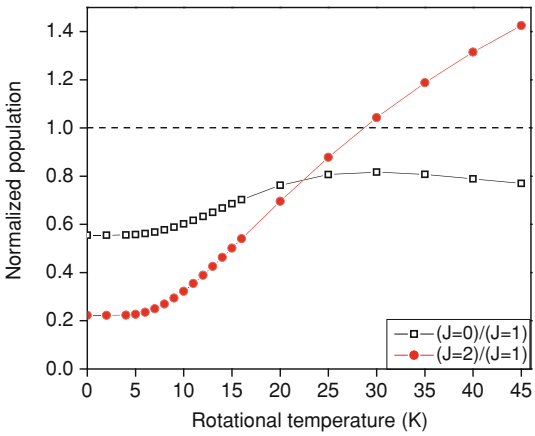

Fig. 4.14 Relative J-level population in ground vibrational state of CH_4 as a function of temperature. Normalized to the $J = 1$ population

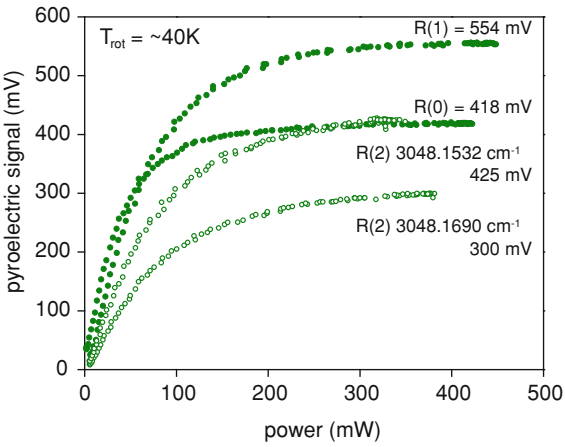

Fig. 4.15 Pyroelectric detector fluence dependences of the first four R-branch transitions for a 100% CH_4 molecular beam using a backing pressure of 3 bar and a nozzle temperature of 200 °C

function of temperature and compare the observed values to determine the temperature of the molecular beam. Figure 4.14 shows the calculated ratios as a function of temperature. At a temperature of 7 K, the calculated ratios of $(J = 0)/(J = 1)$ and $(J = 2)/(J = 1)$ are 0.57 and 0.25. These calculated ratios agree well to the observed values of 0.59 and 0.25. A rotational temperature of 7 K produces a fractional J-level population in the molecular beam of 0.31, 0.55 and 0.14 in $J = 0$, 1 and 2, respectively.

Figure 4.15 shows another experimental demonstration of this method for determining the rotational temperature in a molecular beam using 100% CH_4 with a backing pressure of 3 bar and a nozzle temperature of 200 °C. I present this mixture as an example for two reasons. First, because it is used to produce the 15 kJ/mol data shown in the $S_0(v_3)$ graph that follows. Second, because it demonstrates our ability to estimate rotational temperatures of a molecular beam that show rotational level populations significantly different from the 0 K temperature limit.

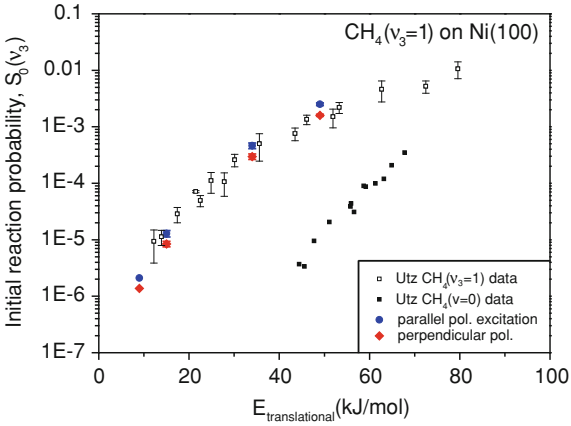

Fig. 4.16 S_0^{exc} versus $E_{translational}$ for $CH_4(v_3 = 0,1)$ on Ni(100). The open and closed *square* data points are from ref [1]

Assuming that RAP is complete for all transitions shown in Fig. 4.15, the $(J = 0)/(J = 1)$ and $(J = 2)/(J = 1)$ ratios are given by the observed ratios of (418 mV)/(554 mV) and (725 mV)/(554 mV) or 0.76 and 1.31, respectively. For a temperature of 40 K, the $(J = 0)/(J = 1)$ and $(J = 2)/(J = 1)$ ratios are calculated to be 0.79 and 1.31, and CH_4 has a fractional J-level population of 0.161, 0.204 and 0.269 in $J = 0$, 1 and 2.

These data demonstrate a straightforward method of determining the rotational temperature of a continuous molecular beam expansion, assuming that the asymptotes in the pyroelectric detector signal reflect the same fractional excitation for all probed transitions (i.e. 100% for complete RAP). With a known rotational temperature (J-level population) in the molecular beam, one can calculate $N_{excited}$ and in turn $S_0(v_3)$. I show $S_0(v_3)$ for $CH_4(v_3)$ excited via R(0) with the laser polarized either parallel or perpendicular to the surface as a function of molecular beam translational energy, in Fig. 4.16. The $CH_4(v_3)$ on Ni(100) data of Juurlink et al. [1] is reproduced in Fig. 4.16 for comparison to our results.

The agreement between the two data sets in Fig. 4.16 is quite good. Furthermore, the level of detail in the experimental results presented in this thesis work is evident in this figure. The Δ_p for $CH_4(v_3)$ excited via R(0) remains essentially constant between translational energies of 10–50 kJ/mol, see Fig. 4.26. Nonetheless, an increase of the translational energy from 10–50 kJ/mol raises $S_0(v_3)$ by approximately 3 orders of magnitude.

Utz et al. [24] published a study on the J-dependence of the sticking probability of $CH_4(v_3 = 1)$ on Ni(100) as a function of rotational state ($J = 0$, 1, 2 and 3). Over a translational energy range of 9–49 kJ/mol, they found that there was less than a factor of 2 difference between the reactivity of the studied rotational states for a given translational energy. To verify their findings, we determined $S_0(v_3)$ on Ni(100) for $CH_4(v_3 = 1)$ excited via R(0), R(1), Q(1) and P(1) to produce $CH_4(v_3 = 1)$ with J (J^{exc}) of 1, 2, 1 and 0, respectively. Figure 4.17 shows $S_0(v_3)$ for a 34 kJ/mol molecular beam of $CH_4(v_3, J = 0, 1, 2)$ dissociating on Ni(100), and is intended to assess whether or not $CH_4(v_3 = 1)$ reactivity is dependent on J^{exc}.

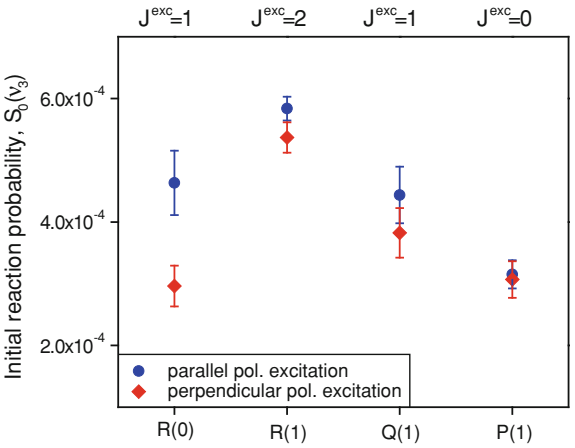

Fig. 4.17 S_0 versus transition used to excite a 34 kJ/mol molecular beam of $CH_4(v_3)$ 1 mm from a Ni(100) surface. The *diamonds* represent the excitation field polarized perpendicular to the surface and the *circles* are for the excitation polarized parallel to the surface

The data presented in Fig. 4.17 show that $S_0(v_3)$ changes by less than a factor of 2 from $J = 0$ to $J = 2$, in agreement with the findings of Utz et al. [24]. There appears to be a J^{exc} dependence on the sticking probability of $CH_4(v_3 = 1)$ on Ni(100), with the sticking probability increasing with increasing J^{exc}. CH_4 ($v_3 = 1$, $J^{exc} = 2$) being about 1.8× as reactive as CH_4 ($v_3 = 1$, $J^{exc} = 0$) on Ni(100). The error bars in Fig. 4.17 are $\pm 2\sigma$ from the repeated measurements of $S_0(v_3)$ for CH_4 ($v_3 = 1$) on Ni(100).

4.3 $CD_3H(v_1 = 1)$ Reactivity and Alignment Effects on Ni(100)

CD_3H is a symmetric top molecule possessing C_{3v} symmetry. Its v_1 normal mode is the infrared active C–H symmetric stretch, centered at 2993 cm^{-1} [25]. It corresponds to a good approximation to a local mode C–H stretch vibration for which the vibrational amplitude is localized in the unique C–H bond of the molecule [26]. Excitation of $CD_3H(v_1 = 1)$ via the R(0), ^{0}R(1), ^{1}R(1), Q(1) and P(1) transitions produces varying degrees of molecular alignment in the laboratory frame. The superscripts on the ^{K}R(1) transitions denote the K-level excited in a K-resolved transition, which is achieved in our experimental setup. Since CD_3H is a symmetric top, each rotational state is described by two quantum numbers, J and K. Here, K is the projection of J onto the symmetric top's figure axis (C_3-axis) with allowed integer values from $-J, \ldots 0, \ldots + J$.

To calculate the $CD_3H(v_1)$ transition frequencies, I used rotational constants found in literature [27, 28]. The rovibrational transition frequencies were calculated by taking the energy difference between the two rovibrational levels involved in a given transition. The formula I used to calculate the energy of individual rovibrational levels is

Table 4.2 $CD_3H(\nu_1)$ rotational constants used to calculate rovibrational transition frequencies [28]

Rotational constant	v = 0 (cm^{-1})	v = 1 (cm^{-1})
ν_o	0	2992.745
B_v	3.27916	3.2236
C_v	2.62896	2.6198
D_J	4.945×10^{-5}	-1.3×10^{-5}
D_{JK}	-3.83×10^{-5}	-1.0×10^{-4}
D_K	1.38×10^{-5}	$-8.(2) \times 10^{-5}$

Table 4.3 $CD_3H(\nu_1)$ transitions used in this thesis to probe steric effects in vibrationally excited methane chemisorption

$CD_3H(\nu_1)$ transition	cm^{-1}
R(0)	2999.193
^{0}R(1)	3005.530
^{1}R(1)	3005.575
Q(1)	2992.681
P(1)	2986.187

$$\tilde{\nu}(v,J,K) = \tilde{\nu}_o(v) + B_v J(J+1) + (C_v - B_v)K^2 - D_J J^2(J+1)^2 - D_{JK}J(J+1)K^2 - D_K K^4 \quad (4.4)$$

Here, B_v and C_v are rotational constants, ν_o is the center frequency of a given vibrational transition and D_J, D_{JK} and D_K are centrifugal distortion terms. Table 4.2 shows the relevant constants [28] used in the calculations.
The calculated transition frequencies for $CD_3H(\nu_1)$ [28] used in our experiments are shown in Table 4.3. The rotational level energies of $CD_3H(\nu_1 = 0, 1)$ along with the first few P-, Q- and R-branch transitions are shown in Appendix C.

Analogous to the $CH_4(\nu_3)$ experiments, Lamb dip frequency stabilization was used to maintain the laser resonant with $CD_3H(\nu_1)$ transitions in the molecular beam. To my knowledge, we are the first group to produce Lamb dip spectra of $CD_3H(\nu_1 = 1)$. Figure 4.18 shows an example Lamb dip spectrum of the ^{0}R(1) and ^{1}R(1) lines of $CD_3H(\nu_1)$. This spectrum was generated with 220 mW of idler power at the input of our room temperature absorption cell filled with 100 μbar of CD_3H. The spectrum in Fig. 4.18 has been baseline corrected to suppress a sloping baseline due to a frequency dependence of the idler power. To correct for the baseline slope, I collected two spectra. The first spectrum collected was an 'absorption' spectrum with a filled gas cell. The second spectrum was a 'background' spectrum over the same frequency range, after evacuation of the cell. Figure 4.18 displays the difference between the 'absorption' and the 'background' spectra.

Using the calculated transitions of the ^{0}R(1) and ^{1}R(1) lines of $CD_3H(\nu_1)$, I calibrated the idler's frequency modulation. The ^{0}R(1) and ^{1}R(1) lines are calculated to have a separation of 0.04579 cm^{-1} (1372.75 MHz). The absorption lines are separated by 10.46 V applied to the frequency determining piezo of the OPO pump seed laser. Dividing the calculated line separation by the observed absorption peak separation (in volts), I find a calibration value for the idler frequency modulation of 131.3 MHz/V (4.376×10^{-3} cm^{-1}/V). The calibration derived here is

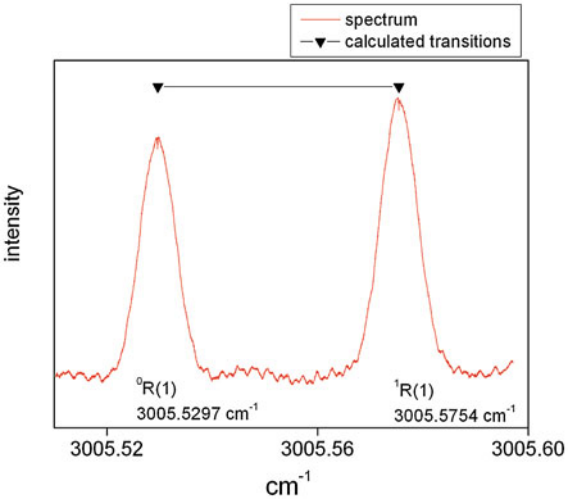

Fig. 4.18 Lamb dipped absorption spectrum of the ^{0}R(1) and ^{1}R(1) lines of $CD_3H(v_1)$ taken with room temperature cell filled to 100 μbar pressure and 220 mW idler power at the cell input

within 7.8% of the calibration derived from a Gaussian fit to the Doppler-broadened profile of $CH_4(v_3)$-R(0) shown in Appendix A with the small difference in calibrations possibly due to a nonlinearity in the frequency modulation since the frequency (or voltage) sweep is significantly larger in the calibration described here than the $\sim$280 MHz used to calibrate the system in Appendix A.

4.3.1 Effect of Hyperfine Depolarization on $CD_3H(v_1)$-R(0)

$CD_3H(v_1)$ excited via the R(0) transition, producing the highest degree of alignment, prepares a state where v = 1, $J = 1$, M = 0 and K = 0. The hyperfine splittings of CD_3H have not been measured, though the largest hyperfine splitting constant of CDH_3 comes from the deuteron and is characterized by quadrupole coupling constant $eqQ = 191.5$ kHz [29]. The reciprocal of the quadrupole coupling constant is 5.2 μs, so we expect hyperfine depolarization to dephase the initial alignment on this timescale.

For $CD_3H(v_1)$ dissociation on Ni(100), disappearance of the alignment dependent reactivity (Δ_p goes to zero) is observed on a timescale of $\sim$6 μs [8], as shown Fig. 4.19. We used a 34 kJ/mol translational energy molecular beam (v = 1895 m/s) of CD_3H excited via the v_1-R(0) transition for the study. The distance between the excitation and surface, shown as upper x-axis, was varied to produce this data. Error bars on the data points in Fig. 4.19 are taken from the standard deviation of seven pairs of molecular beam depositions (parallel vs. perpendicular excitation) performed with a 1 mm excitation to surface distance.

The dephasing of alignment produced in $CD_3H(v_1)$-R(0) is on a faster timescale ($\sim 3\times$ faster) than that of $CH_4(v_3)$-R(0), which is consistent with larger hyperfine splittings in the CD_3H molecule.

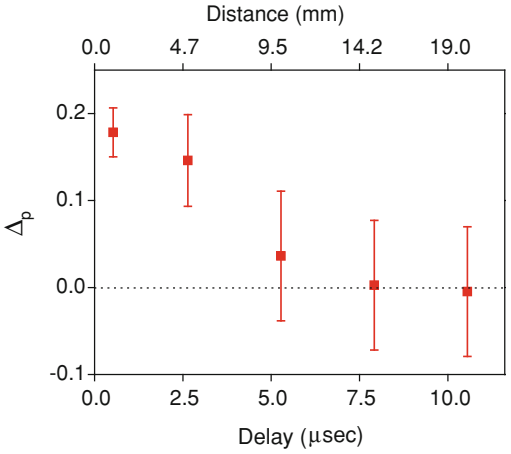

Fig. 4.19 Effect of hyperfine depolarization on $CD_3H(\nu_1)$-R(0) [8]. Error bars represent $\pm 2\sigma$ of up to 7 measurements

We used a 34 kJ/mol (1895 m/s) molecular beam with an excitation-to-surface delay of 530 ns for the bulk of the $CD_3H(\nu_1)$ data presented here. A simple linear extrapolation of the measured Δ_p values to zero delay would estimate the effect of alignment dephasing to cause a reduction of <10% in Δ_p compared to a hypothetical excitation on the surface. In the analysis of the following results, dephasing of the initially prepared alignment is neglected.

4.3.2 *Comparison of Δ_p and Calculated Alignment Coefficients for $CD_3H(\nu_1)$*

Experimentally determined Δ_p values resulting from excitation via the $CD_3H(\nu_1)$-R(0), Q(1), -P(1) and -^{x}R(1) transitions were compared to their corresponding calculated alignment coefficients to determine if the alignment dependent reactivity was due to an alignment of the excited molecule's angular momentum ($\vec{J}$) or its vibrational transition dipole moment. Figure 4.20a and b show a comparison of the calculated alignment coefficients $A_0^{(2)}$ and β_{axis} for $CD_3H(\nu_1)$ to the experimentally determined Δ_p values for $CD_3H(\nu_1)$ prepared via five different rovibrational transitions [8].

The vertical axes of the graph in Fig. 4.20a are scaled such that their origins and the values of Δ_p and $A_0^{(2)}$ coincide for R(0) excitation. Inspection of Fig. 4.20a shows that the sign of the $\vec{J}$ alignment coefficient $A_0^{(2)}$ changes from positive to negative in switching from R- to Q-branch transitions. Similar to $CH_4(\nu_3)$, Δ_p does not change sign (larger reactivity for parallel polarized excitation for R- and Q-branch excitation). This demonstrates that the observed alignment dependent reactivity of $CD_3H(\nu_1)$ on Ni(100) is not dominated by an alignment of the $\vec{J}$ in the laboratory frame.

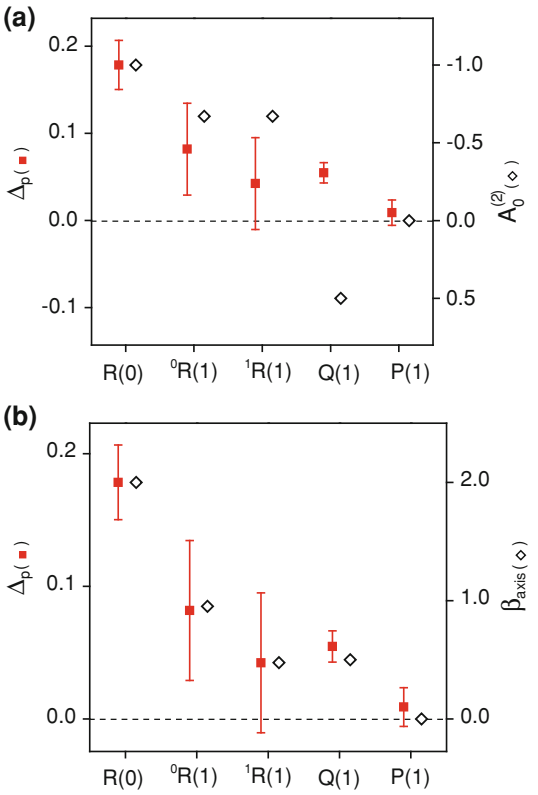

Fig. 4.20 **a** Comparison of Δ_p for $CD_3H(v_1)$ excited via various transitions to their corresponding calculated $\vec{J}$ alignment coefficients $\left(A_o^{(2)}\right)$ [8], **b** Comparison of Δ_p values for five transitions of $CD_3H(v_1)$ to their corresponding calculated vibrational dipole alignment coefficients (β_{axis}) [8]

Figure 4.20b compares the calculated vibrational transition dipole moment alignment coefficients β_{axis} for $CD_3H(v_1)$ transitions to the experimentally determined values of Δ_p for $CD_3H(v_1)$. The vertical axes of the graph are scaled such that their origins and the values of Δ_p and β_{axis} coincide for R(0) excitation. There is impressive agreement between the β_{axis} coefficients and the Δ_p values. Both β_{axis} and Δ_p are positive for all transitions studied and the relative magnitudes of the Δ_p values coincide with the relative magnitudes of the β_{axis} coefficients. This is strong evidence that the observed alignment dependent reactivity is, indeed, due to an alignment of the vibrational dipole moment rather than $\vec{J}$ alignment. These results are similar to our $CH_4(v_3)$ on Ni(100) results and those of Zare et al. for the reaction of $CH_4(v_3)$ and $CD_3H(v_1)$ with Cl atoms [22, 25, 30].

4.3.3 *Effect of Polarization Rotation with Respect to the Surface for $CD_3H(v_1)$-R(0)*

Analogous to the study conducted on $CH_4(v_3)$-R(0), we measured the reactivity for $CD_3H(v_1)$-R(0) excited at several intermediate polarization angles with, in addition

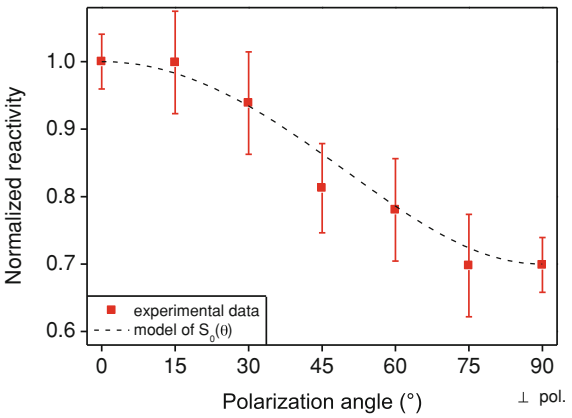

Fig. 4.21 Effect of changing the angle of linear polarization of excitation with respect to the surface for $CD_3H(v_1)$ excited via R(0) [8]. Parallel polarization = 0°. Perpendicular polarization = 90°. Error bars represent $\pm 2\sigma$ from repeated measurements

to 0° (II-pol) and 90° (⊥-pol) measurements [8]. The results are shown in Fig. 4.21. As observed in the $CH_4(v_3)$-R(0) study, there is a continuous decrease in reactivity from parallel to perpendicular polarization. Using the normalized reactivity of $S_0^{\parallel} = 1$ and $S_0^{\perp} = 0.70$ for $CD_3H(v_1)$-R(0) from repeated measurements, I modeled $S_0(\theta)$ with Eq. 4.2. Dashed line in Fig. 4.21). The measured normalized reactivities at the intermediate polarization angles agree with this functional form of $S_0(\theta)$.

The similarity between the angular dependences of $CH_4(v_3)$-R(0) and $CD_3H(v_1)$-R(0) is striking, but the details of the produced alignment is different in the two cases. For the case of $CD_3H(v_1)$-R(0), we excite the C–H stretch which is a parallel vibration. The vibrational transition dipole moment is, therefore, along the C–H bond axis. Consequently, the lone C–H bond axis is excited and aligned in the laboratory frame. It has been shown by Utz et al. [31] that the C–H bond is selectively broken during $CD_3H(v_1 = 1)$ dissociation on Ni(111). Therefore, the linear polarized excitation produces an alignment of the reactive bond in this system. The excited C–H bond can be aligned in space at any angle with respect to the surface by varying the angle that the excitation's polarization axis makes with the surface.

Figure 4.22 shows an illustration of an aligned gas-phase reactant impinging on the nickel surface. On the left-hand side of Fig. 4.22, the case for CD_3H (v_1)-R(0) excited with the laser polarized parallel to the surface is depicted. On the right-hand side, is the case for $CD_3H(v_1)$-R(0) excited perpendicular to the surface. It must be stressed that the molecules are ''aligned'' in these experiments, so one must consider that the excited C–H bond can be either parallel or anti-parallel to the linear polarization of the excitation laser. This is depicted in Fig. 4.22 using two CD_3H molecules.

With the knowledge that the reactive bond (C–H bond) is aligned preferentially along the laser polarization axis, one might expect to find an intermediate polarization angle corresponding to the lowest energy reaction pathway where the reactivity is maximal. Interestingly, we observed a monotonic decrease from

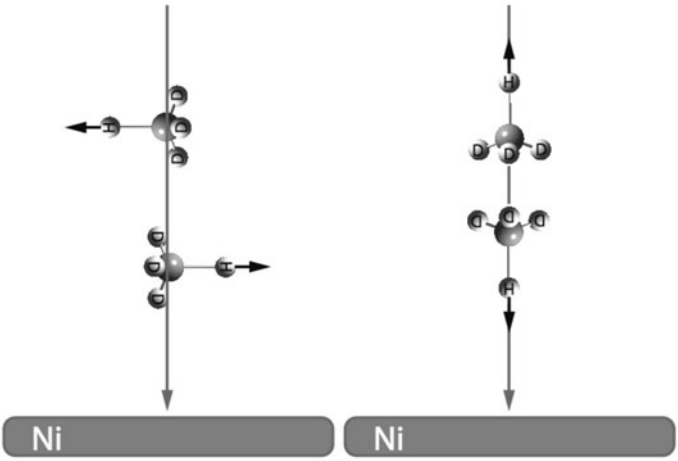

Fig. 4.22 Cartoon depiction of $CD_3H(v_1)$ impinging on a nickel surface with its net vibrational amplitude and C–H bond axis aligned parallel (*left*) and perpendicular (*right*) to the surface

parallel to perpendicular polarization. This finding is discussed in more detail and compared to the $CH_4(v_3)$-R(0) polarization angle study in the following section.

4.4 Discussion of Results

The results presented in this chapter demonstrate steric effects in the chemisorption of $CH_4(v_3)$ and $CD_3H(v_1)$ on Ni(100) by aligning the vibrationally excited molecules with respect to the linear polarization axis of the excitation laser and varying the angle between the laser's polarization axis and the surface. The main observations of the work presented here are:

(1) The reactivity of rovibrationally excited methane depends on the alignment produced in the gas-phase reagent by the linear polarization of the excitation laser.
(2) Alignment of $\overrightarrow{\mu}_{21}$ in space is responsible for the observed steric effects in the dissociation of $CH_4(v_3)$ and $CD_3H(v_1)$ on Ni(100).
(3) The alignment dependence of the methane reactivity disappears on a time scale of the inverse of the hyperfine level splittings for both $CH_4(v_3)$ and $CD_3H(v_1)$.
(4) Absolute sticking coefficient, $S_0(v_3)$, results agree well with previously published results and show a small reactivity dependence on the angular momentum (J) quantum number for $CH_4(v_3)$.
(5) $CH_4(v_3)$ and $CD_3H(v_1)$ dissociation on Ni(100) exhibit nearly identical polarization angle dependence with the reactivity decreasing monotonically from parallel to perpendicular alignment of the polarization relative to the surface.

Excitation by linearly polarized light produces an alignment of $\overrightarrow{J}$ and $\overrightarrow{\mu}_{21}$ in the laboratory frame. Here, the alignment dependent reactivity for $CH_4(v_3)$ and $CD_3H(v_1)$ dissociation on Ni(100) is attributed to an alignment of the net vibrational amplitude similar to the findings of Zare et al. for $CH_4(v_3)$ and $CD_3H(v_1)$ reacting with chlorine atoms [22, 30]. This assertion is based on the agreement of the relative scaling of the experimentally determined Δ_p values with the calculated alignment coefficients for the vibrational transition dipole moment, β_{axis}, for P-, Q- and R-branch excitations for both isotopologues of methane.

The alignment produced during rovibrational excitation is found to persist for hundreds of nanoseconds between the excitation and the surface collision. Variation of the excitation-to-surface distance shows the dephasing of the prepared alignment to occur on a timescale of $\sim$15 μs for $CH_4(v_3)$-R(0) and $\sim$5 μs for $CD_3H(v_1)$-R(0). These timescales are consistent with the hyperfine level splittings in the excited rovibrational state of each methane isotopologues. Therefore, the quantum state-prepared, aligned molecular beam should exhibit insignificant loss of alignment due to hyperfine depolarization if excitation is done in close proximity (1 mm) to the surface resulting in an excitation-to-surface collision delay of $\sim$500 ns for a 2000 m/s molecular beam.

Furthermore, the radiative lifetime of $CH_4(v_3)$ is known to be 39 ms, from the Einstein A_{21} coefficient of 25.6 Hz [7]. The natural lifetime of the excited state is about 5 orders of magnitude longer than the delay between excitation and surface collision, so no deexcitation of the quantum state-prepared molecular beam is expected in our setup unless vibrational energy transfer to the surface via the creation of electron-hole pairs in nickel is a significant process.

Absolute state-resolved sticking probabilities, $S_0(v_3)$ were experimentally determined for $CH_4(v_3)$ on Ni(100) over a translational energy range from 9 to 49 kJ/mol. The $S_0(v_3)$ values found in this work agree well with those found in the literature [1]. The reactivity $CH_4(v_3 = 1)$ excited via R(0) with the laser polarized parallel is $\sim$60% higher than with the laser polarized perpendicular to the surface, and remains essentially constant between translational energies of 9–49 kJ/mol. Nonetheless, an increase of the translational energy from 9 to 49 kJ/mol produces an increase in $S_0(v_3)$ by approximately 3 orders of magnitude. A previous experimental finding by Utz et al. [24] that $S_0(v_3)$ of $CH_4(v_3 = 1)$ on Ni(100) is rather insensitive to the rotational state of the vibrationally excited methane molecule was verified. I find that there is an increase in absolute dissociation probability of $CH_4(v_3 = 1, J^{exc})$ by a factor of 1.85 from $J^{exc} = 0$ to $J^{exc} = 2$.

A simple explanation of the underlying mechanism for the alignment dependence of vibrationally excited methane reactivity on Ni(100) is not obvious. One might expect the preferred alignment direction to reflect the minimum energy path from reactants to products on the multidimensional potential energy surface via the reaction's lowest energy transition state. The transition state structure for the dissociation of methane on Ni(100) has been calculated by several groups [32–35] to be above a single Ni-atom with the dissociating CH bond strongly elongated and

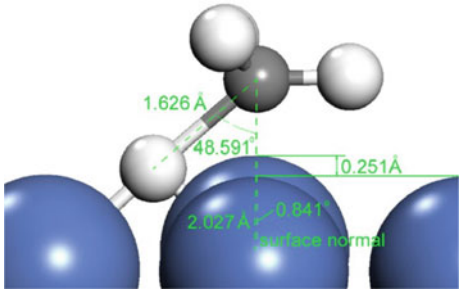

Fig. 4.23 Indicative figure of calculated transition state structure for $CH_4(v = 0)$ dissociation on a Ni(100) surface [33]. Figure is reproduced with permission

oriented towards the metal surface at an angle of about 45° with respect to the surface normal. Figure 4.23 shows an example of a calculated transition state structure of $CH_4(v = 0)$ dissociating on Ni(100).

Excitation of the infrared active C–H stretch fundamental of $CH_4(v_3)$ and $CD_3H(v_1)$ by linearly polarized light aligns the vibrational transition dipole moment $(\vec{\mu}_{21})$ or the net vibrational amplitude preferentially along the laser polarization axis. For the case of $CD_3H(v_1)$, not only the C–H stretch amplitude is aligned but also the unique C–H bond axis. Recently, quantum state-resolved experiments demonstrated unambiguously that $CD_3H(v_1)$ dissociating on a Ni(111) surface is bond-selective [31], where the excited C–H bond is selectively dissociated during the chemisorption reaction. Therefore, we align the reactive bond in space for our $CD_3H(v_1)$ experiments. One might expect to observe a maximum reactivity when the C–H bond is aligned at an angle corresponding to the reaction's lowest energy transition state.

When comparing the polarization direction leading to the highest reactivity of $CD_3H(v_1)$ on Ni(100) with a calculated transition state structure, one must consider that the laser excitation defines the alignment and not the orientation of the C–H bond in space. A simple cartoon depiction of the prepared reactant alignment was given in Fig. 4.22. The measurements, presented here, probe the average reactivity of the parallel and anti-parallel orientations of the unique C–H bond relative to the alignment axis given by the laser polarization. This averaging could shift the maximum of the observed angle dependence away from the transition state angle and towards the parallel polarization direction if C–H orientations pointing away from the surface are rather nonreactive and the variation in reactivity for C–H bond orientations towards the surface is not strong.

Figure 4.24 shows the polarization angle dependence for the dissociative chemisorption on Ni(100) of aligned $CD_3H(v_1)$ and $CH_4(v_3)$ via R(0) excitation. The similar angle dependence for $CD_3H(v_1)$-R(0) and $CH_4(v_3)$-R(0) suggests bond alignment can not be responsible for the observed steric effects in the dissociation reaction. In fact, the largest steric effect ($\Delta_p = 0.216 \pm 0.025$) is observed for $CH_4(v_3)$-R(0), where $\vec{\mu}_{21}$ is aligned in space with no knowledge of the direction of the four C–H bonds. It is more likely that the alignment of the C–H stretch amplitude is responsible for the alignment dependent dissociation probability.

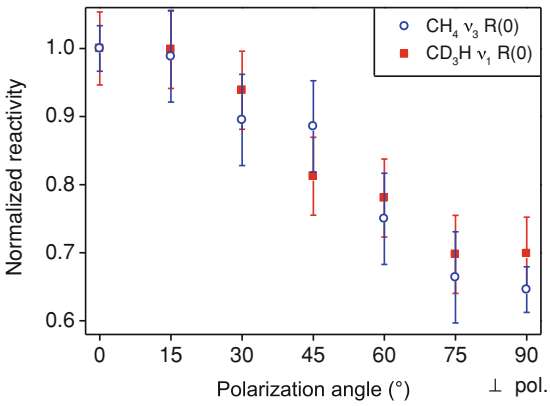

Fig. 4.24 Comparison of the excitation polarization angular dependence with respect to the surface of $CH_4(v_3)$ and $CD_3H(v_1)$ excited via their R(0) transitions. Data is reproduced from Figs. 4.10 and 4.21

Instead of matching the transition state, the alignment dependence of reactivity may be a consequence of deforming the molecule toward the product (dissociated) state. Figure 4.25 shows the calculated lowest energy configuration of the product state by 0.138 eV (or 13.3 kJ/mol) for a ground state CH_4 molecule dissociating on a Ni(100) surface, and has been adapted from results of calculations performed by Jackson et al. [35]. The minimum energy barrier was found to be over a single Ni-atom, with the dissociated H-atom and methyl group moving away from each other toward hollow sites in the nickel lattice.

In our experiments, the highest reactivity is observed when the vibration is aligned parallel to the surface. For $CD_3H(v_1)$, the reactive bond is stretched in a way that resembles the separated dissociation products. For $CH_4(v_3)$, the net vibrational amplitude of the excited molecule is polarized in a similar manner. If the alignment dependent reactivity were due to a distortion of the reactant geometry toward that of the product state, then it would be reasonable to expect that both $CD_3H(v_1)$ and $CH_4(v_3)$ have the highest reactivity when their vibrations are aligned parallel to the surface. This simple idea would predict the highest reactivity for the vibrations aligned parallel to the surface with a monotonic decrease in reactivity to perpendicular alignment. Furthermore, it predicts similar $(\cos^2\theta)$ angular dependences of Δ_p for $CH_4(v_3)$ and $CD_3H(v_1)$. Currently, this idea is speculation, but could be tested by state of the art theoretical modeling.

Another possible explanation for alignment dependent reactivity could come from an early model for vibrational energy transfer between a vibrating molecule and a metal surface [36, 37]. This classical model uses an oscillating dipole interacting with its image dipole induced in the conducting surface. A classical calculation [38, 39], which treats vibrational relaxation as ohmic dissipation of the induced image current, predicts a maximum dissipation rate for alignment of the dipole perpendicular to the surface, which is twice the rate calculated for parallel dipole alignment. The higher predicted dissipation rate for the perpendicular dipole could explain the lower reactivity for the perpendicular alignment if vibrational energy transfer to electron-hole (e-h) pairs were significant during the approach of the vibrating methane molecule towards the metal surface.

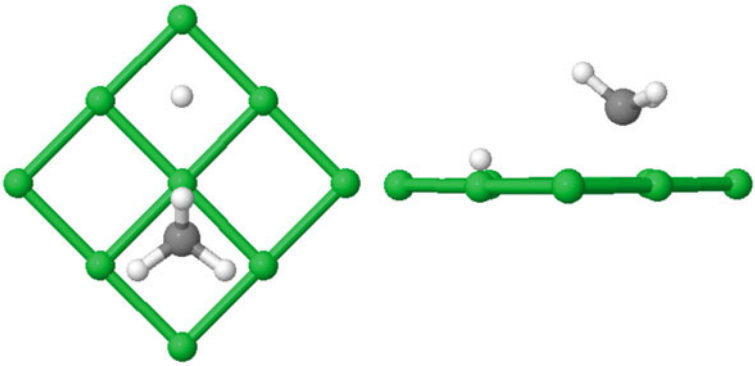

Fig. 4.25 Calculated lowest energy product state configuration for CH_4(v = 0) dissociation on Ni(100) [35]. For simplicity, only the Ni-atoms on the surface plane are shown

It is worth recognizing that this image dipole model could explain the previously observed mode-specific reactivity comparing the nearly isoenergetic symmetric (ν_1) and antisymmetric(ν_3) stretch fundamentals of CH_4 on Ni(100) [4]. The reactivity of $CH_4(\nu_1 = 1)$ [4] was measured to be up to an order of magnitude higher than the reactivity of $CH_4(\nu_3 = 1)$ [1]. Since the infrared in-active symmetric C–H stretch fundamental CH_4 carries no oscillating dipole moment, it lacks this vibrational relaxation channel via the image dipole mechanism. Meanwhile, the ν_3 fundamental of CH_4 is infrared active with a vibrational dipole moment which could conceivably transfer vibrational energy to the metal surface via e-h pairs. Vibrational deexcitation via electron hole pair excitation would leave the gas-phase molecule in its ground state which has a significantly lower reactivity than the vibrationally excited state.

Recent calculations by Tully et al. [40, 41] modeled non-adiabatic coupling of nuclei motion to electron-hole pair excitations in a metal surface. The calculation, for NO(v = 15) impinging on a Au(111) surface, exhibited deexcitation of multiple vibrational quanta by nonadiabatic vibrational energy transfer. The simulations showed that dynamical steering reoriented the impinging molecule toward the geometry having the N-atom pointing toward the surface. The geometry N-atom-down (toward the surface) allowed for the closest approach of the gas-phase molecule to surface. Furthermore, they noted that the closer the molecule approached to the surface, the more likely was nonadiabatic vibrational energy transfer from the gas-phase molecule to the surface. Their model showed that faster molecules did not necessarily penetrate closer to the surface, and attributed it to the idea that slower molecules have more time to be reoriented to have the N-atom-down geometry which permits the closest approach.

Although it is a possibility, nonadiabatic effects in the dissociative chemisorption of methane on Ni(100) are difficult to rationalize due to the negative electron affinity of methane [42]. There may exist a preferential molecular

alignment of $CH_4(v_3)$ and $CD_3H(v_1)$ for nonadiabatic vibrational energy transfer to the surface. If we aligned the vibrationally excited molecular beam to maximize its nonadiabatic energy transfer rate to the surface, we would expect a decrease in reactivity for that alignment. For our experimental results, we would then conclude that alignment of the vibrationally excited methane molecule's net vibrational amplitude perpendicular to the surface would have a higher nonadiabatic vibrational energy transfer rate than that of parallel alignment.

A different explanation for the alignment dependent surface reactivity of methane builds on the effects of surface-induced intra-molecular vibrational redistribution (IVR). The single mode laser radiation prepares the incident methane molecule in a time independent eigenstate, specified by the set of quantum numbers (v_3, J, M) and aligns $\vec{J}$ and $\vec{\mu}_{21}$ of the molecule. As the molecule approaches the surface, the interaction between the vibrationally excited molecule and the metal surface changes the molecule's energy level structure such that the initially prepared state is no longer an eigenstate of the combined molecule/surface system but can still be expressed as a sum of eigenstates (a wave-packet) of the molecule/surface system. The ensuing time dependence, referred to as "surface-induced IVR", leads to vibrational energy flow within the incident molecules as it approaches the metal surface.

Halonen et al. [43] modeled such surface-induced IVR for CH_4 approaching a flat metal surface and showed that different initial eigenstates (v_1, v_3, …) of the isolated molecule, evolve adiabatically towards different vibrational energy localizations towards and away from the surface which can be expected to produce different reactivities. The four-dimensional variational calculations where done for a fixed orientation of CH_4 with a single C–H bond pointing along the surface normal towards the surface but Halonen et al. point out that different initial orientations could lead to different energy flow and localization during the approach to the surface. It could be possible that the alignment dependent reactivity observed here for both $CH_4(v_3)$ and $CD_3H(v_1)$, could result from an alignment dependence of the surface induced IVR process. In other words, $CH_4(v_3)$ and $CD_3H(v_1)$ excited with their vibrational dipole moment ($\vec{\mu}_{21}$) aligned parallel to the surface experience different surface-induced IVR leading to higher reactivity than when $\vec{\mu}_{21}$ is aligned perpendicular to the surface.

To understand the physics behind vibrationally excited methane's alignment dependent reactivity, information about the gas-surface interaction time will be valuable. We experimentally tested the effect of the interaction time between excited, aligned gas-phase molecules and the surface by varying the molecular beam speed. For $CH_4(v_3)$-R(0), the alignment effect (Δ_p) remained essentially constant for incident velocities between 1000–2900 m/s as shown in Fig. 4.26 (a) and (b), where the x-axis is plotted in units of velocity and translational energy, respectively. For $CD_3H(v_1)$-R(0), also shown in Fig. 4.26(a) and (b), Δ_p actually decreases with increasing incident velocity from 1700 to 2700 m/s (28.2 and 71 kJ/mol). This is opposite to what might be expected if steering were significant as gas-phase molecules approach the surface. This finding is similar to the

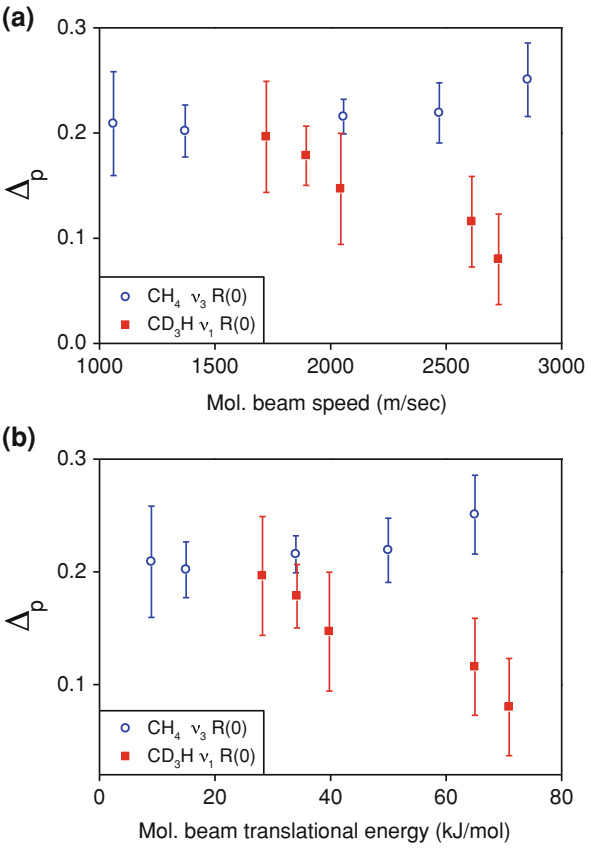

Fig. 4.26 **a** Comparison of the molecular beam speed dependences of Δ_p for $CH_4(v_3)$ and $CD_3H(v_1)$ excited via their R(0) transitions, **b** Comparison of the molecular beam translational energy dependences of Δ_p for $CH_4(v_3)$ and $CD_3H(v_1)$ excited via their R(0) transitions

observation of Wodtke, Auerbach et al. [44] for D_2 desorbing from Cu(111) that was described in the first chapter of this thesis. For D_2 on Cu(111), the decrease in alignment dependent reactivity was attributed to the impinging molecule having enough energy to overcome the reaction barrier in less favorable geometries as the system's total energy is raised by the increase in translational energy.

At this point, I am left to speculate as to why the observed velocity dependence of Δ_p is different for the two methane isotopologues. A decrease in alignment contrast Δ_p with increasing translational energy may contain information on the alignment dependence of the reaction's barrier height. At low translational energy, incident molecules can overcome the barrier only with a most favorable approach, associated with the minimum barrier. This would result in a large Δ_p. With increasing incident energy, Δ_p decreases because the molecules can also overcome higher barriers corresponding to less favorable approaches to the transition state.

The difference between the $CH_4(v_3)$ and $CD_3H(v_1)$ velocity dependence of reactivity might be due to an increased tunneling effect for $CH_4(v_3)$ chemisorption compared to $CD_3H(v_1)$, as there are four equivalent H-atoms in CH_4 to one in

CD_3H. Further experiments over a larger range of incident energies as well as quantum dynamics calculations of methane dissociation using a multi-dimensional PES should be done to explore these open questions.

Although a clear explanation of the physics behind the observed steric effects in the chemisorption of vibrationally excited methane remains an open question, some definite conclusions can be drawn from the observations. The fact that the dissociation probability of methane depends on the initial alignment of the incident molecule, prepared far from the surface (1 mm), implies the absence of significant steering effects under our experimental conditions. In other words, any anisotropic molecule/surface interactions must not be able to reorient or steer the incident molecule into its lowest energy reaction path on the sub-ps timescale [24] of the reactive collision in our experiments. Most modeling of methane dissociation reactions propagates the impinging molecule along its minimum energy pathway to reaction products. Our results imply that this may be an unreasonable simplification in describing molecular beam experiments of methane dissociation on a metal surface.

Observation of quantum state-resolved steric effects in the chemisorption of vibrationally excited methane on a single crystal metal surface, presented here, is an interesting result in itself. It constitutes further evidence for a non-statistical mechanism of methane chemisorption, beyond the previously reported mode-specificity [45] and bond-selectivity [31]. First, It is not only the amount of energy a system possesses that decides the reaction probability, but how the energy is partitioned (E_{TRANS} vs. E_{VIB}). Second, different vibrational modes can produce different reaction probabilities. Now, we show that for the same E_{TRANS} and E_{VIB} (vibrational mode), the reaction probability depends on how the gas phase reactant's vibration is aligned with respect to the surface.

The statistical PC-MURT model developed by Harrison et al. [46–48] assumes that the impinging molecule (i.e. methane) forms a collision complex of CH_4 and *s* surface atoms. The chemisorption probability is determined from unimolecular dissociation and desorption rates. These rates are calculated according to Rice-Rampsperger-Kassel-Marcus (RRKM) theory [49–51]. RRKM theory assumes that the energy of reaction complex is randomly redistributed to all degrees of freedom on a timescale much faster than the reaction. Therefore, reactivity depends only on the amount of energy in the collision complex. Results of the dissociative chemisorption of state-prepared methane on metal surfaces [4, 31, 45] have been demonstrated to be inconsistent with this statistical model.

In conclusion, the alignment dependent reactivity can be described as a consequence of the reaction dynamics on a multidimensional potential energy surface (PES), which is a complex function of all 15 molecular degrees of freedom in the methane/surface system, some of which describe the alignment of the incident molecules prepared by the laser excitation. Theoretical and experimental work must be conducted in tandem to obtain an understanding of gas-surface interactions. The results present here clearly demonstrate that statistical models are not able to capture the physics of a reactive encounter, and are therefore capable of neither qualitative nor quantitative predicting methane chemisorption. Dynamical

calculations on a multidimensional molecule/surface PES are needed to understand which degrees of freedom play a decisive role in the observed steric effects and our state-resolved, alignment dependent data can guide and test such calculations.

References

1. L.B.F. Juurlink et al., Eigenstate-resolved studies of gas-surface reactivity CH4: (nu(3)) dissociation on Ni(100). Phys. Rev. Lett. **83**(4), 868–871 (1999)
2. M.P. Schmid et al., Surface reactivity of highly vibrationally excited molecules prepared by pulsed laser excitation: CH4 (2 nu(3)) on Ni(100). J. Chem. Phys. **117**(19), 8603–8606 (2002)
3. L.B.F. Juurlink et al., Comparative study of C-H stretch and bend vibrations in methane activation on Ni(100) and Ni(111). Phys. Rev. Lett. **94**(20), 208303 (2005)
4. P. Maroni et al., State-resolved gas-surface reactivity of methane in the symmetric C-H stretch vibration on Ni(100). Phys. Rev. Lett. **94**(24), 4 (2005)
5. M.P. Schmid, *Interaction of highly excited molecules with solid surfaces*. 2003, Ecole Polytechnique Fédérale de Lausanne Thesis No. 2662
6. P. Maroni, *Bond- and mode-specific reactivity of methane on Ni(100)*. 2005, Ecole Polytechnique Fédérale de Lausanne Thesis No. 3335
7. L.S. Rothman et al., The HITRAN 2008 molecular spectroscopic database. J. Quant. Spectrosc. Radiat. Transf. **110**(9–10), 533–572 (2009)
8. B.L. Yoder, R. Bisson, R.D. Beck, Steric effects in the chemisorption of vibrationally excited methane on Ni(100). Science **329**(5991), 553–556 (2010)
9. M.P. Schmid et al., Molecular-beam/surface-science apparatus for state-resolved chemisorption studies using pulsed-laser preparation. Rev. Sci. Instrum. **74**(9), 4110–4120 (2003)
10. J.H. Onuferko, D.P. Woodruff, B.W. Holland, LEED structurec-analysis of the Ni(100) (2x2)C(P4G) structure—case of adsorbate-induced substrate distortion. Surf. Sci. **87**(2), 357–374 (1979)
11. W.R. Simpson, T.P. Rakitzis, S.A. Kandel, A.J. Orr-Ewing, R.N. Zare, Reaction of Cl with vibrationally excited CH4 and CHD3: State-to-state differential cross sections and steric effects for the HCl product. J. Chem. Phys. **103**(17), 7313–7335 (1995)
12. R.R. Smith et al., Preference for vibrational over translational energy in a gas-surface reaction. Science **304**(5673), 992–995 (2004)
13. M. Hollas, *High Resolution Spectroscopy* (Wiley, Chichester, 1998)
14. R. Altkorn, R.N. Zare, C.H. Greene, Depolarization of optically prepared molecules by 2 randomly oriented spins. Mol. Phy. **55**(1), 1–9 (1985)
15. A.D. Rudert et al., Collisional effects on angular momentum orientation in acetylene (X)over-tilde (1)Sigma(+)(g) (nu(2)'' = 1, j ''). I. Preparation, detection and conservation in single collisions. J. Chem. Phys. **111**(21), 9549–9559 (1999)
16. M. Rutkowski, H. Zacharias, Depolarisation of the spatial alignment of the rotational angular momentum vector by hyperfine interaction. Chem. Phys. **301**(2–3), 189–196 (2004)
17. M. Rutkowski, H. Zacharias, Depolarisation of the spatial alignment of the rotational angular momentum vector by hyperfine interaction (vol 301, pg 189, 2004). Chem. Phys. **310**(1–3), 321–322 (2005)
18. N.C.M. Bartlett et al., Time-dependent depolarization of aligned HD molecules. Phys. Chem. Chem. Phys. **11**(1), 142–147 (2009)
19. J.L. Hall, C. Borde, Measurement of methane hyperfine-structure using laser saturated absorption. Phys. Rev. Lett. **30**(22), 1101–1104 (1973)
20. J. McHale, *Molecular Spectroscopy* (Prentice-Hall, London, 1999)
21. A.R. Edmonds, Angular Momentum in Quantum Mechanics, in *Investigations in Physics*, ed. by R.H.E. Wigner (Princeton University Press, Princeton, 1968)

22. W.R. Simpson et al., Reaction of Cl with vibrationally excited CH4 and CHD3—state-to-state differential cross-sections and steric effects for the HCl product. J. Chem. Phys. **103**(17), 7313–7335 (1995)
23. A. Amrein, M. Quack, U. Schmitt, High-resolution interferometric Fourier-transform infrared-absorption spectroscopy in supersonic free jet expansions- carbon monoxide, nitric-oxide, methane, ethyne, propyne, and trifluoromethane. J. Phys. Chem. **92**(19), 5455–5466 (1988)
24. L.B.F. Juurlink, R.R. Smith, A.L. Utz. The role of rotational excitation in the activated dissociative chemisorption of vibrationally excited methane on Ni(100). in General Discussion on Excited States at Surfaces. 2000. Nottingham, Royal Soc Chemistry
25. J.P. Camden et al., Comparing reactions of H and Cl with C-H stretch-excited CHD3. J. Chem. Phys. **124**(3), 034311 (2006)
26. L. Halonen, M.S. Child, Local mode theory for C3 V molecules—CH3D, CHD3, SiH3D, and SiHD3. J. Chem. Phys. **79**(9), 4355–4362 (1983)
27. R.S. McDowell, Rotational partition functions for symmetric-top molecules. J. Chem. Phys. **93**(4), 2801–2811 (1990)
28. M. Lewerenz, M. Quack, Vibrational-spectrum and potential-energy surface of the CH chromophore in CHD3. J. Chem. Phys. **88**(9), 5408–5432 (1988)
29. S.C. Wofsy, J.S. Muenter, W. Klempere, Hyperfine structure and dipole moment of CH3D. J. Chem. Phys. **53**(10), 4005 (1970)
30. W.R. Simpson et al., Picturing the transition-state region and understanding vibrational enhancement for the $Cl + CH4- > HCl + CH3$ reaction. J. Phys. Chem. **100**(19), 7938–7947 (1996)
31. D.R. Killelea et al., Bond-selective control of a heterogeneously catalyzed reaction. Science **319**(5864), 790–793 (2008)
32. O. Swang et al., A theoretical-study of the chemisorption of methane on a Ni(100) surface. Chem. Phys. **156**(3), 379–386 (1991)
33. Y.A. Zhu et al., First-principles calculations of CH4 dissociation on Ni(100) surface along different reaction pathways. J. Mol. Catal. Chem. **264**(1–2), 299–308 (2007)
34. B. Xing et al., Investigation the active site of methane dissociation on Ni-based catalysts: A first-principles analysis. J. Mol. Catal. Chem. **315**(2), 187–196 (2010)
35. S. Nave, A.K. Tiwari, B. Jackson, Methane dissociation and adsorption on Ni(111), Pt(111), Ni(100), Pt(100), and Pt(110)-(1x2): Energetic study. J. Chem. Phys. **132**(5), 054705 (2010)
36. B.N.J. Persson, Damping of excited molecules located above a metal-surface. Solid State Commun. **27**(4), 417–421 (1978)
37. B.N.J. Persson, M. Persson, Vibrational lifetime for a CO adsorbed on Cu(100). Solid State Commun. **36**(2), 175–179 (1980)
38. B.N.J. Persson, W.L. Schaich, Electronic damping of a vibrating dipole near a metal. J. Phys. C-Solid State Phys. **14**(35), 5583–5589 (1981)
39. B.N.J. Persson, S. Andersson, Dynamical processes at surfaces—excitation of electron-hole pairs. Phys. Rev. B **29**(8), 4382–4394 (1984)
40. N. Shenvi, S. Roy, J.C. Tully, Dynamical steering and electronic excitation in NO scattering from a gold surface. Science **326**(5954), 829–832 (2009)
41. N. Shenvi, S. Roy, J.C. Tully, Nonadiabatic dynamics at metal surfaces: Independent-electron surface hopping. J. Chem. Phys. **130**(17), (2009)
42. K. Rohr, Cross beam experiment for the scattering of low-energy electrons from methane. J. Phys. B-At. Mol. Opt. Phys. **13**(24), 4897–4905 (1980)
43. L. Halonen, S.L. Bernasek, D.J. Nesbitt, Reactivity of vibrationally excited methane on nickel surfaces. J. Chem. Phys. **115**(12), 5611–5619 (2001)
44. H. Hou et al., The stereodynamics of a gas-surface reaction. Science **277**(5322), 80–82 (1997)
45. R.D. Beck et al., Vibrational mode-specific reaction of methane on a nickel surface. Science **302**(5642), 98–100 (2003)

46. V.A. Ukraintsev, I. Harrison, A statistical-model for activated dissociative adsorption—application to methane dissociation on Pt(111). J. Chem. Phys. **101**(2), 1564–1581 (1994)
47. A. Bukoski, D. Blumling, I. Harrison, Microcanonical unimolecular rate theory at surfaces. I. Dissociative chemisorption of methane on Pt(111). J. Chem. Phys. **118**(2), 843–871 (2003)
48. H.L. Abbott, A. Bukoski, I. Harrison, Microcanonical unimolecular rate theory at surfaces. II. Vibrational state resolved dissociative chemisorption of methane on Ni(100). J. Chem. Phys. **121**(8), 3792–3810 (2004)
49. R.A. Marcus, O.K. Rice, The kinetics of the recombination of methyl radicals and iodine atoms. J. Phys. Colloid Chem. **55**(6), 894–908 (1951)
50. R.A. Marcus, Lifetimes of active molecules. 1. J. Chem. Phys. **20**(3), 352–354 (1952)
51. O.K. Rice, Effects of quantization and of anharmonicity on rates of dissociation and association of complex molecules. J. Phys. Chem. **65**(9), 1588 (1961)

Chapter 5
State-Resolved Steric Effects in $CH_4(v_3)$ Dissociation on Ni(110)

5.1 Introduction

To fully define a reactive encounter, one must have control over every aspect of the collision, including the approach direction and velocity, quantum state and relative orientations of the reaction partners. In the previous chapter, a quantum-state prepared, aligned molecular beam of well defined translational energy was directed at normal incidence on a single crystal metal surface to study steric effects in a dissociative chemisorption reaction. Using an anisotropic, single-crystalline surface, we are able to raise the level of experimental detail to an aligned gas phase reagent dissociating on an aligned surface structure. In this chapter, the study of steric effects in vibrationally excited methane chemisorption is extended to an anisotropic surface, Ni(110), aligning the vibrationally excited molecule with respect to the surface anisotropy (surface rows).

The Ni(110) surface consists of rows of closely packed Ni atoms located in the topmost layer which are separated by parallel troughs as depicted in Fig. 5.1. The (110) surface is generated by a cut across the diagonal of the face-centered cubic lattice that is shown in Fig. 4.1. This cut along with the lattice constant of 3.52 Å for nickel produces a spacing between rows (**a** in Fig. 5.1) of 3.52 Å, while the close-packed Ni atom spacing in each row (**b** in Fig. 5.1) is 2.49 Å [1, 2]. Since the nickel surface sample is a single crystal, the entire 10 mm diameter disk has the same macroscopic orientation of the rows and troughs, which makes it possible to align the direction of the rows in the laboratory frame. By changing the alignment of the surface rows relative to the polarization direction of the excitation laser, we control the alignment of the vibrational amplitude and J-vector relative to the direction of the surface rows of closely packed Ni atoms. Two surface row alignments were prepared to probe their effect on the reactivity of a state-prepared, aligned molecular beam of $CH_4(v_3)$.

With the Ni(110) surface rows aligned vertically in the laboratory frame, we prepare the vibrationally excited molecules with their vibrational amplitude aligned parallel to the surface rows when the laser polarization is vertical (parallel to the surface).

B. L. Yoder, *Steric Effects in the Chemisorption of Vibrationally Excited Methane on Nickel*, Springer Theses, DOI: 10.1007/978-3-642-27679-8_5,

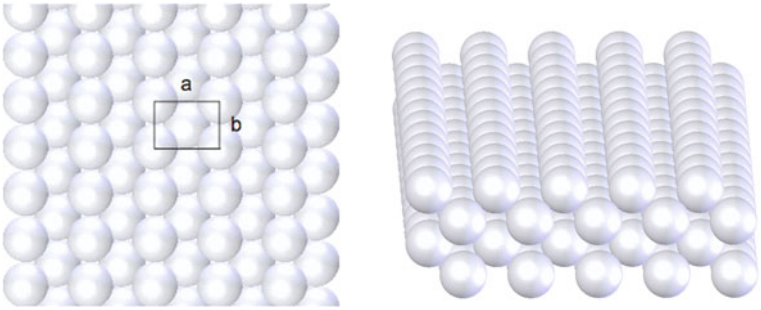

Fig. 5.1 Cartoon depiction of a Ni(110) surface, where $a = 2.49$ Å and $b = 3.52$ Å. (*Left*) surface viewed from above. (*Right*) surface viewed from the side, along the surface rows

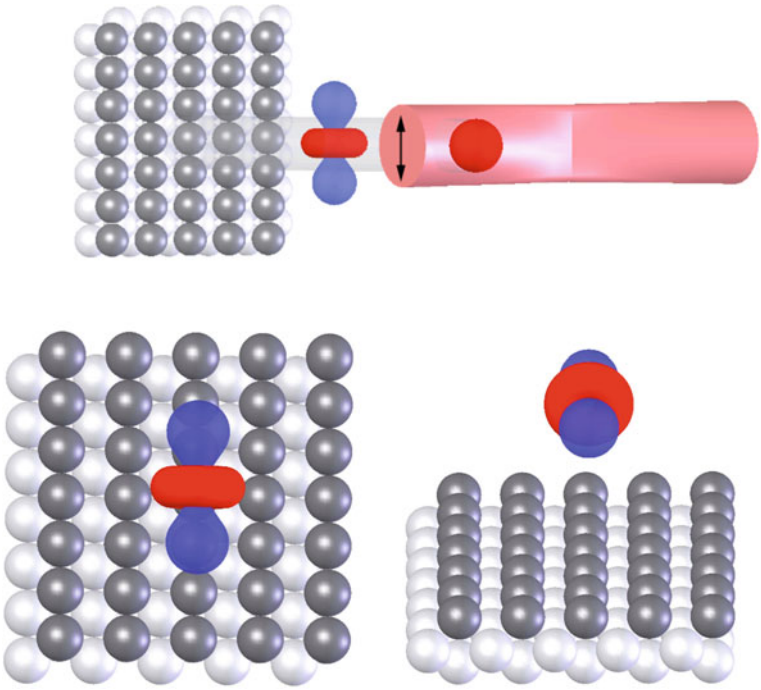

Fig. 5.2 Cartoon depiction of the *parallel* reagent geometry produced with the Ni(110) surface rows aligned vertically in the laboratory frame and $CH_4(v_3)$-R(0) excited with the laser polarized parallel to the surface rows. (*Top*) Perspective view with double-headed arrow showing the laser polarization. (*Lower-left*) system view from above. (*Lower-right*) system viewed from the side

The experimental geometry of the vibrationally excited methane (excited via the R(0) transition) impinging normal to a Ni(110) surface where the excitation is polarized parallel to the surface rows is shown schematically in Fig. 5.2.

As described in Chap. 3, the blue lobes describe the probability distribution of $\vec{\mu}_{21}$ and the red torus represents the aligned $\vec{J}$ distribution for R(0) excitation. The probability distributions of $\vec{J}$ and $\vec{\mu}_{21}$ are of arbitrary units and are merely intended to show spatial alignment, no information of molecule size or vibrational amplitude should be taken from the distributions. I have used dark gray to highlight the Ni(110) surface rows in the following figures; all surface atoms are nickel. The experimental configuration shown in Fig. 5.2 with the excitation field polarized parallel to both the surface plane and the surface rows will be referred to throughout the chapter as *parallel*.

For Ni(110) surface rows aligned horizontally in the laboratory frame, we prepare the vibrationally excited molecules with their vibrational amplitude aligned perpendicular to the surface rows when the laser polarization is vertical. Figure 5.3 shows a schematic representation of the reagent alignments. The experimental configuration in Fig. 5.3 where the laser is polarized parallel to the surface plane but perpendicular to the horizontal surface rows is referred to as *perpendicular* throughout this chapter.

Excitation of the molecular beam with the laser polarization along the surface normal should produce the same reactivity regardless of the direction of the surface rows because of the cylindrical symmetry of the alignment distributions about the surface normal. The lower left-hand side of Fig. 5.4 shows (viewed from above) the case $CH_4(v_3)$-R(0) excited with a laser polarized along the surface normal. Rotation of the surface about the axis defined by the direction of the approaching molecule does not change the relative alignment of the reaction partners. The right-hand side of Fig. 5.4 shows a side view of the aligned molecule approaching the Ni(110) surface. This experimental configuration is referred to simply as *normal* since it has the laser polarized perpendicular to the surface and should be invariant to surface row alignment.

Therefore, *parallel* and *perpendicular* configurations can be compared using a common reference (the *normal* configuration). Alignment dependent reactivity is quantified by determining the *reactivity contrast* Δ_p (as defined in Chap. 4). If the alignment dependent reactivity is observed to be different for the two surface alignments, it should be a result of the difference in reactivity between *parallel* and *perpendicular* configurations. One may expect a relatively high reactivity in the *parallel* configuration if the H and CH_3 move away from each other after dissociation on a ridge Ni-atom to reside on adjacent Ni atoms, as this is the configuration that has the shortest Ni–Ni spacing (2.49 Å) on the surface.

5.2 $CH_4(v_3)$ on Ni(110)-(*Parallel* vs. *Normal*)

Aligning the Ni(110) rows vertically in the laboratory frame makes it possible to have the laser polarization axis parallel to the surface rows. This allows for the *parallel* configuration shown in Fig. 5.2. We align the Ni(110) sample's surface

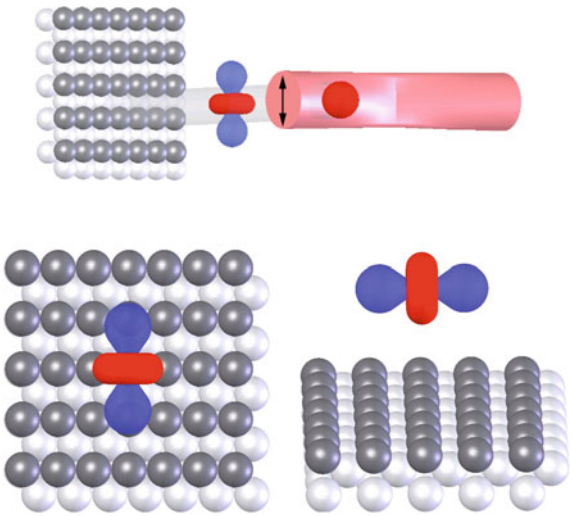

Fig. 5.3 Cartoon depiction of *perpendicular* reagent geometries produced with a Ni(110) surface aligned horizontally in the laboratory frame and $CH_4(v_3)$-R(0) excited with the laser polarized parallel to the surface. (*Top*) Perspective view with *double-headed arrow* showing the laser polarization. (*Lower-left*) system view from above. (*Lower-right*) system viewed from the side

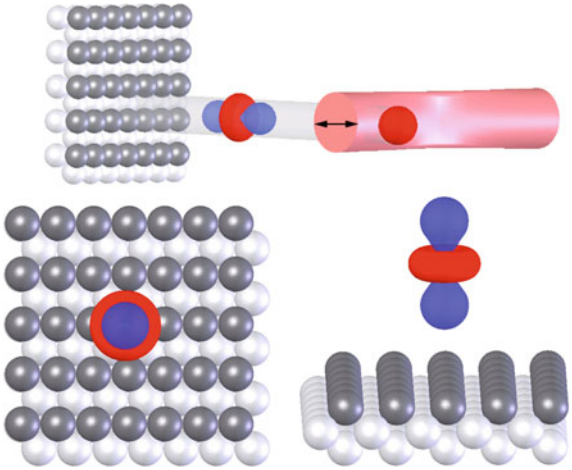

Fig. 5.4 Cartoon depiction of the *normal* reagent geometry produced when $CH_4(v_3)$-R(0) is excited with the laser polarized perpendicular to the Ni(110) surface. (*Top*) Perspective view with *double-headed arrow* showing the laser polarization. (*Lower-left*) system view from above. (*Lower-right*) system viewed from the side

rows by rotating the Ni-sample in its mount/platen. Then, the sample is introduced to the UHV system via a load-lock chamber.

The alignment of the surface rows is assessed using low energy electron diffraction (LEED), see Chap. 2. We clean the surface by sputtering and annealing to

1,000 K, and then turn off the high voltage and current supplied to the filament used to maintain the surface temperature constant and let the surface cool to ~100 K by continuing to flow liquid nitrogen through the cooling line. The filament is turned off to reduce background light on the phosphorescent screen used to detect the low energy electrons, and the surface is cooled to reduce the thermal motion of the Ni-atoms in the crystal lattice. LEED patterns correspond to the reciprocal surface lattice and arise from interference of elastically scattered electrons by the lattice of surface atoms.

Figure 5.5 shows a LEED pattern of Ni(110) with its rows of close-packed atoms aligned vertically in the image frame which results in the larger spacing between diffraction spots in the vertical direction. Large spacing in the reciprocal lattice translates to a small spacing in real space. To determine the degree of alignment of the surface rows in the laboratory frame, I imported the LEED picture into a graphics program, and drew a line across the spots, connecting the two black lines on the flange's bolt circle that define 'horizontal' in the laboratory frame. Then, I drew a line through the nearly horizontal diffraction points across the image. I made a right-triangle from the two constructed lines by giving them a common end point, rotated the two 'grouped'-lines such that one of them was horizontal in the graphics program coordinate system and connected their other end points with a straight line. The result is shown in Fig. 5.5. The angle of misalignment from 'horizontal' was determined to be $\theta = 3.18°$.

Figure 5.6 shows a baseline-subtracted Auger electron spectroscopy AES profile scan of the Ni(110) surface after a pair of 180 s molecular beam exposures of a 34 kJ/mol molecular beam of $CH_4(v_3)$-R(0) excited 1 mm from the surface; the same experiment that was conducted on Ni(100) in the previous chapter. The only experimental parameters changed between the two exposures (depositions) was the linear polarization direction of the excitation field and the deposition coordinates on the Ni(110) surface. It is obvious from the raw data that the reactivity of $CH_4(v_3)$-R(0) is significantly higher for the *parallel* polarization direction than for the *normal* polarization. From the AES C/Ni ratios of the two deposited carbon spots in Fig. 5.6, the *parallel* configuration produces ~2x more chemisorbed carbon than *normal*. For a quantitative analysis of the alignment-dependent reactivity, I calculated the *alignment contrast* or Δ_p values, as described in Chap. 4.

For Ni(110) aligned *parallel* versus *normal*, we determined Δ_p resulting from $CH_4(v_3 = 1)$ preparation via the R(0), Q(1) and P(1) transitions. The experimentally determined Δ_p for Ni(110) study were calculated in the same way as Δ_p in the Ni(100) study, except for the correction of the coverage dependent sticking coefficient correction (S/S_o). The S/S_o correction was not included in the calculation for Ni(110) Δ_p as we did not determine the saturation coverage of carbon on a Ni(110) surface, since the low energy electron deflection (LEED) pattern of Ni(110) produced 'streaks' of carbon from the dissociation of methane. As shown in the previous chapter, the S/S_o correction is small (a few percent) and would cause the Δ_p values to be larger. Therefore, the Δ_p values reported in this chapter should be regarded as lower limits to the true Δ_p. The Δ_p values are significantly larger for Ni(110) than Ni(100), even without the S/So correction. The Δ_p for

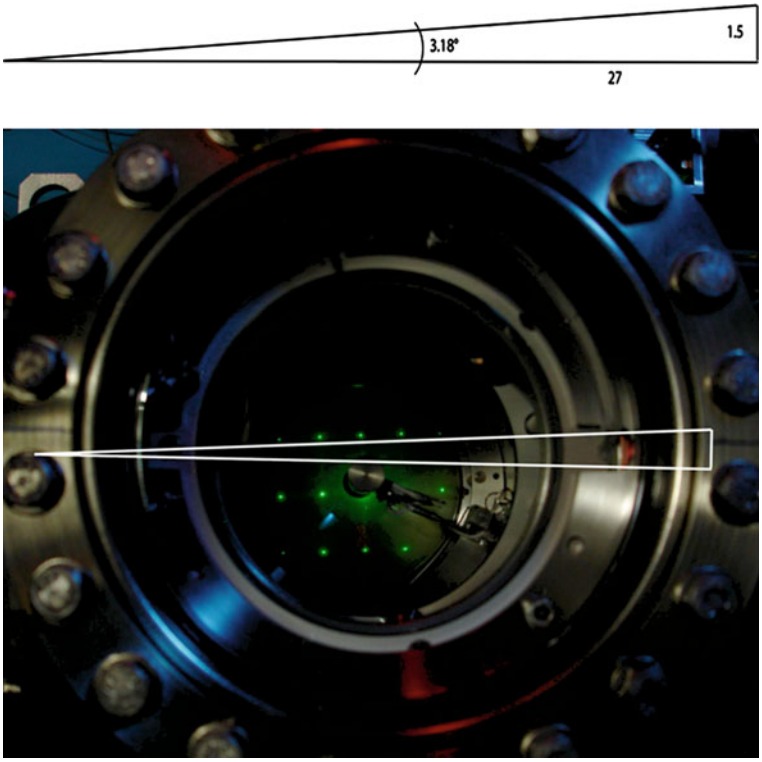

Fig. 5.5 LEED pattern of Ni(110) single crystal with rows aligned vertically in the laboratory frame. This surface row alignment is used to produce the *parallel* experimental configuration

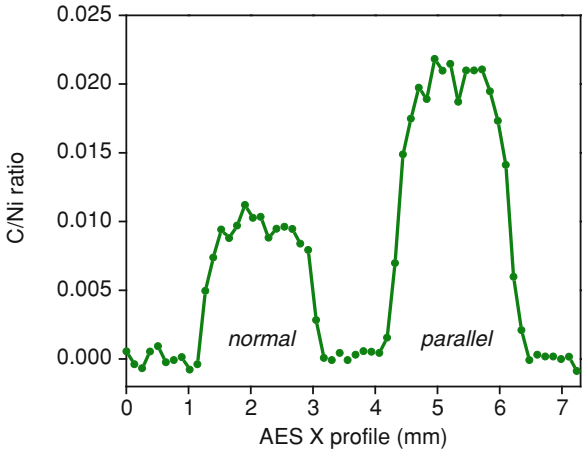

Fig. 5.6 Baseline-subtracted AES profile of two carbon spots on a Ni(110) surface after $CH_4(v_3)$-R(0) molecular beam depositions excited in the *normal* (*left*) and *parallel* (*right*) configuration

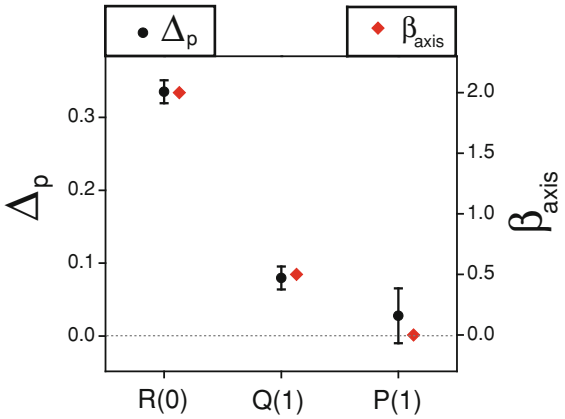

Fig. 5.7 Comparison of Δ_p for $CH_4(v_3)$ excited via different branches with the corresponding calculated vibrational dipole alignment coefficients (β_{axis}). Data taken on a Ni(110)-(*parallel* vs. *normal*)

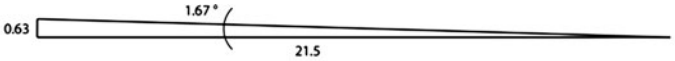

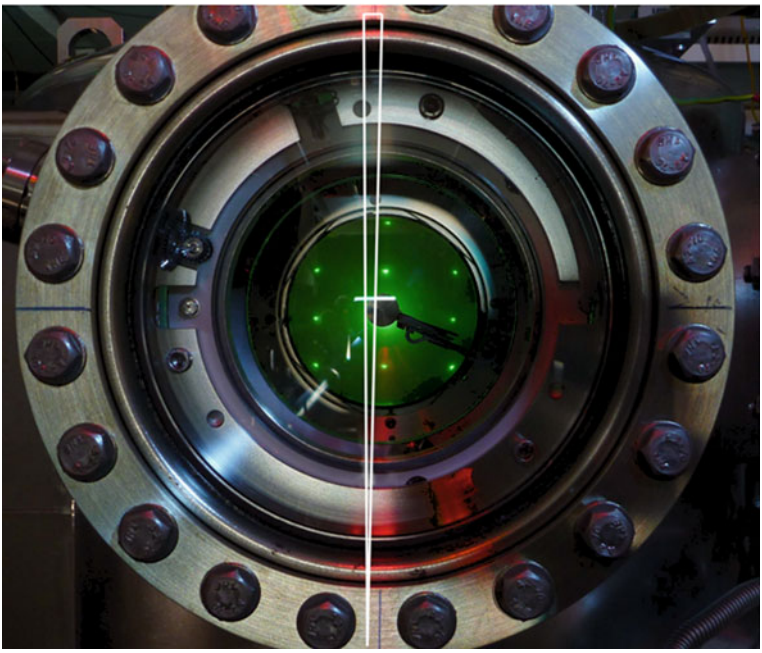

Fig. 5.8 LEED pattern of Ni(110) single crystal with rows aligned horizontally in the laboratory frame. This surface row alignment is used to produce the *perpendicular* experimental configuration

$CH_4(v_3)$-R(0) on Ni(110)-(*parallel* vs. *normal*) is 0.334 ± 0.014 compared to Δp of 0.216 ± 0.025 found for $CH_4(v_3)$-R(0) on Ni(100).

Figure 5.7 shows Δ_p values for three transitions versus the calculated $CH_4(v_3)$ alignment coefficients for the case of strong optical pumping. See Chap. 3 and appendix B for the calculation β_{axis}. The vertical axes of the graphs are scaled such that their origins and the values for Δp and β_{axis} coincide for the R(0) transition. As was the case for $CH_4(v_3)$-R(0) on Ni(100), the Δ_p stays positive (larger reactivity for parallel polarization for both R(0) and Q(1) excitation), and the observed alignment effect on reactivity coincides well with β_{axis} alignment coefficients.

The relative scaling Δ_p with β_{axis} strongly suggests that the observed alignment effect is due to an alignment of the vibrational dipole moment or net vibrational direction, similar to our findings for $CH_4(v_3)$ and $CD_3H(v_1)$ on Ni(100) and the findings of Zare and coworkers for the reaction of $CH_4(v_3)$ and $CD_3H(v_1)$ with gas phase Cl atoms [3, 4]. For its dissociation on both Ni(100) and on Ni(110), the alignment of the $CH_4(v_3)$ vibration parallel to the surface produces a higher reactivity than alignment normal to the surface.

5.3 $CH_4(v_3)$ on Ni(110)-(*Perpendicular* vs. *Normal*)

Aligning the Ni(110) rows horizontally in the laboratory frame makes it possible to have the laser polarization axis perpendicular to the surface rows which produces the reactant configuration termed *perpendicular*, see Fig. 5.3. This configuration has the rows aligned perpendicular to the impinging methane's aligned vibrational amplitude, which was determined to be responsible for the alignment dependent reactivity on Ni(100) in Chap. 4 and Ni(110) in the previous section. Figure 5.8 shows the LEED pattern of the Ni(110) surface in the configuration used for *perpendicular* experiments. In an analogous procedure to that outlined in the previous section, the alignment of the surface rows within 1.7° from the true horizontal in the laboratory frame.

For *perpendicular* compared to *normal*, we quantified the alignment dependent reactivity resulting from $CH_4(v_3)$ excited via the R(0) transition. The Δ_p value resulting from four molecular beam depositions of a 34 kJ/mol beam of $CH_4(v_3)$-R(0) on Ni(110) *perpendicular* versus *normal* is 0.385 ± 0.031.

Figure 5.9 shows the experimentally determined Δ_p for $CH_4(v_3)$-R(0) dissociation on Ni(100) and Ni(110)-(*parallel* vs. *normal*) and (*perpendicular* vs. *normal*). It is clear that the alignment contrast for $CH_4(v_3)$-R(0) is significantly larger on the Ni(110) than on Ni(100). Furthermore, the $CH_4(v_3)$-R(0) Δ_p value for Ni(110)-(*perpendicular* vs. *normal*) appears modestly but reproducibly larger than that of Ni(110)-(*parallel* vs. *normal*).

In Fig. 5.9, it is interesting to see that alignment dependent reactivity for a 34 kJ/mol beam of $CH_4(v_3)$-R(0) is significantly different from one single crystal nickel surface to another. Furthermore, alignment of the net vibrational amplitude

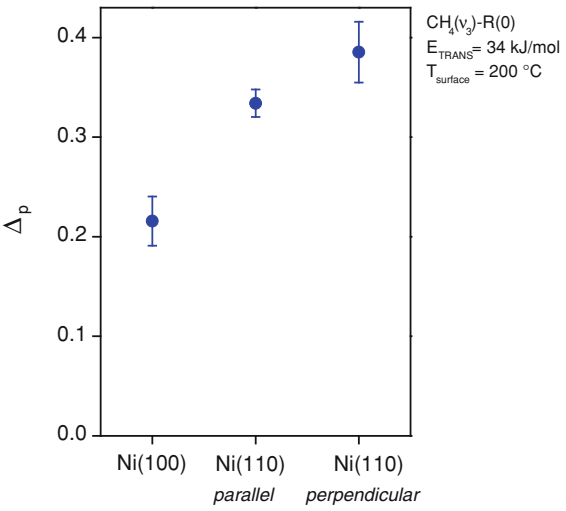

Fig. 5.9 Comparison of Δ_p for $CH_4(v_3)$-R(0) on Ni(100) and on Ni(110)-(*parallel* vs. *normal*) and Ni(110)-(*perpendicular* vs. *normal*)

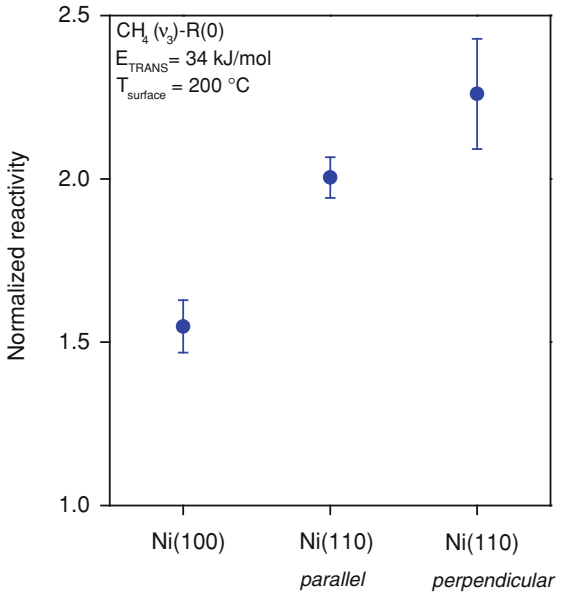

Fig. 5.10 Comparison of normalized reactivity for $CH_4(v_3)$ on Ni(100) and on Ni(110)-(*parallel* vs. *normal*) and Ni(110)-(*perpendicular* vs. *normal*). Each data set is normalized to the reactivity produced when the excitation is polarized along the surface normal

of $CH_4(v_3)$-R(0) parallel or perpendicular to surface-rows of a Ni(110) appears to have an effect on the alignment dependent reactivity.

The result of Ni(110)-*perpendicular* being more reactive than Ni(110)-*parallel* should be studied further. To date, we have performed four molecular beam deposition experiments for each configuration on Ni(110). For Ni(110)-*perpendicular*, we found $CH_4(v_3)$-R(0) Δ_p values of 0.367, 0.429, 0.362 and 0.382. For Ni(110)-*parallel*, we found $CH_4(v_3)$-R(0) Δ_p values of 0.327, 0.349, 0.318 and

0.341. The difference in Δ_p values for the two configurations is small and the experiment should to be repeated to reduce the error bars of the measurements.

5.4 Discussion of Results

The stereodynamics study of vibrationally excited CH_4 chemisorption on Ni(110) yields some interesting results. First, the alignment dependence of $CH_4(v_3)$ chemisorption on Ni(110) is due to an alignment of $\vec{\mu}_{21}$ in the laboratory frame with alignment parallel to the surface being more reactive than perpendicular alignment. Second, the alignment dependence of $CH_4(v_3)$-R(0) chemisorption is much more pronounced, as quantified by Δ_p, on Ni(110) than on Ni(100). Third, aligning the vibration perpendicular to the surface rows produces a higher reactivity than aligning $\vec{\mu}_{21}$ parallel to the surface rows. These results are considered in more depth in this section.

The alignment dependence of $CH_4(v_3)$ chemisorption on Ni(110) appears to be due to an alignment of the vibration in the laboratory frame. This is illustrated in Fig. 5.7 by the Δ_p of R(0), Q(1) and P(1) scaling well with the calculated β_{axis} alignment coefficients for said transitions. Similar to the study of $CH_4(v_3)$ dissociation on Ni(100), alignment of the net vibrational amplitude parallel to the surface produces a higher reactivity than perpendicular alignment. Again, the alignment dependent reactivity appears to be due to aligning the vibration in space without any knowledge of where the C–H bond axes are located in space, as is the case for $CH_4(v_3)$ excited via the R(0) transition.

The alignment dependence of $CH_4(v_3)$-R(0) chemisorption is much more pronounced on Ni(110) than on Ni(100). This is illustrated in Fig. 5.9, but may have more impact when presented as normalized reactivity as seen in Fig. 5.10. Each data set (i.e. Ni(100), Ni(110) *parallel*, and Ni(110) *perpendicular*) has been normalized to the lower reactivity excitation polarization direction (the excitation polarized along the surface normal for each experimental configuration). Therefore, the data in Fig. 5.10 shows an enhancement in reactivity obtained from rotating the excitation laser's polarization from perpendicular to parallel to the surface.

On Ni(100), aligning $\vec{\mu}_{21}$ parallel to the surface produces a reactivity 1.55x ($\pm$ 0.08) higher than aligning the vibration along the surface normal, as shown in Fig. 5.10. On Ni(110), aligning the vibration parallel to the surface produces a reactivity 2.00x ($\pm$0.06) and 2.26x ($\pm$0.17) higher than aligning the vibration along the surface normal for alignment of the vibration parallel to the surface rows and perpendicular to the surface rows, respectively. This difference between Ni(100) and Ni(110) is striking.

As discussed in the introduction of this chapter, excitation of the molecular beam with the laser polarized along the surface normal is expected to produce the same reactivity regardless of the Ni(110) surface row alignment, see Fig. 5.4. Therefore, the *normal* configuration should be able to serve as a common

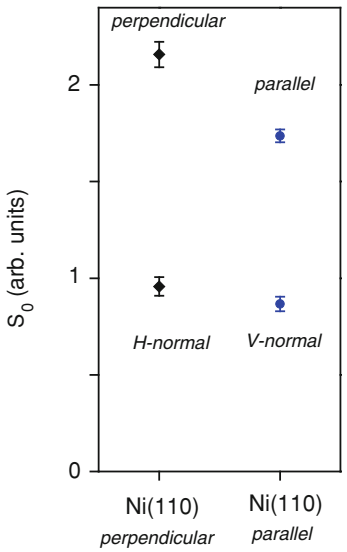

Fig. 5.11 Comparison of $CH_4(v_3)$-R(0) dissociation of Ni(110) in *perpendicular* and *parallel* configurations with their corresponding *normal* configuration reactivity shown as a reference for the two cases that are achieved by a rotation of the Ni(110) sample and therefore require the sample to be taken out of vacuum

denominator for the comparison of *parallel* and *perpendicular* configurations. The results presented in Fig. 5.11 show this idea to be reasonable.

Figure 5.11 shows the relative reactivity of $CH_4(v_3)$-R(0) on Ni(110) for four different experimental configurations: (1) (*perpendicular*) the laser polarized parallel to the surface plane and perpendicular to the surface rows which are horizontal in the lab frame, (2) (*H-normal*) the laser polarized normal to the surface with the surface rows horizontal in the lab frame, (3) (*parallel*) the laser polarized parallel to the surface plane and parallel to the surface rows which are vertical in the lab frame, and (4) (*V-normal*) the laser polarized normal to the surface with the surface rows vertical in the lab frame. The reactivity for excitation with the laser polarization along the surface normal appears to be independent of azimuthal orientation (surface row alignment) as seen by the overlapping error bars for the *H-normal* and *V-normal* configurations in Fig. 5.11. However, for the excitation polarized parallel to the surface, there is clear difference in the reactivity for alignment parallel and perpendicular to the closed packed rows. Therefore, the difference in Δ_p values for Ni(110) *perpendicular* and *parallel* configurations shown in Fig. 5.11 is, indeed, due to a reactivity difference associated with the vibration being aligned parallel or perpendicular to the surface rows. Aligning the net vibrational amplitude of $CH_4(v_3)$ perpendicular to the surface rows produces a higher reactivity than aligning the vibration parallel to the surface rows.

When attempting to explain the origin of the observed steric dependence of $CH_4(v_3)$ dissociative chemisorption on Ni(100) and Ni(110), there are several factors to consider. The reaction barrier for CH_4 dissociative chemisorption on Ni(110) is probably different between the two surfaces. Jackson and coworkers [5] calculated a minimum barrier of 0.908 eV (87.6 kJ/mol) for methane dissociation on Ni(100). I have not found theoretical data on the barrier height for methane

dissociation on a Ni(110) surface, but we will be able to assess the difference in the dissociation chemisorption barrier height between Ni(100) and Ni(110) when we determine 'absolute' dissociation probabilities on Ni(110). In the state-resolved, alignment dependent reactivity measurements of $CH_4(v_3)$ on Ni(100) and Ni(110), we used the same translational energy and rovibrational state of methane, namely 34 kJ/mol translational energy and 3028.75 cm^{-1} (36.2 kJ/mol) vibrational energy from R(0) excitation of $CH_4(v_3)$. Therefore, the dissociating methane molecule had $\sim$70 kJ/mol of energy available to overcome the reaction barrier of $\sim$88 kJ/mol on Ni(100). If Ni(110) had a higher barrier than Ni(100), one might expect a smaller cone of acceptance (stronger steric effect) for vibrationally excited CH_4 chemisorption on Ni(110). If the system does not have enough energy to overcome the reaction barrier, only those molecules with a most favorable alignment would pass through the reaction barrier to dissociation products.

The idea of a higher barrier height for CH_4 dissociation on Ni(110) than on Ni(100) being responsible for the stronger alignment dependence (higher Δ_p) for Ni(110) is not consistent with the molecular beam velocity dependence of $CH_4(v_3)$-R(0) dissociating on Ni(100), shown in Fig. 4.26. It was observed that the alignment dependence of $CH_4(v_3)$-R(0) dissociation on Ni(100) was essentially unchanged as the translational energy was increased from 9 to 49 kJ/mol. For the Ni(100) study, even as the energy available to the reactants was raised, the dependence of the reactivity was constant. It is more likely that the aligned vibration allows the impinging molecule to sample a part of the potential energy surface that has a lower barrier to dissociation. The two potential energy surfaces of vibrationally excited methane dissociating on Ni(100) and Ni(110) must be different. The 'preferred' (most reactive) alignment could 'lower' the reaction barrier more in the case of Ni(110) than for Ni(100).

Also, the two surfaces have different electronic structure. The Ni(110) surface may be more efficient at deexciting the $CH_4(v_3)$ by electronic friction than Ni(100) for the perpendicularly aligned vibration. Modeling of the steric dependence of vibrational relaxation as a vibrating dipole approaches a conducting surface could provide information as to why the observed alignment dependent reactivity is different for Ni(100) and Ni(110). Tully and coworkers [6–9] have developed a theoretical framework to model non-adiabatic behavior of vibrationally excited NO impinging on a cesium-covered Au(111) surface. They found a strong orientation dependence of the nonadiabatic transition rate for their system. Granted, the low work function of the surface and the highly vibrationally excited molecule modeled lends itself to non-adiabatic behavior, but it may be worthwhile to use their model to study the steric dependence of $CH_4(v_3)$ deexcitation as it approaches Ni(100) and Ni(110) surfaces.

Another plausible explanation for the alignment dependent reactivity of $CH_4(v_3)$ on Ni(110) is that we are preparing a gas-phase reactant that has elongated C–H bonds. The direction of the net bond elongation can be controlled in the laboratory frame by rotation of the excitation field's polarization. The most reactive gas phase reactant alignment could resemble a dissociation product state which may increase the tunneling rate of the reaction.

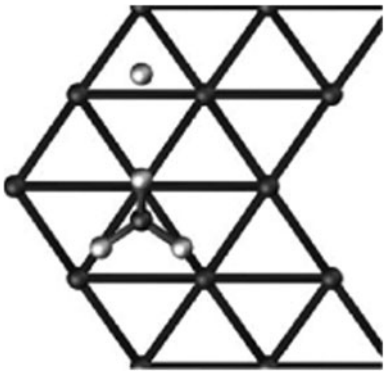

Fig. 5.12 Calculated lowest energy, product state structure for CH_4 dissoication on Pt(110)-(1 × 2) Here, the Pt-rows are aligned horizontally with respect to the page, the Pt-ridge is in the middle, and the valleys are at the *top* and *bottom*. Figure is reproduced with permission [5]

Recently, Jackson and coworkers [5] published a thorough study of methane dissociation along with CH_3 and H adsorption on five surfaces: Ni(111), Pt(111), Ni(100), Pt(100) and Pt(110)-(1 × 2). For all surfaces studies, the minimum energy pathway for dissociation was found to be over a top site with the dissociating H-atom directed toward the surface. Furthermore, the barriers were insensitive to rotation of the spectator CH_3-group as well as the azimuthal orientation of the dissociating C–H bond. For Ni(111) and Ni(100), it was noted that the resulting CH_3 and H adsorbed on the surface migrated away from the top site after dissociation. The most stable configuration by far (0.176 eV for Ni(111) and 0.138 eV for Ni(100)) of CH_3 and H dissociation products was found to be above a hollow site.

If this type of data [5] were available for Ni(110), one could begin to develop a physical picture to understand why aligning the vibration parallel to the surface but perpendicular to the Ni(110) surface rows is more reactive than aligning the net vibrational amplitude direction parallel to the surface plane and rows. If the transition state for methane dissociation on Ni(110) is similar to those found on Ni(111), Pt(111), Ni(100), Pt(100) and Pt(110)-(1 × 2) and then the CH_3 and H products migrated away from the transition state perpendicular to the surface rows, one could attribute the higher reactivity of this alignment to the directed net vibrational amplitude toward the most stable product state. If the most stable product state for methane's dissociative chemisorption had the CH_3 and H products separated perpendicularly to the surface rows, it would make physical sense that we were matching the 'product state' by aligning the vibrating molecule such that the net vibrational amplitude was along the surface plane, but perpendicular to its rows.

For the calculations of CH_4 dissociating on Pt(110)-(1 × 2) [5], Jackson and coworkers found the lowest energy transition state structures to have the dissociating CH bond above a ridge Pt-atom. The difference in energy between the transition state with dissociating CH bond parallel and perpendicular to the Pt-ridge was only 1.2 kJ/mol. However, the most stable product structure by nearly 14 kJ/mol had the H-atom residing in the valley of the corrugated Pt-surface, after a migration perpendicular to the surface rows. Figure 5.12 shows the most stable product state configuration for CH_4 dissociation on Pt(110)-(1 × 2). If Ni(110)

behaves similarly to Pt(110)-(1 × 2), we may expect an increased tunneling effect if $\vec{\mu}_{21}$ is aligned perpendicular to the surface rows.

The stereodynamics study of the dissociative chemisorption $CH_4(v_3)$ on Ni(110) is presented, here, as an example of the level of detail attainable with this experimental setup. We have exerted control over several aspects of a gas-surface reaction, including the gas-phase reactants' approach direction and velocity, quantum state and relative alignments of both reaction partners in the laboratory frame. More experiments are needed to fully characterize this molecule/surface system, including the saturation coverage of carbon on the Ni(110) surface which is needed to calculate absolute initial sticking coefficients and to apply the S/S_0 correction in the Δ_p determination. An angular dependence of the alignment with respect to the surface and a molecular beam speed dependence for Ni(110) would be interesting to compare to those of Ni(100).

A comparative study of the alignment dependent reactivity of vibrationally excited methane on Ni(111), Ni(100) and Ni(110) would establish if surface corrugation plays a role in determining the magnitude of Δ_p. Surface corrugation increases from (111) to (100) to (110) surfaces.

References

1. D.F. Mitchell, P.B. Sewell, M. Cohen, Kinetic study of initial oxidation of Ni(110) surface by RHEED and X-ray emission. Surf. Sci. **69**(1), 310–324 (1977)
2. W. Neil, N.D.M. Ashcroft, *Solid State Physics* (Saunders College Publishing, Fort Worth, 1976)
3. W.R. Simpson, S.A. Kandel, A.J. Orr-Ewing, R.N. Zare, Reaction of Cl with vibrationally excited CH_4 and CHD_3: State-to-state differential cross sections and steric effects for the HCl product. J. Chem. Phys. **103**(17), 7313–7335 (1995)
4. W.R. Simpson et al., Reaction of Cl with vibrationally excited CH_4 and CHD_3 - state-to-state differential cross-sections and steric effects for the HCl product. J. Chem. Phys. **103**(17), 7313–7335 (1995)
5. S. Nave, A.K. Tiwari, B. Jackson, Methane dissociation and adsorption on Ni(111), Pt(111), Ni(100), Pt(100), and Pt(110)-(1x2): Energetic study. J. Chem. Phys. **132**(5), 054705 (2010)
6. N. Shenvi, S. Roy, J.C. Tully, Dynamical Steering and Electronic Excitation in NO Scattering from a Gold Surface. Science **326**(5954), 829–832 (2009)
7. N. Shenvi, S. Roy, J.C. Tully, Nonadiabatic dynamics at metal surfaces: Independent-electron surface hopping. J. Chem. Phys. **130**(17), 1 (2009)
8. S. Roy, N.A. Shenvi, J.C. Tully, Model Hamiltonian for the interaction of NO with the Au(111) surface. J. Chem. Phys. **130**(17), 174716 (2009)
9. S. Roy, N. Shenvi, J.C. Tully, Dynamics of open-shell species at metal surfaces. J. Phys. Chem. C. **113**(37), 16311–16320 (2009)

Chapter 6
Summary and Outlook

6.1 Summary

The results in this thesis work demonstrate steric effects in the dissociative chemisorption of vibrationally excited methane on nickel for the first time. A linearly polarized excitation laser was used to prepare a molecular beam of methane in a specific quantum state while simultaneously aligning its angular momentum ($\overrightarrow{J}$) and vibrational transition dipole moment ($\overrightarrow{\mu}_{21}$).

The three model gas-surface reactions used in this thesis work are:

$$CH_4(v_3 = 1, J)(g) \xrightarrow{Ni(100)} CH_3(ads.) + H(ads.)$$

$$CD_3H(v_1 = 1, J)(g) \xrightarrow{Ni(100)} CD_3(ads.) + H(ads.)$$

$$CH_4(v_3 = 1, J)(g) \xrightarrow{Ni(110)} CH_3(ads.) + H(ads.)$$

Here, v_3 and v_1 denote the antisymmetric stretch mode of CH_4 and the C–H stretch mode of CD_3H, respectively. For each system, excitation of the gas-phase reactant with the laser polarization parallel to the surface produced a higher reactivity than when the laser was polarized perpendicular to the surface.

Dephasing of the prepared alignment was observed for $CH_4(v_3)$-R(0) and $CD_3H(v_1)$-R(0) on Ni(100) by increasing the excitation-to-surface distance. Complete dephasing was observed on a timescale of $\sim$15 μs for $CH_4(v_3)$-R(0) and $\sim$6 μs for $CD_3H(v_1)$-R(0). These dephasing times appear consistent with the hyperfine splittings for the excited state of each ro-vibrationally excited isotopologue. For the typical excitation-to-surface delay times ($\sim$500 ns) in our experiments, dephasing of the initially prepared alignments should be limited, and was neglected during the data analysis.

B. L. Yoder, *Steric Effects in the Chemisorption of Vibrationally Excited Methane on Nickel,* Springer Theses, DOI: 10.1007/978-3-642-27679-8_6,

Varying degrees of alignment were produced through excitation of $CH_4(v_3)$ and $CD_3H(v_1)$ by P-, Q- and R-branch transitions. The observed alignment dependent reactivity was quantified by the *alignment contrast* Δ_p defined in Eq. 4.1. For both molecules, the largest Δ_p value was found for excitation via the R(0) transition. No difference in reactivity ($\Delta_p = 0$) due to rotation of the excitation's polarization was observed for either $CH_4(v_3)$ or $CD_3H(v_1)$ prepared via their respective P(1) transition. The experimentally determined Δ_p values were compared to calculated alignment coefficients, $A_0^{(2)}$ and β_{axis}, developed by Zare and others [1–6]. These coefficients describe the alignment of the angular momentum (J-vector) and the vibrational transition dipole moment upon excitation by linearly polarized light and are valid for the case of strong optical pumping in our experiments. As the Δ_p values for $CH_4(v_3)$ and $CD_3H(v_1)$ prepared by P-, Q- and R-branch excitation scale well with β_{axis} but not $A_0^{(2)}$, the alignment dependent reactivity was attributed to an alignment of the vibrational transition dipole moment or the net vibrational amplitude in the laboratory frame.

The angle that the excitation laser's polarization makes with the surface was varied to reveal a monotonic decrease in reactivity from parallel to perpendicular to the surface for both $CH_4(v_3)$-R(0) and $CD_3H(v_1)$-R(0) on Ni(100). This similarity is striking and very interesting since the details of the alignment produced in the two isotopologues are quite different. The alignment produced by $CH_4(v_3)$-R(0) gives no information as to where the C–H bonds are located in space. Classically, the ro-vibrationally excited CH_4 molecule can be visualized as a vibrating ellipsoid with only the major axis of the ellipsoid defined in space and the H atoms being located somewhere on the ellipsoid surface. In contrast, $CD_3H(v_1)$ excited via the R(0) transition aligns the unique C–H bond of the molecule in space along the excitation laser's polarization axis. Furthermore, it has been shown that CD_3H prepared in ($v_1 = 1$) undergoes bond-selective dissociation on Ni(111) by breaking the stretch excited C–H bond [7]. For $CD_3H(v_1)$-R(0), the reactive bond of the system is aligned in the experiment.

The difference in prepared alignment between $CH_4(v_3)$-R(0) and $CD_3H(v_1)$-R(0) in conjunction with their similar angular dependences suggests that we do not observe a steric effect in the dissociation due to bond alignment. Several groups have calculated the lowest energy transition state for methane dissociation on a metal surface to have the dissociating C–H bond extended and at an angle of $\sim 45°$ [8–11] with respect to the surface normal. If the alignment effect were due to bond alignment, one might expect to a maximum in reactivity for $CD_3H(v_1)$-R(0) on Ni(100) when the excitation is polarized at an angle of 45° with respect to the surface. No local maximum in reactivity at an alignment of 45° was observed for $CD_3H(v_1)$-R(0). Furthermore, we observe a larger alignment dependence on reactivity for $CH_4(v_3)$-R(0) than for $CD_3H(v_1)$-R(0) dissociation on Ni(100). These two observations would not be sensible if the alignment dependent reactivity were attributed to bond alignment along the minimum energy reaction pathway.

For the Ni(100), a molecular beam velocity dependence of Δ_p was measured for both methane isotopologues. For $CH_4(v_3)$-R(0) on Ni(100), no significant variation

in Δ_p was observed for molecular beam velocities of 1000–3000 m/sec (9–65 kJ/mol). For $CD_3H(v_1)$-R(0) dissociation on Ni(100), Δ_p decreased by more than a factor of two when the velocity of the molecular beam was increased from 1,700 to 2,700 m/sec (28.2 and 71 kJ/mol). These velocity dependences suggest that 'steering' of the gas phase reactant is not important as it approaches the metal surface. If steering were important, one would expect Δ_p to increase with increasing molecular beam velocity. This expectation stems from a decrease in the gas-surface interaction time as the gas molecule's velocity is increased. A decreased interaction time would allow less time for the gas phase reactant to be reoriented (steered) into the lowest energy pathway to reaction. A decrease in Δ_p with increasing molecular beam velocity could be interpreted as a softening of the steric requirement associated with an 'over the barrier' reaction. As the reaction has enough energy to surmount the reaction barrier, less-favorable reactant orientations will be able to react and the steric effect (requirement) on reactivity should be diminished. A physical explanation for the difference in the observed velocity dependences for the dissociative chemisorption of $CH_4(v_3)$-R(0) and $CD_3H(v_1)$-R(0) on Ni(100) is currently unclear.

Comparison of the alignment dependent reactivity to state-resolved initial reaction probabilities $S_0(v_3)$ for the dissociation of $CH_4(v_3)$ on Ni(100) is interesting. The reactivity of $CH_4(v_3)$-R(0) prepared by parallel polarization is $\sim 60\%$ higher than polarization perpendicular to the surface, and the *alignment contrast* (Δ_p) remains essentially constant between translational energies of 9–50 kJ/mol. Nonetheless, this increase of translational energy causes $S_0(v_3)$ to rise by about 3 orders of magnitude from about 2×10^{-6} to about 2×10^{-3}.

The $S_0(v_3)$ for CH_4 on Ni(100) were compared to those of Utz and coworkers [12] at Tufts University. Increasing the translational energy of CH_4 from 15 to 50 kJ/mol, we observed a rise in $S_0(v_3)$ from 1×10^{-5} to 2×10^{-3} in agreement with the results published by the Tufts group. We assessed the rotational (J) level dependence of $S_0(v_3)$ for $CH_4(v_3)$ dissociation on Ni(100) by state-preparation of $CH_4(v_3)$ in $J = 0$, 1 and 2. We observed less than a factor of 2 difference in reactivity as J was increased from 0 to 2, on $S_0(v_3)$ was observed, in agreement with a similar study by Utz and coworkers [13].

For $CH_4(v_3)$ dissociation on Ni(110), the rows of closed packed surface atoms on Ni(110) were aligned in the laboratory frame. $CH_4(v_3)$ reactivity was probed for the excitation laser polarization parallel to the plane of the surface both for *parallel* and *perpendicular* alignment with respect to the surface rows by aligning the surface rows either vertically or horizontally in the laboratory frame. For both surface row alignments, the excitation field polarization could be made '*normal*' to the surface plane. The '*normal*' excitation produced a similar reactivity for both surface row alignments. This allowed for the comparison of the reactivity of a molecular beam of $CH_4(v_3)$ excited by an excitation field polarized '*parallel*' and '*perpendicular*' to the surface rows.

The alignment angle dependence of the reactivity for $CH_4(v_3)$ on Ni(110) was similar to that of $CH_4(v_3)$ on Ni(100) except that the *alignment contrast* Δ_p observed on Ni(110) is larger than on N(100). Comparison of calculated alignment

coefficients to experimentally determined Δ_p values for R(0), Q(1) and P(1) showed that also on Ni(110), the alignment effect is due to the alignment of net vibrational amplitude. State-resolved, alignment dependent reactivities were measured for $CH_4(v_3)$ on Ni(100), $CH_4(v_3)$ on Ni(110)-'*parallel*' and $CH_4(v_3)$ on Ni(110)-'*perpendicular*' using a molecular beam of 34 kJ/mol translational energy. The three systems/configurations produced Δ_p values for R(0) excitation of 0.216 ± 0.025, 0.334 ± 0.014 and 0.385 ± 0.031, respectively.

For $CH_4(v_3)$-R(0) on Ni(110)-'*parallel*', the reactivity is increased 2.00 x ($\pm$ 0.06) by exciting with the laser polarized parallel to the surface as opposed to normal to it. For $CH_4(v_3)$ on Ni(110)-'*perpendicular*', the reactivity is increased by 2.26 x ($\pm$ 0.17) by excitation with the laser polarized parallel to the surface as opposed to normal. This result shows that aligning the net vibrational amplitude of $CH_4(v_3)$ perpendicular to the surface rows produces a higher reactivity than aligning it parallel to the surface rows. Advanced modeling of the gas-surface reaction is required to explain the alignment dependent reactivities observed in these experiments.

Currently, there are a number of open questions that would need more refined theoretical treatment in order to be answered conclusively. First, why is a vibrationally excited methane ($CH_4(v_3)$ and $CD_3H(v_1)$) molecule more reactive on Ni(100) and Ni(110) when its net vibrational amplitude is aligned parallel to the surface plane rather than perpendicular ($\Delta_p > 0$)? Second, why is the Δ_p of $CH_4(v_3)$-R(0) larger for dissociation on Ni(110) than on Ni(100)? Third, why is $CH_4(v_3)$-R(0) reactivity slightly higher when its net vibrational amplitude is aligned perpendicular to the surface rows of Ni(110) than when it is aligned parallel to the surface rows? In order to answer these questions, a fundamental understanding of the alignment effect is needed. While I have made suggestions on how to explain the alignment effect, I am unable to pinpoint the cause with the experimental results shown in this thesis. The alignment effect appears to be caused by an alignment of the gas-phase reactant's vibration with respect to the metal surface, but I do not understand in detail how that influences the reactivity.

The observed steric effects in the dissociation of vibrationally excited methane on Ni(100) and Ni(110), presented here, constitute evidence for a non-statistical mechanism of methane chemisorption. This is in addition to the previously reported mode-specificity [14] and bond-selectivity [7]. These results demonstrate that the reaction probability is not simply controlled by the available energy but is also sensitive to the initial geometry, a fact that is incompatible with statistical rate theory [15–17], which assumes complete randomization of the initial conditions in the collision complex predicting reaction rates solely on energetics. Statistical theories can at best be made to fit the ensemble average over a distribution of quantum states and steric conditions but are unable to correctly describe the actual reactive event between an incident molecule and solid surface on a microscopic scale.

The observation of quantum state-resolved steric effects in the chemisorption of vibrationally excited methane brings valuable information toward a molecular-level understanding of gas-surface reaction dynamics. Experiment and theory must be conducted in tandem to obtain an understanding of gas-surface interactions.

The experimental findings presented here will be useful to test and improve theoretical models. With improved models, we move toward the goal of a predictive understanding of gas-surface interactions and the development of more efficient catalysts.

6.2 Experimental Improvements

6.2.1 Modulation of Excitation Laser Polarization

We should develop a method to periodically vary the laser polarization during a deposition experiment. With such a method, lock-in detection could be used to monitor the relative reaction probability of excited molecules as a function of their alignment by linearly polarized excitation DURING a deposition experiment. The ability to characterize polarization dependent reactivity during a deposition experiment would allow us to bypass the most time-expensive step of our experiment: Auger electron spectroscopy product detection.

Preliminary tests of rotating the polarization with a Pockel's cell, namely an E-O Q crystal from Day Optics, were conducted. Currently, we are able to periodically rotate the laser polarization by 90° with the Pockel's cell. Figure 6.1 shows the experimental setup for modulating the excitation laser polarization in its current form. Below, I discuss the progress made and to be made with this setup.

The idler beam is well polarized horizontal at the optical parametric oscillator (OPO) output, shown in Fig. 6.1 by a double-headed arrow. A Pockel's cell is placed in the beam path to modulate the laser polarization. A Bertran 225 high voltage (HV) power supply is used to provide the 0–3.2 kV needed to rotate the linear polarization of 3.3 μm light used to ro-vibrationally excite methane, see Pockel's cell specifications. The HV output of the Bertran 225 is modulated via remote control. A 50% duty cycle square wave is produced in Labview and sent from a digital to analog converter (DAQ) to the remote control input of the Bertran 225. The input of 0–5 V is amplified to 0–5 kV (500 μA maximum) at the Bertran HV output. We are able to switch the HV output voltage from 0 to 3 kV at a frequency of 0.5 Hz by placing an 8.7 MΩ resistor (R in Fig. 6.1) in parallel to the Pockel's cell to allow a path to ground for the discharging voltage. To selectively detect vertically polarized light, a linear polarizer (Glan-Taylor in Fig. 6.1) is placed in the laser path after the Pockel's cell and aligned vertically. A power meter is used to measure the power of the light transmitted through the polarizer, which gives a measure of the extent of polarization rotation.

Figure 6.2 shows a modulated signal on the power meter (from Fig. 6.1) when sending a 50% duty cycle 0–2.8 kV square wave at a frequency of 0.5 Hz. For this measurement, the current of the HV-signal varied from 0 to 0.32 mA. The HV was limited to 2.8 kV because arching occurred at higher modulation voltages. We see that the laser power after the linear polarizer (and therefore the linear polarization) is modulated from 0 to ∼130 mW (from horizontal to vertical) periodically. At

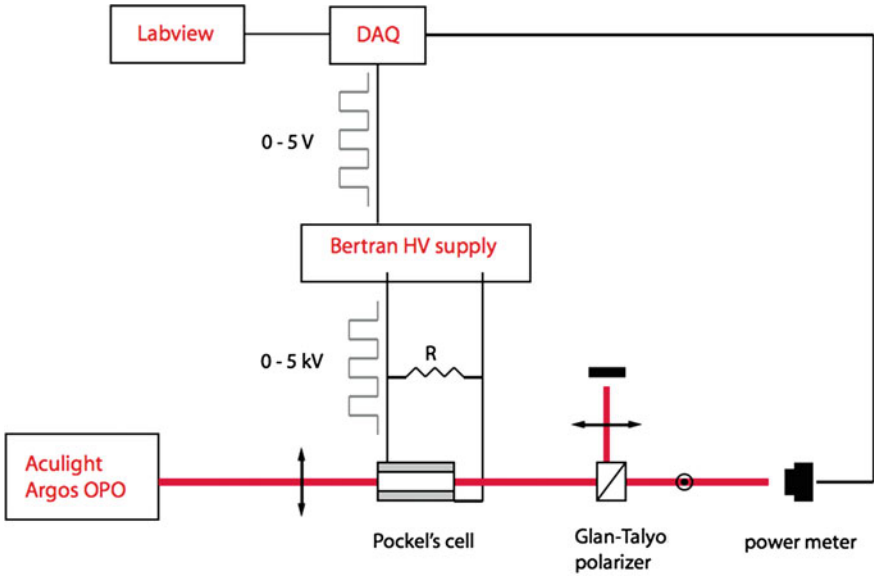

Fig. 6.1 Experimental setup used to characterize the Pockel's cell's ability to rotate the linear polarization of a 3.3 μm wavelength laser beam

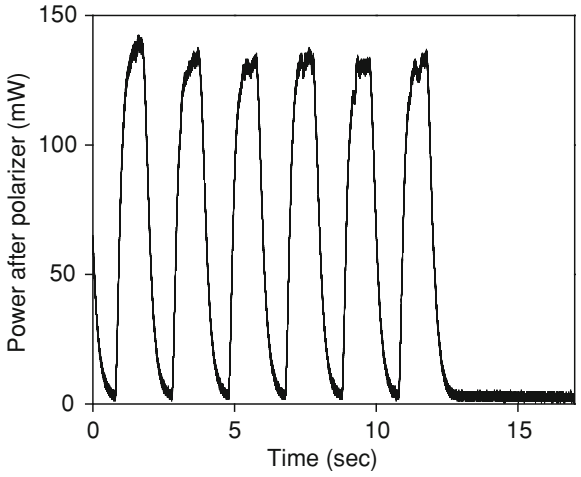

Fig. 6.2 Modulated laser polarization data as seen by the power transmitted through a linear polarizer upon sending a 0–2.8 kV square wave to a Pockel's cell to rotation the linear polarization of a laser beam

this modulation frequency, the HV supply is able to reach its maximum and zero voltages as seen by the measured power on the power meter reaching a maximum and zero power measurement. This modulation signal is promising, but there are a few issues to be addressed in this experimental setup.

The first complication is the transmission of the Pockel's cell. The modulated signal in Fig. 6.2 measured after the linear polarizer varied from 0 to 130 mW, while the power before the Pockel's cell was 360 mW and the power between the Pockel's

cell and the linear polarizer was 165 mW. This means that the Pockel's cell transmission was only 46%. Furthermore, there was a loss of about 22% on the polarizer with a voltage of 2.8 kV applied to the Pockel's cell. This shows that the polarization rotation is incomplete at 2.8 kV because the well aligned linear polarizer has a loss of <10%. The Pockel's cell needs a voltage of ~3.2 kV to rotate 3.3 μm light (wavelength used to excite $CH_4(\nu_3)$ and $CD_3H(\nu_1)$) by 90°. When > 3000 V is applied across the Pockel's cell, there is arching between the cell's electrodes which are spaced by 3 mm by a $LiNbO_3$ crystal. This problem needs to be addressed before modulating the excitation laser polarization can be implemented into the experimental setup. I would suggest purchasing a different Pockel's cell. It would be convenient to have a Pockel's cell that is larger than the laser beam diameter, to allow easier alignment and higher transmission, and is able to rotate the laser polarization 90° with a voltage that does not cause arching across the electrodes.

6.2.2 *Free-Swinging UHV Pendulum for Molecular Beam Chopping*

Modulated King and Wells measurements [18] via molecular beam chopping by a UHV pendulum would eliminate the time consuming data collection step of taking Auger spectroscopy profiles to determine the amount of carbon deposited on the surface during an experiment. The basic experiment is to periodically chop a continuous molecular beam in the UHV chamber at a frequency that is slower than the chamber's pump out time. The pump out time is given by the chamber volume (150 L) divided by the pumping speed (500 L/sec) and is ~0.3 s. When the molecular beam is 'blocked' it would be scattered in the UHV chamber by an inert material (e.g. mica). When the molecular beam is unperturbed by said chopper, it would impinge on the reactive surface in the UHV (e.g. Ni(100)). The partial pressure of gas-phase reactant in the UHV chamber would be monitored by a mass spectrometer. Any molecules that stick to the reactive surface would be registered as a drop in the monitored gas' partial pressure. To measure small partial pressure variations in the monitored gas, we could use phase sensitive detection via a lock-in amplifier referenced to the molecular beam modulation. Figure 6.3 shows the general experimental setup for this modulated King and Wells experiment. The molecular beam is periodically scattered from a mica flag attached to a free-swinging pendulum that is housed in the UHV chamber. When the pendulum blocks the molecular beam, the molecules are scattered in the UHV chamber and are not seen by the reactive surface.

Inspired by a design from a group in the Czech Republic [19], I have developed a functioning pendulum driven by a pair of home-made electromagnets in the UHV chamber. The Mangifer soft magnet cores were purchased from ED FAGAN Inc., formed and annealed in house, then wound with 300 turns of kapton wire (KAP012) purchased from Caburn MDC. KAP012 was chosen because it is flexible enough to be wound around the cylindrical soft magnet cores (diameter

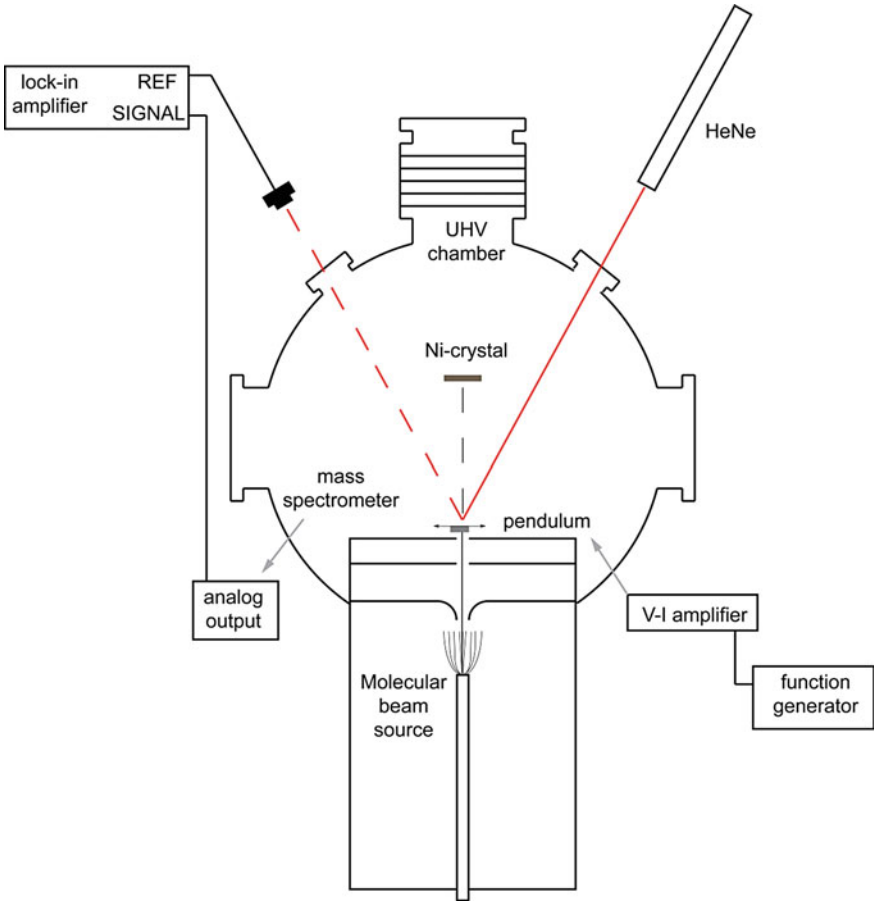

Fig. 6.3 Experimental setup for modulated King and Wells measurements employing a free-swinging pendulum in the UHV chamber

8 mm), its kapton insulation is UHV compatible and its resistance (1.6 Ω/m) was low enough to not cause significant heating when current was applied to it in the UHV chamber. Figure 6.4 shows an assembly drawing of the UHV pendulum.

The rotation axis of the pendulum is located 32 cm above the molecular beam entrance aperture to the UHV. The pendulum arm is composed of the rotation axis (Al), the lever arm (Al), a steel doughnut placed between to two electromagnets (to be pulled by the electromagnets), a counter-weight made of tungsten to tailor the pendulum's center of mass and, in turn its eigenfrequency, a mica flag to scatter the molecular beam and a polished stainless steel reflector to reflect a HeNe laser beam used as the lock-in amplifier reference signal. The pendulum arm has a total mass of 39 mg with its calculated center of mass at a distance of 25 cm from the rotation axis. This translates to an expected eigenfrequency of 0.996 Hz.

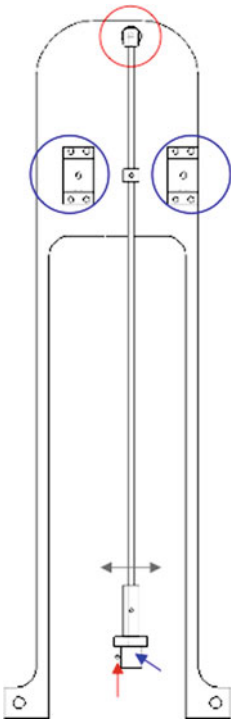

Fig. 6.4 Assembly drawing of UHV pendulum. The two *blue circles* shown positions of home-made electromagnets used to swing the pendulum arm about its pivot point, *circled in red*. The *blue arrow* points to a mica sheet that is swung in and out of the molecular beam path. The*red arrow* points to the molecular beam's input aperture to the UHV chamber

Figure 6.5 shows an experimental determination of the pendulum's eigenfrequency while under vacuum in the UHV chamber. The data is generated by reflecting a HeNe laser beam off of the polished stainless steel reflector. The HeNe reflection is collected by a photodiode and sent to a 12-bit data acquisition card. Data was saved in Labview. The pendulum was set in motion by applying a drive signal to the electromagnets. Then, the drive-current supplied to the electromagnets was stopped. The decreasing photodiode signal in Fig. 6.5 is a measure of the decreasing amplitude of the pendulum with the frequency corresponding to the true eigenfrequency of the pendulum. From the data shown in Fig. 6.5, the pendulum eigenfrequency is 0.9347 Hz, which agrees reasonably well (within 6.5%) what I expected from the calculation above.

The free-swinging pendulum is driven by a single electromagnet ($R \sim 15.5\ \Omega$) using a Stanford Research Systems (SRS) function generator to produce either a 50% duty cycle square wave or a sine wave at 0.935 Hz with an amplitude of ~ 80 mA. A dual channel homebuilt V–I amplifier was made to transform a command voltage sent from either Labview or a function generator to a current needed to drive the electromagnets. A V–I amplifier calibration curve is given in Fig. 6.6 and is linear to 400 mA. The amplifier was constructed to produce 400 mA with a command voltage of <10 V because it was experimentally determined that ~ 400 mA of current through an electromagnet created a strong

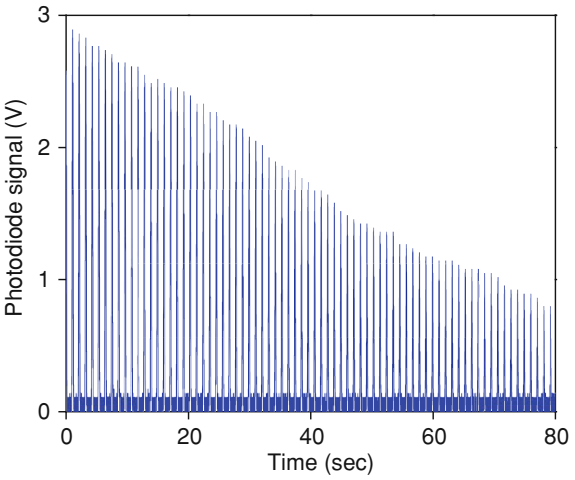

Fig. 6.5 Data showing the eigenfrequency and amplitude decay time of the UHV pendulum

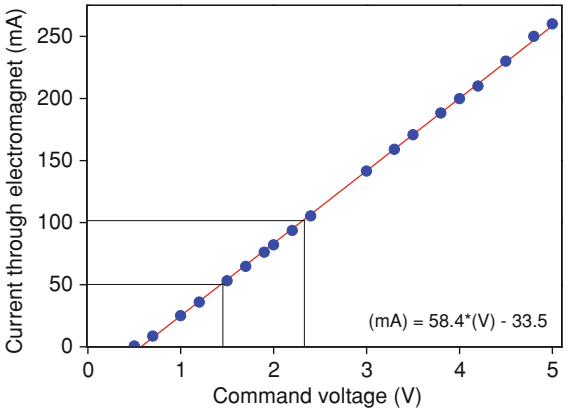

Fig. 6.6 Calibration curve for the V–I amplifier used to drive the pendulum electromagnets. The thin lines show the command and output current ranges for stable swinging of the pendulum (1.4–2.4 V and 49–107 mA, respectively)

enough magnetic field to bring and hold the pendulum arm against said electromagnet. Sending ~400 mA through one of these electromagnets under UHV conditions does cause a pressure rise after a few seconds and should be avoided. But, the pendulum can be swung at a stable amplitude for >1.5 h without a detectable pressure rise in the UHV chamber (at 6.5×10^{-11} mbar).

Placing the pyroelectric detector in the molecular beam path, I was able to lock-in detect the kinetic energy signal of a pendulum-chopped 12% CH_4 in H_2 molecular beam with a backing pressure of 1.7 bar and a nozzle temperature of 26°C (~30 kJ/mol). The lock-in amplifier was set in R, θ mode with a sensitivity of 100 mV and a time constant of 100 ms. Figure 6.7 shows the test result. The lock-in detected signal on the pyroelectric is ~16 mV ± 10% for the time that the molecular beam was ON. This is encouraging data, but the system needs to be optimized as a signal variation of ± 10% is unacceptable.

It has proved difficult to match the command frequency exactly to the eigenfrequency of the pendulum. Figure 6.8 illustrates this. The command signal sent

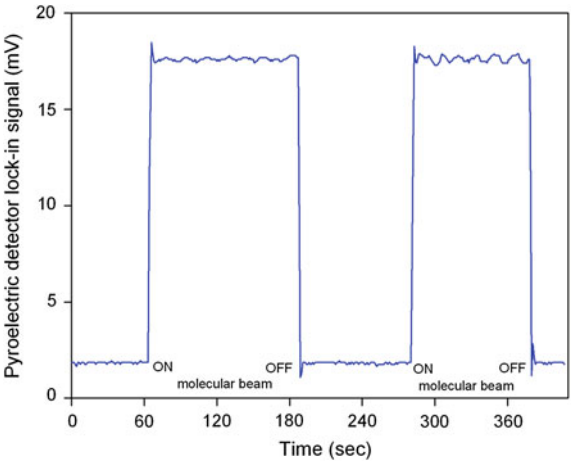

Fig. 6.7 Lock-in detected data from free swinging pendulum chopped molecular beam impining onto the pyroelectric detector

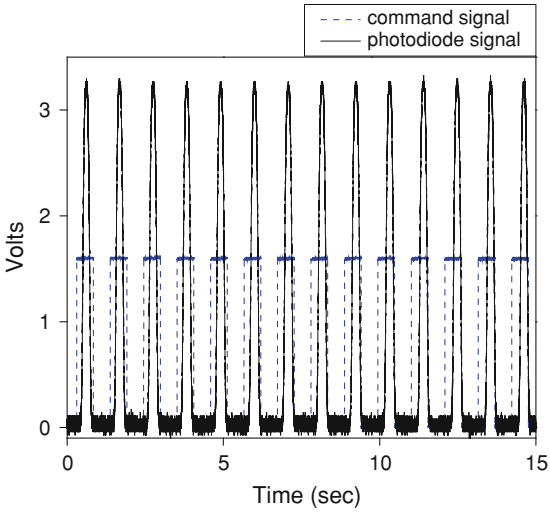

Fig. 6.8 Command signal to electromagnet driven pendulum compared to photodiode signal from reflected He–Ne beam used as a reference for lock-in detection of pendulum chopped molecular beam

from the function generator is constant at 0.935 Hz, but the reference (photodiode) signal given by the photodiode detection of the HeNe laser reflection from the photodiode is varying in frequency. This frequency shift is visible in Fig. 6.8. Close inspection of the photodiode signal shows that the pendulum frequency is varying under the influence of a constant command frequency.

The small mismatch of the command frequency and the pendulum's eigen-frequency is small enough to allow stable swinging of pendulum for extended periods of time. However, the small frequency mismatch produces a varying phase relationship between the command signal and the actual frequency of the pendulum. This phase instability is translated into noise on the lock-in detected signal due to the inconsistent phase of the pendulum. The lock-in phase (represented by

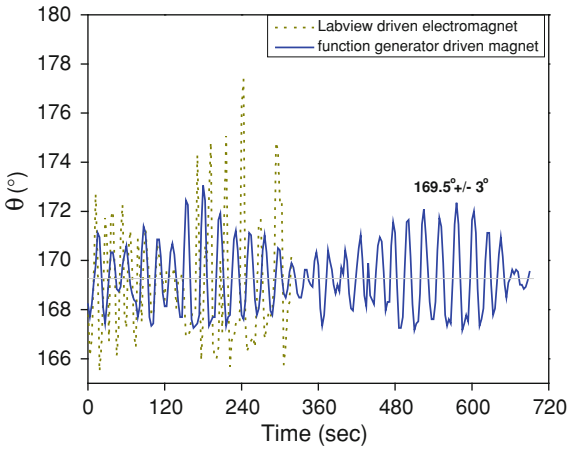

Fig. 6.9 Example of phase instability in the free swinging pendulum in the UHV chamber

the angle θ) is given in Fig. 6.9 to show the instability as a function of time. This is an example of the phase stability of the free swinging pendulum setup, and represents the current state of the experimental setup.

The data in Fig. 6.9 were generated by driving the pendulum with a single electromagnet at 0.935 Hz via a 50% duty cycle square wave producing a drive current in the electromagnet of 0–80 mA. The lock-in reference was the photodiode signal of the reflected HeNe beam. The scattered light signal from the HeNe onto the pyroelectric detector was used as the modulated signal for lock-in detection. The lock-in amplifier settings were 1 V and 1 s in R, θ mode. Data was collected in Labview at a sampling rate of 0.33 Hz. There are two frequencies beating in the lock-in phase measurement, a fast one of 0.04 Hz and a slow one a 0.007 Hz. These instabilities need to be addressed for the pendulum to be useful for data collection. Due to time restraints, I was not able to progress any further on this project.

A Pfeiffer mass spectrometer with analog output has, also, been installed in the UHV chamber and can be controlled by computer software. This mass spectrometer is useful for the experimental setup described here, since it has an analog output that can serve as the lock-in 'signal'. We plan to use the Pfeiffer mass spectrometer to monitor the partial pressure of a gas studied for reactivity measurements (e.g. methane). Optimization of the mass spectrometer settings needs to be completed to maximize the signal-to-noise of the detection system.

6.3 Future Directions

The methods of rovibrational excitation and molecular alignment in the laboratory frame used here can readily be generalized to other vibrational states of methane as well as to different molecule/surface systems. The observations reported in this

thesis should serve as motivation to explore the dynamical stereochemistry of other heterogeneously catalyzed reactions by quantum state-resolved reactivity measurements.

Interesting candidates for steric effect studies of gas-surface reactions are CO_2 antisymmetric stretch excited at $\sim 2390\ cm^{-1}$, CO stretch excited at $\sim 2140\ cm^{-1}$, H_2O stretch excited at $\sim 3600\ cm^{-1}$. I find the antisymmetric stretch of CO_2 to be most attractive. Due to its $D_{\infty h}$ symmetry, CO_2 provides a straightforward interpretation of the alignment dependent reactivity results. Consider the case where the excitation laser is polarized perpendicular to the surface plane. The O–C–O axis will be aligned along the surface normal, and will always present an O-atom to the surface. Therefore, the limitation of averaging over parallel and antiparallel orientations arising from the nature of the experimental setup (linear polarization acts as double-headed arrow and cannot differentiate between parallel and antiparallel orientations) can be circumvented with this molecule. With vibrationally excited CO_2 one could investigate the difference between impinging the molecule on a reactive surface: presenting an O-atom to the surface or presenting the O–C-O length (broadside) to the surface.

It would, also, be interesting to study the alignment dependent reactivity of a vibrationally excited molecule on a semiconductor surface. A semiconductor surface would have a band-gap, and not produce an image charge of the dynamic dipole that is the vibrationally excited, aligned gas-phase reactant. This would allow us to address the question as to whether the steric effect is due to an image charge in the metal as the gas phase reactant approaches it. A reasonable candidate system for this study would be vibrationally excited SiH_4 dissociation on a Si(100) surface, as we have already produced quantum state-resolved measurements on this system [20, 21]. If the steric effect of SiH_4 dissociation on a Si(100) is observed to be similar to that of CH_4 dissociation on metal surfaces, the idea of an impinging gas-phase molecule interacting with its image dipole being responsible for the alignment dependent reactivity could be excluded.

Modulated experiments exploiting lock-in detection to quantify gas-surface reactivity during a deposition experiment should be incorporated into the experimental setup. Two examples of experimental setups toward that goal are shown in the previous section. Optimization of the setups is required to make them routine experiments. Nevertheless, preliminary data shown in the previous section is evidence that both laser polarization modulation and molecular beam chopping via a free-swinging pendulum in the UHV are promising experimental setups.

References

1. R.N. Zare, Optical preparation of aligned reagents. Berichte Der Bunsen-Gesellschaft Phy. Chem. Chem. Phy. **86**(5), 422–425 (1982)
2. R.N. Zare, *Angular Momentum: Understanding Spatial Aspects in Chemistry and Physics* (Wiley, New York, 1988)

3. C.H. Greene, R.N. Zare, Photofragment alignment and orientation. Annu. Rev. Phys. Chem. **33**, 119–150 (1982)
4. A.J. Orr-Ewing, R.N. Zare, Orientation and alignment of reaction products. Annu. Rev. Phys. Chem. **45**(1), 315–366 (1994)
5. W.R. Simpson et al., Reaction of Cl with vibrationally excited CH4 and CHD3—state-to-state differential cross-sections and steric effects for the HCl product. J. Chem. Phys. **103**(17), 7313–7335 (1995)
6. E.H. Van Kleef, I. Powis, Anisotropy in the preparation of symmetric top excited states I. One-photon electric dipole excitation. Mol. Phys. **96**(5), 757–774 (1999)
7. D.R. Killelea et al., Bond-selective control of a heterogeneously catalyzed reaction. Science **319**(5864), 790–793 (2008)
8. O. Swang et al., A theoretical-study of the chemisorption of methane on a Ni(100) surface. Chem. Phys. **156**(3), 379–386 (1991)
9. Y.A. Zhu et al., First-principles calculations of CH4 dissociation on Ni(100) surface along different reaction pathways. J. Mol. Catal. A.Chem. **264**(1–2), 299–308 (2007)
10. B. Xing et al., Investigation the active site of methane dissociation on Ni-based catalysts: A first-principles analysis. J. Mol. Catal. A. Chem. **315**(2), 187–196 (2010)
11. S. Nave, A.K. Tiwari, B. Jackson, Methane dissociation and adsorption on Ni(111), Pt(111), Ni(100), Pt(100), and Pt(110)-(1x2): Energetic study. J. Chem. Phys. **132**(5), (2010)
12. L.B.F. Juurlink et al., Eigenstate-resolved studies of gas-surface reactivity: CH4 (nu(3)) dissociation on Ni(100). Phys. Rev. Lett. **83**(4), 868–871 (1999)
13. L.B.F. Juurlink, R.R. Smith, A.L. Utz, *The role of rotational excitation in the activated dissociative chemisorption of vibrationally excited methane on Ni(100). in General Discussion on Excited States at Surfaces* (Royal Society of Chemistry, Nottingham, 2000)
14. R.D. Beck et al., Vibrational mode-specific reaction of methane on a nickel surface. Science **302**(5642), 98–100 (2003)
15. H.L. Abbott, A. Bukoski, I. Harrison, Microcanonical unimolecular rate theory at surfaces. II. Vibrational state resolved dissociative chemisorption of methane on Ni(100). J. Chem. Phys. **121**(8), 3792–3810 (2004)
16. V.A. Ukraintsev, I. Harrison, A statistical-model for activated dissociative adsorption—application to methane dissociation on Pt(111). J. Chem. Phys. **101**(2), 1564–1581 (1994)
17. A. Bukoski, D. Blumling, I. Harrison, Microcanonical unimolecular rate theory at surfaces. I. Dissociative chemisorption of methane on Pt(111). J. Chem. Phys. **118**(2), 843–871 (2003)
18. D.A. King, M.G. Wells, Molecular-beam investigation of adsorption kinetics on bulk metal targets—nitrogen on tungsten. Surf. Sci. **29**(2), 454 (1972)
19. P. Dobransky, J. Pavlicek, J. Hanzlik, An UHV molecular-beam chopper with continuously varying frequency. Meas. Sci. Technol. **1**(7), 657–658 (1990)
20. R. Bisson et al., Cavity ring-down spectroscopy of jet-cooled silane isotopologues in the Si-H stretch overtone region. J. Chem. Phys. **127**(24), (2007)
21. R. Bisson et al., Vibrational activation in direct and precursor-mediated chemisorption of SiH4 on Si(100). J. Chem. Phys. **129**(8), (2008)

Appendix A
Procedure for 'Locking' OPO Idler Frequency to Lamb Dip

1. Turn on Pump Source of Argos 2400 OPO.
   - steps of 3 W in pump power
   - waiting $\sim$20 s between steps
2. Allow $\sim$1 h for the pump laser to stabilize.
3. Turn on Bristol Wavemeter and open its software.
4. Fill Photodiodes #1 and #2 with liquid N2 and plug in power supplies.

   Judson (J10D-M204-R01M-30) diode with PA-7-60 preamp
   - connect AC coupled preamp output of diode #2 to LaseLock 'input A'
     - gain of 2.5×10^4 V/A
   - connect DC coupled preamp output of diode #2 to scope for viewing
   - DC output of diode #1 is power measurement for saturation curves
5. Fill 1.6 m absorption cell with $\sim$20 microbar of CH_4 (see Fig. A.1)
6. Turn LaseLock system ON.
   - best to connect BNC to Pump laser after LaseLock is ON
   - there is a voltage spike sent from LaseLock when switched ON/OFF
7. Use the DC offset of Laselock to tune near the resonance of interest.
   - pump piezo tuning of 0–90 V continuously tunable 50 GHz
8. Connect 4 BNC outputs of LaseLock to a 4 channel oscilloscope (Fig. A.2)
   - DC output diode #2 preamp
   - SCAN MONitor at LaseLock rear
   - MODulation OUTput on LaseLock front panel
   - ERROR OUTput on LaseLock front panel

B. L. Yoder, *Steric Effects in the Chemisorption of Vibrationally Excited Methane on Nickel*, Springer Theses, DOI: 10.1007/978-3-642-27679-8,

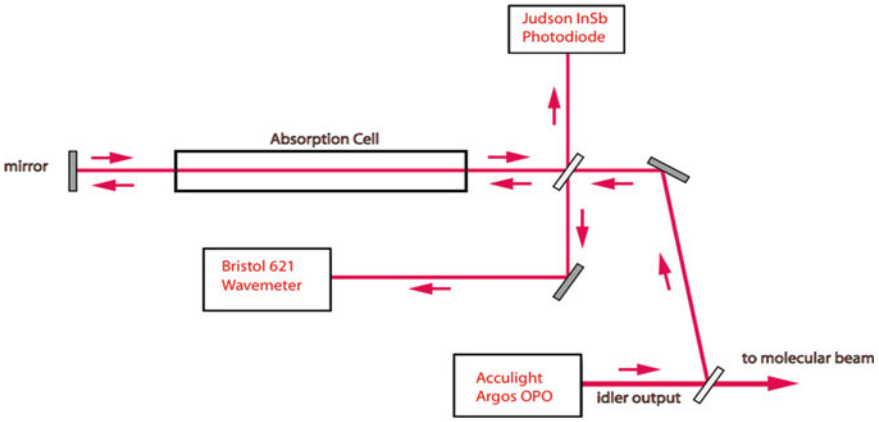

Fig. A.1 Optical layout used to produce Lamb dip signal from ~40 mW OPO idler output

Fig. A.2 Example scope traces observed when one 'modulates' quickly while 'scanning' through a lamb dip

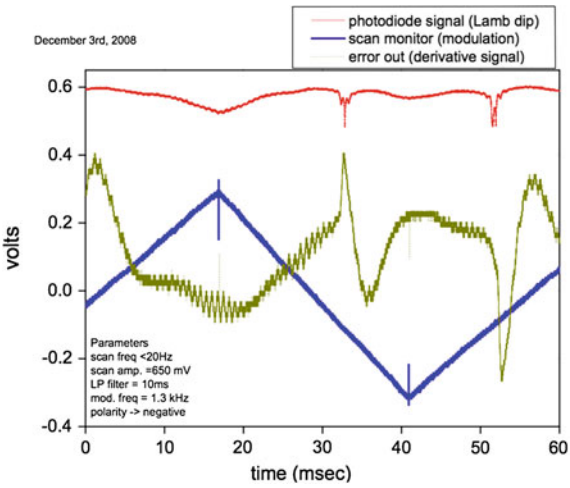

9. Turn on 'scan' generator (triangle wave)
   - scan at <100 Hz and ~1 V_{pp} to find the absorption line
   - center line in 'SCAN' sweep
   - zoom on Lamb Dip by decreasing scan amplitude (~2/10 trim. pot.)
10. Turn on 'LockIN Amplifier'
    - start with modulation amplitude large (> 6/10 on trim. pot.)
    - modulation frequency should be >> than scan frequency
    - the goal is to differentiate the scanned spectrum with fast modulation

11. Modulation is sent to 'regulator'/'slow output' internally
    - no need to connect MOD OUTput to MOD input via front panel
    - variable modulation from 0–13 mVpp after 3 kHz LPass at pump input
    - dial settings

      $9 = 13.0\ mV_{pp}$
      $8 = 12.0$
      $6 = 9.0$
      $5 = 6.5$
      $4 = 5.5$
      $3 = 4.0$
      $2 = 2.0$
      $1.5 = \sim 1.0$ with ~ 0.7 mV of noise

12. Set LowPass filter
    - Should be 'slower' than the modulation frequency
    - dial settings

      $0 = 300$ ms
      $1 = 100$ ms
      $2 = 30$ ms
      $3 = 10$ ms
      $4 = 3$ ms
      $5 = 1$ ms
      $6 = 300\ \mu s$
      $7 = 100\ \mu s$

    - this determines the speed of your correction signal (error out)
13. If derivative signal starts as negative going on rising edge of 'scan' use negative polarity
14. Optimize phase of LockIN to give maximum derivative signal on LIAX
    - this is the real component of the lockIN signal
    - BNC output at rear of LaseLock
15. Disable the 'search' function by turning thresholds to their limits
    - lower threshold to its left stop
    - upper threshold to its right stop
    - search speed becomes irrelevant
16. Set 'set point' to zero
    - this will be used to shift the stabilization point to symmetrize the 2f component of your DC diode signal assuring that we stabilize

17. Start with modest PID settings
    - P = 0 (1 × internal jumper), I = 20% (1x), D = 0 (10x), Gain = 1−2/10 (pot.)
18. With modulation and scan ON, verify derivative signal on scope
    - all termination = 1 Mohm DC
19. Turn regulator to 'align', and see derivative on top of 10 Hz sq. wave
    - used to optimize PID settings
20. Turn off 'scan'
    - if PID is working the rise and fall of the sq. wave acts as a quick perturbation to the locked system. Good PID settings will bring the 'error signal' to zero quickly (before next perturbation) with minimal oscillations.
21. Fine Adjust DC offset until you 'catch' the Lamb Dip with the PID loop
    - look at error signal to know what to do
    - error signal offset can be due to…
    - too low a setting on the total gain amplifier
    - Integrator offset (I setting too low)
    - +we changed the Integrator speed (Ispeed/100 via internal jumper)
    - +this slows the speed at which the integrator reaches the setpoint for a given gain and allows us to use more gain and more I, which in turn reduces problems of error signal offset…
22. Optimize the PID settings
    - increasing P speeds response (causes oscillations)
    - increasing D reduces oscillations
    - increasing gain amplifies the PID response
    - +requirements for stabile functioning of PID controller
      - I needs to be more the 20% of its full scale
      - total gain needs to be more than 2/10 on its trim pot.
23. Close regulator loop (see Fig. A.3)
    - the error signal should be centered about 0 V
24. Increase scan amplitude to (>6/10) to allow larger locking window
25. When turning OFF unit, set DCoffset = '0' and disconnect BNC to pump first (Figs. A.4, A.5)

Optimized Settings for $CH_4 \nu_3$ R(0) Lamb Dip Stabilization

1. INPUT
   a. Diode-preamp 10^5 gain AC coupled to Input A of LaseLock
   b. Input gain = 1 (0 dial setting)

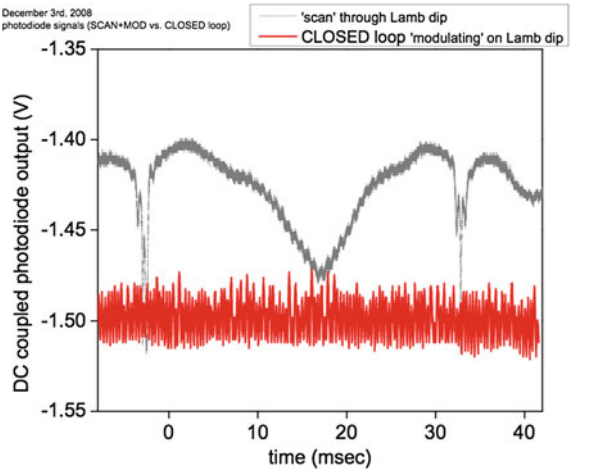

Fig. A.3 Using the DC output of photodiode preamp to demonstrate that we indeed 'lock' to the lamb dip

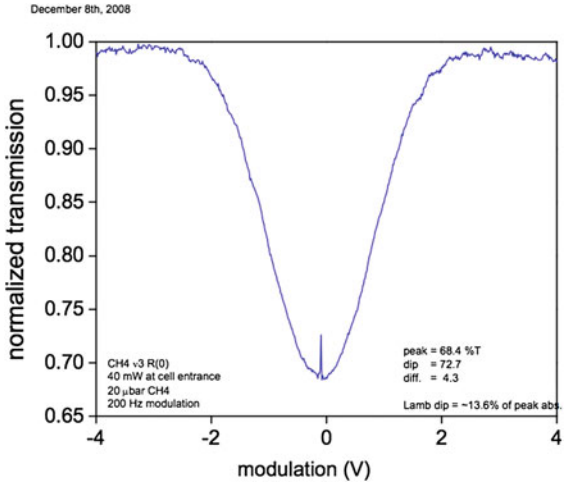

Fig. A.4 Example of lamb dip in Doppler-broadened methane transition

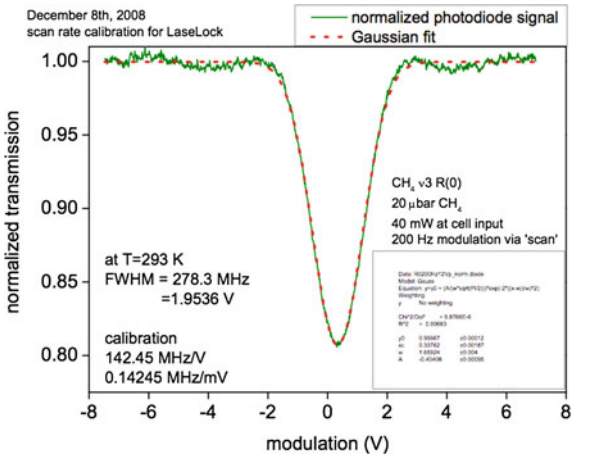

Fig. A.5 Calibration MHz/V via Doppler broadened R(0) line

2. LockIN

   a. Frequency = 3.2 = ∼2 kHz
   b. Phase = 170°
   c. Amplitude = 2/10 = ∼2 mVpp
   d. LP filter = 2 = 30 ms

3. Slow Output Regulator

   a. Polarity = negative
   b. Set point = 0
   c. Total gain = 4
   d. P = <10% (1x)
   e. I = ∼75% (1x)
   f. D = 20% (10x)

4. Scan generator

   a. Frequency = 5.3 = <100 Hz
   b. Amplitude = 2/10 (OPEN regulator loop)
   c. Amplitude = 10/10 (CLOSED regulator loop)

Appendix B
Beta Axis Calculation for R(0), R(1), P(1), Q(1) With and Without K-Resolution

In our experimental setup, alignment of the vibrational transition dipole can be quantified by the alignment coefficient β_{axis}. It was shown in Chap. 3 that

$$\beta_{axis} = \sum_{M} P(M) \sum_{K} P(K) \frac{5[3M^2 - J(J+1)][3K^2 - J(J+1)]}{J(2J+3)(J+1)(2J-1)}.$$

Below, I calculate the β_{axis} coefficients for the various transitions used in this thesis work assuming that $CH_4(v_3)$ and $CD_3H(v_1)$ are equivalently described by β_{axis}. The case of strong optical pumping is implemented into the β_{axis} calculation by assuming that all allowed transitions are equally probable, which differs from the work of Zare and coworkers [1, 2] in that they carried out the calculation in the weak optical pumping limit. In the weak pumping limit, allowed transitions are not equally probable, but their probability is given by the square of their Clebsch-Gordan coefficients.

B.1 Calculation of β_{axis} for $CH_4(v_3)$-R(0) and $CD_3H(v_1)$-R(0) With or Without K-resolution Yields the Same Answer

The rovibrational excited state is described by

$$|JKM\rangle = |100\rangle.$$

The probability (P) of finding $|JKM\rangle$ making projections M and K is

$$P(M = 0) = 1$$
$$P(K = 0) = 1$$

B. L. Yoder, *Steric Effects in the Chemisorption of Vibrationally Excited Methane on Nickel*, Springer Theses, DOI: 10.1007/978-3-642-27679-8,

This makes the calculation of β_{axis} trivial

$$\beta_{axis} = \frac{5[1 \cdot 3 \cdot 0^2 - 1(1+1)][1 \cdot 3 \cdot 0^2 - 1(1+1)]}{1(2 \cdot 1 + 3)(1+1)(2 \cdot 1 - 1)}$$
$$\beta_{axis} = \frac{5[0-2][0-2]}{1(5)(2)(1)}$$
$$\beta_{axis} = 2$$

B.2 Performing the Calculation of β_{axis} for $CH_4(v_3)$-P(1) and $CD_3H(v_1)$-P(1) with or Without K-Resolution Yields the Same Answer

The rovibrational excited state is described by

$$|JKM\rangle = |000\rangle$$
$$P(M=0) = 1$$
$$P(K=0) = 1$$

Again, the calculation of β_{axis} is trivial.

$$\beta_{axis} = \frac{5[1 \cdot 3 \cdot 0^2 - 0(0+1)][1 \cdot 3 \cdot 0^2 - 0(0+1)]}{1(2 \cdot 0 + 3)(0+1)(2 \cdot 0 - 1)}$$
$$\beta_{axis} = 0$$

This corresponds to an isotropic (unaligned) state.

B.3 Performing the Calculation of β_{axis} for $CD_3H(v_1)$-R(1) with and Without K-Resolution Produces a Difference in the Tabulated Alignment Coefficient. First, I Consider the Case Without K-Resolution

This valid for $CD_3H(v_1)$-R(1) without K-resolution and $CH_4(v_3)$-R(1).

$|JKM\rangle = \left\{ \begin{array}{ccc} |211\rangle & |201\rangle & |2-11\rangle \\ |210\rangle & |200\rangle & |2-10\rangle \\ |21-1\rangle & |20-1\rangle & |2-1-1\rangle \end{array} \right\}$ are all equally probable final states.

Therefore,

$$\begin{aligned} P(M=1) &= \frac{1}{3} & P(K=1) &= \frac{1}{3} \\ P(M=0) &= \frac{1}{3} \quad \text{and} & P(K=0) &= \frac{1}{3} \\ P(M=-1) &= \frac{1}{3} & P(K=-1) &= \frac{1}{3} \end{aligned}$$

Calculation of β_{axis} becomes

$$\beta_{axis} = \frac{5\left\{\begin{array}{c} \frac{1}{3}\left[3\cdot -1^2 - 2(2+1)\right] + \cdots \\ \frac{1}{3}\left[3\cdot 0^2 - 2(2+1)\right] + \cdots \\ \frac{1}{3}\left[3\cdot 1^2 - 2(2+1)\right] \end{array}\right\}_{M=0,\pm 1} \left\{\begin{array}{c} \frac{1}{3}\left[3\cdot -1^2 - 2(2+1)\right] + \cdots \\ \frac{1}{3}\left[3\cdot 0^2 - 2(2+1)\right] + \cdots \\ \frac{1}{3}\left[3\cdot 1^2 - 2(2+1)\right] \end{array}\right\}_{K=0,\pm 1}}{2(2\cdot 2+3)(2+1)(2\cdot 2-1)}$$

$$\beta_{axis} = \frac{5\cdot\frac{1}{3}\{[3-6]+[0-6]+[3-6]\}\cdot\frac{1}{3}\{[3-6]+[0-6]+[3-6]\}}{2(7)(3)(3)}$$

$$\beta_{axis} = \frac{5\cdot\frac{1}{9}\{-12\}\{-12\}}{126} = \frac{80}{126} = 0.635$$

B.4 Considering $CD_3H(v_1)$-R(1) Case With K-Resolution…

–For $CD_3H(v_1)$-R(1) K = 0,

$$|JKM\rangle = \left\{\begin{array}{c} |201\rangle \\ |200\rangle \\ |20-1\rangle \end{array}\right\} \text{ are all equally probable final states.}$$

$$\begin{aligned} P(M=1) &= \frac{1}{3} & P(K=1) &= 0 \\ P(M=0) &= \frac{1}{3} \text{ and} & P(K=0) &= 1 \\ P(M=-1) &= \frac{1}{3} & P(K=-1) &= 0 \end{aligned}$$

This gives a β_{axis} coefficient of

$$\beta_{axis} = \frac{5\left\{\frac{1}{3}\left[3\cdot -1^2 - 2(2+1)\right] + \frac{1}{3}\left[3\cdot 0^2 - 2(2+1)\right] + \frac{1}{3}\left[3\cdot 1^2 - 2(2+1)\right]\right\}_{M=0,\pm1} \left\{1\cdot\left[3\cdot 0^2 - 2(2+1)\right]\right\}_{K=0}}{2(2\cdot 2+3)(2+1)(2\cdot 2-1)}$$

$$\beta_{axis} = \frac{5\cdot\frac{1}{3}\{-12\}\{-6\}}{2(7)(3)(3)} = \frac{120}{126} = 0.952$$

–For $CD_3H(\nu_1)$-R(1) K = ±1,

$$|JKM\rangle = \begin{Bmatrix} |211\rangle & |2-11\rangle \\ |210\rangle & |2-10\rangle \\ |21-1\rangle & |2-1-1\rangle \end{Bmatrix} \text{ are all equally probable final states.}$$

$$P(M=1) = \frac{1}{3} \qquad P(K=1) = \frac{1}{2}$$
$$P(M=0) = \frac{1}{3} \quad \text{and} \quad P(K=0) = 0$$
$$P(M=-1) = \frac{1}{3} \qquad P(K=-1) = \frac{1}{2}$$

$$\beta_{axis} = \frac{5\begin{Bmatrix} \frac{1}{3}\left[3\cdot -1^2 - 2(2+1)\right] + \cdots \\ \frac{1}{3}\left[3\cdot 0^2 - 2(2+1)\right] + \cdots \\ \frac{1}{3}\left[3\cdot 1^2 - 2(2+1)\right] \end{Bmatrix}_{M=0,\pm1} \begin{Bmatrix} \frac{1}{2}\left[3\cdot -1^2 - 2(2+1)\right] + \cdots \\ \frac{1}{2}\left[3\cdot 1^2 - 2(2+1)\right] \end{Bmatrix}_{K=\pm1}}{2(2\cdot 2+3)(2+1)(2\cdot 2-1)}$$

$$\beta_{axis} = \frac{5\cdot\frac{1}{3}\{-12\}_{M=0,\pm1}\{-3\}_{K=\pm1}}{126} = \frac{60}{126} = 0.476$$

Consider the average of the K-resolved β_{axis}

$$\frac{\beta_{\text{axis(K=0)}} + \beta_{\text{axis(K=1)}} + \beta_{\text{axis(K=-1)}}}{3} = \beta_{\text{axis(unresolved-K)}} = 0.635$$
$$= \frac{0.972 + 0.476 + 0.476}{3}$$

B.5 $CD_3H(\nu_1)$-Q(1) With or Without K-resolution or $CH_4(\nu_3)$-Q(1)

$$|JKM\rangle = \begin{Bmatrix} |111\rangle & |1-11\rangle \\ |11-1\rangle & |1-1-1\rangle \end{Bmatrix} \text{ are all equally probable final states.}$$

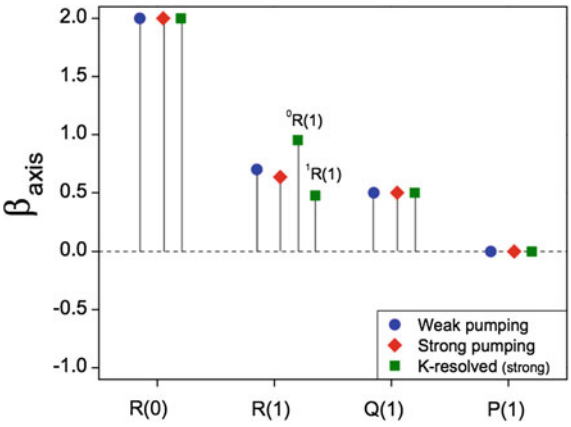

Fig. B.1 Comparison of alignment coefficients for the vibrational transition dipole in the case of strong and weak pumping

$$\begin{aligned} P(M=1) &= \frac{1}{2} & P(K=1) &= \frac{1}{2} \\ P(M=0) &= 0 \quad \text{and} & P(K=0) &= 0 \\ P(M=-1) &= \frac{1}{2} & P(K=-1) &= \frac{1}{2} \end{aligned}$$

$$\beta_{axis} = \frac{5\left\{\begin{array}{c}\frac{1}{2}\left[3\cdot -1^2 - 1(1+1)\right]+\ldots \\ \frac{1}{2}\left[3\cdot 1^2 - 1(1+1)\right]\end{array}\right\}_{M=\pm 1}\left\{\begin{array}{c}\frac{1}{2}\left[3\cdot -1^2 - 1(1+1)\right]+\ldots \\ \frac{1}{2}\left[3\cdot 1^2 - 1(1+1)\right]\end{array}\right\}_{K=\pm 1}}{1(2\cdot 1+3)(1+1)(2\cdot 1-1)}$$

$$\beta_{axis} = \frac{5\{-1\}_{M=\pm 1}\{-1\}_{K=\pm 1}}{1(2\cdot 1+3)(1+1)(2\cdot 1-1)} = \frac{5}{10} = 0.5$$

Figure B.1 is a graph comparing our calculations of in the limit of strong optical pumping to those of Zare [1] under weak pumping conditions.

As shown in Fig. B.1, The alignment produced by R(0), Q(1) and P(1) excitation is independent of the level of optical pumping since they are comprised of a single $|M|$-level transition. This figure does match Simpson et al. [2] for the R(1) calculation under weak pumping conditions, but not for strong pumping because I assumed equally probable all allowed M/K-transitions… If I use the square of the Clebsch-Gordon coefficients for the different M and K transitions…

$$\begin{aligned} P(M=1) &= 0.3 & P(K=1) &= 0.3 \\ P(M=0) &= 0.4 \quad \text{and} & P(K=0) &= 0.4 \\ P(M=-1) &= 0.3 & P(K=-1) &= 0.3 \end{aligned}$$

Taken from the square of the Clebsch-Gordon coefficients

$$\begin{array}{ll} CG(M=1) = 0.5 & CG(K=1) = 0.5 \\ CG(M=0) = 0.67 \quad \text{and} & CG(K=0) = 0.67. \\ CG(M=-1) = 0.5 & CG(K=-1) = 0.5 \end{array}$$

I tabulate β_{axis} with unresolved K-structure to be 0.7 (exactly, what is given in Simpson et al.).

References

1. R.N. Zare, *Angular Momentum: Understanding Spatial Aspects in Chemistry and Physics* (Wiley, New York, 1988)
2. W.R. Simpson et al., Reaction of Cl with vibrationally excited CH4 and CHD3 - state-to-state differential cross-sections and steric effects for the HCl product. J. Chem. Phys. **103**(17), 7313–7335 (1995)

Appendix C
$CD_3H(\nu_1)$ Rovibrational Transitions

Table C.1 Rotational energy levels

CD_3H		v = 0	$\nu_1 = 1$
J	K	E (cm^{-1})	E (cm^{-1})
0	0	0.0000	2992.7454
1	1	5.9080	2998.5888
1	0	6.5581	2999.1928
2	2	17.0735	3009.6715
2	1	19.0232	3011.4835
2	0	19.6732	3012.0878
3	3	33.4963	3025.9926
3	2	36.7441	3029.0123
3	1	38.6931	3030.8262
3	0	39.3428	3031.4311
4	4	55.1760	3047.5512
4	3	59.7196	3051.7777
4	2	62.9659	3054.8016
4	1	64.9140	3056.6179
4	0	65.5634	3057.2236
5	5	82.1126	3074.3462
5	4	87.9490	3079.7778
5	3	92.4900	3084.0115
5	2	95.7343	3087.0405
5	1	97.6813	3088.8599
5	0	98.3303	3089.4667

B. L. Yoder, *Steric Effects in the Chemisorption of Vibrationally Excited Methane on Nickel*, Springer Theses, DOI: 10.1007/978-3-642-27679-8,

Table C.2 R-branch transitions

CD_3H K	$^{K}R(J'')$ J''	ν_1 E (cm^{-1})
0	0	2999.1928
1	1	3005.5754
0	1	3005.5296
2	2	3011.9388
1	2	3011.8029
0	2	3011.7579
3	3	3018.2815
2	3	3018.0575
1	3	3017.9248
0	3	3017.8808

Table C.3 Q-branch transitions

CD_3H K	$^{K}Q(J'')$ J''	ν_1 E (cm^{-1})
0	0	–
1	1	2992.6808
0	1	–
2	2	2992.5980
1	2	2992.4602
0	2	–
3	3	2992.4963
2	3	2992.2683
1	3	2992.1331
0	3	–

Table C.4 P-branch transitions

CD_3H K	$^{K}P(J'')$ J''	ν_1 E (cm^{-1})
0	0	–
1	1	–
0	1	2986.1873
2	2	–
1	2	2979.5656
0	2	2979.5196
3	3	–
2	3	2972.9274
1	3	2972.7904
0	3	2972.7450

References

1. R.S. McDowell, Rotational partition functions for symmetric-top molecules. J. Chem. Phys. **93**(4), 2801–2811 (1990)
2. M. Lewerenz, M. Quack, Vibrational-spectrum and potential-energy surface of the CH chromophore in CHD3. J. Chem. Phys. **88**(9), 5408–5432 (1988)